Experimental and Numerical Investigation of Transonic Turbine Cascade Flow

by

Tibor Kiss

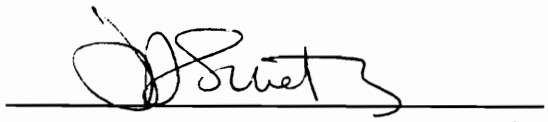
Dissertation submitted to the Faculty of the
Virginia Polytechnic Institute and State University
in partial fulfillment of the requirements for the degree of

Doctor of Philosophy

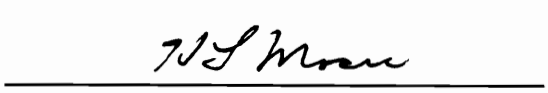
in

Aerospace Engineering

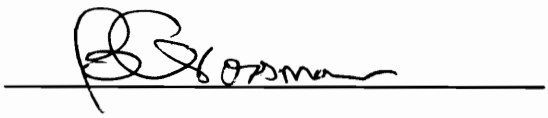
APPROVED:



Dr. J. A. Schetz, Chairman



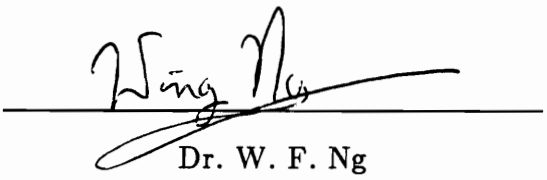
Dr. H. L. Moses



Dr. B. Grossman



Dr. R. W. Walters



Dr. W. F. Ng

December, 1992

Blacksburg, Virginia

Experimental and Numerical Investigation of
Transonic Turbine Cascade Flow

by

Tibor Kiss
Dr. Joseph A. Schetz, chairman
Aerospace Engineering

(ABSTRACT)

A comprehensive study of the flowfield through a two-dimensional cascade of the high pressure turbine blades of a jet engine is presented. The main interest is the measurement and prediction of the mass-averaged total pressure losses. Other experiments, such as flow visualization, are aimed at the validation of the code that was used to obtain the numerical results and also to further knowledge about the details of the loss generation. The experimental studies were carried out on a cascade of eleven blades in a blow-down tunnel. Total pressure measurements were taken upstream of the cascade and also by traversing on downstream planes. The static pressures needed for the mass averaging and the probe bow shock correction were obtained by pressure taps on the cascade tunnel side wall. The static pressure was also measured on the surface of some instrumented blades. Shadowgraph pictures were taken for study of the trailing edge shock structure and for the turbulent transition location. A single-plate interferometer technique was used for density field measurements. The major goal of the numerical studies was the prediction of the mass-averaged total pressure losses, but all other measured quantities were also generated from the computed flowfield. A critical issue was the generation of a proper grid. For the studied type of flow, a non-periodic C-type grid turned out to be the most advantageous. For use in the moderately compressible attached turbulent boundary layer, a Clauser-type eddy viscosity model was developed and tested. In the trailing edge and wake region, the Baldwin-Lomax model was used. Good

agreement of calculations and measurements was obtained for the blade surface and cascade tunnel side wall static pressures, the trailing edge shock structure, and the density field. The agreement between the measured and calculated total pressure drop profiles was not quite as good; however, that quantity is known to be difficult to predict accurately. The mass-averaged total pressure loss coefficient, calculated from the total pressure drop profiles, was again in good agreement with the measurements. The difference between the measured and computed total pressure drop profiles suggested that the Baldwin-Lomax model underpredicted the eddy viscosity in the trailing edge region.

ACKNOWLEDGEMENTS

I am most grateful to Dr. J. A. Schetz, my advisory comittee chairman, who offered me this wonderful opportunity of earning my Ph.D. degree at VPI & SU. Without his continuous help and guidance this work could not have been possible.

I am also very grateful to Dr. H.L. Moses, who guided much of the experimental work in this research. His experience and insights were a tremendous help for me.

Dr. R.W. Walters, who is the first author of the CFD code used in this research gave me very valuable suggestions about the application of his code. I also learned the necessary CFD knowledge from his class.

I would also like to thank to Dr.B. Grossman and Dr. W.F. Ng for serving on my comittee.

I thank GE Aircraft Engines for their financial and technical support, in particular, to B. A. Gregory and M. L. Shelton of the turbine aero and cooling design.

Being almost four years on this project, I was lucky to work with a number of good

fellow graduate students. I made the first step of learning things around the cascade tunnel with the guidance of Omar Zeidan. His humor certainly helped me to get through the hard times of a beginner. Remi Bertsch, Jeff Collie and Roger Doughty joined the project later. Their hard work and great companionship made work so much easier. I will especially miss working with Roger, together with whom I went through almost three years of research. Mike Walls joined us only recently, and his help in taking the flow visualization pictures should be thanked. To him and to Roger I wish the best luck with the continuation of this project.

I received help from other graduate students who were not working on this project. Special thanks to Curtis Mitchell, who spent many hours with me when I was learning how to use the CFD code.

Thanks also go to the personnel of the machine shops of both the Mechanical and Aerospace Engineering Departments for all the work on the equipment. Also, many thanks to Gary Stafford who helped out when the compressor or the electronic equipment were down.

When I was in need of more than just technical assistance, I got support from Linda and my parents. The greatest thanks to you.

TABLE OF CONTENTS

1 INTRODUCTION 1

2 TOTAL PRESSURE LOSS MEASUREMENTS 8

2.1 The Cascade Studied 9

2.2 Instrumentation 10

2.3 Data Acquisition 12

2.4 Data Reduction 14

2.5 Uncertainty Analisys 19

2.6 Previous Results 25

2.7 Search for the Cause of the Scatter 26

2.8 Recent Results 29

2.9 Conclusions 32

3 FLOW VISUALIZATION 33

3.1 Transition Study with Shadowgraph Technique 34

3.2 The Single-Plate Interferometer 36

3.3 Fringe and Image Formation 38

3.4 Interpretation of the Single-Plate Interferograms 41

3.5 Evaluation of the Density Field from Interferograms 49
3.6 The Apparatus 51
3.7 The Shutter 52
3.8 Application to the Original Cascade 55
3.9 Trailing Edge Study on Large Scale Blades 57
3.10 Evaluation of the Large Scale Interferogram 60
3.11 Uncertainty Analysis 64
3.12 Discussion of the Large Scale Blade Results 66
3.13 Some Suggestions for Future Improvements 66

4 COMPUTATIONAL STUDIES 69
4.1 The Computer code 69
4.2 Grid Generation 70
4.3 Turbulence Modeling 76
4.3.1 A New Rational Extension of the Clauser Eddy Viscosity Model . 80
4.3.2 The Baldwin-Lomax Model 94
4.4 Extensions to the CFD code 98
4.4.1 Periodic Boundary Conditions for Non-Periodic Grid 99
4.4.2 Implementation of the Clauser Compressible Model 100
4.4.3 Implementation of the Baldwin-Lomax Model 101
4.5 Supplementary Programs 102
4.5.1 Exit Mach Number 102
4.5.2 Generation of the Numerical Fringes 103
4.5.3 Traverse Interpolation 104
4.6 Running the Code 105
4.7 Convergence 109
4.8 Results 112

5 CONCLUSIONS 117

REFERENCES 121

TABLES 128

FIGURES 136

VITA 291

LIST OF TABLES

Table 2.1 The Experimental Uncertainties(95% confidence level) 129
Table 2.2 Loss Results for Station 1 130
Table 2.3 Loss Results for Station 2 132
Table 5.1 Exit Mach Numbers for the Different Measurements 135

LIST OF FIGURES

Figure 2.1 The definition of the total pressure losses 137

Figure 2.2 Blade Geometry 138

Figure 2.3 The cascade 139

Figure 2.4 Schematic of the cascade tunnel 140

Figure 2.5 Pressure measurement instrumentation 141

Figure 2.6 Blade surface pressure taps 142

Figure 2.7 Schematic of the data aquisition system 143

Figure 2.8 Summary of pressure data for data reduction 144

Figure 2.9 Previous results for Station 1 (by day) 145

Figure 2.10 Results of consequtive runs, same M_e attempted 146

Figure 2.11 Data of Fig.2.10 now as function of run number 147

Figure 2.12 Data of Fig.2.12 now as function of relative humidity 148

Figure 2.13 Previous and recent data for Station 1 149

Figure 2.14 Previous and recent data for Station 2 150

Figure 2.15 Recent data, Station 1 (by days) 151

Figure 2.16 Recent data, Station 2 (by days) 152

Figure 2.17 Recent data, Station 1 (by humidity) 153
Figure 2.18 Recent data, Station 2 (by humidity) 154
Figure 2.19 Recent data, Station 1 (by different losses) 155
Figure 2.20 Recent data, Station 2 (by different losses) 156
Figure 2.21 Pressure data for two runs with same M_e but different loss 157
Figure 2.22 The effect of different corrections for probe bow shock 158
Figure 2.23 Recent data for both stations 159
Figure 3.1 Shadowgraph, $M_e = 0.8$ 160
Figure 3.2 Shadowgraph, $M_e = 0.9$ 161
Figure 3.3 Shadowgraph, $M_e = 1.0$ 162
Figure 3.4 Shadowgraph, $M_e = 1.1$ 163
Figure 3.5 Shadowgraph, $M_e = 1.2$ 164
Figure 3.6 Shadowgraph, $M_e = 1.28$ 165
Figure 3.7 Shadowgraph, large cascade, trailing edge region, $M_e = 1.2$ 166
Figure 3.8 Shadowgraph, large cascade, suction side transition, $M_e = 1.2$ .. 167
Figure 3.9 The Mach-Zehnder interferometer 168
Figure 3.10 The single-plate interferometer 169
Figure 3.11 Fringe spacing vs. wedge angle 170
Figure 3.12 Image separation 171
Figure 3.13 Figure for Equation (3.10) 172
Figure 3.14 Interpretation: A and B separated in the x direction 173
Figure 3.15 Figure 3.14 viewed from the y direction 174
Figure 3.16 Extension of interferogram into a homogeneous density field 175
Figure 3.17a Setup when Eqs.(3.18a), (3.22a) and (3.28a) hold 176
Figure 3.17b The second setup when Eqs.(3.18a), (3.22a) and (3.28a) hold ... 177
Figure 3.17c Setup when Eqs.(3.18b), (3.22b) and (3.28b) hold 178
Figure 3.17d The second setup when Eqs.(3.18b), (3.22b) and (3.28b) hold ... 179
Figure 3.18 Interpretation: A and B are on the same fringe 180

Figure 3.19 Figure 3.18 when viewed from the y direction 181
Figure 3.20 Generation of the combined rule 182
Figure 3.21 Strategy to determine the density field 183
Figure 3.22 The basic idea of the Bragg-cell shutter 184
Figure 3.23 The complete Bragg-cell shutter 185
Figure 3.24 Time dependence of the signals defined in Fig.3.23 186
Figure 3.25 The placement of the glass windows in the original cascade 187
Figure 3.26 Interferogram: Original cascade with tailboard. $M_e = 1.2$ 188
Figure 3.27 Shadowgraph: Large cascade, Blade #2 189
Figure 3.28 The placement of the glasswindows in the large scale cascade ... 190
Figure 3.29 Large cascade interferogram. $M_e = 1.2$ 191
Figure 3.30 The arrangement of the pressure taps in the reference domain .. 192
Figure 3.31 The geometry of the working domain 193
Figure 3.32 Digitized fringes of the working domain 194
Figure 3.33 Contour lines of the fringe function interpolated on a 88 by 90 grid 195
Figure 3.34 Contour lines of the ρ/ρ_{inlet} field in the reference domain 196
Figure 3.35 The evaluation of the trailing edge interferogram 197
Figure 3.36 The ρ/ρ_{inlet} contour lines obtained from the interferogram 198
Figure 3.37 The "two-plate" interferometer 199
Figure 4.1 H-, O-, and C-type grids 200
Figure 4.2 Computational domain and turbulence modeling 201
Figure 4.3 C-type grid, periodic on the periodic boundaries (Ref.[27]) 202
Figure 4.4 Non-periodic C-type grid from Ref.[27] 203
Figure 4.5 The non-periodic C-type grid used for the present studies 204
Figure 4.6 Trailing edge region of the 437×45 grid 205
Figure 4.7 Incompressible, pseudo-laminar profiles 206
Figure 4.8 Pseudo-laminar, compressible profiles for $M_e = 4$ 207

Figure 4.9 Van Driest transformed pseudo-laminar profiles for $M_e = 4$ 208

Figure 4.10 The effect of the Van Driest transformation on the edge velocity 209

Figure 4.11a Defect law-type plot of the transformed pseudo-laminar profiles, $M_e = 0$ 210

Figure 4.11b Defect law-type plot of the transformed pseudo-laminar profiles, $M_e = 2$ 211

Figure 4.11c Defect law-type plot of the transformed pseudo-laminar profiles, $M_e = 4$ 212

Figure 4.11d Defect law-type plot of the transformed pseudo-laminar profiles, $M_e = 6$ 213

Figure 4.12 Transformed pseudo-laminar profiles for all edge Mach numbers 214

Figure 4.13 The transformed pseudo-laminar velocity profiles and velocity defect law 215

Figure 4.14a Normal variation of the predicted eddy viscosity, $M_e = 4$, $u_0/u_e = 0.4$ 216

Figure 4.14b Normal variation of the predicted eddy viscosity, $M_e = 4$, $u_0/u_e = 0.7$ 217

Figure 4.15 Calculated and measured velocity profiles for $M_e = 3.7$ experiment [52] 218

Figure 4.16 Calculated and measured velocity profiles for $M_e = 4.86$ experiment [53] 219

Figure 4.17 F_{WAKE} selection for attached boundary layer 220

Figure 4.18 F_{WAKE} selection for separated boundary layer 221

Figure 4.19 F_{WAKE} selection for wake 222

Figure 4.20 Periodic boundary condition for non-periodic grid 223

Figure 4.21 Turbulent boundary layer with edge defined by $\omega_e/\omega_{max} = 0.01$ rule 224

Figure 4.22 Residual drop for all Mach numbers and all grids 225

Figure 4.23 Residual history for converging and oscillating solutions (219×23 grid) 226

Figure 4.24 Pitot pressure drop traverses, $M_e = 0.9$, 219×23 grid 227
Figure 4.25 Oscillation in loss coefficient 228
Figure 4.26 Density contours for $M_e = 1.2$ 229
Figure 4.27 Pressure contours for $M_e = 1.2$ 230
Figure 4.28 Temperature contours for $M_e = 1.2$ 231
Figure 4.29 Mach number contours for $M_e = 1.2$ 232
Figure 4.30 Velocity vectors around the trailing edge for $M_e = 1.2$ 233
Figure 4.31 Isentropic Mach number profiles, $M_e = 0.8$, Station 1 234
Figure 4.32 Isentropic Mach number profiles, $M_e = 0.8$, Station 2 235
Figure 4.33 Isentropic Mach number profiles, $M_e = 0.9$, Station 1 236
Figure 4.34 Isentropic Mach number profiles, $M_e = 0.9$, Station 2 237
Figure 4.35 Isentropic Mach number profiles, $M_e = 1.0$, Station 1 238
Figure 4.36 Isentropic Mach number profiles, $M_e = 1.0$, Station 2 239
Figure 4.37 Isentropic Mach number profiles, $M_e = 1.1$, Station 1 240
Figure 4.38 Isentropic Mach number profiles, $M_e = 1.1$, Station 2 241
Figure 4.39 Isentropic Mach number profiles, $M_e = 1.2$, Station 1 242
Figure 4.40 Isentropic Mach number profiles, $M_e = 1.2$, Station 2 243
Figure 4.41 Isentropic Mach number profiles, $M_e = 1.28$, Station 1 244
Figure 4.42 Isentropic Mach number profiles, $M_e = 1.28$, Station 2 245
Figure 4.43 Blade surface isentropic Mach numbers, $M_e = 0.8$ 246
Figure 4.44 Blade surface isentropic Mach numbers, $M_e = 0.9$ 247
Figure 4.45 Blade surface isentropic Mach numbers, $M_e = 1.0$ 248
Figure 4.46 Blade surface isentropic Mach numbers, $M_e = 1.1$ 249
Figure 4.47 Blade surface isentropic Mach numbers, $M_e = 1.2$ 250
Figure 4.48 Blade surface isentropic Mach numbers, $M_e = 1.28$ 251
Figure 4.49 Pitot pressure drop, $M_e = 0.8$, Station 1 252
Figure 4.50 Pitot pressure drop, $M_e = 0.9$, Station 1 253
Figure 4.51 Pitot pressure drop, $M_e = 1.0$, Station 1 254

Figure 4.52 Pitot pressure drop, $M_e = 1.1$, Station 1 255
Figure 4.53 Pitot pressure drop, $M_e = 1.1$, Station 2 256
Figure 4.54 Pitot pressure drop, $M_e = 1.2$, Station 1 257
Figure 4.55 Pitot pressure drop, $M_e = 1.2$, Station 2 258
Figure 4.56 Pitot pressure drop, $M_e = 1.28$, Station 1 259
Figure 4.57 Pitot pressure drop, $M_e = 1.28$, Station 2 260
Figure 4.58 Measured and calculated loss coefficients, Station 1 261
Figure 4.59 Measured and calculated loss coefficient, Station 2 262
Figure 4.60 Interferogram, $M_e = 0.8$, setup of Fig.3.17b 263
Figure 4.61 Numerical interferogram, $M_e = 0.8$, setup of Fig.3.17b 264
Figure 4.62 Interferogram, $M_e = 0.9$, setup of Fig.3.17b 265
Figure 4.63 Numerical interferogram, $M_e = 0.9$, setup of Fig.3.17b 266
Figure 4.64 Interferogram, $M_e = 1.0$, setup of Fig.3.17b 267
Figure 4.65 Numerical interferogram, $M_e = 1.0$, setup of Fig.3.17b 268
Figure 4.66 Interferogram, $M_e = 1.1$, setup of Fig.3.17b 269
Figure 4.67 Numerical interferogram, $M_e = 1.1$, setup of Fig.3.17b 270
Figure 4.68 Interferogram, $M_e = 1.2$, setup of Fig.3.17b 271
Figure 4.69 Numerical interferogram, $M_e = 1.2$, setup of Fig.3.17b 272
Figure 4.70 Interferogram, $M_e = 1.28$, setup of Fig.3.17b 273
Figure 4.71 Numerical interferogram, $M_e = 1.28$, setup of Fig.3.17b 274
Figure 4.72 Interferogram, $M_e = 0.8$, setup of Fig.3.17d 275
Figure 4.73 Numerical interferogram, $M_e = 0.8$, setup of Fig.3.17d 276
Figure 4.74 Interferogram, $M_e = 0.9$, setup of Fig.3.17d 277
Figure 4.75 Numerical interferogram, $M_e = 0.9$, setup of Fig.3.17d 278
Figure 4.76 Interferogram, $M_e = 1.0$, setup of Fig.3.17d 279
Figure 4.77 Numerical interferogram, $M_e = 1.0$, setup of Fig.3.17d 280
Figure 4.78 Interferogram, $M_e = 1.1$, setup of Fig.3.17d 281
Figure 4.79 Numerical interferogram, $M_e = 1.1$, setup of Fig.3.17d 282

Figure 4.80 Interferogram, $M_e = 1.2$, setup of Fig.3.17d 283

Figure 4.81 Numerical interferogram, $M_e = 1.2$, setup of Fig.3.17d 284

Figure 4.82 Interferogram, $M_e = 1.28$, setup of Fig.3.17d 285

Figure 4.83 Numerical interferogram, $M_e = 1.28$, setup of Fig.3.17d 286

Figure 4.84 Calculated density contours, large blade, $M_e = 1.2$ 287

Figure 4.85 Isentropic Mach numbers, large cascade, $M_e = 1.2$, $x/c = -0.250$ 288

Figure 4.86 Isentropic Mach numbers, large cascade, $M_e = 1.2$, $x/c = -0.162$ 289

Figure 4.87 Isentropic Mach numbers, large cascade, $M_e = 1.2$, $x/c = -0.074$ 290

NOMENCLATURE

c	speed of light
c_f	skin friction coefficient
c_p	specific of heat
C	axial chord
C_M, C_1, C_2	factors
d	image separation
g	Blasius variable
i	angle of incidence
F	velocity defect variable
F^*, F^+, F^{++}	transformed F-s.
f_{AB_f}	number of fringes between A and B, with flow
f_{AB_n}	number of fringes between A and B, no flow
K	constant, see Eq.(3.11)
k	constant, see Eq.(3.3)
L_1	loss coefficient, no mass ave., no correction
L_2	loss coefficient, exit pressure uniform

L_3	loss coefficient, exit pressure variable
l_m	mixing length
m	see Eq.(17)
M	Mach number
n	index of refraction
P	pitch
p	pressure
R	gas constant
s	difference in traveles, Eq.(3.5)
T	temperature
t	thickness of wedge plate
u	x velocity component
u_τ	friction velocity
V	absolute velocity
v	y velocity component
u^*	Van Driest transformed u
x	streamwise coordinate
y	normal coordinate
Y	normal coordinate in the incompressible plane
w	wedge angle
δ	boundary layer thickness
δ^*	displacement thickness
δ_k^*	kinematic displacement thickness
δ_{VD}^*	displacement thickness calculated from the Van Driest transformed profile
γ	ratio of specific heats
η, η^+, η^{++}	transformed Blasius coordinates
$\overline{\eta}$	Blasius coordinate

η^*_{VD}	η, where $y = \delta^*_{VD}$
λ	wavelength
ρ	density
μ_T	eddy viscosity
ψ	compressible stream function
τ_w	wall shear stress
ω	vorticity

Subscripts

e	free stream value
e	at cascade exit
w	wall, actual
0	wall, pseudo-laminar
t	total value
d	downstream value
p	probe, behind probe bow shock, if present

1 INTRODUCTION

The emergence of gas turbine engines in the 1940's gave rise to revolutionary developments in aviation. The continuous effort to reduce the operational cost of these high output power stations has resulted in engines with high overall efficiency, and by now progress in increasing the efficiency has slowed. However, because of their huge fuel consumption rates, every percent efficiency increase means significant savings of money. Therefore, the race to develop even more efficient engines continues.

An important part of the jet engine is the high pressure turbine, which makes a significant contribution to the overall efficiency. Improvements to the high pressure turbines have been researched extensively. For low size-to-power and weight-to-power ratios the turbine stages operate with high stage work. That can be achieved with high turning of the flow through the rotor and with high exit flow velocity, However, above exit Mach number of 1.0 losses due to the trailing edge shocks increase rapidly, and that sets an upper limit for the outlet velocity. As a result, the high pressure turbines in modern engines have $60 - 70°$ exit flow angle and transonic throughflow. For thermal efficiency, the inlet temperature is high which in turn means the blades need to be cooled. Even with cooling the trailing edges of the blades cannot be too thin because of possible thermal failure. To accelerate

the flow to high exit velocities, the blades in a stage have to act as assemblies of converging-diverging nozzles, and that can be achieved by high blade thickness. High thickness is also needed to accomodate the high load and the cavities for the coolant inside the blades.

The framework of developing new turbine blades can now be seen. The aerodynamic loss is one important factor in this trade off process. Control over the this loss would certainly be desirable, since this could lead to higher efficiency while maintaining the same stage work, or to higher stage work with the same efficiency. However, control over the aerodynamic losses is a distant goal today. The flow is three-dimensional, highly unsteady, turbulent, and significant heat transfer is taking place between the blades and the flow. Our CFD capabilities and the available computer power is not enough today to obtain numerical loss data that could be used effectively in the design process. Even the easier task of accurately measuring the aerodynamic losses is a challenging problem. Measurement of the efficiency through the real turbine is very expensive, and finding the satisfactory blade design may require measurements on several sets of blades. Detailed study of the flowfield is almost impossible in a rotating model.

The above mentioned problems have led to the use of the two-dimensional, stationary cascade approximation. Accurate knowledge of the cascade flowfield can be effectively used for estimating the performance of the real turbine. Again, CFD tools are not reliable today for even this simplified problem. Therefore a lot of experiments have been carried out on cascades of transonic turbine blades. These measurements are cheap compared to measurements in a real engine, and details of the flowfield are easier to study. Cascade measurements can be useful especially when comparing different designs where the difference is more important than the absolute value of the losses. With this kind of information, design decisions can be made. Cascade measurements are also advantageous for the purpose of comparisons

with numerical results. Since more details of the flowfield can be available than for a real engine test, more aspects of the flowfield can be compared with the numerical results. Therefore, there are better chances to develop adequate turbulence models for calculating the cascade flow, and stemming from that, the three-dimensional unsteady flow in the real turbine.

A number of experiments can be found in the literature about total pressure loss measurements in cascades of transonic turbine blades. References [1-8] are some representative examples, with most of them published in recent years. A study of the amount and quality of this published data reveals that low scatter and repeatable measurements are not easy to accomplish. In fact, many of these publications give only a few measured points which are not enough to obtain information about the scatter [1-4]. Some references give a higher number of points, and the scatter can be determined just by looking at the data. For example, Ref.[5] shows 6-20% scatter, and Ref.[6] gives scatter up to 50%. This latter reference is especially interesting since the same blades were tested in four different tunnels, and the importance of the tunnel effect is clearly shown. Only Refs.[7] and [8] contain some estimates for the uncertainties, and they both report an uncertainty of 20% or higher in the measured loss values.

Total pressure loss measurements are usually carried out for comparison between different blade designs, cooling techniques, trailing edge geometries etc., and the effect of these parameters on the losses is often not very high. Uncertainty levels, which in some of the above publications can be found, make it difficult to draw proper conclusions. Therefore, very careful measurements of the total pressure losses are essential, and there is room for improvement of the measurement techniques. Detailed uncertainty analysis can help the preparations for successful measurements.

Total pressure loss measurements at Virginia Tech started in 1987 when the blow-down cascade tunnel was built. Zaccaria [9] described the development of the facility in detail, and also carried out some preliminary measurements. More extensive loss measurements in the facility were reported by Singer [10], who studied trailing edge coolant injection on the losses, and Zeidan [11], who studied the effect of the trailing edge thickness on the losses. At the time of these experiments the tunnel control, instrumentation, and data aquisition system were less sophisticated, and the data reported in these works had significant scatter. Since then, many improvements have been made to the facility and the scatter has been lowered. First, the introduction of a differential pressure transducer for the measurement of the total pressure drop resulted in a great improvement. Next, the tunnel control was changed to a partial feedback system, and since then we have been able to maintain a constant total pressure during the tunnel runs much more accurately. In a second study on the effect of the trailing edge injection, Bertsch [12] obtained much better data due to these improvements, as did Doughty [13], who reported on the effects of the solidity on the losses. Other publications about these previous works in the cascade tunnel at Virginia Tech include Refs.[14-17].

In spite of all the improvements, the scatter could not be lowered to the level where slight differences between the performance of similar designs could be detected. One way to deal with the scatter is the application of statistical methods, as was attempted in Ref.[18]. In that way, significant differences between different blade designs could be determined, even when those differences were not convincing to the naked eye. However, the cause of the scatter was still unknown.

In the following, past work in the numerical prediction of transonic cascade flowfields will be considered, with special interest in total pressure loss prediction. For the prediction of the loss coefficient the first problem is that the total pressure loss can almost be on the order of the numerical errors. Therefore, high resolution of

the grid is essential. As a consequence, considerable computer power is needed to achieve a solution in a reasonable time. Because of a lack of computer power, the numerical prediction of total pressure losses in some of the past studies was attempted by coupling inviscid calculations of the main flow with a boundary layer calculations around the blade. References [19] and [20] applied this method and they obtained fairly good agreement with experimental data. Xu and Denton's work [20] is especially significant. They used an Euler solver for the inviscid flowfield and an integral method for the boundary layer prediction. Finally, they provided the mixed out losses as a function of the exit Mach number for several turbine cascades. Their accuracy in the prediction of the mixed out loss coefficient was within 20% of the measured data for most cases.

While the coupled inviscid-viscous methods are time efficient, they have disadvantages. The base pressure (or trailing edge pressure) is known to have a large contribution to the total pressure losses. Although some references (e.g. Ref.[21]) report that the base pressure can be predicted accurately by inviscid methods, the question is probably still debatable. Also, with the inviscid methods the trailing edge shock structure and shock strength and the actual development of the wake cannot be predicted well. These features of the flowfield have been recognized lately as important factors for the coupled performance with a downstream blade row [22]. Therefore, in recent years, a few cascade flow calculations were reported in which the Navier-Stokes equations were solved for the whole flowfield (see Refs.[22]-[27]). Since in a transonic turbine cascade flow there is a high turning in the flowfield, another difficulty is the generation of a proper grid. Especially for good total pressure loss results, the grid has to resolve the trailing edge region and the wake region at the same time, and still remain unskewed. In Refs.[22]-[27] a variety of grid types were used, and there is still room for improvements in grid generation. Also, for consistently good predictions of the total pressure losses, adequate turbulence mod-

eling with proper treatment of transition is essential. Most of Refs.[22]-[27] used the Baldwin-Lomax model or different $K\epsilon$ type models, and the transition was treated with different empirical correlations. Turbulence modeling is still considered as one of the major issues to be improved. All of Refs.[22]-[27] report good blade surface pressure predictions and fairly good trailing edge shock structure predictions. Total pressure losses, however, are only reported in Refs.[26] and [27]. The predictions in the case of Ref.[26] have a 10-20% error. The test cases included exit Mach numbers of 0.8-1.2 for three different cascades. The loss predictions are more accurate in Ref.[27]; they are within 10%. However, in this work only three different exit Mach number cases were included for only one cascade, and it is not certain that for another cascade the method would work equally well.

We are not aware of studies in which a specific CFD code was applied to a number of different cascades, and good predictions were obtained for all of the test cases. As of today, the prediction of the loss coefficient is considered a problem for which reliable solution without adjustments for the specific problem, cannot be obtained. A good indicator of how engineers still do not trust the numerical loss predictions is the number of experimental cascade studies going on currently.

The goal of this dissertation is to contribute to the improvement of both the measurement and the prediction of the total pressure losses and other important aspects of transonic turbine cascade flowfields. In this study only one blade shape was studied. The experimental flow was adiabatic, neither heating of the main flow, nor cooling of the blades was implemented. It is possible to study some effect of the cooling on the aerodynamic losses in adiabatic flow using heavy gas injection, as was attempted in some previous work in the same facility. However, for the present work, studies in that direction were not pursued. After this introduction, the experiments for obtaining the total pressure losses are described and the results are presented in Chapter 2. In this chapter it is shown, how a careful uncertainty

analysis can help to improve the quality of the experimental data. Chapter 3 reports the flow visualization studies that were carried out for better understanding of the flowfield. First some shadowgraph experiments are discussed which were carried out to determine the transition location on the blades and to visualize the trailing edge shock system. Then, an interferometer is described in detail, including a derivation for the interpretation of the interferograms. The interferometry is applied first to a sizable region of the exit flowfield and then to the flow very close to the trailing edge. The numerical studies are discussed in Chapter 4. First the CFD code is introduced, then the extensive work on the generation of a computational grid is discussed. Next, the turbulence modeling is described, including the development of a new turbulence model. The details of the work with the CFD code, the boundary conditions and the convergence properties are also discussed. The comparisons of numerical predictions and the flowfield measurements are presented and evaluated at the end of the chapter. The conclusions on both the experimental and numerical results are summarized in Chapter 6.

2 TOTAL PRESSURE LOSS MEASUREMENTS

As was emphasized in the Introduction, the mass averaged total pressure loss in the turbine of a jet engine is directly related to the efficiency of the turbine, therefore there is a great interest in the measurement and the prediction of this quantity. The defining equation of the mass-averaged total pressure loss is

$$L = \frac{\int_{y_u}^{y_u+P} p_{tu}(y)\,\rho_u(y)\,V_u(y)\,dy - \int_{y_d}^{y_d+P} p_{td}(y)\,\rho_d(y)\,V_d(y)\,dy}{\int_{y_u}^{y_u+P} p_{tu}(y)\,\rho_u(y)\,V_u(y)\,dy}, \qquad (2.1)$$

where P is the blade spacing or pitch, p_{tu}, ρ_u and V_u are the total pressure, the density and the absolute velocity, respectively, on an upstream plane, and p_{td}, ρ_d and V_d are the total pressure, the density and the absolute velocity, respectively, on a downstream plane (see Fig.2.1). Assuming constant inlet properties, this equation can be rewritten using the continuity equation to obtain

$$L = \frac{\int_{y_d}^{y_d+P} \frac{p_{tu}-p_{td}(y)}{p_{tu}}\,\rho_d(y)\,V_d(y)dy}{\int_{y_d}^{y_d+P} \rho_d(y)\,V_d(y)\,dy}. \qquad (2.2)$$

From here on, the mass-averaged total, pressure loss coefficient as calculated with Eq.(2.2) will be referred to simply as loss coefficient.

In the following first the cascade, the facility and the instrumentation will be described, and the data reduction will be discussed. Then, some previous results will be presented, and it will be shown that the scatter was higher then it should have been on the basis of a thorough uncertainty analysis. Possible reasons for the scatter will be analyzed, and a new operation of the tunnel will be shown to reduce the scatter to the predicted level for cases with exit Mach number less then 1.22. Also, an improvement to the data reduction will be introduced. For the old data, the static pressure across the exit was taken constant, which for higher Mach numbers was a crude approximation. The new data was reduced in this way too, but it also was reduced accounting for the static pressure variation across the exit. The effect on the results will be discussed.

2.1 The Cascade Studied

Real turbine blades change cross section, chord length and shape with increasing radius, therefore choosing a representative two-dimensional profile is not trivial. A reasonable option is to take the cross section at half radius, and use it as the cross section of the two-dimensional blades. Another consideration is that high turning in a wind tunnel is not practical, since the flow usually has to be turned back in the original direction, and that may cause disturbances in the exit flowfield if there is not enough room between the blades and the location of the turning. It is also harder to achieve good periodicity of the flow in the case of high turning. Therefore, in the present application, the tested blades had zero inlet angle, thereby the turning was reduced considerably. This modification however, was assumed to have little effect on the final conclusions.

The cross section and the dimensions of the blades that were used are shown in Fig.2.2. In previous works such as Refs.[11], [12] and [13], these blades were referred

to as the Baseline blades. The tangent of the camber line near the trailing edge was 67°. The radius of the trailing edge was 0.02 in., the axial chord was 1.5 in. and the span was 6 in. The blades were manufactured from stainless steel.

Eleven of these blades were built in a cascade, which is shown in Fig.2.3. The blades were numbered from bottom to top. The pitch of the cascade was 1.4674 in., and the throat line then spanned from very near the trailing edge on the pressure side of one blade, to a point at about 68% the axial chord on the suction side of the next blade below. The frame of the cascade was two Plexiglass plates, referred to from here on as endwalls, and the blades were mounted between them with a screw and a pin on both sides. Also, an endblock was placed below the first blade and another above the eleventh. This way, ten blade passages were created which later proved to be enough for good periodicity of the flow. In most cases, the flow conditions in the cascade were set by the upstream total pressure and the exit pressure. However, sometimes a tailboard was used to turn the flow and thereby to set the exit Mach number (see Fig.2.3).

The cascade was placed in the test section of the cascade tunnel at Virginia Tech, which is a blow-down type tunnel. A schematic of the tunnel can be seen in Fig.2.4. The tunnel is described in detail in Refs.[9],[10],[11] and [12]. Here we only mention that the tunnel was equipped with a feedback control system for the opening of the main valve in order to achieve fairly constant upstream total pressure in time. In this way, the upstream total pressure could be maintained level ($\pm 1\%$) for about 20 seconds, which determined the maximum time for data acquisition.

2.2 Instrumentation

Figure 2.5 summarizes the instrumentation used for the measurement of the pressure data that is needed for the loss calculation. The x axis in the figure was chosen such

that it would be parallel to the inlet flow. The x and y axis both are tangents to Blade 4 near the trailing edge, and they will be used throughout this dissertation. In front of the blades, a single Pitot probe of 1 mm inner diameter was used to measure the total pressure. (In the figure it is not shown at its real location.) This Pitot probe was mounted on the door of the test section, and it reached in far enough to be outside of the boundary layer. A previous study [9] showed that this total pressure, from here on the upstream total pressure, p_{tu}, was constant within 1% throughout the whole flowfield just upstream of the blades, therefore the use of a single probe was justified.

Another Pitot probe of the same diameter was used for total pressure measurements downstream of the cascade. This Pitot probe traversed at midspan on a line parallel to the plane of the trailing edges, or, which is the same, parallel to the y axis. The x-location of the probe could be continuously adjusted. The tip of the probe was angled to be parallel with the average exit flow. The regions of traverses are also shown in the figure. A RAPIDSYN, model 34D-9209 step motor was used to move the probe. The time response of the probe allowed for a traversing speed of 0.1220 pitch/second.

Static pressure measurements in the exit area could not be done with a traversing probe, since that task is very difficult for transonic flows. Therefore, static pressure taps of 1 mm inner diameter were applied on the cascade endwalls, and they will be referred to from now on as wall static pressure taps. Two rows of taps were implemented. The first was 0.25 in. behind the trailing edges, and this location will be called Station 1. The second row was at 1 in. behind the trailing edges, and that location will be called Station 2. Each row consisted of 13 taps, and their locations can be seen in Fig.2.5. The spacing between the taps within a row was 1/10-th of the pitch. Note, that the downstream Pitot probe always traversed on the line of one of these rows of pressure taps, that is, it traversed at either Station

1 or Station 2.

Static pressure measurements were also done on the surface of some specially instrumented blades. The 5-th blade was instrumented with 9 taps on the suction side. The 6-th blade was instrumented with five taps on the pressure side and with one tap right on the trailing edge. All these blade surface static pressure taps were located at midspan. Their exact axial locations are shown in Fig.2.6.

In addition to the pressure measurements, the total temperature was measured with an OMEGA, type K (Chromel-Alumel) thermocouple and the relative humidity was measured with an OHMICO, Model DPS-00-1 polymer resistive humidity sensor well upstream of the blades. These measurements were introduced only towards the end of this study in an effort to find the source of the scatter in the measured loss data.

2.3 Data Acquisition

A schematic of the data acquisition system is shown in Fig.2.7. The upstream total pressure, p_{tu}, was read with a single channel gage pressure transducer. For the downstream total pressure, rather than reading the total pressure on the traversing probe, the difference of the upstream total pressure and the traversing probe pressure, $\Delta p_{tp} = p_{tu} - p_{tp}$, was measured. Measuring this differential total pressure was important for low scatter, since otherwise the small difference between two high quantities would have had to be calculated. A Kulite, type XT-190 miniature differential pressure transducer was used. With a miniature transducer it was possible to achieve a good time response, which is an issue, because the total pressure changed quickly while the probe was traveling through wakes and shocks. Both transducers were calibrated with an AMETEK, model MK100 deadweight tester. The voltage output from both transducers were taken for 8 calibration pressures, and a linear

line was fitted to the calibration points of each transducer with the least squares polynomial approximation. These linear relationships served as calibration curves for the transducers. The calibration curves were checked daily.

For the measurement of the exit static pressures and the blade surface pressures, a PSI Pressure Systems model 780B system was used. This measurement system had a 32 channel transducer (model ESP-32), which was scanned so fast that practically simultaneous readings could be obtained on all 32 channels. An on-line calibration unit allowed the calibration of each channel before each tunnel run.

The tunnel was operated at different tank pressures. An average tunnel run for low tank pressures took about 25 seconds, 5 seconds of which were taken for the upstream total pressure to settle. For the high tank pressures, the settling time was rather 10 seconds, and the total time for the runs was accordingly longer. During the 20 seconds valuable run time, 800 readings of the total pressures took place, which was a rate of 40 readings/second. The traversing probe traveled at 0.1220 pitch/second, which meant 328 readings were taken over a one pitch stretch. The pressure measurement system took 5 measurement sets, one at the instant when the total pressure measurements started, and then one set after every 5 seconds. In fact, for better accuracy, each pressure of each set was an average of 50 readings over a half a second time frame.

The whole data acquisition was controlled by an IBM 5170 personal computer (control PC). The upstream total pressure was displayed by a stripchart, and when it seemed to settle the data acquisition was started manually. The control PC communicated with both the pressure measurement system and with another IBM 5150 personal computer, on which Labtech Notebook was run for taking the total pressure, total temperature and relative humidity data. The stepmotor used for the traversing was also controlled by the control PC. The data was saved on floppy

disks and processed during the time available before the next tunnel run.

2.4 Data Reduction

The goal of the experiments was to determine the loss coefficient as a function of the exit Mach number. A sample of the measured data from which these quantities can be evaluated is shown in Fig.2.8. Note that the measured data originally is a function of readings, but with the data acquisition frequencies it can be converted into a function of time. With the traversing speed, the total pressure drop can then be converted to a function of y. The probe traversed more then two blade passages behind the 4^{th} and 5^{th} blade, and the wakes of the two blades can be seen as peaks in the total pressure drop curve. Equation (2.2) can then be evaluated behind two blades. The difference between the two evaluations characterizes the periodicity of the flow, and the average of the two evaluations reduces the error from non-periodicity. Therefore

$$L = \frac{L_1 + L_2}{2} \tag{2.3}$$

As was mentioned before, 328 readings were taken while the probe traversed one blade passage. Now, two 328 reading stretches of the data in Fig.2.8 have to be chosen for the evaluation of the integral of Eq.(2.2) around the two wakes, respectively. If one assumes the flow to be periodic, then there is some freedom where exactly to put these stretches. This freedom is advantageous when at the beginning or at the end of the run p_{tu} is not maintained very well on the required level, and the stretches for integration can be moved to avoid those regions. Now let stretch a (a=1 or 2) have a starting point j_a, then the mass averaged total pressure loss coefficient can be approximated as

$$L_a = \frac{\sum_{j_a}^{j_a+327} [(p_{tu_j} - p_{td_j})/p_{tu_j}]\, \rho_{d_j}\, u_{d_j}}{\sum_{j_a}^{j_a+327} \rho_{d_j}\, u_{d_j}} \tag{2.4}$$

where the j index means the j-th reading, or for dependent variables, the value derived from the j-th reading of the measured variables. It can be seen that Eq.(2.4) integrates in time instead of space, which is an approximation when perfectly steady flow is not achieved.

More work is still left to determine p_{td_j}, ρ_{d_j} and u_{d_j}. First of all, the static pressure at the probe location, p_{d_j}, is needed. As was mentioned before, the way to obtain the static pressure changed recently, and some of the data that will be presented here was reduced in the old way. Therefore, both ways will be discussed. Earlier, it was argued that the static pressure did not vary excessively in y, therefore an average static pressure of the top ten wall pressure taps, p_{a_j} was used all across the blade passages. The average static pressure was obtained five times during a run from the pressure measurement system scans. The static pressure was needed for every reading of the differential total pressure, therefore between those five measured points, linear interpolation could be used to obtain p_{a_j}. The p_{a_j} curve obtained in this way is included in Fig.2.8 as dotted line. Finally, the assumption was that $p_{d_j} = p_{a_j}$, and that is how Eq.(2.4) was carried out.

Recently, another version of the data reduction program was developed, which was able to calculate the loss coefficient incorporating the effect of the static pressure variation over the traversed region. For that purpose, interpolation of the wall static pressure data in both time and space had to be carried out. The initial position of the probe was important then, and therefore it was measured. For a given j^{th} reading of the total pressures, first the location of the traversing probe was determined from the 328 readings/pitch data acquisition speed. If the probe location turned out to be outside of the range of the top 11 pressure taps, then with the assumption of periodicity an equivalent probe position was found within that range. Then, the two wall static pressure sets were identified which were taken before and after the j^{th} total pressure reading, respectively. Each of these sets were

interpolated for the location of the probe, and the resulting two static pressures were interpolated for the time of the j^{th} reading. The p_{d_j} curve obtained this way is also included in Fig.2.8.

Now we can move on to how p_{td_j}, the total pressure at the location of the traversing probe, was calculated. First, we had to check whether a correction to the measured pressure drop had to be made or not. If the condition

$$\frac{p_{d_j}}{p_{tu_j}} > 0.528 \tag{2.5}$$

held, the flow was considered subsonic and no correction was needed. When Condition (2.5) did not hold, the flow at that point was considered supersonic, and a correction to the measured total pressure drop was needed because of the additional total pressure drop through the bow shock ahead of the traversing probe. The problem was solved iteratively, and, in this description, the j index will be omitted for simplicity. The upstream total pressure, p_{tu}, and the differential total pressure, $\Delta p_{tp} = p_{tu} - p_{tp}$ were given as measured on the transducers, and p_d was given as the static pressure at the probe location obtained with either of the two methods above. The Mach number could be assumed just ahead of the bow shock to be M'_d. Then the static pressure behind the bow shock (Ref.[28]) was

$$p'_{tp} = p_d \left(1 + \frac{2\gamma}{\gamma+1}(M'^2_d - 1)\right) \tag{2.6}$$

The Mach number behind the shock (Ref.[28]) was

$$M'_p = \sqrt{\frac{1 + [(\gamma-1)/2]M'^2_d}{\gamma M'^2_d - (\gamma-1)/2}} \tag{2.7}$$

Then, the total pressure behind the shock could be written as

$$p'_{tp} = p'_p\left(1 + \frac{\gamma-1}{2}M'^2_p\right)^{\frac{\gamma}{\gamma-1}}. \tag{2.8}$$

Finally, iteration was carried out in M'_d until

$$p_{tu} - p'_{tp} = p_{tu} - p_{tp} \tag{2.9}$$

was achieved. Then, the true Mach number ahead of the shock was

$$M_d = M'_d, \tag{2.10}$$

and the corrected total pressure drop was

$$\Delta p_t = p_{tu} - p_d \left(1 + \frac{\gamma - 1}{2} M_d^2\right)^{\frac{\gamma}{\gamma - 1}} \tag{2.11}$$

The velocity and density still had to be determined at the probe location. First, the temperature was calculated by assuming the total temperature being the upstream total temperature and also using the Mach number relation:

$$T_d = T_{tu}(1 + \frac{\gamma - 1}{2} M_d^2). \tag{2.12}$$

(Note, that the total temperature actually can be factored out from both the numerator and the denominator of Eq.(2.4), and therefore it cancels out). Then, the velocity was calculated as

$$u_d = M_d \sqrt{\gamma R T}, \tag{2.13}$$

and the density was calculated as

$$\rho_d = \frac{p_d}{RT}. \tag{2.14}$$

Equations (2.11),(2.12) and (2.13) had to be evaluated for all of readings of stretch a, and then L_a could be calculated from Eq.(2.4). Finally, the average of the two losses, L, could be obtained. From now on the short "measured losses" term will be used for the approximation of the mass-averaged, total pressure losses obtained in the way described above.

As was mentioned before, the exit Mach number was assumed to control the flow through the cascade, that is, all important flow variables were preset by it. The

Mach number across the exit was obviously not uniform, therefore its measurement could have been carried out in several ways, resulting in different quantities for the same flow. However, the method has to be consistent for all compared blade types if comparison between different blade types is planned. Also, when comparing numerical and measured flowfields, the numerical flowfield has to be identified in the same way.

In order to obtain the Mach number at any point of the flowfield, the knowledge of the static pressure and the total pressure is sufficient. For the purpose of identifying the different runs, it is enough to estimate the local total pressure with the total pressure upstream of the blades, p_{tu}, since the total pressure is constant within a few percent throughout the whole flowfield. Mach numbers obtained in this way can be called isentropic Mach numbers, since in case of isentropic flow they would be the true Mach numbers. Also, some kind of spatial average of these Mach numbers is needed across the exit, since then much better repeatability can be achieved. The location where this can be carried out could be Station 1, since we have static pressure data there. Then our definition of the instantaneous average isentropic exit Mach number, M_{e_j}, is

$$M_{e_j} = \sqrt{\left[\left(\frac{p_{tu_j}}{p_{e_j}}\right)^{\frac{\gamma-1}{\gamma}} - 1\right]\frac{2}{\gamma-1}}, \tag{2.15}$$

where p_{e_j} is the instantaneous, spatially averaged exit static pressure, or with our previous notation, p_{a_j} at Station 1.

The instantaneous isentropic exit Mach number is changing throughout the run because of the imperfect control of the upstream total pressure, therefore averaging in time is also desired. The averaging should be carried out over the same two stretches of the 800 readings as were used for the losses, therefore the average

isentropic exit Mach number can be written as

$$M_e = \frac{1}{328} \sum_{j=j_1}^{j_1+327} M_{e_j} + \frac{1}{328} \sum_{j=j_2}^{j_2+328} M_{e_j} \tag{2.16}$$

For our cascade experiments, the average isentropic exit Mach number was obtained in the way described above, and from here on the short term "exit Mach number" will be used for M_e.

2.5 Uncertainty Analysis

The presentation of measured data is only complete when some estimation to the errors in the measurements are given. Conclusions from comparisons between different measurements or between measurements and numerical results can only be drawn properly after a careful uncertainty analysis.

The uncertainty analysis is also a good tool to check whether an experiment is well controlled, that is, all the variables significant in determining the primary measured variable (L for our case) are accounted for. If the predicted uncertainty is significantly less than the actually measured uncertainty, the experiment is not well controlled. In other words in that case, there exists some hidden and changing variable(s) which does (do) not affect the control variables (we assumed M_e to be the only control variable), but has an effect on the primary measured variable.

The uncertainty or accuracy of an experiment is usually given with two figures, the bias error and the imprecision (Ref.[29]). The bias error is the difference between the mean value of the measured quantities and the true value, and the imprecision is the standard deviation of the measured values.

Any change in the circumstances in the course of a measurement can change the experimental uncertainty. Therefore, different subsets of the measured data can have

different uncertainties. For example, a recalibration can change the bias error for the data taken after the recalibration. A change in the atmospheric conditions from one day to the other can cause different bias errors for the data taken on different days. Also, the different bias errors for the different subsets would actually appear as a precision error when the whole set of data is considered together. Therefore, when presenting the uncertainty in some measured data, it should be stated what circumstances were allowed to change during the acquisition of that data. A generalized way to deal with this problem was suggested by Moffat [30], who introduced the notion of replication levels. He considered the precision errors only, stating that the bias error can be removed with careful design. His definition of the 0^{th}, the 1^{st} and N^{th} replication level is the following:

a) 0^{th} order replication level: The only component on this level of uncertainty is the finite resolution of the measuring device. For an analog instrument it is the half of the lowest division, and for a digital device, it is the half of the lowest digit.

b) 1^{st} order replication level: At this order, the random variations in the display of each instrument is involved in the uncertainty. In other words, the effect of the noise in the output of the instrument is incorporated.

c) N^{th} order replication level: At this order, the instruments, the geometry and basically everything is considered variable. The N^{th} order uncertainty allows results from one experiment to be compared with results from another ostensibly similar one, or with true values, or with numerical results.

In fact, more replication levels can be defined for a certain experiment according to the actual course of the data acquisition. It is argued here that the uncertainties on the different replication levels can include bias errors too. In fact, the bias errors are difficult to determine and to eliminate. Instead, it can be stated that the bias error

of lower order replications appears as a precision error on the higher replication level. For example, let us say that an experiment is repeated over many days, and the transducers are calibrated at the beginning of each day. Then, the calibration error which is a bias error for one day's worth of data would appear as a precision error when many days' data are analyzed together.

It can be seen that it is important to describe the actual course of the data acquisition so that the replication levels can be defined. In our experiments, we usually made 15 to 20 tunnel runs each day. This took about four hours, and it covered the whole 0.7-1.4 Mach number range for one measurement station. During one day, the Mach numbers were usually picked randomly, but sometimes we picked the same Mach number for several consecutive runs. Several days of data was obtained for both stations, enough to obtain a good estimation of the amount of scatter. Also, every few weeks the tunnel was taken down for a few weeks, and then it was put back together. The calibration of the transducers used for the total pressure measurements were checked daily, and when they were off more than acceptable (about $\pm 0.5\%$), they were recalibrated. The pressure measurement system recalibrated itself before each run. Also important to note is that the upstream total pressure control was not perfect, therefore there was a random deviation of the exit Mach number from its mean value during each run.

After the above discussion, we arrive at the point where the replication levels for our experiments can be defined, and the different sources of uncertainties can be assigned for the different replication levels. The uncertainties on a certain replication level will be marked with the level number and a letter for future reference.

1^{st} order replication level: For our experiments it is reasonable to combine the 0^{th} and the 1^{st} levels as they are in Moffat's sense into a new 1^{st} order replication level. Then, this level is defined as a few consecutive tunnel runs. According to the above

definition, bias errors here are the drift in the atmospheric pressure (1a), the drift in the p_{tu} transducer calibration (1b) and the drift in the Δp_t transducer calibration (1c). The precision errors include the finite resolution of the data interface card for the p_{tu} transducer (1d) and the Δp_{tp} transducer (1e), the finite number of decimals the pressure measurement system can measure (1f), the calibration error of the pressure measurement system (since it is recalibrated after each run) (1g), the lowest division in the barometer (1h), and the interpolation errors for the static pressure (1i). The interpolation errors for the p_{tu} transducer and the Δp_{tp} transducer are neglected because of the large number of readings. The last but not least error results from the fact that the exit Mach number could not be held exactly constant during the tunnel runs (1j).

2nd order replication level: Data taken on one day belongs here. The daily work usually took four hours, therefore big changes in the atmospheric condition could not happen on this level. However, drift in the atmospheric condition, which was a bias error on Level 1, appears as a precision error here. The same is true for the drift in calibration. So, the bias and precision errors of Level 1 appear as precision errors on Level 2. Additional bias errors on Level 2 are the calibration errors for the day for the p_{tu} transducer (2a) and the Δp_{tp} transducer (2b). Once again, these calibration errors are a lot greater than the errors just from the drift during the few hours of run time. No additional precision errors can be found on this level.

3rd order replication level: The reason for defining this level is the fact that after a few days of operation the cascade was removed from the tunnel, or even more, the whole tunnel was taken apart for a few weeks break. Putting the cascade back in the tunnel can be a source of uncertainty, since it would never go back the same exact way. Therefore, a replication level should be defined for all the data taken within periods when the cascade was not removed. All previous precision and bias errors are precision errors on this level. Additional bias error is the error coming

from the present cascade misalignment (3a).

4^{th} order replication level: All the data taken over a long period of time in the cascade facility using the present instrumentation, tunnel operation and data reduction, are on this level. All previous bias and precision errors appear on this level as precision errors. No additional precision errors can be found. However, a number of bias errors are added at this level. These include errors from the geometrical inaccuracies in the blades and in the cascade endwalls, from the deformation of the cascade due to aerodynamic loads, from the three-dimensionality and nonperiodicity of the flow, from inlet flow condition disturbances such as freestream turbulence and boundary layer development, from calibration of certain instruments such as barometer and traverse mechanism, etc.. It should be mentioned that for the time when the data reduction was done with spatially averaged downstream static pressure, the induced error appeared on this level as a bias error. Later in the discussion of the results the value of this error will be visible.

5^{th} order replication level: This is the N^{th} order replication level in Moffat's sense. If other facilities would also investigate the aerodynamic efficiency of our blades using maybe different approaches (for example a continuous tunnel), then all the data obtained in all these facilities would be on this 5^{th} order replication level. Since other facilities may have this level other than the fifth order, it is better to call it the N^{th} order level. On this level by definition, only precision errors can occur as long as truly the same thing is attempted to be measured in each facility.

Obviously, data obtained on the N^{th} order would be desirable for the designer of the blades for the best judgement. Our 4^{th} order data would be equivalently good, if the bias errors could be determined. Unfortunately, all that can be done with the 4^{th} order bias errors is to neglect them, since they cannot be estimated.

Giving specific values to the above defined errors took a thorough study down to the small details of the data acquisition and also some intuition (see Table 2.1 and note that the errors are listed on the level where they appear as precision errors). Then, we were ready to attempt the evaluation of the errors induced by these raw data errors on the mass-averaged, total pressure losses and in the exit Mach number. Since the data reduction program involves integration and iteration, it is rather complicated to analytically determine the errors in these variables. Therefore, a jitter program (Ref.[30]) was written which perturbates an input variable around some reference case. The uncertainties had to be assumed Mach number dependent, therefore two reference cases were chosen; a low and a high Mach number one. Let the output of the data reduction program with the original measured data of one of these reference cases be L_1 and M_{e_1}. Then, in one of the input data, say x, some Δx error can be introduced, and the output then would be $L_1 + \Delta L$ and $M_{e_1} + \Delta M_e$. Then, the $\Delta L/\Delta x$ and $\Delta M_e/\Delta x$ can be considered as the derivative of L and M_e with respect to the x input variable. If the actual error in the variable is multiplied with the appropriate derivative, the result is the error in L or M_e induced by the error in the input variable. In this way all the errors could be calculated, and these results are also summarized in Table 2.1. The error combined up to the j^{th} replication level $L_{j,comb}$, was calculated with the

$$\Delta L_{j,comb} = \sqrt{\Delta L^2_{j-1,comb} + \Delta L^2_{j,1} + ... + \Delta L^2_{j,n}} \tag{2.17}$$

rule (Ref.[29]), where $L_{j,i}$ means the precision errors that come into consideration on the j^{th} level. From the last row of the table we can conclude, that on the fourth order, or in other words, for all the data obtained in our facility with the present conditions, the precision error in the mass averaged total pressure loss coefficient is less than $\pm 0.12\%$ for all Mach numbers, and the precision error in the exit Mach number is less than ± 0.01 for all Mach numbers. The bias error on this level cannot really be estimated, and once again, our hope is that it is negligible.

Table 2.1 reveals the fact that for further lowering of the uncertainty in our experiments the p_{tu} control (which, in turn, is M_e control) should be improved, and the Δp_{tp} transducer should be upgraded. Better p_{tu} control would be possible with the application of a fast response hydraulic valve, however, significantly better pressure transducers are not available today.

2.6 Previous Results

In the previous section it was concluded that the precision error or scatter in our measurements should be around $\pm 0.12\%$ in the loss coefficient and ± 0.01 in the exit Mach number. It should be emphasised here again that this is only true when the experiments were "controlled" well, that is there were no hidden variables affecting the loss coefficient. In other words, the loss coefficient was truly determined by the exit Mach number only.

A great amount of loss coefficient versus exit Mach number data for Station 1 is shown in Fig.2.9. The data was taken over a long period of time, and they represent the measurement of the same flow with the same tunnel operation, instrumentation and data reduction. This data, which we refer to as "previous" data, was obtained with the assumption of $p_d(t,y) = p_a(t)$. The loss coefficients obtained this way we define as the "Loss 2" or shortly L_2 quantities, therefore in Fig.2.9 Loss 2 is plotted against the the exit Mach number for the previous data. Looking at the data one can notice that the scatter is in the predicted $\pm 0.12\%$ range in the subsonic regime, however, at and above $M_e = 1.0$, the scatter is significantly greater. More careful study shows that the scatter for that part of the data is about $\pm 0.4\%$. The uncertainty analysis was very carefully revised and reevaluated, but this high scatter could not be justified by any means. This problem finally instigated a search for possible variable(s) which could control the loss coefficient along with the exit Mach

number.

2.7 Search for the Cause of the Scatter

The fact that the uncertainty analysis was carried out on the individual replication levels now comes in handy. The symbols in Fig.2.9 mark the data taken on different days, but there is not enough data for one day and for one Mach number to determine whether the scatter also takes place on the 2^{nd} replication level, that is, within the data taken on one day. Therefore, some tests were conducted in which, within a few hours, the same exit Mach number was run over and over. Even if we intended to run the same Mach number, there still was some variation, and therefore in Fig.2.10 the losses are shown against the exit Mach number on a fine scale. The conclusion from the figure is that definitely scatter takes place on the one day level. The amount of scatter even suggests that the differences between the different days play an insignificant role compared to the changes within one day. To learn more, in Fig.2.11 the losses are plotted as function of the run number, or what is basically the same, as a function of time. This plot shows that the scatter on the 1^{st} level is rather good, that is consecutive runs generally have a scatter of about only the predicted $\pm 0.12\%$ level. On the other hand, there is a very definite correlation between time and losses on the long term, or on the level of what was called the 2^{nd} replication level. Therefore, the conclusion was that some variable must have changed during the hours of one day's measurements, and that variable had a strong effect on the losses.

The fact that the high scatter only appeared in the supersonic regime suggested that some mechanism related to the shock losses caused the problem. Several possible effects were considered. One was the total temperature changes in the storage tank. The total temperature was measured from there on, but no correlation with

the scatter could be found. As a matter of fact, the total temperature turned out to be nearly the same ($\pm 3°K$) for all of the runs. Also, if the total temperature had an effect, the loss coefficient should have been considerably different for the two surveyed wakes, since the total temperature dropped during the run considerably. This difference between the wakes, however, was not found. Another assumption was that the changes in the tunnel temperature due to cooling during the day could cause the scatter due to the changing heat transfer. Generally, a slight increase in the losses with time was found, but not for all the cases and not convincingly enough at all. Finally, a third assumption seemed more promising. The fact that high humidity could lead to condensation or condensation shocks was well known before. At high Mach numbers, the air cools down considerably near the exit area, possibly even below the dewpoint. With a simple model it was checked what the minimum absolute humidity was in order for the moisture in the air to not saturate at the exit. A very low value was found, which was not believed to be possible in our tunnel. However, saturation does not necessarily mean condensation, since there may not be enough time for that, or there may not be enough cores on which the saturation can be started. Although the fact that visual signs of saturation were not observed did not support the basic idea, the question of humidity effects was studied in detail.

When the data shown in Figs.2.10 and 2.11. was obtained, it was already anticipated that the humidity could be the reason for the scatter, and the relative humidity gage was already installed. Therefore, now we can plot the same data as a function of the relative humidity, and that is shown in Fig.2.12. The figure definitely suggests that the losses and the humidity are correlated. Even more, except for one point the scatter in Fig.2.12 is about $\pm 0.1\%$, the predicted scatter for the experiment in the case of control. These results were very promising, but further proof was sought. It made sense to attempt to obtain results with very low, or ideally zero

humidity instead of trying to set the humidity at some other value. Efforts were made therefore to explore the different options to lower the relative humidity in the storage tank of the wind tunnel.

A trivial option was to install a new higher capacity dryer between the compressor and the storage tank. The option of heating the air in the storage tanks was also considered. However, both of these options would have meant a significant investment of both money and time, therefore a third option was tried out first. The idea in this third option is that the compressor can be operated at different working conditions resulting in different humidities. The working cycle of the compressor can be modeled as an adiabatic compression to the pressure in the storage tank and then a cooling process to about 300°K. At the end of the cooling, the partial pressure of the water is much higher than the vapor pressure and the water saturates and condenses. The condensed water is removed from the compressor stages, and the air advancing towards the dryer has 100% relative humidity. From this model, it follows that the relative humidity cannot be changed by operating the compressor differently. However, the absolute humidity can be lowered by operating the compressor at higher pressures. Compressing the air to higher pressure means that the partial pressure of the water will be higher too, and more water would condense in the compressor stages. For the data shown in Figs.2.9-2.12, the storage tank pressure was between 160 and 240 psig depending on the Mach number. New data was taken now with a storage tank pressure of 360 psig for all Mach numbers.

2.8 Recent Results

The new results which were obtained running the tunnel with 360 psig tank pressure is presented in this section. Table 2.2 contains the data for Station 1, and Table 2.3 contains the data for Station 2. The total pressure losses calculated in three different ways are included. Loss 1, or L_1, is the loss calculated with no bow shock correction and no mass averaging. Loss 2, or L_2, was defined before, but here it is repeated that it is the loss calculated with the assumption of $p_d(t,y) = p_a(t)$. Loss 3 is the losses calculated with the new method, that is with $p_d = p_d(t,y)$. The average total temperature and humidity are also included. It can be seen from the humidity data, that with the high tank pressure we seemed to achieve our goal and decreased the relative humidity to around 5-8% in most cases.

The central question of whether the scatter in the loss data was reduced or not is answered in Figs.2.13 and 2.14. These figures contain the old and new Loss 2 data for Station 1 and 2, respectively. The new data shows very low scatter up to about $M_e = 1.22$, only on the order of the predicted $\pm 0.12\%$ level. It also seems to go right through the mean values of the previous data. This fact is a little surprising, since in connection with Fig.2.12 we found that lower humidity meant lower losses, and therefore the recent data should be more like a lower envelope to the previous data.

It is interesting that above $M_e = 1.22$ the same amount of scatter is found for the recent data that characterized the old data above $M_e = 1.0$. Figures 2.15 and 2.16 are shown here to check whether the scatter was due to some variable changing from one day to another. The answer is obviously no. In Figs.2.17 and 2.18 the check is on the humidity, as the Loss 3 data is plotted with different symbols for different humidity ranges. There really is no convincing conclusion. In general, higher humidity gave higher losses for the same Mach number, but the humidity

range $6\% < rh < 7\%$ confuses the picture. For this range, the losses change widely for $M_e > 1.22$

Another check can be whether the scatter is present in all three different losses. In Figs.2.19 and 2.20, the Loss 1, Loss 2 and Loss 3 quantities are plotted together for Station 1 and Station 2, respectively, and it can be seen that the scatter exists for all three of them. The presence of the scatter in Loss 1 is the most important information, because it means that the measured variables already carry the scatter, and the scatter is not the result of the data reduction.

It is possible to obtain more insight by comparing the measured variables for two runs which have almost the same exit Mach numbers and very different losses. Let us call the first of these two runs Run 1, and that run had an exit Mach number of 1.304 and $L_1 = 6.71\%$ loss. The other run, referred to as Run 2 had $M_e = 1.309$ and $L_1 = 7.64\%$. Incidentally, the relative humidity values were 6.01% for Run 1, and 9.75% for Run 2, which means that for the case of these two runs, the run with higher relative humidity really had a considerably higher loss. The upstream total pressures, the Pitot pressure drops and the average exit static pressures for the two runs are compared in Fig.2.21. The differences in all three kinds of pressure data are obvious. The Pitot pressure drops do not reveal any region where most of the difference takes place; the two curves seem to be more or less shifted compared to each other. The only thing that can be stated is that, between the two wakes, the difference between the pressure drops is somewhat greater than before the first wake. The foregoing suggests that some process affecting the whole flowfield causes the scatter, and that could be condensation through the trailing edge shocks that impinge on the neighboring blades.

Again, the fact that no visual signs of condensation were ever noticed during regular tunnel runs does not support the previous assumption. The scatter for the

$6\% < rh < 7\%$ high M_e data also cannot be explained on that basis. The influence of the humidity, however, is not ruled out by any means. The scatter at that specific humidity may mean that there is another variable in control and not accounted for, or, more possibly, there is some part of the flowfield unstable for those conditions.

Let us leave the problem of the scatter now and analyze what effect the new data reduction method has on the measured losses, that is, how the Loss 2 and Loss 3 values compare. In Figs.2.19 and 2.20, we already plotted them together. It can be seen that for $M_e < 1.0$ the effect is negligible. The reason is that for low Mach numbers the exit static pressure variation is low, since there are no shocks crossing the traversed line. Also there is no probe bow shock present for those cases. As the Mach number increases, the difference is increasing, and above about $M_e = 1.15$ it is substantial. For Station 1, the difference is greater than for Station 2 which is a result of the fact that the static pressure differences are more smeared out at Station 2. Quantitavely, at $M_e = 1.3$, the differences between the Loss 2 and Loss 3 data are about 0.8% for Station 1 and about 0.6% for Station 2, respectively. For more information on how this difference is generated consider Fig.2.22. Here, some pressure data is shown for an $M_e = 1.2$ run for Station 1. Both static pressure functions are included in the figure. The time and space interpolated value is denoted with p_d, and the spatially averaged is denoted by p_a as before. The three wake survey curves include the Pitot pressure drop, Δp_{tp}, the Pitot pressure drop corrected for the probe bow shock with the spatially averaged static pressure, Δp_{ta}, and the Pitot pressure drop corrected with the time and spatially interpolated static pressure, Δp_{td}. Note, that integrating the Δp_{ta} and the Δp_{td} curves we obtain almost exactly the Loss 2 and Loss 3 values, since the mass averaging has a small effect. It can be seen that over much of the region between the wakes, the Δp_{ta} curve is running way above the Δp_{td} curve, and that can account for the difference between the Loss2 and Loss3 values. The reason is, that in that region, the exit

static pressure is overestimated for Loss2, therefore a lower local Mach number and therefore lower bow shock correction results. Also, it can be noticed that, due to the underestimation of the exit static pressure just around the wake, the local Mach number is overestimated, and the resulting high bow shock correction causes the Δp_{ta} curve even to go below zero. That means an increase of the total pressure which is physically wrong.

Finally, let us present now the recent Loss 3 data for Station 1 and Station 2 together in Fig.2.23. The mixing losses taking place between the two stations are readily obtained from the figure. For exit Mach numbers 0.9, 1.0, 1.1, 1.2 and 1.3, Loss 3 value differences of 0.2, 0.25, 0.8, 1.2 and 1.5 can be given. It is also interesting that the data for each station seem to follow two straight lines joined at $M_e = 1.0$. In other words, the data have breakpoints at $M_e = 1$. This sudden increase in the rate of loss generation as the exit Mach number exceeds 1.0 cannot really be explained by the appearance of the trailing edge shocks, because the derivative of the total pressure loss through a shock with respect to the upstream Mach number is zero at $M = 1.0$.

2.9 Conclusions

The recent changes in the tunnel operation and data acquisition resulted in data with a considerably lower scatter than the data of Refs.[9]-[13] have. The consequences are far reaching. A lot of the previous work, such as trailing edge thickness, trailing edge injection and solidity effect studies could be repeated to arrive at much more meaningful conclusions than before. The aerodynamic performance differences would be much less hidden by the scatter.

The data in Fig.2.23 is the latest and best data available for the blades tested (Baseline blades), and will serve for comparison with numerically obtained results.

3 FLOW VISUALIZATION

In this chapter, shadowgraph and interferometer studies of the cascade flowfield will be discussed. The shadowgraph studies provide the location of the turbulent transition, a piece of information that will be used later in the numerical investigations. The shadowgraph study also provides visualization of the trailing edge shock structure. The interferometer studies provide information on the density field. A single-plate interferometer is used, which is not a commonly known type. After a description of the single-plate interferometer, the interpretation of the interferograms is derived. Then, the actual evaluation strategies are discussed. The interferometer is applied to the exit flowfield, and interferograms useful for later validation of the numerical density field are obtained. Finally, the interferometer is applied to the trailing edge flow of an enlarged cascade, and the density field is obtained in this restricted region.

3.1 Transition Study with Shadowgraph Technique

When calculating turbulent flows, it is an important issue to determine which region of the flowfield is going to be turbulent. Especially when the calculation of the

aerodynamic losses is attempted, an accurate knowledge of the transition location is essential for good final results. Some turbulence models incorporate provisions to determine the location of transition, however, that is probably the hardest problem of turbulence modeling, and no reliable method is known today for cascade flows. Therefore, experimental methods are preferable to deal with the problem of transition. Then, turbulence modeling can be applied to the regions which were determined to be turbulent by the experiments.

A fairly simple way to locate transition for cascade flow is the shadowgraph method, which makes the turbulent eddies visible, and thereby shows the turbulent regions. Unfortunately, the size of the blades that we studied was fairly small. As a consequence, the developing boundary layers were thin, and the analysis of the photographs was difficult. Because of the availability of this experimental method and because other aspects of the flow such as shock structure could also be studied this way, we pursued the transition study with the shadowgraph technique anyhow.

The shadowgraph pictures were taken on the fast, type 57 Polaroid film. A nanopulser was used for the light source, a parabolic mirror with 2 m focal length for the collimator, and another parabolic mirror of 30 in. focal length to generate the picture focusing on the test section. Shadowgraph pictures were taken for the six nominal Mach numbers taking extra care for as perfect setup as possible. Unfortunately, the light source was not strong enough so that we could have passed the light through a really small pinhole, therefore the quality of these pictures were limited. However, workable pictures were obtained, and they are shown in Figs.3.1-3.6. Since these are copies of the original pictures, the transition location of the boundary layers can hardly be seen, however, the wake is clearly turbulent for all Mach numbers. In the original pictures, the transition could be detected in the boundary layers, but not very accurately. Interestingly, for all Mach numbers, the transition was found at about x=-0.2 in. on the suction side, which was about 15% of the axial chord back

from the trailing edge. The flow, however, was found to be laminar for the whole pressure side. Even the trailing edge separation on the pressure side was found to be laminar.

Since a cascade of enlarged blades was available, some shadowgraph pictures of the flow through that cascade were also taken. The enlarged blades had an axial chord of 5 in., otherwise they had exactly the same shape as the original blades. The Reynolds number which was based on inlet conditions and on the axial chord was $8.3 \cdot 10^5$ for $M_e = 1.2$. This was an approximately threefold increase compared to the Reynolds number for the $M_e = 1.2$ runs with the original cascade, therefore the transition location was expected to be different. Two pictures are presented here. Figure 3.7 is a shadowgraph of the trailing edge flow. The conclusion from this picture was that on the pressure side, transition even for the large blades cannot be detected. Since the real size of these blades were so much larger, the turbulence is shown much more clearly than for the smaller blades. The laminar separation at the trailing edge is much more obvious, and in the original picture it can be seen how the turbulence is diffused to the pressure side of the wake. Figure 3.8 clearly shows the location of transition on the suction side. Due to the higher Reynolds number, the transition truly occurred well upstream of the location where it occurred for the original blades. From this picture, which only shows part of the blade, the location of the transition can be determined to be at 35% axial chord back from the trailing edge.

The transition locations given above are not very accurate, mostly because of the small size of the blades. However, it was believed that they still were more accurate than any kind of analytical predictions, therefore this data was used for the numerical studies.

3.2 The Single-Plate Interferometer

The measurement of the complete density field in the cascade can be helpful for understanding the detailed mechanisms of the generation of the total pressure losses. Also, such data serves as a powerful tool for validating turbulence models and CFD codes.

For a cascade flow it is hard to reach into the areas between the blades with any kind of probes. Also, most of the time the length scale is so small compared to the size of the probe, that the probe itself would considerably alter the flowfield that is to be measured. This is especially true for the trailing edge region. Therefore nonintrusive methods for measuring flow variables in a cascade are preferable. Such a method is interferometry which, in general, allows for the determination of the complete density field. The interferometry has other advantages too. With a probe, simultaneous and spatially continuous measurements are impossible. Interferometry provides simultaneous results for a whole domain of the flowfield.

The most widely used type interferometer is the Mach-Zehnder [31], which is depicted in Fig.3.9. The Mach-Zehnder interferometer consists of a spark light source, a lens, a filter to obtain monochromatic light, a collimator lens or mirror to make parallel light beam, two beamsplitters, P1 and P4, and two flat mirrors, P2 and P3, to split up the beam into a working and a reference beam and to bring them back together, and a screen or photographic plate. The two mirrors are usually fixed, and the angles of the two beamsplitters are adjustable. With fine adjustment of the beamsplitters, the working and the reference beam have a very low angle after being brought together by the beam splitter P4, and that leads to fringe formation. When the wind tunnel is not running, both beams are passing through uniform density regions, and the fringes are parallel. When the wind tunnel is running, the density variation in the path of the working beam causes a warping of the wavefronts of the

working beam, which results in a distorted fringe formation. The density distribution over the domain through which the working beam passed can be determined from the fringe pattern.

Two difficulties should be pointed out with respect to the construction and application of the Mach-Zehnder interferometer. First, the angles of the beam splitters have to remain constant within less then about 1 second of arc. These angles are crucial for the fringe formation, therefore very solid vibrationless mounting of the beamsplitters and mirrors is necessary. Second, the spark light source has a low coherence length, which requires the optical pathlengths of the two beams to be almost identical. For cases when the density in the test section is considerably different from the ambient, a so called compensation chamber with density in it similar to the test section density has to be placed in the reference beam. These two problems make the Mach-Zehnder interferometer costly to build and difficult to use.

With the invention of laser, new, more rugged and cost effective interferometer types were reported. The laser has long coherence length, and the compensation chamber is no longer needed. However, using the laser with the conventional Mach-Zehnder interferometer produced low quality pictures due to different new fringe families arising from the beam splitters and windows. The fact that each of these optical plates was capable to forming fringes by itself, however, gave the idea to create a different kind of interferometer, the single-plate interferometer [32].

A single-plate interferometer applies a laser light source as shown in Fig.3.10. The laser beam passes through a beam expander and a spatial filter to obtain high quality light which can be considered to come from a point-like source. The opening beam is collimated by a parabolic mirror and is lead through the test section perpendicular to the plane of the flow. The laser beam then hits a glass wedge plate, which has

a very low (typically 10-30 seconds of arc) wedge angle. Part of the beam reflects from the front surface of the wedge plate, while the rest of the light penetrates into the plate and reflects from the back surface. In this way two overlapping beams are created which have a slight angle between them. The optical path lengths of the two beams are different, but due to the long coherence length of the laser light, the result is still a fringe pattern which is dependent on the density field in the test section. Pictures are taken of this fringe pattern focusing on the test section with a second parabolic mirror. It can be seen from Fig.3.10 that an object in the test section has two images on the picture. This "double image" feature is characteristic of the single-plate interferometer.

Some advantages of the single-plate interferometer compared to the Mach-Zehnder interferometer can easily be seen now. It has already been mentioned that a compensation chamber is not needed. Also, since the wedge angle of the plate does not change with the possible vibration of the wind tunnel environment, there is no need for heavy vibration free mounting of the wedge plate. Furthermore, only a single wedge plate is needed which can be an old schlieren quality wind tunnel window, compared to two beam splitters and two mirrors for the Mach-Zehnder interferometer. A disadvantage is though that the picture qualities are not quite as good and the interpretation of the interferograms is more difficult. More precisely, as we will see later, a domain in the flowfield with known density distribution is required for effective measurements.

Due to the advantages discussed above, for the present project the single-plate interferometer was chosen for density field measurements in the cascade.

3.3 Fringe and Image Formation

In this section some of the key formulas presented in Ref.[32] will be summarized.

First we need to make some definitions (see Fig.3.11). The vector of the light is a unit vector in the direction of the light incoming to the wedge plate, and is denoted by $\bar{l}$. The unit normal to the front surface of the plate is $\bar{n}$. The wedgeness vector, $\bar{w}$, is defined as a vector which is in the plane vertical to both the front and the back surface of the wedge plate, and which is parallel to the front surface and points in the direction of the opening. The vector of the image separation, $\bar{d}$, is the vector which would move one image onto the other on the screen. Its direction will be specified more precisely later.

Now let us first discuss exactly how the fringes are formed and what relationships can be found between the geometry and the fringe spacing. This analysis will be restricted to the case when $\bar{l}$,$\bar{n}$ and $\bar{w}$ all fall in the same plane. In Fig.3.11, a wedge plate with strongly exaggerated wedge angle is depicted. Two light rays are also shown: Ray 1 is denoted with solid line and Ray 2 is denoted with a dashed line. The part of Ray 1 which penetrates the front surface of the wedge plate, reflects from the back surface and refracts when it again crosses the front surface is Ray 1″. Ray 2 hits the front surface at essentially the same spot as where the returning Ray 1″ crosses the front surface. The reflected part of Ray 2 is Ray 2′. The angle of incidence for both rays is i_1 when they arrive at the front surface of the plate. The angle of incidence for Ray 2′ is obviously i_1 too. Ray 1″ however has a slightly different angle of incidence i_3 when leaving the wedge plate, due to the wedgeness of the plate. The wedge angle is denoted by w, and the wavelength is denoted by λ in the figure. The wavefronts belonging to the two rays are also depicted. Where a wavefront of Ray 1″ crosses a wavefront of Ray 2′, a local maximum of laser light intensity occurs. Where a wavefront of either of the rays crosses a negative wavefront of the other, a local elimination of the laser light is the result. (The negative wavefronts are not included in the figure). Now it is helpful to imagine that these wavefronts are moving down along the paths of the rays together, and

the high and low intensity spots separated by a are sweeping over parallel planes vertical to the plane of the figure. If a screen is placed in the way, the result is a fringe pattern of parallel lines with fringe spacing a. With the notation of the figure, the fringe spacing can be obtained from the following three equations:

$$\sin i_3 = n \sin\left[\sin^{-1}\left(\frac{\sin i_1}{n}\right) + 2w\right]$$

$$\Delta i = i_3 - i_1 \tag{3.1}$$

$$a = \frac{\lambda}{2 \sin \frac{\Delta i}{2}} = \frac{\lambda}{\Delta i}$$

where n was the index of refraction of the wedge plate. It should be emphasised that for reasonable fringe spacing, Δi has to be in the order of magnitude of seconds of arc. In that case, Ray $1''$ and Ray $2'$ hit the screen at essentially the same place, so it does not happen as the figure suggests, that the two rays depart from each other considerably.

Another issue is the image separation. Figure 3.12 can be used to find the relationship for the image separation. If we imagine that an object is placed in the way of Ray 1, then obviously there will be two images of that object on the photographic plate, one where Ray $1'$ hits it and one where Ray $1''$ hits it. For the image separation, the very low wedgeness of the plate does not make a difference, and the plate can be considered parallel. Then angles i_1 and i_3 are the same. If the thickness of the plate is t, then the magnitude of the image separation d can be expressed as

$$d = 2t \sqrt{\frac{\sin^2 i_1 - \sin^4 i_1}{n^2 - \sin^2 i_1}} \tag{3.2}$$

Also, the vector of the image separation, $\bar{d}$, is such that $\bar{l}$,$\bar{n}$ and $\bar{d}$ all fall in the same plane. At this point, it should be mentioned that the orientation of the fringes and the image separation can be set independent of each other. The image separation

orientation can be set by rotating the wedge plate and the screen around $\bar{l}$, whereas the fringe orientation can be set by the rotation of the wedge plate around its own unit normal $\bar{n}$.

In the foregoing, we talked about the fringe formation by the single plate interferometer in general, and we assumed that the light beam arriving at the wedge plate was perfectly collimated. When the originally collimated light beam travels through some variable density domain before arriving at the wedge plate, than the collimation is not perfect any more, and the fringe pattern changes accordingly. In the next section an analysis is presented to determine the relationship between the fringe pattern and the density field. We restrict the analysis to the case when the vector of the incidence light, $\bar{l}$, the unit normal of the wedge plate, $\bar{n}$, and the wedgeness vector $\bar{w}$, all fall in the same plane.

3.4 Interpretation of the Single-Plate Interferograms

The interpretation of single-plate interferograms is considerably more difficult then the interpretation of the interferograms taken with the Mach-Zehnder interferometer. For the former, both beams may pass through a variable density medium, while that does not have to be the case with the latter. The author is not aware of any publication where the interpretation for the single-plate interferogram is precisely given, therefore a detailed discussion of the problem follows. We again restrict the analysis to the case where the vector of the incident light, $\bar{l}$, the unit normal of the wedge plate, $\bar{n}$, and the wedgeness vector of the wedge plate $\bar{w}$ all fall in the same plane. Note that in that case the image separation vector $\bar{d}$ is vertical to the fringes.

The single-plate interferometer, just like the Mach-Zehnder interferometer, is based on the fact that the index of refraction for a gas is changing with the density of the

gas. For air the following equation describes this relationship:

$$n - 1 = k\frac{\rho}{\rho_{ref}}, \tag{3.3}$$

where n is the index of refraction, ρ_{ref} is a reference density (1.2518kg/m^3) and $k = 3 \cdot 10^{-4}/\text{kg}$ [33].

Now a basic equation necessary for further discussion will be derived. Consider Fig.3.13, in which two rays, Ray 0 and Ray 1, travel through a medium of width L. The density in the medium is constant in the z direction, but variable in the x direction. For Ray 0, the density is ρ_0 and for Ray 1 the density is ρ_1. The two rays start their travel at Wall 1 at the same time. The question is how much Ray 1 will be ahead of Ray 0 when they both arrive at Wall 2. The solution depends on the speed of light for ρ_0 and ρ_1, which we denote with c_0 and c_1 respectively. Then, the time for Ray 1 to reach the second wall is

$$t_1 = L/c_1. \tag{3.4}$$

In the same time Ray 0 travels $t_1 c_0$. The difference between the travel of the two rays is

$$s = L - t_1 c_0 = L - (L/c_1)c_0. \tag{3.5}$$

The speed of light is related to the index of refraction, n, as

$$c = c_{vacuum}/n \tag{3.6}$$

therefore

$$s = L(1 - n_1/n_0). \tag{3.7}$$

Equation (3.7) can also be written as

$$s = \frac{L}{n_0}\left[(n_0 - 1) - (n_1 - 1)\right] \tag{3.8}$$

and then Eq.(3.3) can be used to obtain

$$s = \frac{L}{n_0}\left[k\frac{\rho_0}{\rho_{ref}} - k\frac{\rho_1}{\rho_{ref}}\right]. \tag{3.9}$$

Finally

$$s = K(\rho_0 - \rho_1) \tag{3.10}$$

where

$$K = \frac{Lk}{n_0\rho_{ref}} \tag{3.11}$$

In the followings, the problem first will be addressed with respect to two points on the interferogram separated in the direction of the image separation only. Secondly, the problem will be addressed with respect to two points on the same fringe on the interferogram. Finally, the two results will be combined into a general rule.

For the first problem, consider Fig.3.14. The direction of the image separation is defined as the direction of the vector which translates the "left" image (Image 1) onto the "right" one (Image 2), and let that direction be the x direction. Obviously, there is some freedom in picking which one is the "left" and which one is the "right" image. Then, the y direction can be defined as the "up" direction, or the direction which is obtained by rotating x counterclockwise 90 degrees in the plane of the picture. The z direction is obviously chosen such that x, y and z constitute a right-handed orthogonal coordinate system. Now let us pick points A and B such that $x_A > x_B$ and $y_A = y_B$, that is A and B are separated in the direction of the image separation only. Two pairs of wavefronts are also illustrated in Fig.3.14. L and R are the two wavefronts with a slight angle between them approaching points A and B when there is flow in the test section, and they would be $L0$ and $R0$ respectively, if there were no flow. Note, that one of them represents a refracted ray and the other a reflected ray. In other words, one of them was reflected from the front surface of the wedge plate, and the other was reflected from the back surface. As yet, we do

not know which is which. The notation of L and R is simply coming from the fact that when we view the interferogram from the z direction, the L type waves seem to come from the left and the R types seem to come from the right. Now, let us look at Fig.3.14 from the y direction and that view is depicted in Fig.3.15. A dashed line is also included in this figure, which is simply the R wavefront translated in such a way that its endpoint on line b coincides with the endpoint of L on line b.

Let us introduce here the fringe function, $f = f(x, y)$, as the number of fringes between the (x, y) point and a reference point P_{ref}. For the sign of f_{AB}, consider the following. The interferogram picture can be extended into a bigger frame if we assume a continuous smooth extension of the flowfield blending into constant density surroundings as in Fig.3.16. Note that in that case, the fringes blend into the no-flow fringe pattern of parallel lines along the edges of the extended interferogram. Then, the fringes can be numbered growing in the x direction, the zeroth being the one on which P_{ref} can be found. We can also denote the fringe number difference between two points, A and B, as $f_{AB} = f_A - f_B$. For example, in Fig.3.16 $f_{AB} = 3 - 2 = 1$ and $f_{CD} = 2 - 3 = -1$. Note, that if the extension of the flowfield and interferogram is not performed, f_{CD} could easily be taken $+1$, which would not be correct.

Now let us go back to Fig.3.15. From the figure it is clear that for no flow the number of fringes between A and B is

$$f_{AB_n} = p/\lambda_0 > 0 \tag{3.12}$$

and for the flow case it is

$$f_{AB_f} = q/\lambda_0. \tag{3.13}$$

It has to be mentioned that q can be negative (for example if R were the dotted line in Fig.3.15, and then we would face the kind of situation represented by points C and D in Fig.3.16. From the geometry q can be expressed with p and s:

$$q = \left[p + s_{RA} + (s_{LB} - s_{RB})\right] - s_{LA} \tag{3.14}$$

or rewriting

$$q = p - \left[(s_{RB} - s_{RA}) - (s_{LB} - s_{LA})\right] \tag{3.15}$$

The s quantities are functions of the densities through which a particular point of a particular wavefront traveled. In this regard, the following definitions can be made. If A is a point on the interferogram, then A_1 is the point in the test section whose location compared to the object in the test section is the same as the location of A in the interferogram compared to Image 1 of the object. Similarly, A_2 is the point in the test section whose location is the same compared to the object as the location of A compared to Image 2 of the object in the interferogram. From this definition, it follows that one of the two rays which arrives at the interferogram at A passes through the test section at A_1 and the other passes through at A_2. Now let us consider Fig.3.17a, where the situation in Fig.3.15 is illustrated but extended with a setup of the test section and wedge plate. In this figure only the wavefronts of the no-flow case are included. Points A_1, A_2, B_1 and B_2 are the points obtained with the definition above. It can be seen from the figure, that for this special case of $\beta > 90°$, the $L0$ wavefront is associated with points A_1 and B_1 in the test section, and the $R0$ wavefront is associated with the A_2 and B_2 points in the test section. Therefore, using Eq.(3.10), the following relationships can be written:

$$\begin{aligned} s_{RB} &= K(\rho_0 - \rho_{B_2}) \\ s_{RA} &= K(\rho_0 - \rho_{A_2}) \\ s_{LB} &= K(\rho_0 - \rho_{B_1}) \\ s_{LA} &= K(\rho_0 - \rho_{A_1}) \end{aligned} \tag{3.16}$$

and all these can be substituted into Eq.(3.15) to obtain:

$$\left[K(\rho_0 - \rho_{B_2}) - K(\rho_0 - \rho_{A_2})\right] - \left[K(\rho_0 - \rho_{B_1}) - K(\rho_0 - \rho_{A_1})\right] = p - q. \tag{3.17}$$

Now we can use Eqs.(3.12) and (3.13) in Eq.(3.17) to obtain

$$(\rho_{A_1} - \rho_{B_1}) - (\rho_{A_2} - \rho_{B_2}) = \frac{\lambda_0}{K}(f_{AB_f} - f_{AB_n}) \qquad (3.18a)$$

After studying Fig.3.17b, it can be concluded that the same equation is valid for that case also.

Figs.3.17a and 3.17b are, however, not the only two ways Fig.3.15 can be extended. Figs.3.17c and 3.17d are two different extensions. They are similar to Fig.3.17a and 3.17b, respectively, but, for these, the wedgeness vector is oriented the opposite, or in other words, $\beta < 90°$. This little difference, however, results in the fact that the $L0$ wavefronts for these cases are associated with A_2 and B_2 in the test section, and the $R0$ wavefronts are associated with A_1 and B_1 in the test section. Then in the above derivation Eqs.(3.16) have to be changed accordingly, and the final result for the cases in Figs.3.17c and 3.17d is

$$(\rho_{A_1} - \rho_{B_1}) - (\rho_{A_2} - \rho_{B_2}) = -\frac{\lambda_0}{K}(f_{AB_f} - f_{AB_n}) \qquad (3.18b)$$

It has to be mentioned, that Figs.3.17a-3.17d include all the possible relevant cases, which means either Eq.(3.18a) or Eq.(3.18b) has to hold for a particular interferogram. Note, that the only difference between Eq.(3.18a) and Eq.(3.18b) is the sign of the first term on the right hand side.

So far, we have determined the meaning of the number of fringes between two points separated in the x direction only. Now, attention is turned to what the meaning of two points being on the same fringe of an interferogram is. Let us take an interferogram and define a coordinate system on it just like we did for the previous problem. Let us pick A and B now in such a way that they are on the same fringe and $x_A > x_B$ as in Fig.3.18. The two wave fronts, L and R, which are producing the fringe are also included in Fig.3.18. The projection of the intersection line of L and R on the plane of the interferogram is the fringe between A and B. Plane A

and Plane B are two flat planes parallel to the $x-z$ plane, and they go through A and B respectively. For clarity Fig.3.19 is included which is Fig.3.18 as viewed from the y direction. In Fig.3.19, lines LA and LB are the intersection lines of wavefront L with plane A and plane B respectively. Similarly, lines RA and RB are the intersection lines of wavefront R with Plane A and Plane B respectively. The wavefronts for the no-flow case are also included, and they are $R0$ and $L0$ respectively. One should picture them as wavefronts L and R would be $L0$ and $R0$ if there was ambient air in the test section. Note that for no flow, the wavefronts are not warped, so their intersection line is the same with Plane A as with Plane B. The advancement of wavefront R compared to $R0$ is s_{RA} and s_{RB} at points A and B respectively. Similarly, the advancement of wavefront L compared to $L0$ is s_{LA} and s_{LB} at points A and B respectively. The dashed line which is parallel with $R0$ and crosses $L0$ right above B helps the derivation. It defines r, and with r, the number of fringes between A and B in the no flow case is

$$f_{AB_n} = r/\lambda_0 > 0. \tag{3.19}$$

r, however, can also be expressed in the following way:

$$r = (s_{LA} - s_{RA}) - (s_{LB} - s_{RB}) \tag{3.20}$$

The s quantities are dependent on the densities, but to determine which densities, we are left with some more work. We can view the interferogram again from the y direction, and the orientation of the wedge plate and test section may be the same again as in Fig.3.17a or Fig.3.17b. In that case, $A2$ and $B2$ are associated with the $R0$ type wavefronts and $A1$ and $B1$ are associated with the $L0$ type wavefronts. The advancement of a light ray due to traveling through a medium of variable density, Eq.(3.10), was already applied in Eqs.(3.16). Equations(3.16) are equally true here, so from Eq.(3.20) we obtain

$$r = [K(\rho_0 - \rho_{A_1}) - K(\rho_0 - \rho_{A_2})] - [K(\rho_0 - \rho_{B_1}) - (\rho_0 - \rho_{B_2})] \tag{3.21}$$

or with Eq.(3.19) after simplification

$$(\rho_{A_1} - \rho_{B_1}) - (\rho_{A_2} - \rho_{B_2}) = -\frac{\lambda_0}{K} f_{AB_n} \tag{3.22a}$$

for the setups of Fig.3.17a and 3.17b. For the setups of Figs.3.17c and 3.17d Eqs.(3.16) again have to be rewritten, and than for those cases the final result is

$$(\rho_{A_1} - \rho_{B_1}) - (\rho_{A_2} - \rho_{B_2}) = \frac{\lambda_0}{K} f_{AB_n} \tag{3.22b}$$

Now, we are ready to make a composite rule from the two rules found for the special cases above. Consider the interferogram on Fig.3.20 which was made with either the setup in Fig.3.17a or Fig.3.17b. A and B now are on different fringes, and they are separated not only in the direction of the image separation, therefore neither of the two cases discussed above is applicable. However, a point C can be defined as the one on the fringe of point A and having the same y coordinate as B. Now for points C and B Eq.(3.18a) can be applied giving

$$(\rho_{C_1} - \rho_{B_1}) - (\rho_{C_2} - \rho_{B_2}) = \frac{\lambda_0}{K}(f_{CB_f} - f_{CB_n}) \tag{3.23}$$

For A and C, Eq.(3.22a) can be applied to obtain

$$(\rho_{A_1} - \rho_{C_1}) - (\rho_{A_2} - \rho_{C_2}) = -\frac{\lambda_0}{K} f_{AC_n} \tag{3.24}$$

The sum of Eq.(3.23) and Eq.(3.24) provides

$$(\rho_{A_1} - \rho_{B_1}) - (\rho_{A_2} - \rho_{B_2}) = \frac{\lambda_0}{K}(f_{CB_f} - f_{AC_n} - f_{CB_n}) \tag{3.25}$$

Obviously

$$f_{AB_n} = f_{AC_n} + f_{CB_n} \tag{3.26}$$

and

$$f_{AB_f} = f_{CB_f} \tag{3.27}$$

Therefore, the final formula for the arrangements of Figs.3.17a and 3.17b is given as

$$(\rho_{A_1} - \rho_{B_1}) - (\rho_{A_2} - \rho_{B_2}) = \frac{\lambda_0}{K}(f_{AB_f} - f_{AB_n}) \qquad (3.28a)$$

For the cases in Figs.3.17c and 3.17d the same derivation can be carried out, except that Eqs.(3.18b) and (3.22b) have to be applied instead of Eqs.(3.18a) and (3.22a). The final result for those cases is

$$(\rho_{A_1} - \rho_{B_1}) - (\rho_{A_2} - \rho_{B_2}) = -\frac{\lambda_0}{K}(f_{AB_f} - f_{AB_n}) \qquad (28b)$$

Again, the only difference between Eqs.(3.28a) and (3.28b) is the sign of the first term on the right hand side. Since Fig.3.17a-d cover all relevantly different arrangements of the test section, screen and wedge plate, the problem of interpretation of the single-plate interferograms is solved.

A problematic part of the evaluation of Eq.(3.28a) or (3.28b) can be the determination of the sign of f_{AB_f}. The extension of the interferogram as was discussed in connection with Fig.3.16 is practically not feasible in many cases. However, a restricted knowledge of the density field is enough, since taking the wrong sign gives an obviously wrong result.

3.5 Evaluation of the Density Field from Interferograms

Now we can summarize how to evaluate a single plate interferogram in general.

1. Assume an $x - y$ coordinate system on the interferogram in such a way that the image separation is in the x direction.

1. Pick A and B on the interferogram, such that $x_A > x_B$

2. Determine f_{AB_n}, the number of fringes between A and B for the case of no

flow. Take the sign of F_{AB_n} such, that it is positive when $x_A > x_B$, and negative otherwise.

3. Determine how many fringes there are between A and B in the case of flow to find the magnitude of f_{AB_f}. Determine the sign of f_{AB_f}.

4. Determine points A_1, A_2, B_1 and B_2 in the test section using the definition in Section 3.4

5. Apply Eq.(3.28a) if the arrangement is such as in Figs.3.17a or 3.17b, or apply Eq.(3.28b) if the arrangement is such as in Figs.3.17c or 3.17d.

Looking at Eqs.(3.28a) and (3.28b), it is clear that if the absolute value of the density at a given point is to be found with the single-plate interferometer technique, the density has to be known at three other location. This inherent feature in general is not to the advantage of this technique. It can be shown, however, that if the density is known in a band of width d (the image separation distance), then the density can be found anywhere else in the test section. In Figure 3.21, Band 1 has a width of d, and the density is known in it. Band 2 is another band of width d and it is adjacent to Band 1. If we assume an A_2 point in Band 2, then A_1 will be in Band 1. B_1 and B_2 can be assumed on the edges of Band 1, and, that way, the density at A_1, B_1 and B_2 is known, therefore the density at A_2 can be calculated from either Eq.(3.28a) or Eq.(3.28b). In this way, the density can be obtained at any point in Band 2, and now Band 2 can take the role of Band 1 to advance further in determining the density field. This process can be continued to determine the density at any location left of Band 1. In a similar way, the density field can be determined to the right of Band 1 too.

It should be mentioned that the single-plate interferometer pictures can be useful for the comparison with numerical results even if the absolute density is not

known anywhere in the picture. The numerical results can be used to generate corresponding fringes numerically using Eq.(3.28a) or (3.28b), and this numerical interferogram can be compared with the real interferogram. In case of agreement, however, it cannot be unequivocally concluded that the calculated density field is accurate. It can be shown that if the numerical results have a linear error of $b+c\cdot x$, the numerical fringes will be exactly the same as the ones obtained with the right density field. To prove this, it is enough to show that

$$(\rho_{A1}-\rho_{B1})-(\rho_{A2}-\rho_{B2})=(\rho'_{A1}-\rho'_{B1})-(\rho'_{A2}-\rho'_{B2}) \tag{3.29}$$

where the prime means the quantity in error. If the error is substituted in the right hand side and $x_{A1}-x_{A2}=x_{B1}-x_{B2}=d$ is noticed, the equality is easily obtained.

3.6 The Apparatus

In this section, some details about the specific single-plate interferometer assembly used in these studies will be given.

A 15mW Helium-Neon laser was used for the light source. This type of laser has a 633 nm wavelength. The diameter of the collimated beam should be set such that the area of interest can receive enough illumination everywhere. This condition required a beam of about 6 in. diameter for our experiments. The diameter and divergence of the original laser light, the focal length of the collimator mirror and the diameter of the collimated beam determines what focal length for the beam expander lens assembly is needed. For our application, a 32 mm focal length for the beam expander was adequate. The maximum pinhole size that still produced a clean, disturbance-free beam was 100μm, and that was used in general.

The wedge plate was 6 in. diameter, and had a thickness of 0.88 in. With $n=1.520$ and a 45° incidence angle, we found 0.654 in. image separation using Eq.(3.2).

The wedgeness angle was not known in advance. The fringe spacing for no-flow conditions was found to be 0.09 in. for 45 degree incidence angle, and from Eq.(3.1) that gave a 15 seconds of arc wedge angle. The second mirror that produced the picture had a 30 in. focal length.

Polaroid, type 57 film was used, which was the fastest available Polaroid film. Achieving adequate exposure time was still so troublesome, that a separate section is dedicated to the problem.

3.7 The Shutter

For the photographic visualization of high speed flows a very short exposure time may be needed when fast fluctuations present in the flowfield tend to make the picture blurred. When a nanopulser is used, like for the Schlieren, shadowgraph or conventional interferometer pictures, the length of the exposure time is not an issue because the nanopulser has a flash of duration of the order of nanoseconds. The exposure time is always short enough to "freeze" the flowfield. When laser light is to be used for the flow visualization, a pulse laser would accomplish a similarly short exposure time. However, pulse lasers are very expensive.

For the present single-plate interferometer studies, we had to use continuous laser. With a continuous laser, finding a way to make the exposure time sufficiently small in the microsecond range is not trivial. Mechanical shutters are out of the question, since they can only operate in the millisecond range. There are some fluid crystal shutters which can work much faster, but still not quite fast enough. They are also expensive.

It is possible to build a very fast shutter with the application of a Bragg-cell. The Bragg cell can be driven by very short square signal to deflect the laser beam for a

correspondingly short time. Then, a primitive shutter can include the Bragg-cell, the driving unit, power supply for the Bragg-cell, a function generator to generate short square signal, a lens assembly and a pinhole (Fig.3.22). The laser beam first goes through the Bragg-cell, then enters the lens assembly which focuses the light on the plate of the pinhole. When the Bragg cell is not excited, the light is blocked by the plate of the pinhole. When the Bragg-cell is excited, part of the beam hits the plate of the pinhole right where the pinhole is, thereby that part of the light can travel through. The result is a nice, disturbance-free, homogeneous expanding laser beam for the time of the square signal.

The above described operation is ideal, but, in practice, a few corrections are needed. The not perfect quality of the laser and the Bragg-cell allows for some scattered laser light to go through the pinhole even when the Bragg-cell is not excited. This light has very low intensity compared to the main beam, but still causes problems. In normal operation, the Polaroid film would be sitting with the camera open for a few seconds, and that is enough for the weak scattered light to ruin the picture. A solution to this problem is the implementation of an additional, mechanical shutter. The mechanical shutter is slow but still fast enough to reduce the amount of scattered light that reaches the film to such a low level that there will be no effect on the film. Of course, the implementation of the mechanical shutter causes new problems. The excitation of the Bragg cell now has to be synchronized with the triggering of the mechanical shutter. This task could be achieved by electrically triggering the mechanical shutter and using a time circuit for proper retardation for the trigger to the Bragg-cell. Unfortunately, the Bragg-cell and the mechanical shutter have to be placed close to each other, and the electrical (solenoid) triggering of the mechanical shutter causes disturbances in the Bragg-cell. Also, the actual time between issuing the trigger to the mechanical shutter and the actual opening is not consistent enough.

The solution to the problem of synchronizing can be the implementation of a photodiode assembly, such as shown Fig.3.23. When the mechanical shutter opens, the main beam hits the lens assembly and partly reflects from it. A photodiode can be placed in the way of this reflected light. This photodiode can then give a voltage signal to trigger the function generator which activates the Bragg-cell. This arrangement was tried, but the result was periodic flashing during the opening of the mechanical shutter. The explanation was that when the Bragg-cell became excited the intensity of the main laser beam fell, and when the excitement was over, it rose again. Therefore just when the flash was over, a new trigger was arriving to the function generator, and the Bragg-cell was excited again. This continued until the mechanical shutter closed. The solution to this problem was the employment of another function generator.

Figure 3.24, which is the time course of the events during the opening of the mechanic shutter, helps to understand how the final version of the shutter assembly worked.

First of all it should be mentioned, that the function generators were operated in such a way that they started with the low voltage part of the square wave when the trigger arrived. The second function generator was placed between the photodiode and the first function generator. The frequency of the signal from this second function generator was set to a value such that the mechanical shutter closed before a single pulse was over. This pulse triggered the first function generator which excited the Bragg-cell. It can be seen that there could be only one trigger signal going to the first function generator, and therefore there could be only a single flash. The above described shutter worked fine for as low as $3\mu s$ exposure time. It probably could have produced even much shorter exposure times, however, that could not be tried because of the lack of laser power.

3.8 Application to the Original Cascade

In a wind tunnel application, the light has to go through the wall of the wind tunnel, therefore part of the wall has to be transparent. The Plexiglass which was used for the cascade endwall for the shadowgraph pictures is not satisfactory for interferometer pictures. The flatness of the window has to be at least $\lambda/4$, and good parallelism is also necessary. Such window can only be manufactured from glass. Quality glass windows, however, are quite expensive, especially when mounting holes are bored in them too. Therefore, it was not feasible to simply change the Plexiglass endwall to a glass endwall. The option of making a new cascade with an aluminum endwall with embedded glass windows was then considered. A window extending well upstream of the blades was an attractive idea, since then the domain with constant density would have been available for the evaluation of the pictures. However, support of the blades still would have required holes in the glass windows. Also, the significant load on the blades could have broken the windows near the stress concentrating holes. Even if that had not happened, the stress on the windows could have distorted the fringe pattern. For all these reasons it was decided that only small glass windows without holes would be used, and they would be embedded into the Plexiglass at some location where no support screw or pin would be in the way.

An obvious choice for the glass windows was the exit region. The actual geometry of the window placement can be seen in Fig.3.25. The windows were placed as far upstream as possible without being too close to the support pins. The windows were 2×2 in. rectangular pieces with $\lambda/4$ flatness, and they were made of Crown glass. Their thickness was 3/8 in., which was not the same as the 1/2 in. thickness of the Plexiglass. Their inner side was flush with the Plexiglass, and silicon glue secured them in place.

The cascade with the embedded glass windows otherwise was exactly the same as the one with which the loss measurements were carried out. The problem with this cascade was that there was no large enough domain with known density which could have been used as a reference domain. Within the area covered by the glass windows, the density could have been obtained only on the lines of the traversing, and even there not very accurately. Therefore, this cascade was only good for interferometer pictures useful for comparison with numerically generated fringes.

As was discussed before, for the case of fringes vertical to the image separation vector still two different interferograms of the same flowfield can be taken. One can be obtained with the setup of either Fig.3.17a or 3.17b, and the other with the setup of either Fig.3.17c or 3.17d. It was worthwhile to take both kinds of pictures since it was expected that one of the two kinds was going to make a fringe pattern better suited for further study. The setups of Figs.3.17b and 3.17d were chosen and, with each, pictures were taken for all six nominal Mach numbers. The images in the original pictures were half of the real size, and the exposure time was 25μs. These parameters were chosen because higher exposure time caused untolerable blur, and larger picture size caused the light intensity to be too low for pictures with good contrast. It also has to be mentioned, that the repeatability was not great due again to the instability of the flowfield. The interferograms are presented in Chapter 5, along with the numerically calculated fringes.

The small sizes of the original pictures were certainly not helpful for the processing, and therefore some solution for increasing the stability of the flow was sought. The use of the tailboard was believed to help, since then a stable surface would have turned the flow instead of an unstable free shear layer. Indeed, pictures with good contrast were obtained with exposure times as high as 100μs, and that allowed for real size pictures. However, the shocks reflecting from the tailboard caused the interferogram to be so disturbed, that comparison with numerically calculated

fringes was not possible. One picture for $M_e = 1.2$ is presented here in Fig.3.26 as an example. Note, that the orientation for this picture is such that here the flow is coming from the right, as opposed to coming from the left, which was the case for the previous pictures. The reason is that a little flat mirror was used to turn the light between the second mirror and the camera in the case of the real size picture of Fig.3.26. Otherwise, due to the equal object and image distances, the wedge plate would have been right between the second mirror and the camera, and would have caused disturbing scattered light on the film.

3.9 Trailing Edge Study on Large Scale Blades

A possibility for absolute density measurement was still sought. Again, the trailing edge region was the main interest, since that is the domain of the flowfield which is the least understood. Then, a domain of the flowfield close to the trailing edge was needed where the density could be measured somehow. This reference area would then serve as Band 1 in Fig.3.21. With the original cascade, most of the domain covered by the glass windows was behind the trailing edge shocks and the total pressure was not available in a big enough region. However, if the windows could have been moved a little more upstream, then they could have covered a region upstream of the trailing edge shocks, where, outside of the boundary layer, the total pressure can be taken as the upstream total pressure, and the total temperature can be taken as the upstream total temperature. Only one more flow variable would then be needed to calculate the density, and that could be the static pressure which can be measured by wall pressure taps. For these reasons, our attention was turned to the idea of using a cascade of 3 1/3 times enlarged blades which was already available. This cascade consisted of only 4 blades. Since the blades were so much bigger, the support pins were much further upstream of the trailing edges, and a greater part of the glass windows could be placed upstream of the trailing edge. The

use of the big blades seemed to be advantageous in other ways too. The thickness of the trailing edges of the original blades was so small that good resolution with the interferometer could hardly be achieved. With the big blades, not only the trailing edge resolution, but also the boundary layer resolution was expected to be much better.

The use of the large cascade however, introduced some questions. The Reynolds number was different from the Reynolds number in the original cascade, and it was not known how serious an effect that could have had on the flow. Also the two-dimensionality of the flow may have been not sufficient with a span to axial chord ratio of 1.2. Fortunately the second question seemed to be answered, since dye flow visualization experiments showed that the two-dimensionality of the flow was still acceptable.

Next we had to decide which blade was the best to use for the trailing edge study. In this regard, we had to do the following considerations. The trailing edges of the large blades were 1/8 in. thick, which is still quite small. In order to not loose many details, the size of the interferogram had to be at least real size, but preferably larger. In turn, the exposure time used for the large blade pictures had to be at least four times longer than it was used for the half size pictures because of the lower light flux. With the original cascade with no tailboard, we were already at the longest exposure time which still did not cause considerable blur. Therefore, it was expected that using no tailboard in the large cascade would result in an unacceptable blur. For this reason, the large scale pictures were planned from the beginning to be made with using tailboard, and changes in the tailboard were done to facilitate its application with the large scale cascade. With the use of the tailboard, it had to be checked whether reflected shocks were making any disturbances near the trailing edge region. In Fig.3.27 the second blade from the top can be seen on a shadowgraph picture. Clearly, the reflected shock is hitting

the blade just above the trailing edge, therefore this blade could not be considered for the trailing edge studies. A shadowgraph picture of the trailing edge of Blade 3 was already shown in Fig.3.7, and that picture showed nice undisturbed flowfield. Also, shadowgraphs of the blade passage between Blade 3 and 4 were taken, which revealed no shocks all the way down to the trailing edge of Blade 3. This was important for the determination of the reference density field, as was mentioned before. For these reasons the trailing edge region of Blade 3 was chosen for the study.

In the next step, decisions had to be made about the glass windows. The fact that we wanted to study a region very near the trailing edge allowed us to use the same small 2×2 in. windows that were used in the original cascade. In determining the exact location for the windows, we had to take into account the image separation, that is we had to place the windows far enough upstream to also cover the reference area. The exact placement can be seen in Fig.3.28. Note, that due to the application of a flat mirror just like for the original cascade with tailboard, the interferograms were going to be such that the flow was coming from the right, and this orientation was therefore used for all figures for the large scale study. After deciding about the placement of the windows, new endwalls were manufactured for the large scale cascade.

The interferograms were taken with the setup of Fig.3.17b. The original image sizes were the real blade size. An exposure time of 100μs was needed with this size for good contrast pictures. Originally it was planned that interferograms would be taken for all 6 nominal Machs numbers. However, because of the blurring so much time and effort went into taking the picture for just the design Mach number of 1.2, that the pictures for the other Mach numbers were not pursued. In fact, it took about twenty trials before a real workable picture was obtained for this Mach number, and this picture is shown in Fig.3.29. The other attempts resulted in pictures

which were sharp in some parts but blurred in others.

The second part of the large scale study was the determination of the reference density field. As discussed before, this was achieved by measuring the static pressures on the wall. The domain of these measurements was determined by knowing that translating the area covered by the pressure taps by one image separation, this area had to cover the trailing edge region. Because of the limited number of pressure transducer channels, only 15 pressure taps were applied for this reference domain. These were arranged in three columns, 5 taps in each column. The geometry of the arrangement is shown in Fig.3.30. Since this domain obviously overlapped the domain of the glass windows, different endwalls with appropriate pressure taps and without glass windows had to be used. Therefore, taking the pictures and measuring the wall static pressures could not be carried out at the same time. However, good care was taken to achieve the same flow conditions for the two measurements. The angle of the tailboard was the same, and the tunnel control was exactly the same, which resulted in very similar upstream conditions, and exit Mach numbers differing by only about 0.002. Also, 12 sets of wall static pressures were taken to reduce uncertainty from repeatability errors.

3.10 Evaluation of the Large Scale Interferogram

Let us now analyze what exactly we can see on the interferogram of Fig.3.29. For better understanding Fig.3.31 is presented. In this figure, both images of Blade 3 and the windows are depicted. The first images are drawn with dashed lines and the second images with solid lines. Although in reality the images of the pressure taps in the reference area do not appear, their first images would be found in the shaded area in Fig.3.31. Note that the location of this shaded area is the same compared to Image 1 as the location of the reference domain compared to Blade 3.

The shaded area is the area in the picture on which we have to work, and therefore let us call it the working domain. The domain in the real cascade, which is the same in relation to Blade 3 as the working domain in relation to Image 2 of the Blade 3 in the interferogram, is the actual domain where the density can be determined, and let us call it the studied domain. Our plan is to determine the fringe function, f, in the working domain and to determine the density field in the reference domain, so that, from the two, we can determine the density field in the studied domain.

The first step was to digitize the working domain of the interferogram. In order to not lose resolution, the picture had to be blown up photographically. The picture in Fig.3.29 was already this blown up version. Then the working domain, where digitization was necessary had to be assigned. The ratio between the real size and the blown up picture was determined by knowing that the height of the glass window was 2 in. in reality. The (0,0) point in the blown up picture was obtained by putting tangents to the trailing edge. Then from the dimensions of Fig.3.31 and the size ratio, the coordinates of the working domain on the blown up picture could be determined.

The digitization of the interferogram was carried out on a Silicon Graphics IRIS 4D/70 workstation. Coordinates of points on each fringe were taken and saved. 5 to 70 points were used on a single fringe, depending on the length of the fringe. The working domain, as digitized, is shown in Fig.3.32.

Next the digitized working domain was converted into a scalar field over an 88 by 90 grid. This meant fringe values were assigned to the grid points, which obviously did not have to fall on an actual fringe. The interpolation first was carried out along the k lines of the grid. As was expected, this method did not do a good job in areas where the main direction of the fringe lines was parallel with the k lines. Therefore, another interpolation was carried out the same way but now along

the j lines of the grid. This method naturally gave bad result in areas where the main direction of the grid lines was parallel with the j lines. The two results were, therefore, combined, keeping one in an area where it was better than the other, and dropping it where it was worse. The results of this combination of the two interpolations is given in Fig.3.33, which will be called the fringe scalar field. Note, that Fig.3.33 is actually the contour lines of the fringe scalar field, and, as that, the lines in it are supposed to be a good approximation of the fringes. Obviously, there could have been a better way for creating the fringe scalar field, but it would have required some serious programming effort that was not justified at this point. One problem with the previously described method was that near the lines where the domains with different interpolation joined, the fringe values did not quite match on the two sides, however, this problem did not introduce considerable error.

So far, we have generated the fringe scalar function over the working domain. In the next step, the density distribution in the reference domain was determined. The reference domain with the locations of the pressure taps was shown in Fig.3.30. The measured static pressures for the 12 tunnel runs were converted into isentropic Mach numbers using the measured upstream total pressure. This way, 12 Mach numbers were obtained for each of the 15 tap locations. These sets of 12 Mach numbers were averaged to obtain one Mach number for each tap location. These Mach numbers then could be converted into densities from the upstream conditions using isentropic relationships. When actually calculating the densities for the interferogram evaluation, those upstream conditions were used which were measured when the interferogram was taken. This procedure was justified because the repeatability of the Mach numbers was much better than that of the upstream conditions.

Once the density was determined at the tap locations, the rest of the reference density field could be obtained again by interpolation. The same grid as was used for the working domain was used for the reference domain. This was an obvious

choice, since in this way on the interferogram, where the reference domain covers the working domain, the fringe function and the reference densities would be given at the same points. The interpolation on the grid points was carried out in a simple way. First, the particular triangular area was determined in which the grid point in question fell (these triangles were marked in Fig.3.30). Then a linear interpolation over this triangle was carried out. The contour lines of the resulted reference density field are shown in Fig.3.34. It can be seen that there is some break in these contour lines due to the relatively crude resolution of the reference field with the pressure taps. Unfortunately, the pressure transducer did not have enough channels to achieve higher resolution.

Now we arrive to the point that we have all tools to evaluate Eq.(3.28a) for the trailing edge region of the large cascade. For this, consider Fig.3.35. The upper part of the figure is Image 2 of the blade, and the working domain. The lower part of the figure is the actual trailing edge region with the studied domain and the reference domain. In the working domain points A and B are assumed, and their counterparts in the studied domain are A_2 and B_2, and their counterparts in the reference domain are A_1 and B_1 respectively. Obviously, A_1 and A_2 are separated by the image separation d, just as B_1 and B_2 are. Note that the studied domain and the reference domain overlap somewhat since they are wider than d, and we were able to choose point A such that A_2 fell in this overlap region. Then, the densities in A_1, A_2 and B_1 are known, since they are all in the reference domain, and Eq.(3.28a) can be used straightforwardly to obtain the density at B_2.

Obviously, there is some freedom where exactly to choose point A. Probably a good choice is such that A_2 will be as close to the trailing edge as possible. Having A_2 close to a pressure tap is also advantageous for reducing error from the interpolation. Furthermore, to chose A on a fringe is also advantageous for the same reason. A point that satisfied more or less all three requirements was the (68,52) point of the

working domain. Obviously, then A_1 is the (68,52) point of the reference domain. Since the image separation is 67 in terms of grid spacing in the j direction, A_2 is the (1,52) point of the reference domain. The B point can be chosen anywhere in the working domain, let it be the (j,k) point. Then, B_1 is the (j,k) point of the reference domain. B_2 is the point in the studied domain, in which we want to determine the density. The studied domain can also be covered with the same size 88 by 90 grid as the reference and the working domains were, and then B_2 is the (j,k) point of the studied domain. Let us denote the densities in the reference domain by ρ_{ref} and in the studied domain by simply ρ, and the foregoing relationships can be written:

$$\begin{aligned} \rho_{A_1} &= \rho_{ref_{68,52}} \\ \rho_{A_2} &= \rho_{ref_{1,52}} \\ \rho_{B_1} &= \rho_{ref_{j,k}} \\ \rho_{B_2} &= \rho_{j,k}. \end{aligned} \tag{3.31}$$

Substituting Eqs.(3.31) into Eq.(3.28a) the density in the B_2 point of the studied domain can be expressed as

$$\rho_{j,k} = \frac{\lambda_0}{K}(f_{AB_f} - f_{AB_n}) + \rho_{ref_{1,52}} - (\rho_{ref_{68,52}} - \rho_{ref_{j,k}}). \tag{3.32}$$

B_2 can run through all (j,k) points in the grid, and in that way, in every grid point of the studied domain the density is obtained. The density contours then can be plotted and they are shown in Fig.3.36.

3.11 Uncertainty Analysis

Looking at Eq.(3.32) it can be seen that the uncertainty in the density field measured with the single-plate interferometer originates from the uncertainty in the fringe functions and the uncertainty in the reference density field. The error in f_{AB_n}

is around 0.1 at all locations. The error in f_{AB_f} depends whether A and B are located somewhere where the fringes are running close or running far away from each other. A reasonable estimation for the error of the fringe function is about $\Delta f = \pm 0.2 ... \pm 0.5$. That can be converted to an error in the fringe function difference of $\Delta f_{AB_f} = \pm\sqrt{2}\cdot 0.2 ... \pm\sqrt{2}\cdot 0.5$. The error in the densities of the reference area is on the order of the error in the isentropic Mach number, that is ± 0.002. Here, the error in the static pressure measurement on the wall is not included, since that can hardly be estimated, as we discussed in the section of the uncertainties for the loss measurements. Anyhow, there is no doubt that the interpolation error for the reference densities is much greater, and therefore dominant. By looking at the contour plot of the reference density field, that error can be estimated to be about ± 0.02. The individual uncertainties than can be combined applying Eq.(2.17) on Eq.(3.32) to obtain

$$\Delta\rho = \pm 0.04 \tag{3.33}$$

It should be noted that the most significant component in this fairly high uncertainty is the uncertainty in the reference density, and therefore the increase in the number of the wall pressure taps should be the first step for improvement. As an alternative, numerical results could be used for the reference densities, since in the isentropic region they are usually predicted accurate enough.

For the uncertainty given in Eq.(3.33), it was assumed that the fringes were identified without doubt. In fact, looking at Fig.3.29. one can question whether that was possible in our case. The author has to admit that some intuition had to be exercised during the digitization, and it cannot be ruled out that through the wake region the fringe function shifted one or two fringes. This fact should be kept in mind, however, the effect on the uncertainty is not estimated here. It just should be mentioned, that if shorter exposure times could have been achieved, the fast fluctuations in the wake would have been "frozen", and the picture in Fig.3.29 would

have been sharp even in the wake region.

3.12 Discussion of the Large Scale Blade Result

The density field obtained with the interferometer is in good qualitative agreement with the physics of the flowfield. The contour lines show that the density is considerably higher on the pressure side than it is on the suction side. On both the suction and pressure sides, the development of the trailing edge shocks from the compression waves can be detected. The density rise through these shocks is clearly seen. Also, the expansion wave is clearly shown on the pressure side trailing edge lip. Furthermore, the density decrease in the boundary layers on both sides is indicated, as is the density decrease in the wake.

3.13 Some Suggestions for Future Improvement

As was emphasized several times before, the biggest problem to achieve better performance of the single plate interferometer is the limited laser power. A pulse laser would be the best solution which would provide enough laser energy in sufficiently short time. If that is not available, a continuous laser of 0.5 - 1.0 W laser power would give a drastic improvement. In fact, a laser like that was tried out at one point during the course of the project. This laser produced very nice fringes when it was operated in the low power ranges, however, when the power was turned up, the quality of the pictures decreased very seriously. It turned out, that, in high power output operation, the light was not monochromatic any more, which resulted in a great loss of contrast of the fringes to the extent that the interferograms were not workable any more. The solution to this problem could have been a laser equipped with a so called ethalon, which is basically a filter with extra low transmission bandwidth. Unfortunately, a laser like that was not available to us, and the experiments

were continued with the 15mW laser.

However, even using the same low power laser still there is room for improvement. About 80% of the laser light is lost on the wedgeplate because most of the light goes straight through, reflecting on neither the front nor the back surface. Coating the back surface for complete reflection, and appropriate partial coating of the front surface can reduce the loss greatly.

Another possible way to achieve lower exposure time is to reduce the size of the beam. This would cause the domain that can be studied with the interferometer to decrease in size. In case of trailing edge studies, that is not necessarily a problem, especially, for the original size blades. The problem with decreasing the collimated laser beam diameter is that, below a certain size, the reflected and the refracted beams do not overlap any more, and fringe formation is impossible. For those cases the setup in Fig.3.37 can be proposed. A glass plate of the same thickness as the wedge plate can be used to separate the original low diameter collimated beam into two parallel beams. One of these beams can go through the domain to be studied (working beam) and the other can go through a domain where the density is known (reference beam). On the other side of the tunnel the wedge plate brings the two beams together to overlap and to form fringes. In fact one can consider this interferometer as a Mach-Zehnder interferometer for which beam splitter P1 and mirror P3 (see Fig.3.9) are brought together in one optical part, and beamsplitter P4 and mirror P2 are brought together into a second one.

This new interferometer, which could be called a "two-plate interferometer", is still a rugged one, not sensitive to vibrations. Although the two plates can vibrate independently, the two beams are vibrating together because both beams go through the same optical parts. Also, the collimation may be less of a problem, because it may not be necessary to use a magnifying lens. A low quality laser beam usually

expands enough over a few feet travel that it reaches the fairly small diameter needed. The new plate actually does not have to be completely parallel. A wedge plate with about the same order of magnitude wedgeness as the first would do just as well. However, with not completely collimated light and two wedge plates the evaluation of the interferograms may be different from what was found for the single-plate interferometer, and that would certainly need more study. The increased shadowgraph effect due to the small studied domain may complicate the evaluation even more. Also, note that coating the plates is really important for this interferometer, because loosing 80% of the intensity 2 times, would leave as little as 4% of the original intensity.

The above described setup was tried out, and interferograms of the trailing edge flow were obtained. However, the quality of these pictures were not sufficient, and they are not presented here. The wedge plates that were used were old scratched wind tunnel windows and the homemade coating on them also did not prove to be good enough. Furthermore, the alignment with this two-plate interferometer is much more difficult than for the single-plate interferometer, and, for efficient application, more sophisticated alignment mechanisms should be designed and built.

4 COMPUTATIONAL STUDIES

The computational studies of the measured transonic turbine cascade flow are presented in this chapter. First, the CFD code used in this investigation is introduced briefly. Next, an analysis is carried out in an effort to find the most suitable grid for the transonic turbine cascade flow application, and as a result a non-periodic C-type grid is generated. The grid generation is followed by a discussion on turbulence modeling. A new, Clauser-type eddy viscosity model is derived, and tested. The application of this new model and the application of the Baldwin-Lomax model for the cascade problem is also described. Next, the software developed for analyzing the numerical results is discussed. The treatment of the boundary conditions and the actual work with the CFD code is also explained. Finally, the results are presented along with the experimentally obtained results.

4.1 The Computer Code

The numerical studies reported here were carried out with a code called "ANSERS". This code was originally developed by R.W. Walters and A.C. Taylor, and it has been modified and further developed by a number of graduate students at Virginia

Tech (Ref.[34]). Some features and capabilities of the code important to this study are described in the following. The code is capable of solving the two-dimensional, cell-centered finite-volume formulation of the complete Navier-Stokes equations. The upwind formulation is implemented with either Van Leer's flux vector splitting method [35] or the less dissipative flux difference splitting algorithm of Roe [36]. To remove spurious oscillations near discontinuities, flux limiting is possible with the choice of the continuously differentiable Van Albada's limiter [37] or the less dissipative Min-Mod limiter [38]. A number of options are available in the code for spatial discretization and variable interpolation. The resulting formulation of the full Navier-Stokes equations are solved with global iteration, and the available time integration/relaxation algorithms include the m-stage Runge-Kutta algorithm [39], a spatially split approximate factorization method [38] and line Gauss-Seidel iteration [40]. There are numerous boundary conditions available, however, as part of this project a new periodic boundary condition was added. Turbulence modeling originally included the Baldwin-Lomax model for boundary layers [41], the McDonald-Camarata model [42], and the Johnson-King model [43]. For this project, turbulence modeling had to be added for the wake region, and the appropriate formulation of the Baldwin-Lomax model was chosen. Also, a new Clauser-type model was developed and added for the attached boundary layer portion of the flow.

4.2 Grid Generation

When generating a grid for use with a CFD code, the first thing to be determined is what type of grid is suitable for the code. ANSERS can only use structured, non-adaptive grids. Also, it can handle only a single grid; coupled calculations on different zones are not possible. Some general rules have to be considered when generating a structured grid. It is advantageous to have the spacing between the grid points small at locations where the flow gradients are large. In this way, the

numerical derivatives are more accurate. This is especially true near shock waves, since they would be smeared out in case the density of the grid were low. Another general rule to consider is that the grid lines should intersect at close to right angles. In the case of excessive grid skewness, it has been shown that the truncation errors are exaggerated [44]. It is also desirable that the transition between low and high grid density domains be smooth. In other words, adjacent grid cells should not differ greatly in their sizes [44].

The structured grids are usually classified into three types. They can be H-grids, O-grids or C-grids [45]. In Fig.4.1 an ellipsoid shaped blade is used to illustrate these three grid types. For an H-type grid, the blade is cut into two halves, and the $k = 1$ and $k = k_{max}$ grid lines are like the boundary of a channel. For an O-type grid, the $j = 1$ and $j = j_{max}$ grid lines are identical, the $k = 1$ grid line is the blade contour itself, and the rest of the k grid lines are running around the blade, forming an O-shape. In the C-type grid, there is a j_1 and a j_2 grid point on the $k = 1$ grid line such that the part between j_1 and j_2 forms the blade contour, and the parts between $j = 1$ and $j = j_1$ and between $j = j_2$ and $j = j_{max}$ are placed identically in space. The rest of the k grid lines form C-shaped curves. Depending on the problem, any of the three grid type can be the best choice. For wall bounded or channel flows the H-type grid is usually sufficient. For infinite flowfields around airfoils the O-type grid is considered the best. For periodic, cascade flows all three kinds have been used. A good summary of the advantages and disadvantages of the different types of grids as applied to cascade problems is given in a recent work by Arnoe et.al. [27]. In the following analysis some of their conclusions will be incorporated.

The H-grid, which is probably the easiest to generate, has poor resolution of the flowfield near the leading and the trailing edges when they are blunt. Also, on the leading edge, because of the grid distortion, there is spurious entropy generation

[27] which is carried downstream on the blade surface. For an O-type grid that problem is avoided, but others arise. If one needs to go far downstream, then for sufficient resolution of the wake and trailing shock area a great number of O-grid lines are needed. These grid lines pass through upstream of the blade too, causing a much higher grid density there than would be necessary, thereby wasting efficiency. Also, for domains not extending too far in the wake area, a high distortion of the grid cells cannot be avoided.

If multiple zones are allowed for the grid in the CFD code, the best choice probably is to use two zones. One of them would be an O-type grid around the blade and extending downstream only about the same amount as it extends upstream. Then, the second zone would be an H-type grid which would be attached to the O-subgrid and which would extend downstream as far as needed. In this way, there would be less spurious entropy generated at the leading and at the trailing edge, and also the trailing edge shock system and the wake would be resolved sufficiently. When a grid with a single zone is needed, however, probably a C-type is the best choice. The C-type grid is like the O-type near the leading edge and like the H-type near the trailing edge. In this way there is less spurious entropy addition at the leading edge, and the different domains of the flowfield can be filled up with grid points at the right density. At the trailing edge, the grid still would be distorted to some extent, but the resulting inaccuracy is not as severe as the inaccuracy that would results in the wake region in the case of using an O-type grid. For these reasons, a C-type grid was chosen for the present application.

Now that the grid type has been chosen, the computational domain can be assigned. The cascade consists of blades with high turning and blunt leading and trailing edges. As little as 1 in. upstream of the blades the flow can be considered uniform. The computational domain however, should extend at least 1.8 in. downstream in axial direction, so that the comparison with the interferometer results

can be possible. Also, to avoid complications in the wake turbulence modeling, the domain needs to contain the wake for most of the downstream part, which means the computation domain has to turn with the flow. The domain obviously has to surround the blade, leaving approximately the same room above and below the blade. Because of the periodicity of the flow, the upper and lower edges of the domain have to be such, that a translation of the lower edge in the $+y$ direction by one blade pitch (1.4764 in.) would move it right onto the upper edge. The upper and lower edge should follow the turning of the flow far enough downstream. At the farthest downstream, those edges can curve to make right angle with the outflow boundary. The computational domain selected to meet these criteria can be seen in Fig.4.2.

Let us now further analyze how the best C-type grid can be obtained on the computational domain. For the following, a few terms will be defined. Periodic boundaries are those on which the flow variables have to be the same. On Fig.4.2, two pairs of periodic boundaries are marked. The "outer periodic boundaries" are periodic boundaries because of the periodicity of the flowfield. The "split periodic boundaries" are periodic, because they are physically in the same location. The grid is called periodic on a pair of periodic boundaries if the grid points on these boundaries match when the two boundaries of the pair are brought together by a translation in y direction. The easiest way to implement periodic boundary conditions is to generate a C-grid which is periodic at both periodic boundaries, that is, the mesh points on the upper and lower boundaries are at the same x locations. A C-grid like that, taken from Ref.[27], is shown in Fig.4.3. It can be seen though that quite serious skewness occurs, and that cannot be resolved with a periodic grid. Arnoe et.al. [27] proposed, therefore, a grid which was not periodic on the split periodic boundary, and their grid, which is shown in Fig.4.4 reveals very good features. Low skewness, and reasonably uniform resolution is characteristic of this grid.

However, the constraint of grid periodicity can just as well be removed from the outer periodic boundaries, as was also pointed out by Arnoe et. al. [27]. For our application, this arrangement proved to be more advantageous, and to understand why, let us go ahead and look at our final grid shown in Fig.4.5 and the grid in Fig.4.4 together. In Arnoe's grid, the outer periodic boundary is nicely matched, however on the split periodic boundary the grid cells have very different lengths very close to the trailing edge. On our grid that is not a problem. Arnoe had the computer power to use a great number of grid points. He could have enough points on the trailing edge, still his grid was not considerably finer in that region than elsewhere. We wanted to keep at least as many grid points on the trailing edge as he did, but elsewhere our grid had to be less fine. Also, our trailing edge was considerably smaller in curvature which caused an additional clustering of grid points. This much higher relative clustering near the trailing edge in our grid requires clustering on the outer boundaries as well, in order to take up a great number of grid lines coming from the trailing edge region without making the grid badly skewed. Now, for a grid periodic on the outer boundary, the center of clustering has to be at the same x location on the lower and upper boundaries. This would definitely lead to highly skewed grid cells. Also, we would much rather have the grid lines coming from the trailing edge region to run parallel with the trailing edge shocks, thereby extending the trailing edge clustering to the domain of the flow where it is the most needed. In this way, the trailing edge shock system will be nice and sharp, facilitating effective comparison with shadowgraph and interferometer pictures.

A few more considerations for obtaining the final grid, Fig.4.5, are given here. For sufficient resolution of the boundary layers on the blade surface, one needs the innermost grid points at least $y^+ = 2$ [45]. The distance which is sufficient to achieve this condition can be estimated, but the final arrangement is made by checking y^+ from the calculated results. For our cascade problem, the grid points

closest to the blade surface were $2 \cdot 10^{-5}$ in. away, which provided less than $y^+ = 2$ in the turbulent boundary layer region. Clustering in the wake region is also needed in order to sufficiently resolve the wake. However, the high gradients of the inner boundary layer are missing in the case of the wake, therefore the clustering should not be as severe as for the boundary layer. For the grid in Fig.4.5 the clustering is gradually decreased behind the trailing edge, and, at 0.3 in. behind the trailing edge, the minimum grid point spacing reached $3 \cdot 10^{-4}$ in.

The final grid also should be well suited for grid convergence studies. Probably the best way to do the grid convergence studies is to start out from a basic grid constructed with the highest number of points affordable. Then, a reduced grid is constructed from the first one by leaving out every other grid point in both grid directions. From this second grid a third, even more reduced grid can be constructed the same way. Solutions can be obtained on all three grids, and the solution on an infinite grid can be estimated by extrapolation. In order to do the grid reduction nicely, the number of cell faces in both coordinate direction should be divisible by 4. Also it is desirable that the number of grid cell faces between cornerpoints be divisible by 4, because then the corner points will not be eliminated during the grid reduction.

The final grid was generated using different software. A code was written which distributed the grid points on the grid boundaries according to a density function. Then a grid generating code, GRAPE (Ref.[46]), was run, which had an algorithm based on an elliptic solver. The resulting grid was checked, and the areas which were not satisfactory were identified. Then, the density function was changed accordingly, and the points on the grid boundaries were redistributed. This process continued until a satisfactory grid was obtained. Later, the trailing edge part of the grid was revised, since a much more powerful grid generating software, GRIDGEN (Ref.[47]), became available. The trailing edge region of the final grid can be seen in Fig.4.6.

The size of the grid was 437×45, and a considerably finer grid would have lead to unacceptable CPU time. From this grid, two coarser grids were generated in the above described way. In the following, the 110×12 grid will be called the first grid, the 219×23 grid will be called the second grid, and the 437×45 grid will be called the third grid.

4.3 Turbulence Modeling

The three major regions of total pressure losses in a cascade flow are the boundary layer region on the surface of the blades, the trailing edge and wake region, and the trailing edge shocks. As far as the shock losses are concerned, the total pressure loss can easily be calculated; the physics of the phenomenon is well understood. However, for the former two sources, the situation is much more difficult, since the loss generation is mainly controlled by the turbulence, and our knowledge of turbulence is quite limited. Existing turbulence models for attached boundary layers and far wake regions work fairly well, however, for separated boundary layers, for the near wake, and especially for the trailing edge region, there is a lot of room for improvement.

In Chapter 3 we already emphasized the importance of the knowledge of where exactly the turbulent regions are located. There, we also discussed a shadowgraph study of the transition in our cascade. The results obtained there will be used for the numerical studies, therefore let them be repeated here. For all Mach numbers, the pressure side boundary layer and trailing edge separation was laminar, and on the suction side the transition occurred at $x/C = -0.2in.$. The wake region was fully turbulent.

Now that we have specified the turbulent regions, the selection of appropriate turbulence models for the different regions can follow. Let us start with the suction side

boundary layer. First of all, we assume that the flow is attached all the way down to the trailing edge region. We do this on the basis of the fact that the shadowgraph pictures did not show signs of extended separation. In fact, later this assumption was strengthened, since the numerical results did not indicate any significant separation either. Another aspect of the flow to be considered is that, on the suction side close to the trailing edge, the local Mach number can be as high as 1.6 for higher exit Mach numbers. Therefore, the turbulence model should be applicable for moderately compressible flows. One more fact that could be considered is that the curvature of the blades at that region is fairly low, and the pressure and edge velocity gradients are also fairly low compared to the boundary layer thickness. Boundary layer flows with these properties can be calculated with relatively simple algebraic turbulence models just as well as with more complicated and less time efficient one or two equation models. Two kinds of algebraic methods are usually distinguished, the mixing length and the eddy viscosity methods. Extensions of both kinds were successfully applied to compressible boundary layers. For the inner layer, the extensions are usually supported by some derivation, however, for the outer layer in many cases the extensions are more like *ad hoc* assumptions. A quite popular eddy viscosity model for moderately compressible flows is the Baldwin-Lomax model [41], which has been used by numerous authors in the past decade. The Baldwin-Lomax model, when applied to boundary layer calculation, will be shown to be essentially a Clauser-type formulation, therefore it is not significantly different from other methods. We pursued a study which resulted in a new extension of the Clauser model to compressible flow, and this model was used for calculating the eddy viscosity in the outer part of the boundary layer on the turbine blades. The derivation of this new model will be presented later in this section.

Now, let us discuss options for turbulence modeling in the wake region. For developed wakes, the situation is similar to the boundary layer case. Simple algebraic

models do just as good a job as more complicated and time consuming one or two equation models. A summary of the available methods is given in Ref.[45]. Included there, is the Prandtl method in which the eddy viscosity proportional to the product of the density, the velocity difference across the wake and the half width of the wake. In more complicated flows, such as the cascade flow, it is not trivial how the last quantity can be obtained, and that can introduce some uncertainty in the calculation. Modifications to the method, which make the length scale more accurately defined can be advantageous, and the Baldwin-Lomax model, when applied in the wake region, can be shown to be essentially a Prandtl formulation with such a modification. As will be discussed, the Baldwin-Lomax model has other advantages facilitating numerical applications, therefore this model was chosen for the turbulence modeling in the far wake region.

The last turbulent region for which a sufficient model should be found is the trailing edge and the near wake region. This region is by far the most complicated, and as a consequence, adequate turbulence modeling is very difficult. The turbulence modeling with simple algebraic models in the boundary layer and the far wake regions could be successful because the turbulent flow is developed, or in other words there is a near equilibrium between turbulence generation and dissipation. For the trailing edge and near wake region that is not true by any means. The separation on both sides of the trailing edge suddenly changes the character of the flow, and the suppressing effect of the vicinity of the wall on the size of the turbulent eddies is not in effect any more. Therefore, the length scale goes through a sudden change, and the equilibrium does not hold any more. For a complicated flow like this, models with more adjustable parameters and better capability to be adjusted to the physics of the flow can be advantageous. Therefore, many authors feel the two-equation models, such as different $K\epsilon$-type models, are more applicable to the problem. However, detailed comparisons of the measured trailing edge flow data

and numerical results with these methods are not available. The problem of the turbulence modeling in the trailing edge region remains a very open question.

For the CFD code used in this research there were no one or two-equation turbulence models available, and the implementation of such models was not pursued. Therefore, we had to be satisfied with the application of an algebraic model. There are no widely used and successful algebraic models which were specifically designed for the trailing edge flow. However, again, the Baldwin-Lomax model can be used in this region, and it has some good features. One attractive property of this model is that it provides a smooth continuous transition of the length scale in the boundary layer into the length scale of the far wake. Although previous unpublished calculations by the author showed limited capabilities of the Baldwin-Lomax model in the near wake region, due to a lack of a better algebraic model, still the Baldwin-Lomax model was chosen for the trailing edge and near wake turbulence modeling.

Now we arrived to the point that we can summarize which turbulence models will be used in the different parts of the flowfield, and this summary is shown in Fig.4.2. In accordance with the foregoing, a new extension of the Clauser eddy viscosity model will be used for the suction side boundary layer after transition, laminar flow will be used on the pressure side all the way down to the trailing edge, and the Baldwin-Lomax model will be used in the whole wake region as well as in the suction side trailing edge region. In the following, first the new extension of the Clauser model for compressible flow will be derived, and some technical details about its application will be discussed. Next the Baldwin-Lomax model will be analyzed.

4.3.1 A New Rational Extension of the Clauser Eddy Viscosity Model

The Clauser eddy viscosity model [48] for the calculation of the outer part of an incompressible turbulent boundary layer has been successfully used for many years. This model was based on the sound argument that the outer part of a turbulent boundary layer is similar to a pseudo-laminar boundary layer with a slip velocity at the wall and with the eddy viscosity constant across the outer layer. Comparing calculated pseudo-laminar boundary layer profiles with slip velocity at the wall and the measured velocity defect law for turbulent boundary layers with equilibrium pressure gradients resulted in the well-known formula:

$$\mu_T = 0.018 \rho u_e \delta^* \tag{4.1}$$

Although the Clauser model also has been used for the prediction of compressible boundary layers, its extension for that case has never been done in a systematic manner. Authors usually use the local density for ρ and the incompressible or kinematic displacement thickness, δ_k^*, instead of δ^* (Ref.[45]). However, for high density variation cases, e.g. with light gas injection, the use of the true displacement thickness, δ^*, seemed to give better results (Ref.[45]). In any case, none of these assumptions were based on any theory, and only the fact that they gave satisfactory results in certain cases justified their use.

In this section, a rational extension of the Clauser model to the compressible case will be provided. The fundamental piece of information for the extended model derivation is the observation of Maise and McDonald [50] that the experimental velocity defect law for low Mach number turbulent boundary layer cases remains valid for high Mach number cases, if first the Van Driest transformation is performed on the velocity profiles. The existence of an experimental velocity defect law then can be exploited in a similar manner as in the original Clauser derivation to predict

eddy viscosities. Analogous to that, we need here pseudo-laminar, but now compressible boundary layer profiles with different slip velocities at the wall. These can be calculated from the Blasius solution with slip velocity using the Crocco integral for the temperature distribution in the boundary layer and applying the Howarth-Dorodnitsyn transformation. In this way, we can obtain a set of profiles for different Mach numbers, each set containing profiles with several slip velocities. Since our goal is to compare these pseudo-laminar profiles to the experimental velocity defect law, the Van Driest transformation is applied to the calculated pseudo-laminar profiles. Then, with an appropriate coordinate transformation, the different Mach number, different slip velocity profiles can be brought together into a narrow band and compared to the experimental velocity defect law. The result of this comparison is the new extended Clauser model, which in the case of incompressible flows falls back to the original one.

The derivation of the extended Clauser model will be carried out according to the outline given in the above. We start out in the same way as Clauser did in the original low speed case derivation. First incompressible, pseudo-laminar boundary layers with slip velocities are produced. For the highest generality possible, the viscosity should be allowed to change in the x direction. These profiles can be obtained by solving the well known Blasius differential equation (Ref.[48]),

$$g''' + g \cdot g'' = 0, \quad g = g(\overline{\eta}). \tag{4.2}$$

The boundary conditions, appropriate for the presence of slip velocity, are:

$$\begin{aligned} g'(0) &= \frac{u_0}{u_e} \\ g'(\infty) &= 1 \\ g(0) &= 0. \end{aligned} \tag{4.3}$$

Then

$$\frac{u}{u_e} = g'(\overline{\eta}(Y,x)), \tag{4.4}$$

where

$$\overline{\eta}(Y,x) = \frac{Y}{L(x)}, \tag{4.5}$$

and $L(x)$ is a scaling factor. Our notation is different from that of Clauser [48], since here y and η are reserved for the compressible profiles, and also instead of δ we use L, since we reserve δ for the boundary layer thickness. The resulting velocity profiles are shown in Fig.4.7. These are just the same as the ones Clauser displayed in his original work, except that they are in velocity defect representation.

In the next step, we want to transform these profiles into compressible boundary layer profiles. The Howarth-Dorodnitsyn transformation (Ref.[45]) can be used, which introduces a distortion of the transverse coordinate in the following way:

$$Y = \int_0^y \frac{\rho}{\rho_e} dy \tag{4.6}$$

If we now apply this transformation, the velocity components can be written as

$$u = \frac{\partial \psi}{\partial Y}; \qquad v = -\frac{\rho_e}{\rho}\left[\frac{\partial \psi}{\partial x} + u\left(\frac{\partial Y}{\partial x}\right)_y\right]. \tag{4.7}$$

Substituting into the steady momentum equation for boundary layer flow over a flat plate, the resulting equation is obtained as

$$\frac{\partial \psi}{\partial Y}\frac{\partial^2 \psi}{\partial x \partial Y} - \frac{\partial \psi}{\partial x}\frac{\partial^2 \psi}{\partial Y^2} = \frac{\partial}{\partial Y}\left(\frac{\rho\mu}{\rho_e^2}\frac{\partial^2 \psi}{\partial Y^2}\right). \tag{4.8}$$

This equation is very similar to that for constant density, constant property boundary layer flow, and the similarity becomes functional equivalence when $\rho\mu$ = constant. Assuming μ to be proportional to T, this condition is satisfied, and we can

obtain the compressible boundary layer profiles by applying the reverse transformation,

$$y = \int_0^Y \frac{\rho_e}{\rho} dY, \tag{4.9}$$

to the incompressible solution.

However, we have to know the density distribution in the compressible boundary layer in order to carry out the reverse transformation. For that reason, we need the Crocco integral (Ref.[45]), which relates the temperature and the velocity in a compressible, adiabatic boundary layer for $Pr = 1$, in the following way:

$$T + \frac{u^2}{2c_p} = T_e + \frac{u_e^2}{2c_p}. \tag{4.10}$$

From this, the ratio of the local to the edge temperature can be expressed in terms of the edge Mach number and the velocity ratio:

$$\frac{T}{T_e} = 1 + \frac{\gamma - 1}{2} M_e^2 \left[1 - \left(\frac{u}{u_e} \right)^2 \right]. \tag{4.11}$$

Since the pressure is constant across a boundary layer,

$$\frac{\rho_e}{\rho} = \frac{T}{T_e}. \tag{4.12}$$

With Eqs.(4.11) and (4.12) we obtain ρ_e/ρ as a function of u/u_e. However, u/u_e itself is a function of $\overline{\eta}$ rather then Y (see Eq.(4.4)), therefore Eq.(4.9) has to be rewritten in order to evaluate it;

$$\frac{y}{L(x)} = \int_0^{\frac{Y}{L(x)}} \frac{\rho_e}{\rho} \left(\frac{Y}{L(x)} \right) d\left(\frac{Y}{L(x)} \right) \tag{4.13}$$

Now define η as

$$\eta = \frac{y}{L(x)}, \tag{4.14}$$

and Eq.(4.13) can be rewritten as

$$\eta = \int_0^{\overline{\eta}} \frac{\rho_e}{\rho}(\overline{\eta})d\overline{\eta}. \qquad (4.13.a)$$

The integral has to be carried out numerically, and we obtain a relationship between η and $\overline{\eta}$ in a tabulated form. Next, define $F(\eta)$ to represent the velocity defect profiles as

$$F(\eta) = \frac{u(\eta) - u_e}{u_e} = g'(\overline{\eta}(\eta)) - 1 \qquad (4.15)$$

As can be seen from Eq.(4.11), the transformation is dependent on the edge Mach number, therefore similar profile sets as in Fig.4.7 can be obtained for different edge Mach numbers. A transformed velocity profile set for the case of edge Mach number 4 is shown in Fig.4.7.

In the original Clauser derivation for the incompressible case, the next step was to perform an appropriate coordinate transformation to make the profile set of Fig.4.6 fall approximately on the same line in order to facilitate the direct comparison with the experimental velocity defect law. However, for compressible boundary layers, the velocity defect law is not valid in the same form. As mentioned before, the measured velocity defect profiles do not fall on the same line unless the Van Driest transformation is first performed on them. Therefore, the calculated pseudo-laminar, compressible boundary layer velocity profiles, which were just obtained, have to undergo this transformation too. The Van Driest transformation for the adiabatic case can be written as

$$u^* = (u_e/m^{1/2}) \sin^{-1}(m^{1/2}u/u_e), \qquad (4.16)$$

where

$$m = \frac{[(\gamma - 1)/2]M_e^2}{1 + [(\gamma - 1)/2]M_e^2}, \qquad (4.17)$$

and u^* is the transformed velocity. It can be seen that in the limit of $M_e \rightarrow 0$, $u^* = u$.

Applying the Van Driest transformation on the F function one obtains

$$F^*(\eta) = \frac{u^*(\eta) - u_e^*}{u_e^*}. \tag{4.18}$$

Again the $M_e = 4$ case is chosen as an example, and the resulting transformed velocity profiles for that case are shown in Fig.4.9. It can be seen that the Van Driest transformation did not change the shape of the profiles in Fig.4.7 very much. Most changes occurred in the region close to the wall. The Van Driest transformation, however, caused greater changes in the edge velocity, and that is shown in Fig.4.10. In fact, the significance of this transformation lies more in its effect on the edge velocity than in its effect on the profile shapes.

Having now obtained pseudo-laminar compressible profiles in Van Driest coordinates, we can pick up the logical line followed by Clauser where we left it and develop a coordinate transformation to bring the profiles with different slip velocity and edge Mach number together into a narrow band. The idea is that if the transformation makes the areas above the profiles and the derivatives of the profiles at $y = 0$ the same for all of them, then those transformed profiles will be quite close to each other.

The coordinate transformation will be the simplest possible; it will be only a factor on both coordinates, F^* and η. The transformed coordinates are:

$$F^+ = C_1 \cdot \frac{u^* - u_e^*}{u_e^*} \tag{4.19}$$

$$\eta^+ = C_2 \cdot \eta, \tag{4.20}$$

and the velocity profiles now are given as $F^+ = F^+(\eta^+)$. Note that C_1 and C_2 are actually functions of u_0 and M_e. The previously mentioned two conditions, that will determine C_1 and C_2, can be written now as

$$\int_0^\infty F^+ d\eta^+ = -1. \tag{4.21}$$

for the area constraint and

$$\left[\frac{\partial F^+}{\partial \eta^+}\right]_{\eta=0} = 1 \tag{4.22}$$

for the slope at the wall constraint. These conditions can also be written in terms of F^* and η, with C_1 and C_2 appearing in the formulas:

$$C_1 C_2 \int_0^\infty F^* d\eta = -1. \tag{4.23}$$

and

$$\frac{C_1}{C_2}\left[\frac{\partial F^*}{\partial \eta}\right]_{\eta=0} = 1. \tag{4.24}$$

Next, introduce

$$\delta^*_{VD} = \int_0^\infty \left(1 - \frac{u^*(y)}{u^*_e}\right) dy \tag{4.25},$$

i.e. δ^*_{VD} is a displacement thickness for Van Driest transformed profiles. Then, η^*_{VD} can also be introduced as

$$\eta^*_{VD} = \eta(\delta^*_{VD}, x) = \frac{\delta^*_{VD}}{L(x)}. \tag{4.26}$$

that is η^*_{VD} is the value of η when $y = \delta^*_{VD}$. Incidentally, δ^*_{VD} and η^*_{VD} are the counterparts to δ^* and η_{δ^*} in Clauser's original derivation. If both sides of Eq.(4.25) are divided by $L(x)$, then with the new notation

$$-\int_0^\infty F^* d\eta = \frac{\delta^*_{VD}}{L(x)} = \eta^*_{VD}. \tag{4.27}$$

Now the solution of Eqs.(4.23) and (4.24) for C_1 and C_2 can be written as

$$C_1 = \frac{1}{\sqrt{\left[\frac{\partial F^*}{\partial \eta}\right]_{\eta=0} \cdot \eta^*_{VD}}} \tag{4.28}$$

and

$$C_2 = \sqrt{\frac{\left[\frac{\partial F^*}{\partial \eta}\right]_{\eta=0}}{\eta^*_{VD}}}. \tag{4.29}$$

Substituting C_1 and C_2 back in Eqs.(4.19) and (4.20) we finally obtain

$$F^+ = \frac{u^* - u_e^*}{u_e^* \sqrt{\left[\frac{\partial F^*}{\partial \eta}\right]_{\eta=0} \cdot \eta_{VD}^*}} \tag{4.30}$$

and

$$\eta^+ = \eta \sqrt{\frac{\left[\frac{\partial F^*}{\partial \eta}\right]_{\eta=0}}{\eta_{VD}^*}}. \tag{4.31}$$

Again, it can be seen that this is the transformed equivalent of the relations obtained by Clauser for the incompressible case.

All the $F^+ = F^+(\eta^+)$ profiles do not fall in same band. However, if only the same edge Mach number but different slip velocity cases are plotted, they fall in narrow bands as shown in Fig.4.11a-4.11d. An "average" line can be selected for each of the different edge Mach number cases, and these are presented together in Fig.4.11. From now on we can work with these "average profile" lines, since each of them can be considered as a representative of a bigger, constant edge Mach number group. Also, that will mean that the new model will have to incorporate the edge Mach number.

We arrive now at the last coordinate transformation, which will finally make all the calculated velocity profiles fall on approximately the measured velocity defect law. We introduce F^{++} as

$$F^{++} = C_M F^+, \tag{4.32}$$

where C_M again is just a transformation factor, whose value has to be determined. This factor must be dependent upon the edge Mach number as follows from the previous paragraph, and that is why the M subscript is used. η^+ will be transformed into η^{++}, and the condition that the area above the $F^{++} = F^{++}(\eta^{++})$ curves should be the same as the area above the experimental velocity defect law is used.

Therefore,

$$\eta^{++} = \frac{1}{C_M} \cdot 3.6\eta^{+} \tag{4.33}$$

is the right choice, since the area above the velocity defect law is 3.6 (Ref.[48]). Values for C_M should be given by some simple continuous formula in such a way that the agreement with the experimental velocity defect law is the best possible. The following formula was found to be adequate:

$$C_M = 7.4 - .4M_e \tag{4.34}$$

The resulting transformed pseudo-laminar profiles along with the measured velocity defect law are plotted in Fig.4.13. The agreement is not quite as good as that for the incompressible model. The lower edge Mach number lines fit the experimental velocity defect law somewhat better than the higher edge Mach number lines. However, the agreement is reasonable overall.

Now we are ready to finally develop the desired eddy viscosity model. The equivalence of the experimental velocity defect law and the calculated profiles can be expressed in the following way:

$$\frac{u^* - u_e^*}{u_\tau} = F^{++} \tag{4.35}$$

and

$$\frac{y}{\delta} = \eta^{++}. \tag{4.36}$$

From Eqs.(4.35),(4.32),(4.30) and

$$u_\tau \equiv \sqrt{\frac{\tau_w}{\rho_w}} \tag{4.36a}$$

we can obtain:

$$\tau_w = \frac{1}{C_M^2} \rho_w u_e^{*2} \left[\frac{\partial F^*}{\partial \eta}\right]_{\eta=0} \eta_{VD}^* \tag{4.37}$$

However, τ_w also can be expressed as

$$\tau_w = \mu_T\big|_{y=0}\left[\frac{\partial u}{\partial y}\right]_{y=0} = \mu_T\big|_{y=0}\left[\frac{\partial F}{\partial \eta}\right]_{\eta=0}\frac{\eta^*_{VD}}{\delta^*_{VD}}u_e, \tag{4.38}$$

where

$$\frac{\partial \eta}{\partial y} = \frac{\eta}{y} = \frac{\eta^*_{VD}}{\delta^*_{VD}} \tag{4.39}$$

following from Eqs.(4.14) and (4.26) was used. From Eqs.(4.37) and (4.38), μ_T at the wall can be expressed as

$$\mu_T\big|_{y=0} = \frac{1}{C_M^2}\frac{\left[\frac{\partial F^*}{\partial \eta}\right]_{\eta=0}}{\left[\frac{\partial F}{\partial \eta}\right]_{\eta=0}}\left(\frac{u_e^*}{u_e}\right)\rho_w u_e^* \delta^*_{VD}. \tag{4.40}$$

The ratio of the derivatives can be written as

$$\left[\frac{dF^*}{dF}\right]_{\eta=0} = \left[\frac{du^*}{du}\right]_{u=u_0}\left(\frac{u_e}{u_e^*}\right), \tag{4.41}$$

or, with Eq.(4.16),

$$\left[\frac{dF^*}{dF}\right]_{\eta=0} = \left[1 - m\frac{u_0^2}{u_e^2}\right]^{-\frac{1}{2}}\left(\frac{u_e}{u_e^*}\right), \tag{4.42}$$

where u_0 is the slip velocity of the pseudo-laminar boundary layer. Note that u_0/u_e did not appear in Clauser's original derivation. It is introduced here by the use of the Van Driest transformation, and its appearance cannot be avoided. Substituting Eq.(4.42) into Eq.(4.40), we obtain the following form for the eddy viscosity on the wall:

$$\mu_T\big|_{y=0} = \frac{1}{C_M^2}\left[1 - m\frac{u_0^2}{u_e^2}\right]^{-\frac{1}{2}}\rho_w u_e^* \delta^*_{VD}. \tag{4.43}$$

At this point, it must be pointed out, that the eddy viscosity will have to depend upon the normal coordinate, y. It was mentioned earlier, that for the Howarth-Dorodnitsyn transformation $\mu \propto T$ had to be assumed. Consequentially, the profiles as calculated by Eq.(4.15) were calculated with $\mu \propto T$. Therefore,

$$\mu_T(y) = \mu_T\Big|_{y=0}\frac{T}{T_0} = \mu_T\Big|_{y=0}\frac{T}{T_e}\frac{T_e}{T_0} \tag{4.44}$$

where the temperature ratios can be obtained using Eq.(4.11).

We have not mentioned yet how u_0/u_e is to be determined. A possible way is the extrapolation of the velocity profile to the wall. The extrapolation has to start out from the outer layer, so one can put a tangent on the velocity profile at, say, $y = \delta/4$, and wherever this tangent intercepts the velocity axis will be u_0. This method is adequate, since the pseudo-laminar profiles in the inner region are relatively straight.

In summary, for determining the eddy viscosity with the new method, one first finds the edge Mach number, then calculates C_M from Eq.(4.34), then extrapolates the profiles from $y \sim \delta/4$ to the wall to find u_0/u_e, then calculates T/T_0 from Eq.(4.11), u_e^* from Eq.(4.16) and δ_{VD}^* from Eq.(4.25), and finally substitutes all these in

$$\mu_T = \frac{1}{C_M^2}\left[1 - m\frac{u_0^2}{u_e^2}\right]^{-\frac{1}{2}} \frac{T}{T_0}\rho_w u_e^* \delta_{VD}^*, \tag{4.45}$$

which is our final result, the extended Clauser eddy viscosity model. It is easiest to see how this can work in a computational scheme by considering a simple, explicit "marching" numerical formulation.

The similarity of the original (Eq.(4.1)) and the extended model can be easily recognized. Instead of the constant 0.018, in the extended model we have a $u_0(x)/u_e$-dependent expression. Instead of ρ, u_e and δ^*, now we have ρ_w, u_e^* and δ_{VD}^*, respectively. The only term which does not correspond to anything in the original model is T/T_0, which is responsible for the y dependence of μ_T.

Furthermore, Eq.(4.45) has to reduce to Eq.(4.1) for the case of $M_e = 0$. From Eq.(4.34), $1/C_M^2 = 0.018$ when $M_e = 0$. From Eq.(4.17) $m = 0$ and the magnitude of the square root expression is 1. For incompressible, adiabatic flow $T/T_0 = 1$ and $\rho_w = \rho$. For $M_e = 0$ the Van Driest transformation does not change the velocity as can be seen from Eqs.(4.16) and (4.17), so $u_e^* = u_e$. For the same reason $\delta_{VD}^* = \delta^*$. Substituting all these in Eq.(4.45), we see that Eq.(4.1) does result.

The range of flow variables and geometries for which the extended Clauser model is valid needs some discussion. First, there is little information whether the experimental velocity defect law in the form assumed here using the Van Driest transformation holds for edge Mach numbers higher than 6.0. Next, the pseudo-laminar profiles were calculated up to $M_e = 6.0$ assuming a perfect gas, but it can be debated if that model is truly valid for up to that Mach number. The final conclusion about the validity of the new model for higher Mach numbers must come from comparisons of experimental results and predictions using the new model. Also, an issue is whether the model can be used for non-adiabatic and non-zero pressure gradient cases. The Van Driest transformation used in the derivation here works best for adiabatic cases (Ref.[50]). Since the original, low speed case model was successfully used for pressure gradient cases (at least for equilibrium pressure gradients), the same might be expected for the new, extended model.

It can be informative to investigate how the eddy viscosities predicted by the new model compare to the predictions by the previously mentioned *ad hoc* extensions. For the further discussion, the $\mu_T = 0.018\rho(y)u_e\delta^*$ and the $\mu_T = 0.018\rho(y)u_e\delta_k^*$ extensions will be referred to as the δ^* and the δ_k^* extensions, respectively. The profiles which will be used for this comparison are the $F = F(\eta)$ (Eq.(4.15)) pseudo-laminar profiles obtained during the derivation of the new model, since they resemble the real, turbulent profiles. Obviously, the relation between the predictions by the different methods are dependent on the edge Mach number and the slip velocity, since those are the two factors which determine the $F = F(\eta)$ profiles. Conditions of $M_e = 4$ with $u_0/u_e = 0.4$ and 0.7 were chosen as representative. Also, the predictions by the three models were compared to the eddy viscosity that would be obtained by completely neglecting compressibility; i.e. $\mu_{T,inc} = 0.018\rho_e u_e \delta_k^*$. The results are given in Figs.4.14a and 5.14b. It can be seen that towards the edge of the boundary layer the predicted eddy viscosity is growing for the δ^* and the δ_k^* model,

and decreasing for the new model. Note, that the Klebanoff factor (Ref.[35]), which is often used with the *ad hoc* extensions, would tend to make the predictions by the *ad hoc* extensions somewhat more like the predictions by the new model by depressing the increase as $y \rightarrow \delta$.

Before the application to the cascade flow, the new model was verified by comparing numerical results to measured data for compressible boundary layer flows over a flat plate. The code used for these calculations was the same as the one used for the cascade studies. The eddy viscosity in the inner layer was always calculated with the well-known Reichardt eddy viscosity model (Ref.[30]),

$$\mu_T = \kappa\rho\nu\left[\left(\frac{yu_\tau}{\nu}\right) - y_a^+ \tanh\left(\frac{yu_\tau}{\nu y_a^+}\right)\right], \qquad (4.46),$$

using the local ρ and μ, as is common practice and $\kappa = 0.41$ and $y_a^+ = 9.7$. It is important to note, that the Klebanoff intermittency factor was not applied in any of the cases. It can be argued, that the pseudo-laminar profiles were not calculated with an intermittency factor, and therefore nothing justifies its later introduction.

The first test case is by Coles [52], who measured the boundary layer profile and the skin friction over a flat plate in a Mach 3.7 flow. The freestream total pressure and total temperature were 1.4×10^5Pa and 312 K, respectively. The measurement station was located at 54.6 cm from the leading edge, which is 3.54×10^6 in terms of a Reynolds number. A leading edge trip was used to cause the boundary layer to be turbulent over the whole length of the plate. The calculated and measured boundary layer velocity profiles are presented in Fig.4.15. It can be seen, that the δ^* extension gave the worst result, the δ_k^* extension provided a better result, and the best result was obtained with the new model. In fact, the agreement with the measurement is quite good for the new model. Also, the skin friction coefficients were calculated. With the δ^* extension $c_f = 0.00193$, with the δ_k^* extension $c_f = 0.00185$, and finally with the new model $c_f = 0.00183$ was obtained. All these predictions are

higher than the experimentally obtained 0.00162, but still we can conclude that the prediction obtained by the new model is the best.

The second test case by Lee et. al. [53] is again a flat plate boundary layer, but the flow in this case is not adiabatic. The edge flow variables are $M_e = 4.857$,$T_e = 72.8$K and $p_e = 2327$Pa. The plate is cooled such that the ratio of the wall temperature to the adiabatic wall temperature is 0.74. The boundary layer developed on the wall of a supersonic wind tunnel, so there was no $Re_x = 0$ station to start the calculation from. Therefore, the calculations were carried out between two measurement stations which were 22 in. apart. The displacement thickness Reynolds number for the entrance station was $Re_{\delta^*} = 2.8 \times 10^5$. Since the first measurement point in the boundary layer was at about $y^+ = 10$, a few points were added to the entrance profile in the $y^+ < 10$ region in such a way that the measured skin friction coefficient was matched. The calculated and measured exit profiles are compared in Fig.4.16. Although the new model provides a better profile then the other extensions, the prediction is not quite as good as for the earlier case. An explanation could be that for non-adiabatic boundary layers the Van Driest velocity defect law is not valid as was shown in Ref.[50]. The prediction for the skin friction coefficient, c_f, and the displacement thickness, δ^*, is much better. For the skin friction coefficient the δ^*, the δ_k^* and the δ_{VD}^* extensions gave 7.19×10^{-4}, 7.00×10^{-4} and 7.01×10^{-4}. For the displacement thickness the extensions gave 0.722, 0.742, and 0.753 in., respectively. The measured values for these quantities were $c_f = 7.19 \times 10^{-4}$ and $\delta^* = 0.799$in., therefore it can be concluded that the calculated c_f for all three extensions was basically within the experimental uncertainty, and for the displacement thickness the new model provided the best results.

A new, soundly based extension of the Clauser eddy viscosity model to compressible flow has been derived, analyzed and tested. Although the new model is more complicated than the original one, it is still algebraic and therefore is relatively

easy to implement compared to models using partial differential equations such as a TKE or Kϵ model. The new model provides equivalent or better results than the *ad hoc* extensions for both the velocity profile in the boundary layer and for the skin friction coefficients. The results for the non-adiabatic test case are not as good as for the adiabatic case, as might be expected from the fact that the transformed velocity defect law used in the derivation is not valid for non-adiabatic flow. The applicability of the new model for boundary layer flows with pressure gradients still has not been investigated in detail. One might assume that the pressure gradient issue will not be critically important, since that was the result in the original, incompressible case. In any event, no simple alternative to the Clauser model exists for non-equilibrium pressure gradients.

4.3.2 The Baldwin-Lomax model

Let us now turn our attention to the Baldwin-Lomax model [41], which has been quite popular in the last decade. This model was an attempt to incorporate the modeling of turbulence in attached or separated boundary layer and the wake region in one single model. It also has some nice features for CFD applications, as will be seen later. First, the model will be introduced on basis of the original paper, then some analysis and corrections will follow.

The original paper prescribes the method for calculating the eddy viscosity in the inner layer. This method is the Van Driest [45] formulation, except that the vorticity is used instead of the u velocity gradient. So in the inner region

$$(\mu_T)_{inner} = \rho l_m^2 |\omega| \tag{4.47}$$

where l_m can be obtained from

$$l_m = ky[1 - \exp(-y^+/A^+)], \tag{4.48}$$

ω is the magnitude of the vorticity,and

$$y^+ = \frac{\rho_w u_\tau y}{\mu_w} \tag{4.49}$$

For the outer region

$$(\mu_T)_{outer} = K_C\, C_{CP}\, \rho\, F_{WAKE}\, F_{KLEB}(y) \tag{4.50}$$

where K_C is the Clauser constant, taken as 0.0168, C_{cp} is an additional constant of magnitude 1.6, F_{KLEB} is the Klebanoff intermittency factor, and F_{WAKE} is the smaller of F_{WAKE_1} and F_{WAKE_2} where

$$F_{WAKE_1} = y_{MAX} F_{MAX}$$

$$F_{WAKE_2} = C_{WK}\, y_{MAX}\, u_{DIF}^2 / F_{MAX} \tag{4.51}$$

C_{WK} is a constant, and its value is 0.25. The quantities y_{MAX} and F_{MAX} are determined from the function

$$F(y) = y\,|\omega|\,[1 - \exp(-y^+/A^+)] \tag{4.52}$$

In wakes, the exponential term is set equal to zero. The quantity F_{MAX} is the maximum value of $F(y)$ that occurs in a profile, and y_{MAX} is the value of y where it occurs. The quantity u_{DIF} is the difference between the maximum and minimum velocity in the profile (i.e. at a fixed x station)

$$u_{DIF} = (\sqrt{u^2 + v^2})_{max} - (\sqrt{u^2 + v^2})_{min} \tag{4.53}$$

The second term in u_{DIF} is taken to be zero (except in wakes).

Now we are going to show that the Baldwin-Lomax model is actually a Clauser type of model when F_{WAKE_1} is used, and it is a Prandtl-type model when F_{WAKE_2} is

used. The original paper gave some hints in this matter, but to make things clear we also engaged in some private communication with the authors of this model. In accordance, the rationale behind the Baldwin-Lomax model is as follows.

In a typical plot of u/u_τ versus $\log y^+$ a conspicuous feature in the outer part of the profile is the increase in slope. The value of y at which the slope is maximum is a measure of the width of the boundary layer. The quantity to be maximized is proportional to

$$\frac{\partial u}{\partial \ln y} = y\frac{\partial u}{\partial y} \tag{4.54}$$

To the order of the boundary layer approximation $\partial u/\partial y$ is proportional to vorticity. Vorticity is used in $F(y)$ instead of $\partial u/\partial y$ because typically its magnitude (as computed in Navier-Stokes codes) is much smaller outside the boundary layer. The damping factor is included in $F(y)$ to suppress the peak in slope that occurs in the inner region. F_{MAX} has the dimension of velocity and y_{MAX} has the dimension of length. The dimensionless ratio of $u_e\delta^*$ to $y_{MAX}F_{MAX}$ was found empirically reasonably constant, therefore we can say that the Baldwin-Lomax model falls back to a Clauser-type eddy viscosity model in the boundary layer region and when F_{WAKE_1} is smaller than F_{WAKE_2}. On the other hand the ratio $y_{MAX}u_{DIF}/F_{MAX}$ is a measure of the half width of a wake. This ratio is insensitive to the displacement of the origin from the wake centerline since y_{MAX} is in both the numerator and the denominator and cancels. Consequentially, the ratio of δ to $y_{MAX}u_{DIF}/F_{MAX}$ is reasonably constant and insensitive to the position of the origin. Then $y_{MAX}u_{DIF}^2/F_{MAX}$ is approximately proportional to u_{DIF}. Therefore, with proper calibration again, we can say that the Baldwin-Lomax model in the wake region falls back to something like the Prandtl eddy viscosity model for wakes and jets when F_{WAKE_2} is smaller then F_{WAKE_1}. A word of caution is in order here. When actually calibrating the Baldwin-Lomax model for the wake formulation, it turns out that the constant C_{WK} needs to be set at 1.0 instead of the originally

reported 0.25. Otherwise the well established constant in the Prandtl model cannot be gained back.

From the foregoing it appears that the purpose of Baldwin and Lomax was that by selecting the smaller of F_{WAKE_1} and F_{WAKE_2} their model automatically becomes essentially the Clauser model in the boundary layers and essentially the Prandtl model in the wakes and separated boundary layers.

Let us first of all reconsider what we actually compare when we compare F_{WAKE_1} and F_{WAKE_2}. From Eq.(4.51) the ratio of the two quantities can be obtained:

$$\frac{F_{WAKE_1}}{F_{WAKE_2}} = \frac{\left(\frac{\partial u}{\partial y}\right)^2}{u_{DIF}^2/y_{MAX}^2} \tag{4.55}$$

Note, that here the modified C_{WK} value ($C_{WK} = 1$) was used. Then the

$$F_{WAKE_1} > F_{WAKE_2} \tag{4.56}$$

condition is equivalent with the

$$\left|\frac{\partial u}{\partial y}\right|_{MAX} > \left|\frac{u_{DIF}}{y_{MAX}}\right| \tag{4.57}$$

condition.

Now, look at the case of an attached boundary layer, a separated boundary layer and a wake, respectively, and examine what the relation between $|\partial u/\partial y|_{MAX}$ and $|u_{DIF}/y_{MAX}|$ is. In Fig.4.17 a typical attached turbulent boundary layer can be seen. The exact location of y_{MAX} obviously cannot be given, but where it is marked in the figure is a reasonable approximation. Then, the lines whose tangents are $|\partial u/\partial y|_{MAX}$ and $|u_{DIF}/y_{MAX}|$ can be drawn into the figure. Obviously, the line with $|u_{DIF}/y_{MAX}|$ slope has the higher slope, therefore, for the attached boundary

layer case $F_{WAKE_1} < F_{WAKE_2}$, which means that the model falls back to the Clauser-type formulation.

Next, consider the case of a separated boundary layer. A typical separated turbulent boundary layer profile is shown in Fig.4.18. Again, y_{MAX} can be located fairly accurately, and the two lines with the appropriate slopes can be marked in the figure. It can be seen that for strong enough separation, the slope of the line with $|\partial u/\partial y|_{MAX}$ slope is higher which means $F_{WAKE_1} > F_{WAKE_2}$. Therefore, for a separated turbulent boundary layer, the Baldwin-Lomax model falls back to the Prandtl type formulation, which is known to be good in far wakes.

The third case is the case of a wake, and a representative wake can be seen in Fig.4.19. Note that the $y = 0$ line does not have to be in the center of the wake. Locating y_{MAX} in this case takes a little more thinking because depending on the location of the $y = 0$ line it can be on either side of the wake. However, assuming a symmetrical wake, y_{MAX} has to be located on the side which is further away from the $y = 0$ line, since in that case y_{MAX} and F_{MAX} is greater. As a consequence, the situation becomes similar to the one for separated turbulent boundary layers, and $|\partial u/\partial y|_{MAX}$ is greater than $|u_{DIF}/y_{MAX}|$, which means $F_{WAKE_1} > F_{WAKE_2}$, and the Baldwin-Lomax model falls back again to a Prandtl-type wake formulation. Note, that the actual wake center does not have to be determined, which is an advantage since the wake center is not very well defined for numerical solutions.

4.4 Extensions to the CFD code

In accordance with the foregoing, some extensions to the code ANSERS had to be done to facilitate the use of the non-periodic grid, the wake turbulence modeling and the compressible Clauser model.

4.4.1 Periodic Boundary Condition for Non-Periodic Grid

The cascade flow to be calculated is periodic in the y direction, and one period is 1.4674 in., the pitch of the cascade. The grid generated in Section 4.2 was such that translating the lower boundary by one pitch in the positive y direction it would fall right on the upper boundary. However, at the end of this translation the grid points of the lower boundary would not fall on the grid points of the upper boundary, a quality which is called the "non-periodicity" of the grid. Accordingly, the cell faces do not fall on each other either, and to achieve a periodic boundary condition, we cannot just simply pass the flow variables of the cell faces of the lower boundary to the cell faces of the upper boundary. In the case of grid periodicity, a simple rule can be used for grids with the orientation as the grid has in Fig.4.2. If we pick a cell on the lower boundary, say j_1, then the counterpart on the upper boundary will be $j_{max} - j_1$. For a nonperiodic grid, there is no such rule.

In Fig.4.20, a typical case of the matching is illustrated. Below the k_{max} line, the boundary cells under the upper edge of the grid can be found, and above the k_{max} line the boundary cells above the lower edge of the grid can be found, as they would relate to each other after the above described translation. For the special case in the figure, the boundary conditions for the j^{th} and the l^{th} cells are

$$Q_{j,k_{max}} = \frac{a\,Q_{l+2,k_{max}-1} + b\,Q_{l+1,k_{max}-1} + c\,Q_{l,k_{max}-1}}{a+b+c},$$

and

$$Q_{l,k_{max}} = \frac{c\,Q_{j,k_{max}-1} + d\,Q_{j+1,k_{max}-1}}{c+d}, \tag{4.58}$$

respectively, where Q is the vector of the conserved variables. It can be seen that this process, when applied to all the k_{max} boundary cells, can be written in a matrix formulation, and then applying the boundary conditions simply means a matrix multiplication. This matrix, which consists of the $a, b, c, d \ldots$ etc. quantities

depends on the grid only, and can be set up at the beginning of each run. In this way, the algorithm which generates the matrix does not use considerable computer time.

4.4.2 Implementation of the Clauser compressible model

The only aspect of the implementation of the Clauser compressible model which is not straightforward is the finding the edge of the boundary layer. From Eq.(4.45) it is clear that a relatively small error in the boundary layer thickness can cause error in the final value of the eddy viscosity. In cascade flows, the velocity gradient is high even outside of the boundary layer, therefore the edge of the boundary layer is not very well defined. Actually, the Baldwin-Lomax model avoids this problem by introducing a different length constant. That length constant is well defined even for cascade flows, however it cannot be substituted for the boundary layer thickness, since it is well below that. However, the fact that the vorticity is approaching zero in the potential flow region can be used to find a well defined edge of the boundary layer. We can say for example, that the edge of the boundary layer is located where the vorticity falls below 1% of its maximum value in the boundary layer. The success of this method is shown in Fig.4.21, where u/u_{ref} values are plotted against the normal coordinate to the wall. The point, where the edge of the boundary layer is located following from the above method, is marked. The outcome looks very reasonable. It should be mentioned that this method of locating the edge of the boundary layer is insensitive to the actual value of the limit for the vorticity ratio. Since the vorticity falls so fast in that region, the results would be almost the same using 0.1% for the limit. For the viscous sublayer the Reichardt model was implemented (Eq.(4.46)).

4.4.3 Implementation of the Baldwin-Lomax model

In Section 4.3.2, we introduced the Baldwin-Lomax model as a turbulence model capable of treating both attached and separated boundary layers and turbulent wakes. In the original code, the Baldwin-Lomax model was implemented already, however, only for the boundary layer. Therefore, the original implementation was revised and extended.

First of all the wake constant, C_{WK}, had to be changed from 0.25 to 1.0. Since the Baldwin-Lomax model was used only in the separated boundary layer and in the wake, where the distance from the wall or the distance from the split periodic boundary does not have any significance. Therefore, the use of the Klebanoff factor, which is dependent on those distances, was not justified.

The normal distances from the $k = 1$ boundary needed for the turbulence models were determined along the j grid lines. The grid was generated in such a way that close to the $k = 1$ boundary, the j grid lines were orthogonal to the $k = 1$ boundary. However, at the trailing edge this was obviously not possible, and also, anywhere farther away from the $k = 1$ boundary, the j grid lines turned, and the distance along them was a few percent different from the normal distance from the boundary. This fact introduced a few percent error in the eddy viscosity, however, this error was considered negligible for the final results.

In the wake region the search for the maximum velocity was carried out only in that half of the pitch in which the wake was located. Also, the wake model was not applied close to the grid exit, since there part of the wake was leaving the computational domain due to the turning of the grid.

When we encountered problems with convergence, the Baldwin-Lomax model was also implemented in the wake region in a different way. In this implementation,

the wake line was assumed, and the wake profiles were obtained on orthogonal lines to this assumed wake line. For the first iteration, this interpolation required considerable computer effort, however the relevant information could be stored and after that this interpolation was inexpensive. Then, the eddy viscosities could be calculated on these wake profiles, and interpolated to the cell centers. This implementation was more proper than the first one, however it still required more CPU time, and when it turned out that it did not solve the oscillation problem, its use was not pursued any more. Let it be mentioned, though, that this implementation was worked out in such a way that it could be easily applied to an unstructured grid.

4.5 Supplementary programs

4.5.1 Exit Mach number

Before every restart, there was a need to know whether the exit Mach number for the solution matched reasonably well the target Mach number. Obviously, the exit Mach number had to be calculated in the same way as it was calculated for the experiments. Therefore, the static pressure had to be determined in the computational domain at the same locations as it was determined in the cascade, that is at the wall pressure tap locations. The wall pressure tap locations obviously did not fall on cell centers of the grid, and not even the cell in which a tap fell was known automatically. Therefore, a subroutine had to be developed, which had an (x, y) point as input, and the interpolated flow variables in the (x, y) point as output. This subroutine will be called simply interpolation subroutine. Invoking this interpolation subroutine the static pressures at the locations of the wall pressure taps were determined, and the exit Mach number could be determined using the same kind of averaging as for the experimental results.

4.5.2 Generation of the numerical fringes

From the numerical results, it is possible to generate fringes of an interferogram which would result if the flow was real and interferometer picture of that flow were taken. In Chapter 3, it was shown that the fringes of a single-plate interferogram are determined by the density field, the wedge angle of the plate, the thickness of the plate, the index of refraction of the plate, the orientation of the wedgeness of the plate, and the incidence angle to the plate. However, it is simpler to use the fringe spacing determined from the no-flow picture, the image separation distance, the K constant (see Eq.(3.11)) and the known density field to determine the fringes. With these known, one can use the following procedure. First a reference point, A, has to be chosen, where the value of the fringe function has to be fixed. This value could be any number, but let us say it is zero. Then, a second point needs to be chosen, B, where the value of the fringe function will be determined. These points were chosen in the interferogram and they can be transferred to the real flowfield as was discussed in connection with Figs.3.17a-3.17d. In this way A_1, A_2, B_1 and B_2 points can be obtained. A and B can be chosen such a way, that A_1 and B_1 fall right on cell centers of the grid. Then, the density is known in them without any interpolation. Now, f_{AB_n}, the number of fringes between A and B can be easily determined from the no-flow picture. Obviously, we are going to use either Eq.(3.28a) or (3.28b) to obtain f_{AB_f}, but in order to get that the density should be known also in points A_2 and B_2. A_2 and B_2 are determined by knowing that they are A_1 and B_1 shifted in the x-direction by one image separation, respectively. In other words

$$x_{A_2} = x_{A_1} + d$$

$$y_{A_2} = y_{A_1}$$

and

$$x_{B_2} = x_{B_1} + d$$

$$y_{B_2} = y_{B_1}. \tag{4.59}$$

The new points obtained in this way, A_2 and B_2 are obviously not cell centers, therefore, to determine the density in them, the interpolation subroutine has to be applied. Also, many of the A_2 points fall outside of the boundaries of the grid. If x_{A_2} is less then the x coordinate for the grid exit, the periodicity can be utilized to find a point which has the same density as A_2 has, and which is inside the boundaries of the grid. The interpolation routine in this case, obviously, has to be run for this equivalent point. If x_{A_2} falls behind the exit of the grid, then the density at that point can be taken simply as the density on the exit line in the point whose y coordinate is the same as y_{A_2}. This method can be justified because there are less and less density changes as we approach and pass the grid exit, and also, in this way the density field for A_2 will be continuous. Finally, f_{AB_f} can be expressed from either Eq.(3.28a) or Eq.(3.28b). Running B_2 through the grid points, the fringe function can be determined in every grid point. The fringe lines can be obtained then by simply generating the contour lines of the fringe function, where the fringe function is a round number.

Obviously, we are not interested in the whole grid domain, but only in the domain of which we have actual interferograms. Therefore, B_2 has to run through the cell centers only which fall in this domain, reducing the computational time. Also, the interpolation routine can be run separately and only once, writing the relevant information in a file, and the evaluation of Eq.(3.28a) or Eq.(3.28b) can be done later separately for the individual cases using that file only. Considerable CPU time is saved in this way, since the most expensive part is the interpolation.

4.5.3 Traverse interpolation

The interpolation routine introduced in the foregoing could again be used for the purpose of obtaining the flow properties on the traversed lines. However, a different

interpolation method was used to make the process faster.

For this purpose, imagine the grid in which the cell centers of the original grid are the grid points. Then, the flow properties would be known in the nodes of this new grid. The intersections of the traversed lines with the cell faces of the new grid can be determined then by a fairly simple algorithm, and in these points the flow properties can be interpolated. The actual points in which the flow properties are known at the end of this process are not equivalent with those where the measurements took place, however both the number of the measurement points and the number of these intersection points is high enough so that no significant interpolation error is introduced.

With known flow properties on the traversing lines the mass averaged total pressure losses can easily be integrated.

4.6 Running the Code

In the foregoing, we presented the grid, the code, the new extensions to the code and the turbulence modeling. Now, we arrive to the point that the specific setup for the different flow conditions and the actual running of the code can be discussed.

As was mentioned before, there are six target Mach numbers. Much of the experimental work was carried out with this in mind, therefore the shadowgraph pictures, the interferometer pictures and the blade surface pressure measurements all were targeting these Mach numbers. We also made sure that among the traverse measurements, there were representatives close to these target Mach numbers. Since in the experiments we did not have perfect control over the exit Mach number, the target Mach numbers could not be perfectly achieved. Therefore, for each target Mach number, we chose a total pressure traverse, a wall pressure set, a blade sur-

face pressure set, a shadowgraph, and one interferograms of each kind, for which exit Mach numbers were not perfectly the target value, but still close to it. Then, with the numerical calculations, we were aiming at the average of these exit Mach numbers. In Table 4.1, the actual exit Mach numbers for the different experimental results used in the comparisons with the numerical results are summarized for all six target Mach numbers. The averages of those Mach numbers are also included.

The reference conditions for each Mach numbers were the inlet, or upstream, conditions. It was known that the inlet Mach number was close to 0.2 for all exit Mach numbers, and that value was taken as reference. Then, the measured upstream total pressure could be used to obtain the inlet pressure. Also, the measured total temperature could be used to obtain the inlet temperature. The inlet laminar viscosity was calculated from the Sutherland law, since that model was implemented in the code. The temperature and the pressure gave the density from the ideal gas equation. Finally, choosing the reference length to be the axial chord, the Reynolds number could be calculated. The actual inputs to the code, which determined the rest of the reference conditions, were the reference Mach number, the reference temperature, the reference length and the Reynolds number.

Next, consider the boundary conditions. We already discussed the treatment of the periodic boundaries in Section 4.4. For the outlet, consider that the outlet axial velocity is not supersonic, since the axial component of the exit Mach number is only $\sin 67° \cdot M_e$, therefore supersonic outflow, or "extrapolation" boundary condition cannot be used there. Rather, the flow conditions are determined by the back pressure, and that is what needs to be specified. Actually, this boundary condition is the one which sets the exit Mach number. As a first guess, the exit static pressure can be taken the same as the one which follows from the above discussed "modified" target Mach number and the upstream total pressure. Although in this way we obtain the average static pressure valid at Station 1, with the assumption of

slight change in static pressure downstream of Station 1 (the experimental results support this assumption) this static pressure can be used at the grid exit too. In the input deck of ANSERS then the ratio of this pressure to the inlet pressure, or reference pressure can be specified, and the proper boundary condition selection is the one called "subsonic outflow'. It turned out that without further adjustment, up to $M_e = 1.1$ this method preset the exit Mach number quite close to the target Mach number. Above $M_e = 1.1$ the p_{out}/p_u ratio had to be decreased further to accommodate for the increasing losses between Station 1 and the grid exit. We are left with the inlet boundary condition only. At the inlet physically, the total pressure and the total temperature are determined by the conditions in the storage tank of the wind tunnel and the rate at which the control valve is opened. In principal, these quantities can be set no matter what the conditions are in the calculated domain and behind. If we are upstream far enough, the v velocity can be taken as zero, and the u velocity can be taken uniform, whatever its value may be. In fact, the u velocity is determined not only by the upstream conditions, but also the geometry in the calculated domain. The proper boundary conditions have to reflect the foregoing, and the "subsonic inflow" boundary condition was the right choice. That boundary condition held the entropy and the total enthalpy constant at the reference value, and that was equivalent to holding the total pressure and the total temperature at the reference values. Also, for that boundary condition type, $v = 0$ and the u velocity was extrapolated, which complies with the uniform upstream velocity requirement.

In the input deck to ANSERS the following options were set for the great majority of the tests. The full Navier-Stokes equations were solved, since the thin layer and parabolized approximations were not believed to be sufficient in the trailing edge region. Roe's flux differencing method was used for the upwind formulation. The Min-Mod limiter was chosen for the flux limiting. Upwind, third order spatial

discretization was used in both coordinate directions. Interpolation of the conserved variables was performed with linearization to form all implicit terms taken with respect to those conserved variables. Spatially split approximate factorization was used for time relaxation.

As was mentioned before in Section 4.2, each exit Mach number case was run on all three grid sizes. Not only the grid convergence could be studied this way, but also by initializing the problem with the solution obtained on the coarser grid, the CPU time needed for obtaining the solution on the finer grid was substantially decreased. In fact, it should be born in mind that saving CPU time was a crucial issue throughout the numerical studies. Accordingly first, a calculation was carried out on the 110×12 grid, which we named in Section 4.2 the "first" grid. The flowfield was initialized with the inlet conditions, that is with a low subsonic velocity. Therefore, it turned out to be advantageous to set the back pressure to a very low value at the beginning to accelerate the flow to supersonic speeds near the exit. The Mach number contour lines were checked before each restart, and when the flow seemed to be accelerated enough, the real backpressure was set, and the problem was run further on with that back pressure until a reasonable solution was obtained after about 2-3000 iterations. The total CPU time to obtain solution on the first grid was a few hundred seconds only on an IBM 3090 supercomputer.

Next, the solution on the 110×12 grid was used to initialize the problem on the 219×23 grid, which was named the "second" grid in Section 4.2. Since the first grid was generated from the second by simply taking out every other grid line in both the j and k directions, every cell of the first grid consisted of four cells of the second. Then, for the initialization, those four cells of the second grid were all assigned the flow variables of the one cell of the first grid. The resulting slight lack of smoothness required careful starting of the iterations on the second grid, that is the time step had to be lowered, and the re-use option could not be used

temporarily. However, after a few iterations, the solution was smooth again, and when the problem converged, relatively few, about 1000 iterations were needed. In terms of CPU time that meant about 2000 seconds.

The result obtained on the 219×23 grid was interpolated on the 437×45 grid in order to initialize the problem on this finest grid, which was named the "third" grid in Section 4.2. Again, after careful restarting, convergence was achieved after about 1500 iterations with total CPU time about 6000 sec.

The calculations did not completely converge for some cases, and small oscillations appeared which were enough to have a significant effect in the numerically calculated total pressure losses. Due to its importance, a whole section is devoted for the problem.

4.7 Convergence

Since for some of the cases a completely converged solution could not be obtained, the problem needs some discussion. Generally, a solution is converged when the residual has dropped several orders of magnitude from its initial value and stabilized, and the solution does not change any more. Certainly there is some arbitrariness in deciding when a solution can be considered converged.

If a problem is not converging, then it is either diverging or oscillating around some solution. Depending on the amplitude, the oscillating solution may be more or less meaningful. The oscillation can be measured with different variables. For example, in our case it can be measured in the exit Mach number or the loss coefficient. From the point of view of convergence in exit Mach numbers, all of the cases can be considered converged, since the amplitudes of the oscillations in M_e were only $\pm 0.5\%$. However, the oscillation in the mass-averaged, total pressure loss coefficient

was considerable, since for some cases it reached ±60%. Notice from the definition of the loss coefficient (Eq.(2.1)) though, that relatively small (less then 1%) oscillation in the exit total pressure can result in such a high oscillation of the loss coefficient, since the loss coefficient was calculated as the difference of two large and almost equal quantities.

For those cases which did not converge completely, some condition had to be set for the stopping of the time relaxation. When a steady oscillation, that is an oscillation of the loss coefficient with a constant amplitude around a definite mid-value, was reached and maintained over about 5-10 cycles, and when also the residual was not dropping any more, the iteration was stopped since there was no hope for further convergence. Incidentally, these cycles had a length of 100-300 iteration with a Courant number of 0.5. Let us emphasize again, that these solutions were still quite converged when other aspects of the flow were considered, since the oscillation in most variables remained below 1%.

In Fig.4.22, the residual drops that would have been obtained if the calculations had started from the flowfield initialized with the inlet conditions are shown for all exit Mach numbers and grid sizes. R_0 in this figure is the residual after the first iteration, and because of the grid sequencing procedure explained in the previous section, for the finer grids R_0 values were not available, but had to be calculated just for the sake of this figure. Also, for the same reason, the number of iterations needed for the indicated residual drops are not known. This kind of representation of the residual drops is, however, much more meaningful then giving the residual drops for calculations starting from a flowfield initialized with the solution on a coarser grid. Note, that the greatest drop could be achieved with the first grid, but even with the finest third grid about two orders of magnitude residual drop was obtained. The residual history was not saved for all of the runs, since usually a total of 5-10,000 iterations were executed for one exit Mach number by the time solution

was obtained on the finest grid. As two typical cases, let us show now in Fig.4.23 the residual as a function of the iteration number for two Mach numbers. $M_e = 1.1$ and $M_e = 0.9$ were chosen, because the first represents a converged solution, and the second represents a solution with fairly high oscillation. These calculations were done on the 219×23 grid, and the flowfields were initialized with the solutions on the 110×12 grid. It can be seen that the two residual curves follow each other very closely until at one point they depart from each other.

It may be informative to study more deeply, how the oscillation actually is shown in the flow variables. The total pressure drop is probably the best for this goal, since it carries the largest oscillation. In Fig.4.24, total pressure drop traverses are shown for the 219×23 grid, with $M_e = 1.0$. The code was stopped after every 100 iterations, and a Courant number of 0.4 was used. It can be seen, that the oscillation mostly occurred between the wakes and not in the wakes themselves. The peaks of the wakes were very steady.

Finally, in Fig.4.25 the oscillations in the loss coefficient at Station 1 are given for all Mach numbers and for the second and the third grid. It can be seen that the oscillation is the most severe around $M_e = 0.9$, and it is considerably higher for the finest third grid. Oscillation figures for the first grid are not given, because the calculations always converged on the first grid.

Solutions to the oscillation problem were sought extensively. The attempts included lowering the time step, changing the re-use option within large margins, using different limiters, etc. The oscillation problem could not be solved with any of the options available in ANSERS, except lowering the accuracy of the spatial discretization. This, however, resulted in an unacceptably high loss coefficient. The trailing edge and wake turbulence model was modified too, as was discussed in Section 4.4.3, but that did not solve the problem either. Even the very drastic "freezing" of

the turbulent viscosity did not help. It should also be mentioned, that for inviscid and laminar viscous calculations the oscillation was even higher, and that is why comparisons of inviscid and viscous solutions are not included in this study.

A possible explanation for the oscillation is that the Navier-Stokes equations may not have a unique steady state solution with the imposed boundary conditions. The instabilities that were observed in the flowfield during the flow visualization studies support this assumption. Another possible explanation can be that the so called condition number (see Ref.[54]) was quite high, which resulted in very low convergence rate and therefore could have been the cause for oscillation. The fact that the highest oscillations were found for the cases with exit Mach number close to 1.0 supports this second assumption. It also should be mentioned, that an attempt to calculate the same flow with a different CFD code at GE Aircraft Engines resulted in oscillating solutions too [55].

4.8 Results

In this section, the experimental and numerical results are compared. In general, results obtained with either the third or the second grid are given only, however, for grid convergence considerations some results with the first grid are also presented. Also, for the grid convergence study, it is important that the first grid point in the turbulent boundary layer be within the laminar sublayer. Typical y^+ values for those points were 0.9-2.6 for the 110×12 grid, 0.3-1.6 for the 219×23 grid, and 0.1-0.9 for the 437×45 grid.

First, in Figs.4.26-4.29 let the contour plots of the density, pressure, temperature and Mach number for $M_e = 1.2$ be presented, respectively. These qualitative results show that the calculations reflect the proper physics of the flow. The locations of the trailing edge shocks given in the shadowgraph of Fig.4.5 are well matched. The

velocity vectors in the trailing edge region nicely show the trailing edge separation in Fig.4.30. The lack of symmetry in the trailing edge flow is due to the fact that on the pressure side the separation laminar, whereas on the suction side the separation is turbulent.

In Figs.4.31-4.42, the isentropic Mach number profiles are shown for both stations and for all six target Mach numbers. For the $M_e = 1.1$ case in Figs.4.37 and 4.38, the results from all three grid sizes are included. It can be seen that the results from the second and third grids are almost the same, therefore grid convergence was approached. Another observation is that the measured isentropic Mach numbers are smeared out to some extent through the shock waves. As a matter of fact, these results here obtained with the first grid match the measured data better than the results obtained with the finest third grid. The reason could be the following. In the real flowfield on the cascade endwalls, boundary layers develop in which, close to the wall, the Mach number is less than 1.0. Consequentially, the shocks of the flowfield cannot extend deep into the boundary layers, and, on the wall, the sharp pressure drops through the shocks cannot be detected. In other words, on the wall, the sharp pressure drops across the shocks are smeared out by the boundary layer. Having lower grid density has a similar effect: the larger grid cells cannot resolve the high flow gradients, and the sharp drop of static pressure across the shock is smeared out again.

For the blade surface pressure measurements there is no smearing effect, and the results obtained on the finest grid along with the measured data are shown in Figs.4.43-4.48. Again the $M_e = 1.1$ case in Fig.4.45 was chosen to display the extent of grid convergence. The third and the second grids, again, gave very similar results, while the result on the first grid was somewhat different, indicating well approached grid convergence. The predictions are good for all Mach numbers. The largest deviations from the measured results were obtained on the suction side,

behind the impinging trailing edge shock. However, the predictions are fairly good even in that region. Most importantly, the base pressure predictions are also good, although it is commonly known that the base pressure is difficult to predict.

In Figs.4.49-4.57, the measured and calculated wake traverses are shown for both stations. These are the Δp_{tp} results, that is, for the numerical results, the total pressure loss through the bow shock on the traversing Pitot probe had to be simulated. This kind of presentation of the data was chosen, because due to the error in the static pressure measurements the bow shock correction for the measured total pressure traverse was believed to be less accurate then the correction of the numerical results. From the figures, it is apparent, that the difference between calculation and measurement is the most significant in this case. The $M_e = 1.1$ test case is again presented with results on the three different grid sizes. The results are quite different for the three different grids, and it is not as clear as for the other presented data, that grid convergence was sufficiently approached. However, the fact that the difference between the first grid and second grid results is so much greater than the difference between the second grid and third grid results implies that further refining of the grid would not result in much different results. In general, the wakes are thinner, but have higher peaks for the numerical results. The reason for this is probably the poor turbulence modeling in the trailing edge region, where the mixing is probably much stronger than an equilibrium turbulence model would predict. The mixing effect between the two stations is clearly seen, but the observations on the wake shapes are the same for both stations. It has to be mentioned that these traverse profiles were obtained by stopping the iteration at a point when the loss coefficient was at its mid-value. Stopping the iteration at some other point in the course of the iteration may have resulted in considerably different result, as was already shown in Fig.4.24. It can be estimated, that the integrals of these numerically predicted curves and the measured curves are quite close to each other, which

will mean the loss coefficient predictions are quite good.

Now, we are going to present the measured and calculated mass averaged total pressure loss coefficients in Figs.4.58 and 4.59 for the two stations, respectively. These loss coefficients were calculated with nonuniform exit static pressure, or in other words, these loss coefficients are the Loss 3 values. For oscillatory cases, the mean value of the loss coefficient is presented. Data for all three grid sizes are shown in the figures. The loss coefficients obtained with Richardson [56] extrapolation are also included, and they show that the grid convergence was well approached. It also can be seen that, at least when the mean values are concerned, the predictions of the loss coefficient are quite good for all Mach numbers and for both stations. However, it can be debated how meaningful these mean value results are. Again, it would be interesting to know whether the oscillation is coming from the numerics, or it is inherent in the physics of the flow.

The numerical fringes along with the appropriate interferometer pictures are presented in Figs.4.60-4.83 It can be seen that for the lower Mach numbers the agreement is quite good for both interferometer arrangements. Unfortunately, for higher Mach numbers, the instability and moving waves in the flowfield resulted in some quite disturbed pictures, and the comparison between the numerical and experimental fringes is difficult. However, even for those cases the qualitative agreement is reasonable.

For the comparison with the large blade trailing edge interferogram, a calculation of the flow through the large blade cascade was also carried out for the case of $M_e = 1.2$. The differences compared to the $M_e = 1.2$ flow through the original cascade included different Reynolds number, different upstream conditions and different turbulent transition location. The trailing edge density contours are shown in Fig.4.84. Compared to Fig.3.37, it can be seen that the density predictions by the

two methods are in good agreement on the pressure side, however, on the suction side and on the trailing edge there is a considerable disagreement. This disagreement can be due to the misreading of the fringes through the blurry wake region. However, the calculated result also could be in error, and to really decide, static pressure measurements on the suction side of the trailing edge could be very helpful.

Finally, since for the evaluation of the trailing edge interferogram static pressure data was obtained near the trailing edge on the large cascade endwall, the isentropic Mach numbers calculated from these quantities are compared to the numerically obtained isentropic Mach numbers in Figs.4.85-4.87. The agreement between the numerical and the measured results are very good. In Fig.4.87 the drop in the isentropic Mach number at the lowest y/P values is due to a trailing edge shock passing between the two lowest pressure taps. Again, the measured pressure drop is significantly lower than the calculated, since the boundary layer on the wall is smearing out the large pressure gradient.

5 CONCLUSIONS

A comprehensive study of flow through a transonic turbine cascade was presented. Compared to previous measurements, improved data was obtained for the mass-averaged total pressure loss coefficient. The quality of the data is better than that found in most of the references. For the $M_e < 1.22$ region, the scatter was below ± 0.12, as was predicted by an uncertainty analysis. The scatter above $M_e = 1.22$ could not be eliminated. Probably the relatively high humidity was the cause for this scatter, however, this study did not prove that hypothesis unequivocally. In the future, it would be desirable to operate the cascade tunnel at even higher tank pressures. The result may be low scatter even for the $M_e > 1.22$ tunnel runs.

The loss coefficient was higher for Station 2 than for Station 1 for all exit Mach numbers, as was expected. The difference was small for subsonic exit flows, and it increased rapidly for increasing supersonic exit Mach numbers. It was also shown that using the exit static pressure profile instead of the average exit static pressure for the data reduction makes a significant difference when the exit Mach number is higher than about 1.1. Loss coefficients obtained using the static pressure profiles are lower than those obtained with the average exit static pressures. This difference

is greater at Station 1 where the static pressure variation across the exit is more significant.

Shadowgraph studies were carried out for determining the location of the turbulent transition. For the original blades, the transition on the suction side was found at 15% axial chord ahead of the trailing edge, whereas on the pressure side no sign of transition was found. The location of the transition was found to be independent of the exit Mach number. For the enlarged blades, the suction side transition took place at 35% axial chord back from the trailing edge, and again, no transition took place on the pressure side.

The interferometer studies showed that the single-plate interferometer can be a useful tool for cascade measurements. On one hand, it can serve as a check on the calculated mainflow results. On the other hand, it can be used for density measurements in restricted and highly viscous regions of the flowfield, such as the trailing edge region. The assembling and the application of the single-plate interferometer turned out to be much easier than that of a Mach-Zehnder interferometer, however, the evaluation of the interferograms was more difficult. In fact, it was found that for obtaining the actual density field in a domain of the flowfield, the density had to be known in another well defined domain of the flowfield. With the evaluation technique developed in this work, physically reasonable results were obtained for the density field in the trailing edge region of an enlarged blade. A source of trouble that was encountered with the application of the single-plate interferometer was the instability of the flowfield. The instability could be lowered by using a tailboard to help turn the flow through the cascade, but it could not be eliminated completely. Due to the instability, the interferograms were blurred unless the exposure time was sufficiently short. Exposure times on the order of 20 μs were achieved by a special shutter built with a Bragg-cell and a photodiode. Workable pictures were obtained with such exposure times, however, lower exposure times would be desirable in the

future for better quality of the pictures. Ideally, a pulse laser could be used which produces enough light energy for pictures in just a few nanoseconds.

The grid generated for the numerical results was smooth, fairly orthogonal, and had the right density of grid points in the different parts of the flowfield. A non-periodic C-type grid proved to be the best to achieve these features. The grid convergence was successfully approached with a maximum size of 437×45. A new Clauser-type turbulence model was developed, successfully tested and applied for the outer part of the attached suction side boundary layer. Full convergence could not be achieved for some of the test cases. The oscillation was the highest for the finest grid and for exit Mach numbers around 0.9-1.0. The oscillation was significant only in the loss coefficient calculated from the numerical flowfield.

The numerical results matched the experimentally obtained data quite well for most aspects of the flow. The isentropic Mach number profiles and the blade surface isentropic Mach numbers agreed the best with the experimental data. Even the trailing edge isentropic Mach numbers were predicted well. The total pressure drop traverses showed the greatest deviations from the measurements, but that flow variable is known to be difficult to predict accurately (As a matter of fact, none of the references show such comparisons). However, the integral of the total pressure drops, which is essentially the loss coefficient, agreed with the measurements quite well.

The calculated total pressure wakes were thinner and higher than the measured ones. This was also in agreement with the interferometer results, which showed less density variation across the wakes than follows from the computed results. It can be concluded from these observations that there was a much stronger mixing in the trailing edge region than the Baldwin-Lomax turbulence model predicted. Interestingly, similar observations about the density wakes can be made looking at

the interferogram and the numerical density fields in Ref.[22]. In that reference, a two-equation turbulence model was used. It would be interesting to investigate whether this underprediction of the mixing in the trailing edge and near wake region is a general drawback of the available turbulence models. The total pressure wake surveys coupled with interferometer pictures can be useful experimental information for such a study.

REFERENCES

[1] Goobie, S. M., "An Experimental Investigation of the Effect of Incidence on the Two-Dimensional Performance of an Axial Turbine Cascade," ISABE Paper 89-7019, 1989

[2] Hoheisel, H., Kiock, R., Lichtfuss, H. J. and Fottner, L., "Influence of Free-Stream Turbulence and Blade Pressure Gradient on Boundary Layer and Loss Behaviour of Turbine Cascades," *Journal of Turbomachinery*, Vol.109, pp.210-218

[3] T. Yoshida, et.al., "Low and High-Speed Cascade Tests of Air-Cooled Turbine Blades," Conference Paper, Gas Turbine and Fluids Engineering Conference, New Orleans, La, March 1976

[4] MacMartin, I. P., Norbury, J. F., "The Aerodynamics of a Turbine Cascade with Supersonic Discharge and Trailing Edge Blowing," ASME Paper 74-GT-120, 1974

[5] Prust, H. W. and Helon, R. M., "Effect of Trailing Edge Geometry and Thickness on the Performance of certain Turbine Stator Blading," NASA TN D-6637, 1972

[6] Kiock, R., Lehthaus, F., Baines, N. C. and Sieverding, C. H., "The Transonic flow

Through a Plane Turbine Cascade as Measured in Four Europian Wind Tunnels," ASME Paper 85-IGT-44, 1985

[7] Mee, D. J., Baines, N. C., Oldfield, M. L. G. and Dickens, T. E., "An Examination of the Contributions to Loss on a Transonic Turbine Blade in Cascade," ASME Paper 90-GT-264, 1990

[8] Vijayaraghavan, S. B., Kavanagh, P., "Effect of Free-Stream Turbulence, Reynolds Number, and Incidence on Axial Turbine Cascade Performance," ASME Paper 88-GT-152, 1988

[9] Zaccaria, M. A., "Development of a Transonic Cascade Facility," M.S. thesis, VPI&SU, 1988

[10] Singer, R. T.,"An Experimental Examination of the Effect of Trailing Edge Injection on the Aerodynamic Performance of Gas Turbine Blades," M.S. thesis, VPI&SU, 1988

[11] Zeidan, O., "An Experimental Examination of the Effect of Trailing Edge Thickness on the Aerodynamic Performance of Gas Turbine Blades," M.S. thesis, VPI&SU, 1989

[12] Bertsch, R., "An Experimental Examination of the Influence of Trailing-Edge Coolant Ejection on Blade Losses in Transonic Turbine Cascades," M.S. thesis, VPI&SU, 1990

[13] Doughty, R. L., "The Effect of Blade Solidity on the Aerodynamic Loss of a Transonic Turbine Cascade," M.S. thesis, VPI&SU, 1991

[14] Moses, H. L., Kiss, T. and Bertsch, R., "Aerodynamic Losses due to Pressure Side Coolant Ejection in a Transonic Turbine Cascade," AIAA paper 91-2032, 1991

[15] Collie, J. C., Moses, H. L. and Kiss, T., "The Effect of Square Trailing Edges on Turbine Blade Performance," AIAA paper 91-2130, June 1991

[16] Doughty, R. L., Moses, H. L. and Gregory, B. A., "The Effect of Blade Solidity on the Aerodynamic Loss of a Transonic Turbine Cascade," AIAA paper 92-0393, Jan. 1992

[17] Moses, H. L., Schetz, J. A. and Gregory, B. A., "Cooled Transonic Turbine Cascade Testing," X ISABE, Nottingham, UK, Sept 1991

[18] Shelton, M., L., Gregory, B. A., Doughty, R. L., Kiss, T. and Moses, H. L., "A Statistical Approach to the Experimental Evaluation of Transonic Turbine Airfoils in a Linear Cascade," ASME paper 92-GT-5, June 1992

[19] Martelli, F. and Boretti, A.,"A simple Procedure to Compute Losses in Transonic Turbine Cascades," ASME Paper 89-GT-278, 1989

[20] Xu, L. and Denton, J. D., "Numerical Prediction of Turbine Profile Loss," ASME Paper 90-GT-311, 1990

[21] Denton, J. D., and Xu, L., "The Trailing Edge Loss of Transonic Turbine Blades," ASNE Paper 89-GT-278

[22] Hah, C., and Selva, R. J., "Navier-Stokes Analysis of Flow and Heat Transfer Inside High-Pressure-Ratio Transonic Turbine Blade Rows," *J. Propulsion*, Vol.7, No.6

[23] Davis, R. L., Ni, R-H, and Carter, J., E., "Cascade Viscous Flow Analysis Using the Navier-Stokes Equations," *J. Propulsion*, Vol.3, No. 5,

[24] Davis, R. L., and Dannenhoffer III., J. F., "Adaptive Grid Embedding Navier-

Stokes Technique for Cascade Flows," *J. Propulsion*, Vol.7, No.5

[25] Kwon, O. K., "Navier-Stokes Solution for Steady Two-Dimensional Transonic Cascade Flows," *Journal of Turbomachinery*, Vol.110, pp 339-346, July 1988

[26] Nakahashi, K., Nozaki, O., Kikuchi, K., and Tamura, A., "Navier-Stokes Computations of Two- and Three-Dimensional Cascade Flowfields," *J. Propulsion*, Vol.5, No.3

[27] Arnoe, A., Liou, M.-S. and Povinelli, L. A.,"Transonic Cascade Flow Calculations Using Non-Peridoic C-Type Grids," NASA Technical Memorandum, 103624, ICOMP-90-23, October 1990

[28] Anderson, J. D., "*Modern Compressible Flow with Historical Perspective*," McGraw-Hill, 1982

[29] Doebelin, E., O., "*Measurement Systems, Application and Design*," McGraw-Hill, 1990

[30] Moffat, R. J., "Contributions to the Theory of Uncertainty Analysis for Single-Sample Experiments," *Proceedings of the 1980-81 AFOSR-HTTM-Stanford Conference on Complex Turbulent Flows*, Vol. 1, pp.40-56

[31] Liepmann, H. L., "*Elements of Gasdynamics*," Wiley, 1967

[32] Sedney, R., Rowe, R., Bush, C. and Voelker, L., "Conventional Flow Visualization Using Laser Light Source," AIAA Paper 66-127, January, 1966

[33] Weinberg, F. J., "*Optics of Flames*," Butterworths, 1966

[34] Taylor III, A. C., "Convergence Acceleration of Upwind Relaxation Methods

for the Navier-Stokes Equations," Ph.D. Dissertation, VPI&SU 1989

[35] Van Leer, B., "Flux-Vector Splitting for the Euler Equations," ICASE Report 82-30, September 1982

[36] Roe, P. L., "Approximate Riemann Solvers, Parameter Vectors, and Difference Schemes," *Journal of Computational Physics*, Vol.43, 1981, pp.357-372

[37] Van Albada, G. D., Van Leer, B. and Roberts Jr., W. W., "A comparative Study of Computational Methods in Cosmic Gas Dynamics," *Astron. Astrophys.*, Vol. 108, 1982, pp.76-84

[38] Hirsch, C., "*Numerical Computation of Internal and External Flows*," Volume 2., John Wiley & Sons, 1990

[39] Jameson, A., Schmidt, W., and Turkel, E., "Numerical Solutions of the Euler Equations by Finite Volume Methods Using Runge-Kutta Time Stepping Schemes," AIAA Paper 81-1259, 1981

[40] Anderson, D. A., Tannehill, J. C. and Pletcher, R. H., "*Computational Fluid Mechanics and Heat Transfer*," Hemisphere Publishing Corporation, 1984

[41] Baldwin, B. S. and Lomax, H., "Thin Layer Approximation and Algebraic Model for Separated Turbulent Flows," AIAA Paper 78-257, 1978

[42] H. McDonald, and Camarata, F. J.,"An extended Mixing Length Approach for Computing the Turbulent Bouundary Layer Development," *Proceedings, Stanford Conference on Computation of Turbulent Boundary Layers,*", Vol.1, p.83-98, 1969

[43] Johnson, D. A., and King, L. S., "A New Turbulence Closure Model for Boundary Layer Flows with Strong Adverse Pressure Gradients and Separation," AIAA

Paper 84-0175, 1984

[44] Fletcher, C. A. J., "*Computational Techniques for Fluid Dynamics*, Volume II," Springer-Verlag, 1988

[45] Schetz, J. A., "*Boundary Layer Analysis*," Prentice-Hall, 1993

[46] Sorenson, R. L., "A Computer Program to Generate Two-Dimensional Grids about Airfoils and Other Shapes by the Use of Poisson's Equation," NASA TM 81198

[47] Steinbrenner, J. P., Chawner, J. R., Fouts, C. L., "The GRIDGEN 3D Multiple Block Grid Generation System," WRDC-TR-90-3022, Vol.1-2, July 1990

[48] Clauser, F. H., "The Turbulent Boundary Layer," in *Advances in Applied Mechanics*, Vol.IV, Academic Press, New York, 1956.

[49] Cebeci, T. and Smith, A. M. O., "*Analysis of Turbulent Boundary Layers*," Academic Press, 1974

[50] Maise, G. and McDonald, H., "Mixing Length and Kinematic Eddy Viscosity in a Compressible Boundary Layer," *AIAA J.*, Vol.6, pp. 73-80, 1968

[51] Klebanoff, P. S., "Characteristics of Turbulence in a Boundary Layer with Zero Pressure Gradient," NASA TN-3178, 1954

[52] Coles, D., "Measurements of Turbulent Friction on Smooth Flat Plate in Supersonic Flow," *J. Aero. Sci.*, Vol. 21, No. 7, pp.433-448, July 1954

[53] Lee, R. E., Yanta, W. J. and Leonas, A. C., "Velocity Profile, Skin-Friction Balance and Heat-Transfer Measurements of the Turbulent Boundary Layer at Mach

5 and Zero-Pressure Gradient," NOLTR 69-106, June 1969

[54] Godfrey, A. G., "Topics on Spatially High Order Accurate Methods and Preconditioning for the Navier-Stokes Equations with Finite Rate Chemistry," Ph.D. Dissertation, VPI&SU, December, 1992

[55] Shelton, M. L., Private communication

[56] Burden, R. L., and Faires, J. D., "*Numerical Analysis*," PWS-KENT Publishing Company, Boston, 1989

TABLES

Table 2.1 Uncertainties (95% confidence level

Replication level	Error type	Error magnitude	precision error, M_e=0.9		precision error, M_e=1.32	
			ΔL [%]	ΔM_e	ΔL [%]	ΔM_e
1st	1d	60 Pa	0	0	0	0
	1e	15 Pa	0	0	0	0
	1f	0.7 Pa	0	0	0	0
	1g	140 Pa	0.001	0.002	0.017	0.002
	1h	10 Pa	0.001	0	0.001	0
	1i	700 Pa	0.003	0.005	0.060	0.005
	1j	0.01	0.02	0	0.060	0
combined for Level 1			0.020	0.006	0.090	0.006
2nd	1a	20 Pa	0.002	0	0.002	0
	1b	125 Pa	0.016	0.002	0.009	0.001
	1c	30 Pa	0.022	0	0.016	0
combined up to Level 2			0.034	0.007	0.092	0.007
3rd	2a	375 Pa	0.050	0.006	0.028	0.001
	2b	90 Pa	0.070	0	0.05	0
combined up to Level 4			0.092	0.009	0.108	0.007

Table 2.2 Loss Results for Station 1

Run	Exit Mach	Loss 1	Loss 2	Loss 3	Rel. Hum.	T total
JUL28R1	1.154	3.032	2.647	2.454	5.780	290.8
JUL28R2	1.221	3.900	3.099	2.684	5.640	291.1
JUL28R3	1.342	6.353	4.231	3.266	5.940	290.5
JUL28R4	1.311	5.815	4.110	3.310	5.820	291.4
JUL28R5	1.273	5.234	3.948	3.330	6.020	292.1
JUL28R6	0.969	1.573	1.487	1.487	5.760	292.3
JUL28R7	0.864	1.317	1.236	1.239	5.610	294.3
JUL28R8	0.863	1.303	1.220	1.222	5.520	294.8
JUL28R9	1.105	2.529	2.320	2.199	6.020	295.1
JUL28R10	1.123	2.729	2.473	2.333	6.010	295.6
JUL28R11	1.203	3.734	3.068	2.747	6.890	296.2
JUL28R12	1.027	1.907	1.796	1.769	6.420	296.5
JUL28R13	1.123	2.765	2.496	2.369	6.990	297.1
JUL28R14	1.136	2.910	2.595	2.448	7.080	296.6
JUL28R15	1.026	1.897	1.786	1.767	6.730	297.8
JUL28R16	1.072	2.231	2.075	2.007	5.050	299.5
JUL28R17	0.669	0.789	0.743	0.748	5.010	300.1
JUL28R18	0.712	0.880	0.824	0.828	5.140	300.2
JUL28R19	0.781	1.063	0.993	0.998	4.970	300.9
JUL28R20	0.841	1.218	1.135	1.140	4.920	300.6
JUL28R21	0.946	1.510	1.415	1.420	4.810	301.4
JUL28R22	0.901	1.379	1.283	1.287	4.870	301.7
JUL28R23	1.100	2.516	2.309	2.194	4.900	301.2

Table 2.2 continued

Run	Exit Mach	Loss 1	Loss 2	Loss 3	Rel. Hum.	T total
AUG9R16	0.912	1.471	1.385	1.391	5.900	295.8
AUG9R17	1.214	3.902	3.142	2.776	6.940	296.4
AUG9R18	1.233	4.340	3.433	3.011	7.860	296.1
AUG9R19	0.836	1.251	1.173	1.181	6.940	297.2
AUG9R20	0.982	1.613	1.522	1.526	7.200	297.1
AUG9R21	1.114	2.676	2.442	2.321	7.960	297.4
AUG9R22	1.270	5.617	4.397	3.875	7.860	298.2
AUG10R1	1.076	2.330	2.163	2.080	7.850	297.9
AUG10R2	1.217	3.898	3.135	2.761	5.020	296.4
AUG10R3	1.256	4.906	3.821	3.300	5.130	296.3
AUG10R4	1.218	3.882	3.112	2.734	5.100	297.1
AUG10R5	1.324	6.140	4.289	3.445	5.180	297.1

Table 2.3 Loss Results for Station 2

Run	Exit Mach	Loss 1	Loss 2	Loss 3	Rel. Hum.	T total
JUL29R1	0.751	1.055	1.027	1.026	5.530	291.7
JUL29R2	0.797	1.209	1.177	1.175	5.580	291.3
JUL29R3	1.221	4.954	4.308	4.161	5.650	289.9
JUL29R4	1.225	5.071	4.380	4.241	5.800	289.7
JUL29R5	0.984	1.783	1.747	1.747	5.940	290.2
JUL29R6	0.783	1.173	1.143	1.142	5.940	290.2
JUL29R7	1.107	3.198	3.051	3.043	6.090	291.0
JUL29R8	1.266	6.141	4.847	4.656	6.080	290.6
JUL29R9	1.225	5.012	4.334	4.185	5.940	291.1
JUL29R10	1.304	6.710	4.689	4.297	6.010	291.4
JUL29R11	1.016	2.007	1.966	1.965	5.590	294.2
JUL29R12	1.088	2.853	2.749	2.744	5.590	295.6
JUL29R13	1.098	3.048	2.923	2.916	5.540	294.6
JUL29R14	1.060	2.507	2.437	2.435	5.610	296.2
JUL29R15	1.169	3.948	3.556	3.492	5.610	296.1
JUL29R16	1.134	3.464	3.213	3.191	5.590	296.5
JUL29R17	0.899	1.518	1.480	1.479	5.530	297.5
JUL29R18	0.818	1.234	1.201	1.200	5.560	297.7
JUL29R19	0.934	1.602	1.563	1.562	5.440	298.0
JUL29R20	1.243	5.637	4.733	4.598	6.450	297.4
JUL29R21	1.281	7.036	5.441	5.169	7.770	297.7
JUL29R22	1.309	7.644	5.679	5.241	9.750	299.0
JUL29R23	0.871	1.386	1.347	1.345	6.840	299.1
JUL29R24	0.838	1.300	1.266	1.265	6.990	298.8
JUL29R25	0.941	1.636	1.594	1.593	7.470	300.4
JUL29R26	1.255	6.615	5.517	5.366	10.420	299.2

Table 2.3 continued

Run	Exit Mach	Loss 1	Loss 2	Loss 3	Rel. Hum.	T total
JUL30R1	1.135	3.475	3.223	3.191	7.100	290.5
JUL30R2	1.165	3.746	3.373	3.281	5.790	291.0
JUL30R3	1.216	4.897	4.291	4.135	5.820	290.5
JUL30R4	1.262	6.090	4.879	4.739	5.960	290.2
JUL30R5	1.303	6.757	4.779	4.397	6.060	290.3
JUL30R6	1.359	8.181	5.803	5.203	6.080	290.0
JUL30R7	1.317	7.125	5.014	4.512	6.160	291.6
JUL30R8	1.278	6.523	4.980	4.681	6.200	291.2
JUL30R9	1.326	7.544	5.387	4.868	6.610	291.3
AUG8R14	0.804	1.248	1.216	1.215	5.470	294.4
AUG8R15	0.894	1.504	1.460	1.460	5.420	294.9
AUG8R16	1.145	3.558	3.284	3.229	5.470	294.4
AUG8R17	1.209	4.716	4.147	4.020	5.550	294.8
AUG8R18	1.289	7.005	5.474	5.094	6.520	294.6
AUG8R19	1.158	3.760	3.444	3.369	5.880	296.2
AUG8R20	1.095	2.849	2.742	2.736	5.690	296.7
AUG8R21	1.231	5.018	4.247	4.066	5.590	297.5
AUG8R22	1.038	2.229	2.171	2.170	5.270	297.2
AUG8R23	1.226	5.051	4.351	4.215	5.410	296.9
AUG8R24	1.315	7.540	5.755	5.240	6.450	296.9
AUG8R25	0.856	1.363	1.328	1.328	5.940	298.2
AUG8R26	1.018	1.995	1.950	1.950	6.460	301.7
AUG8R27	1.146	3.658	3.376	3.316	7.690	299.4

Table 2.3 continued

Run	Exit Mach	Loss 1	Loss 2	Loss 3	Rel. Hum.	T total
AUG8R29	1.161	4.031	3.691	3.631	8.660	299.0
AUG9R1	1.180	4.112	3.687	3.593	10.830	293.8
AUG9R2	1.237	5.415	4.589	4.464	6.100	291.5
AUG9R3	1.280	6.751	5.340	4.998	6.210	291.5
AUG9R4	1.091	2.771	2.677	2.669	6.110	291.6
AUG9R5	1.121	3.290	3.110	3.090	6.770	291.8
AUG9R6	1.278	6.970	5.580	5.303	8.000	291.3
AUG9R7	1.112	3.153	3.007	2.996	7.160	292.2
AUG9R8	0.868	1.454	1.415	1.415	6.470	293.3
AUG9R9	0.955	1.716	1.675	1.674	6.130	293.6
AUG9R10	1.049	2.348	2.290	2.288	5.850	293.8
AUG9R11	1.306	7.021	5.246	4.775	5.900	293.0
AUG9R12	0.904	1.571	1.529	1.529	5.680	293.9
AUG9R13	1.287	6.579	5.053	4.702	5.740	292.6
AUG9R14	1.182	4.108	3.671	3.567	5.710	293.2
AUG9R15	1.212	4.797	4.219	4.083	5.750	294.4

Table 5.1 Exit Mach Numbers for the Different Measurements

M_{target}	Wall M_{is}	Blade surf. M_{is}	traverse Station 1	traverse Station2	interfer. type "a"	interfer type "b"	Target for CDF code
0.8	0.808	0.803	0.809	0.804	0.818	0.815	0.807
0.9	0.905	0.904	0.901	0.904	0.908	0.895	0.903
1.0	0.988	0.985	0.989	0.984	0.981	0.997	0.987
1.1	1.103	1.103	1.100	1.107	1.112	1.108	1.104
1.2	1.190	1.193	1.192	1.182	1.196	1.188	1.190
1.28	1.276	1.286	1.273	1.278	1.277	1.277	1.276

FIGURES

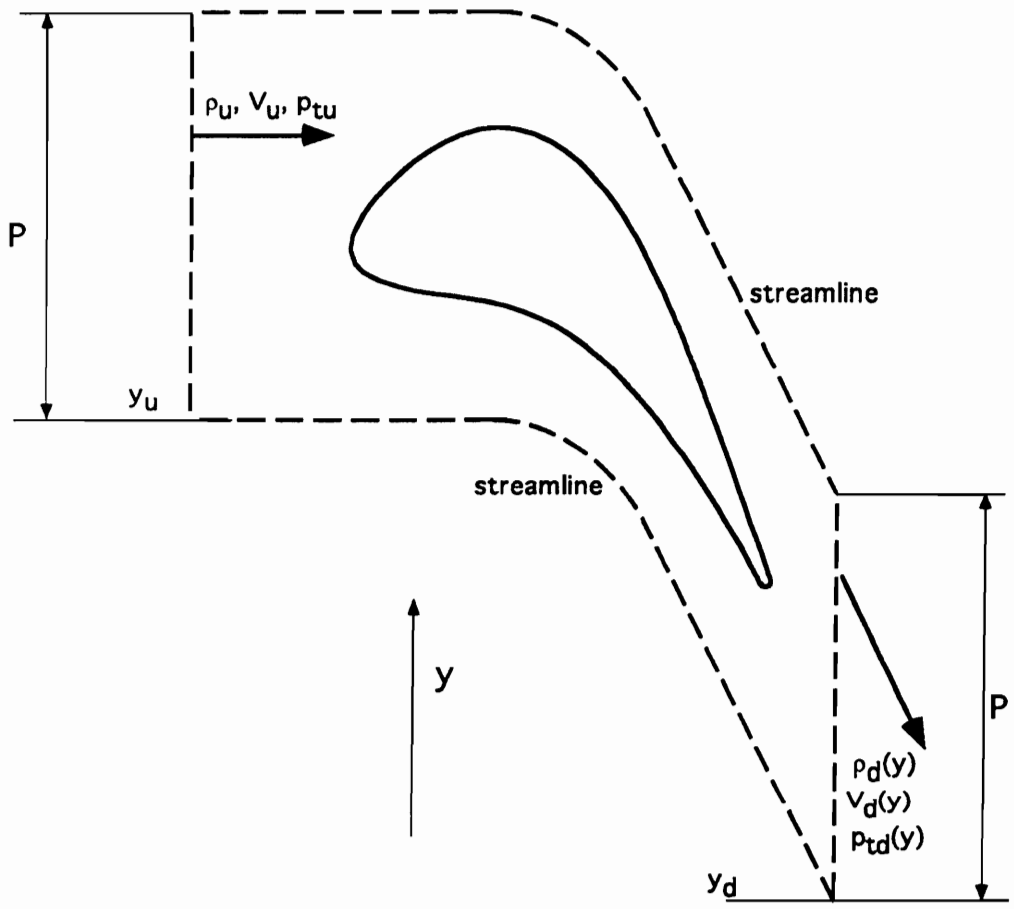


Fig.2.1 The definition of the total pressure losses

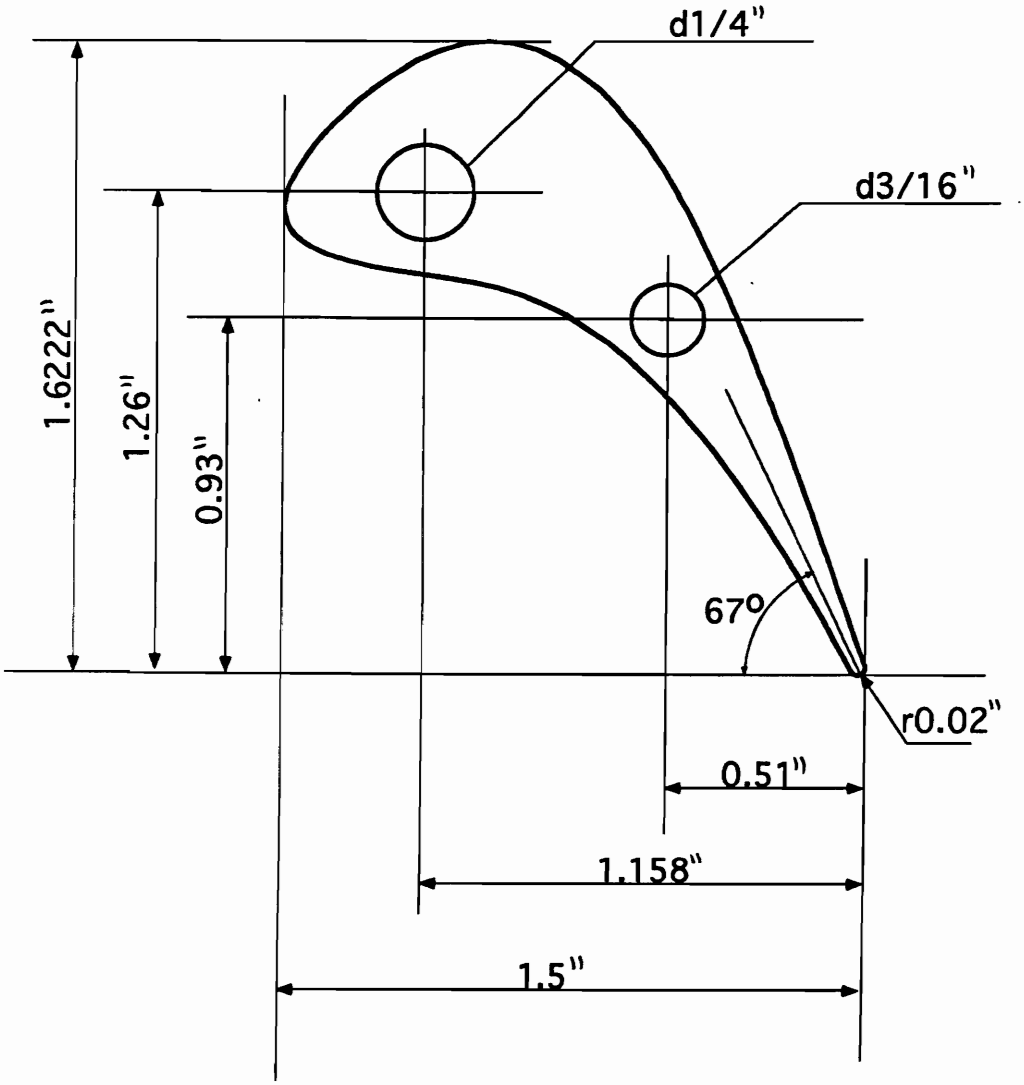


Fig.2.2 Blade geometry

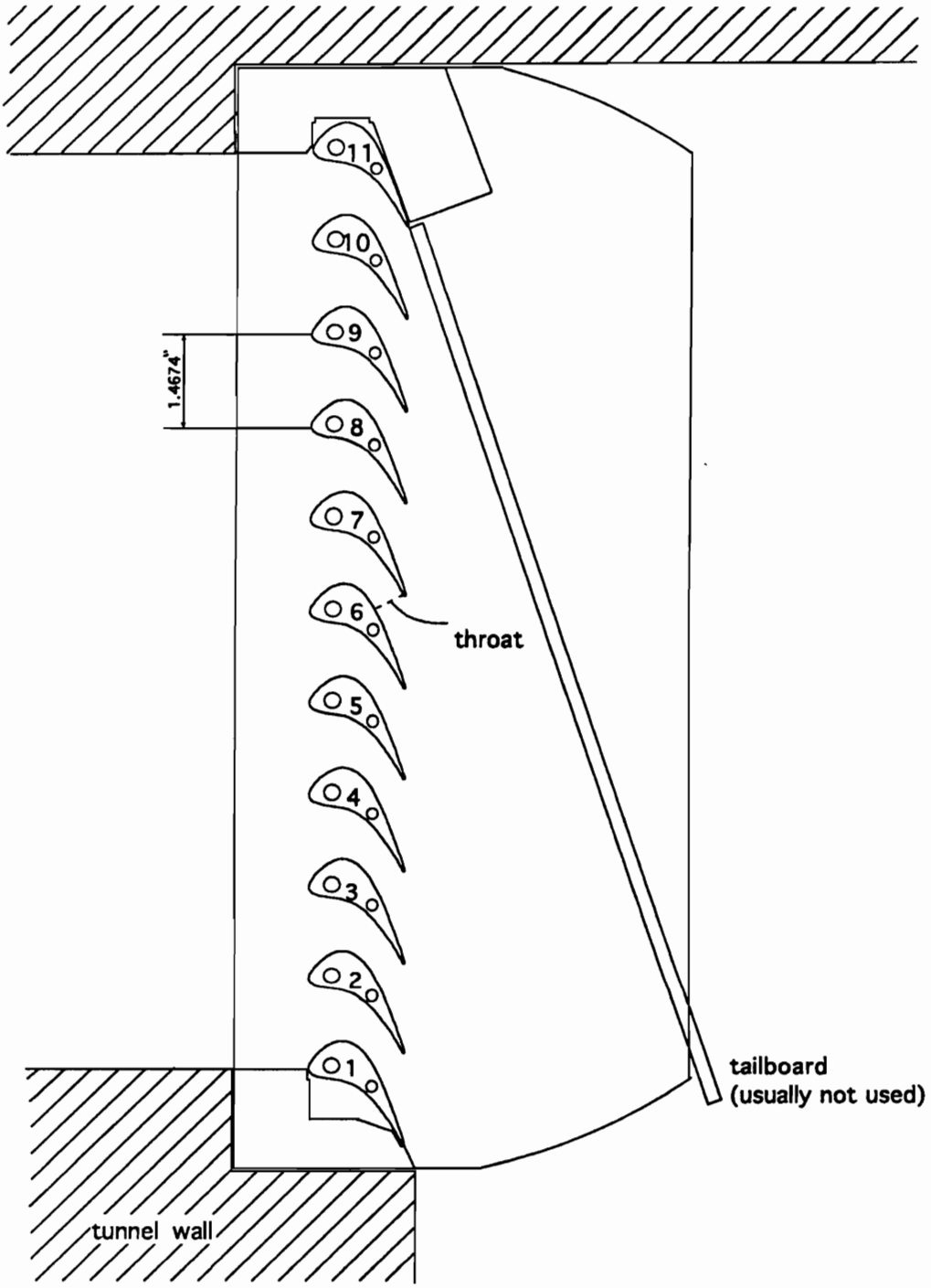


Fig.2.3 The cascade

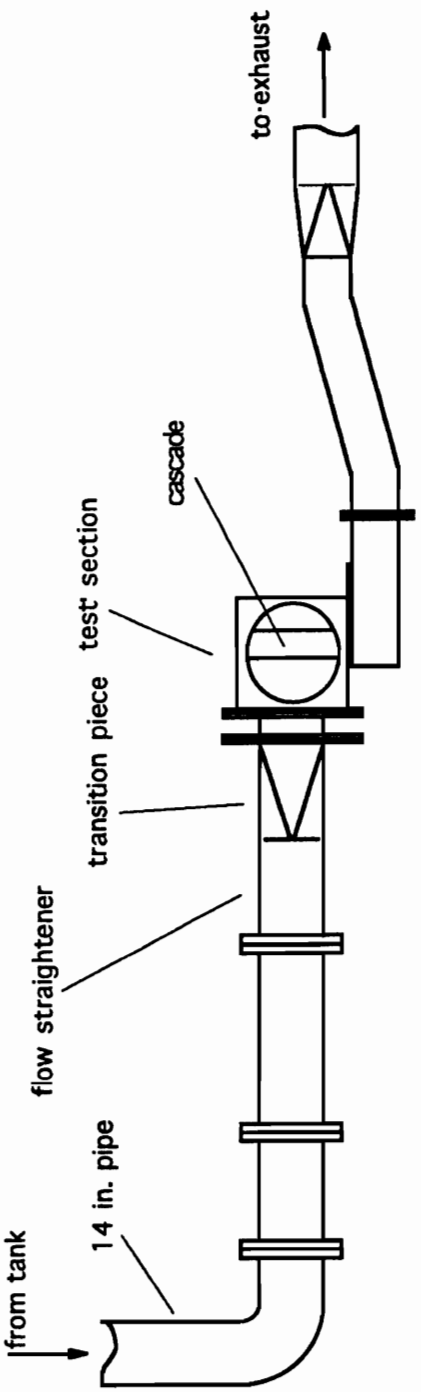


Fig.2.4 Schematic of the cascade tunnel

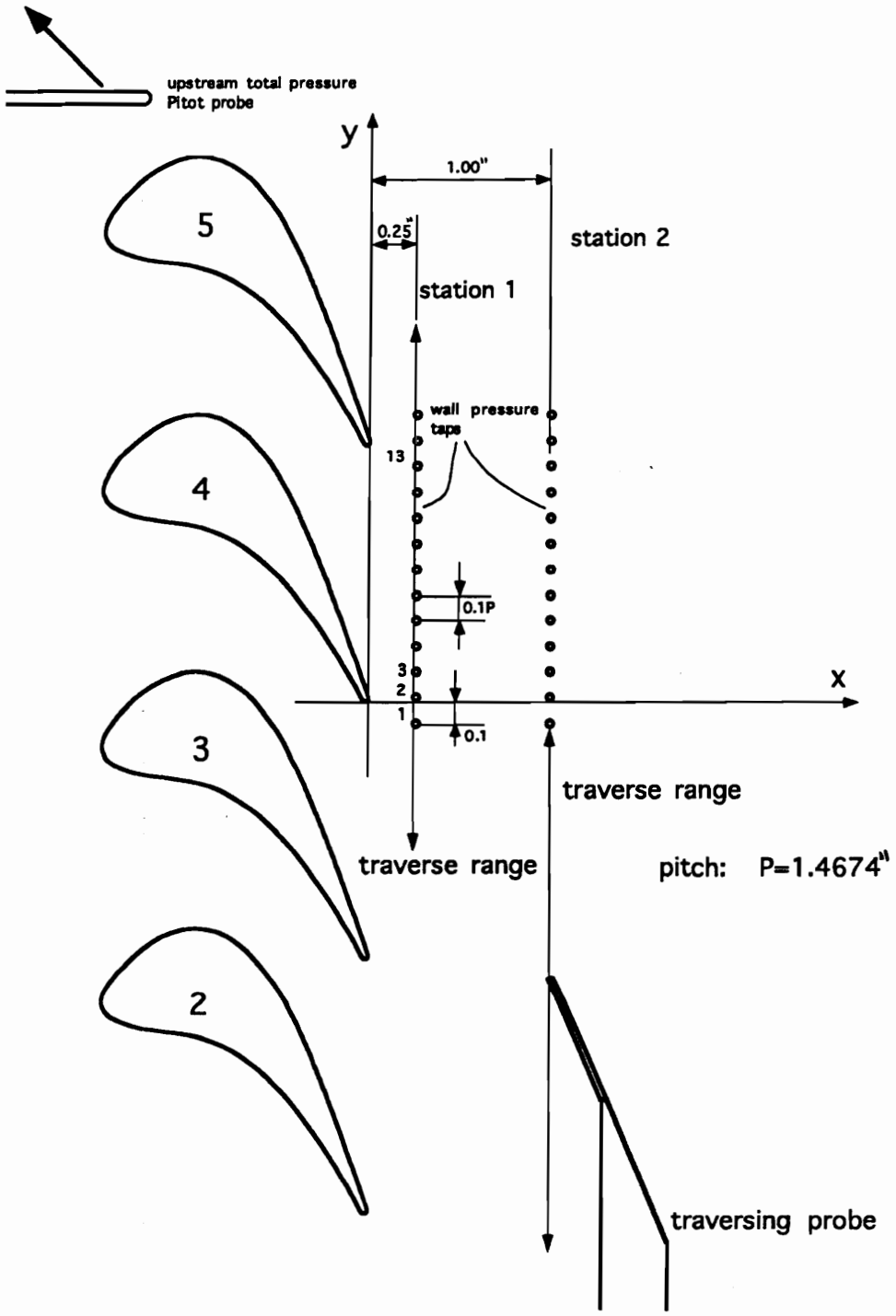


Fig.2.5 Pressure measurement instrumentation

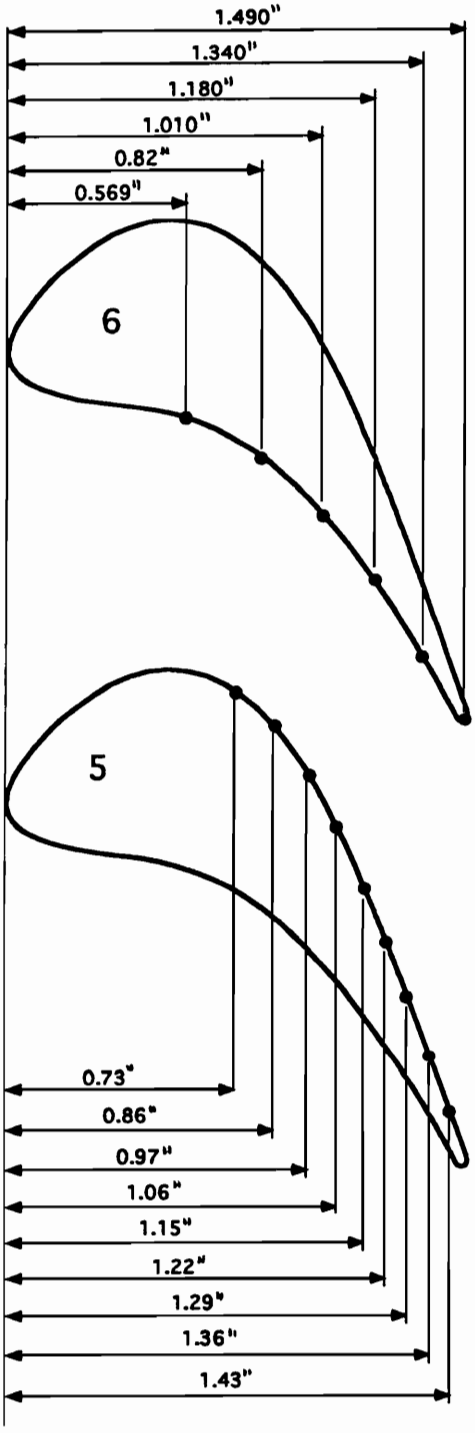


Fig.2.6 Blade surface pressure taps

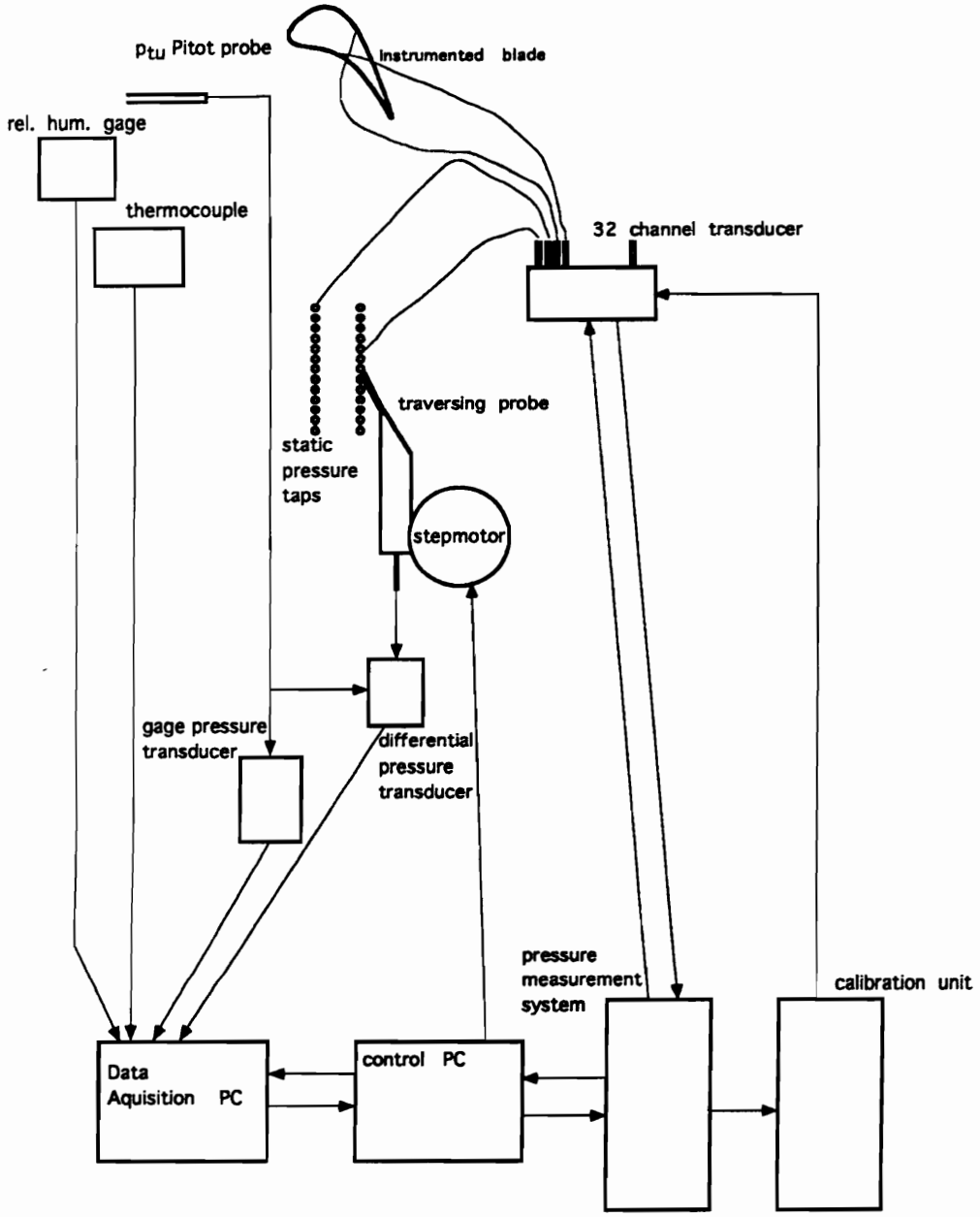


Fig.2.7 Schematic of the data acquisition system

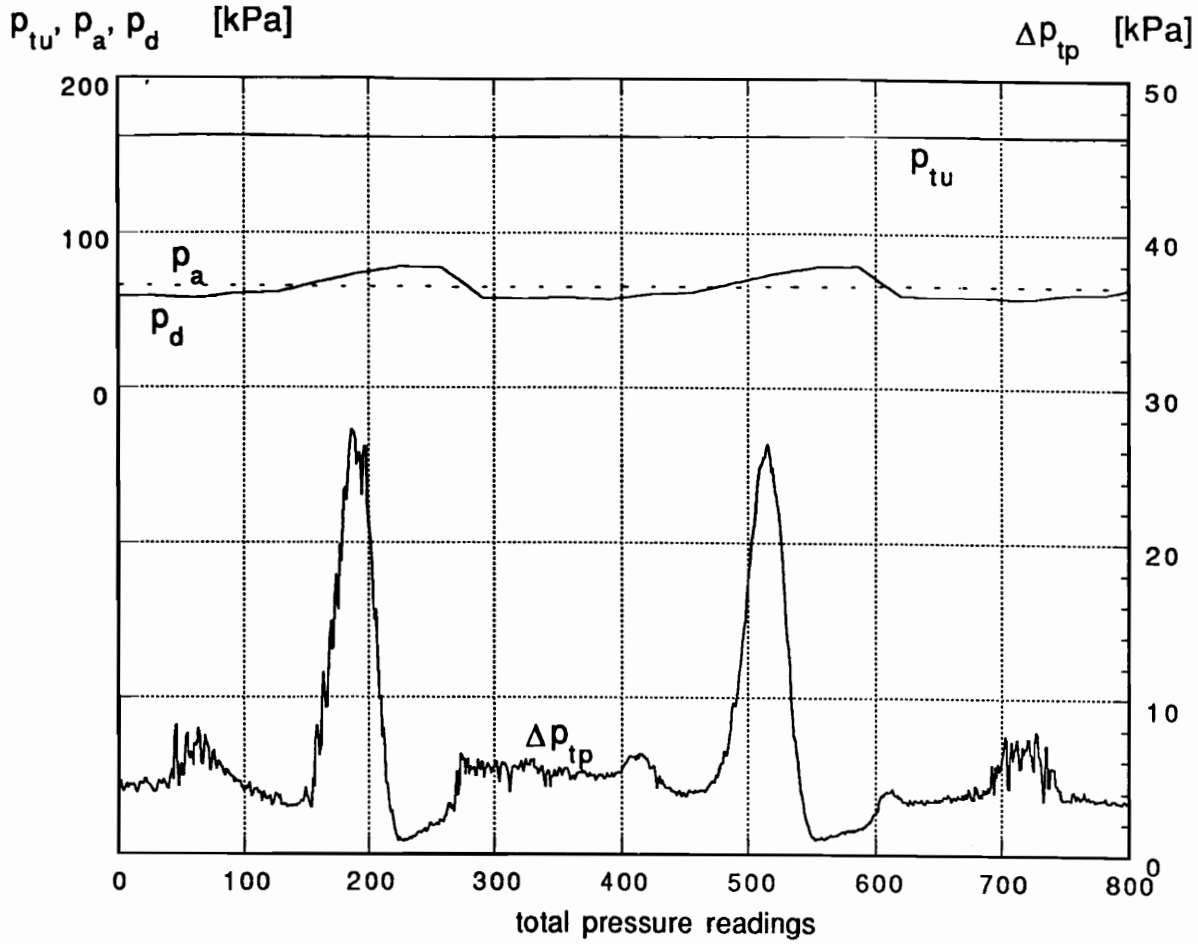


Fig.2.8 Summary of pressure data for data reduction

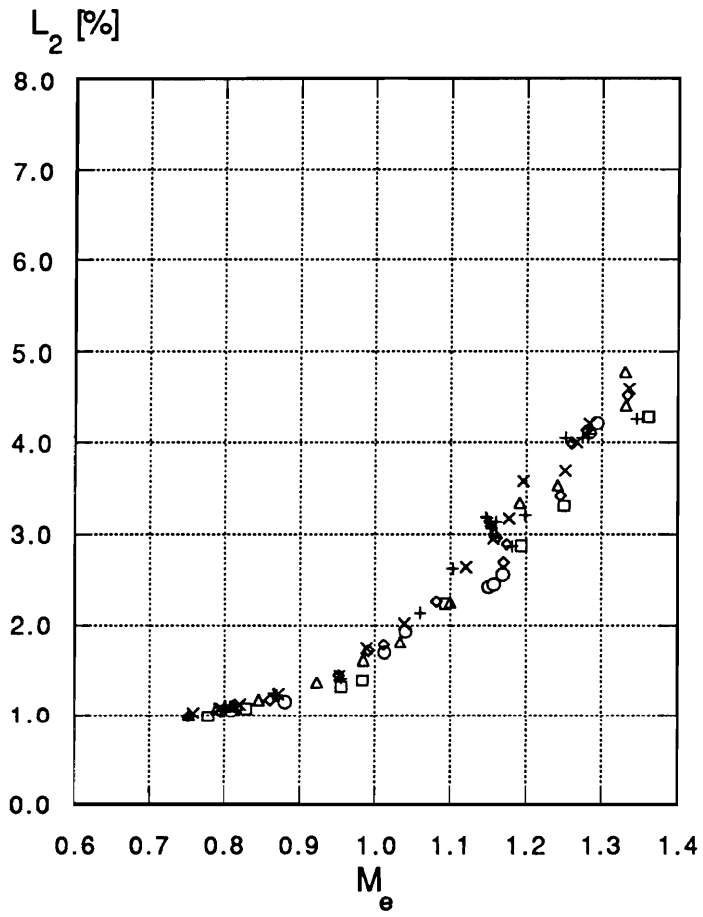


Fig.2.9 Previous results for Station 1 (by day)

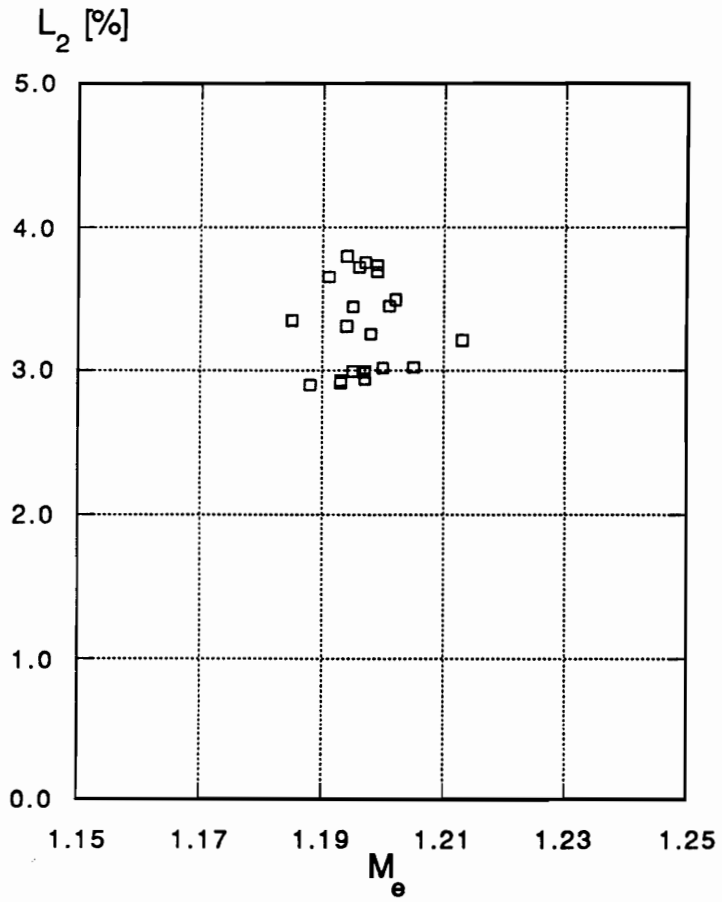


Fig.2.10 Results of consequtive runs, same M_e attempted

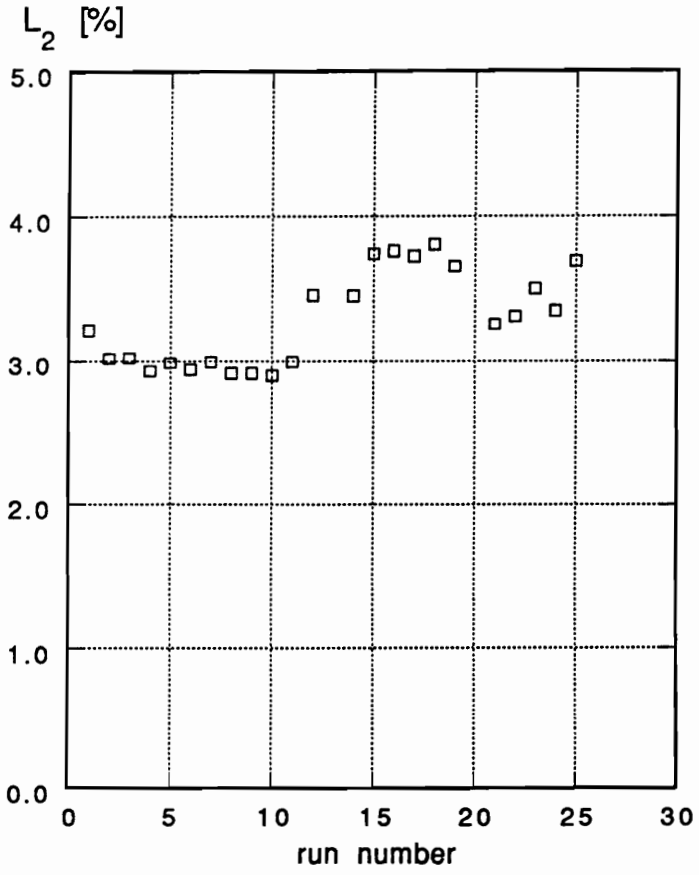


Fig.2.11 Data of Fig.2.10 now as function of run number

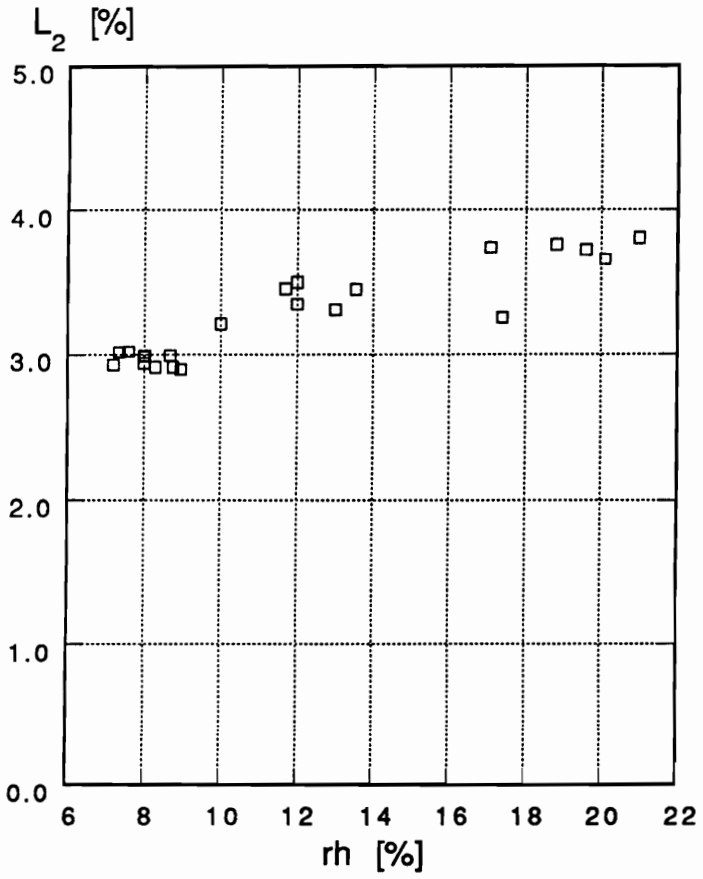


Fig.2.12 Data of Fig.2.10 now as function of relative humidity

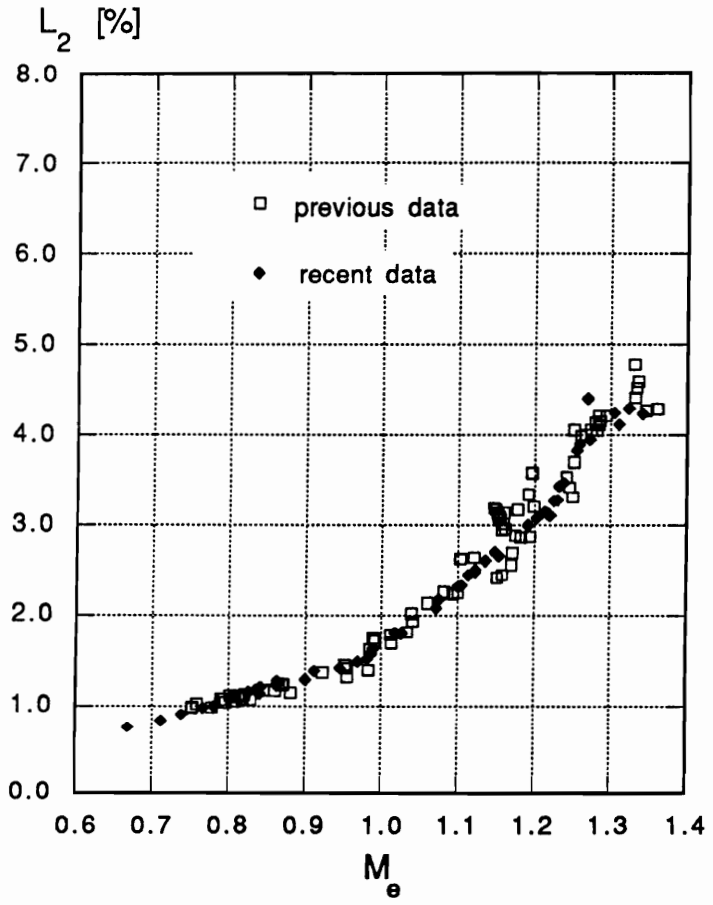


Fig.2.13 Previous and recent data for Station 1

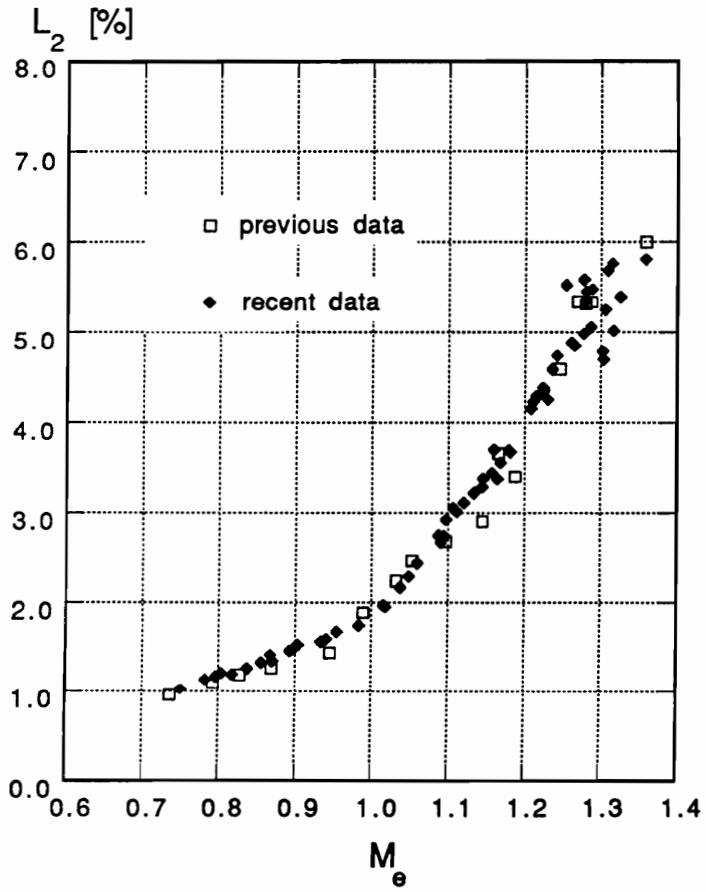


Fig.2.14 Previous and recent data for Station 2

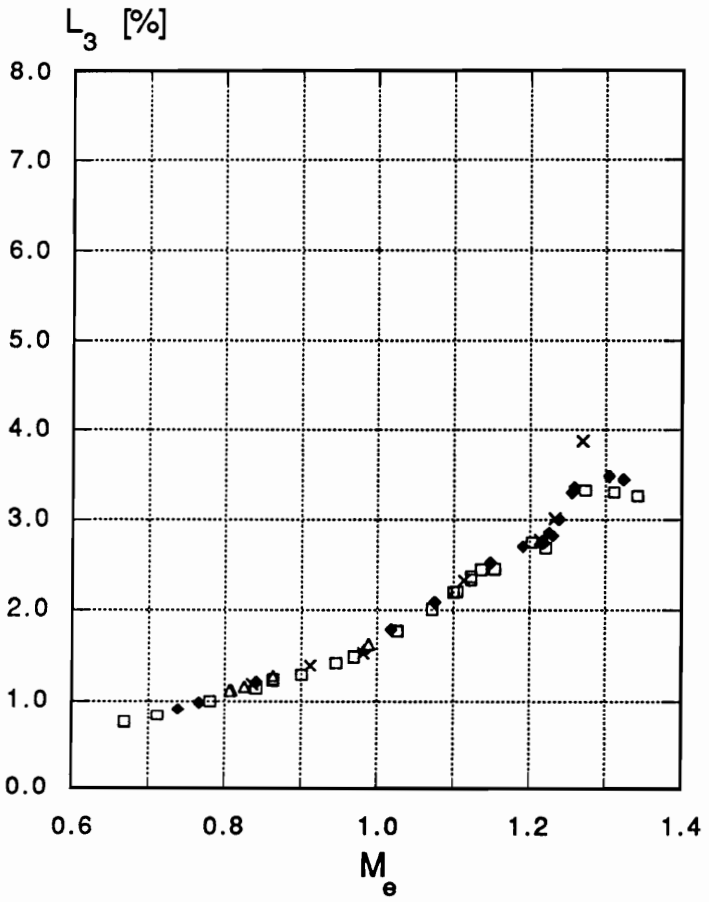


Fig.2.15 Recent data, Station 1 (by days)

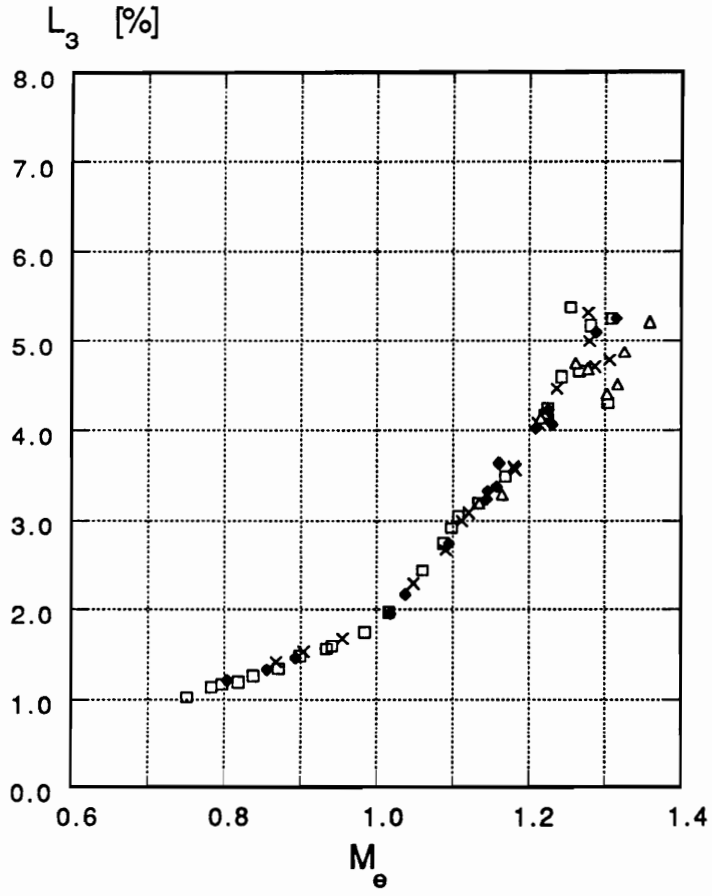


Fig.2.16 Recent data, Station 2 (by days)

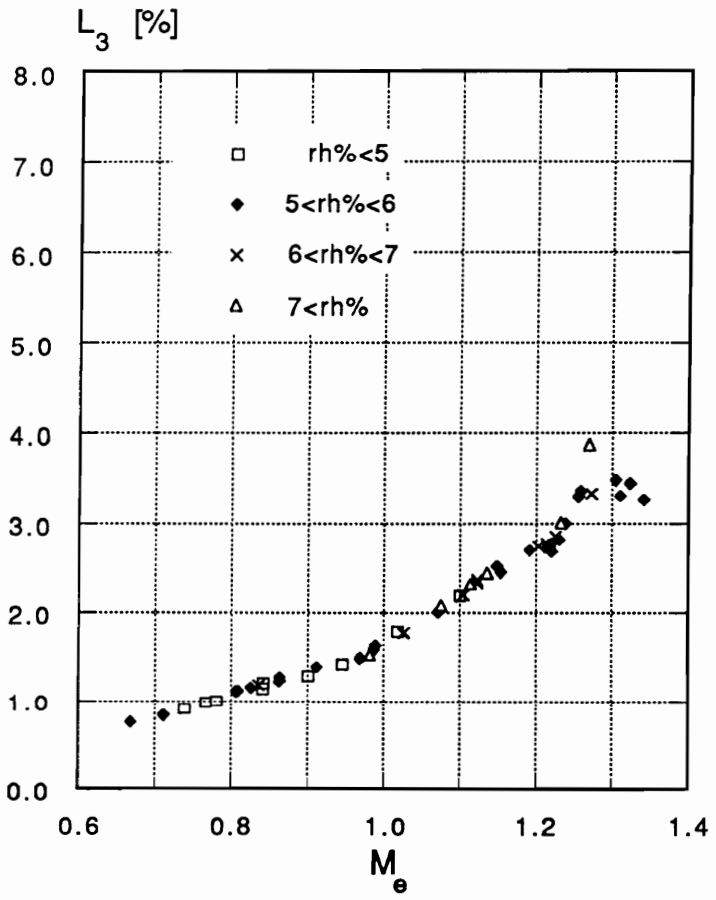


Fig.2.17 Recent data, Station 1 (by humidity)

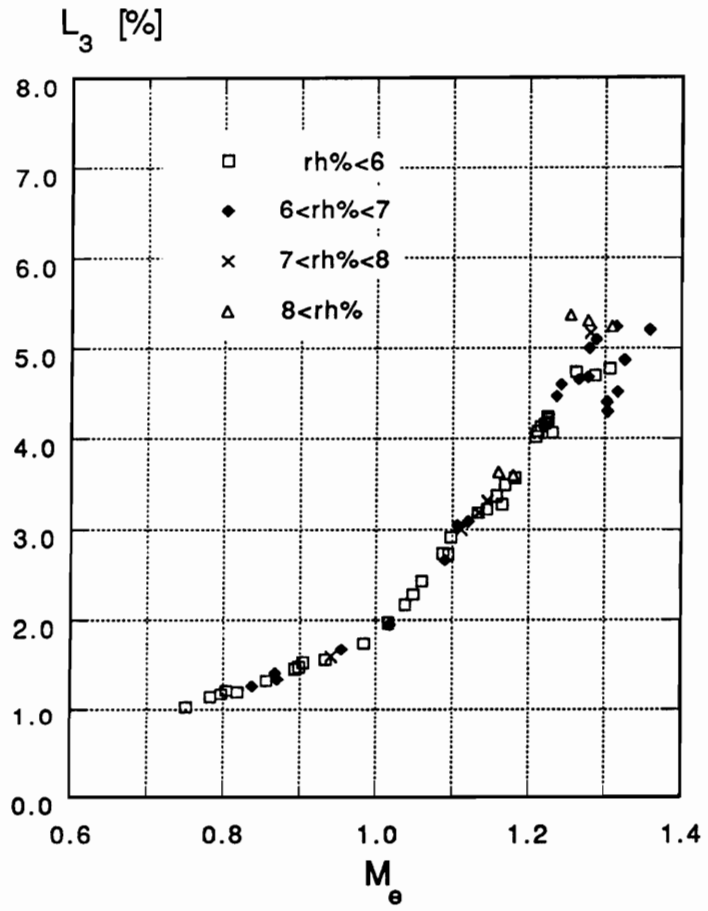


Fig.2.18 Recent data, Station 2 (by humidity)

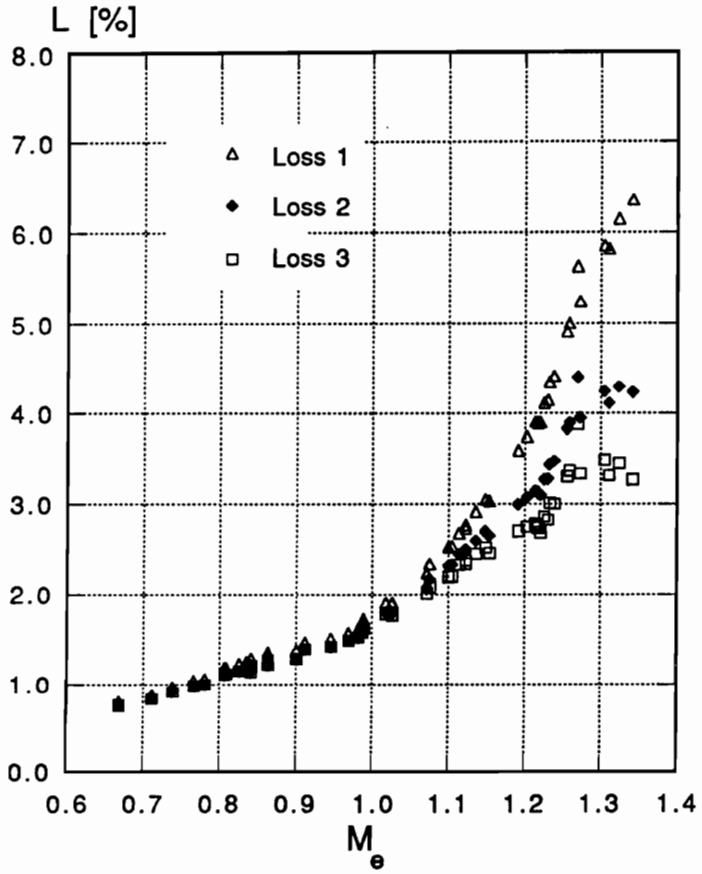


Fig.2.19 Recent data, Station 1 (by different losses)

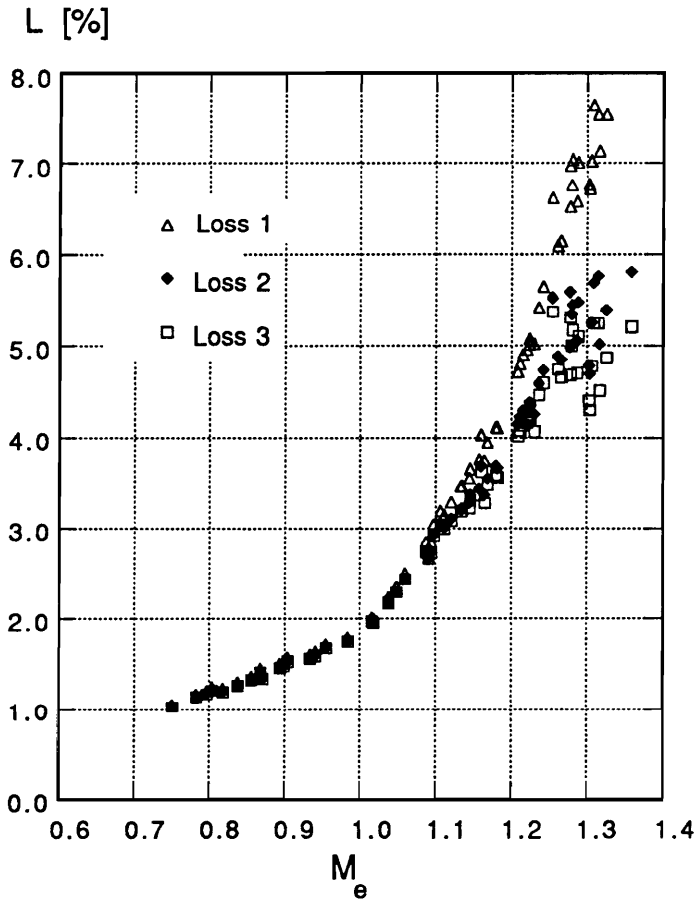


Fig.2.20 Recent data, Station 2 (by different losses)

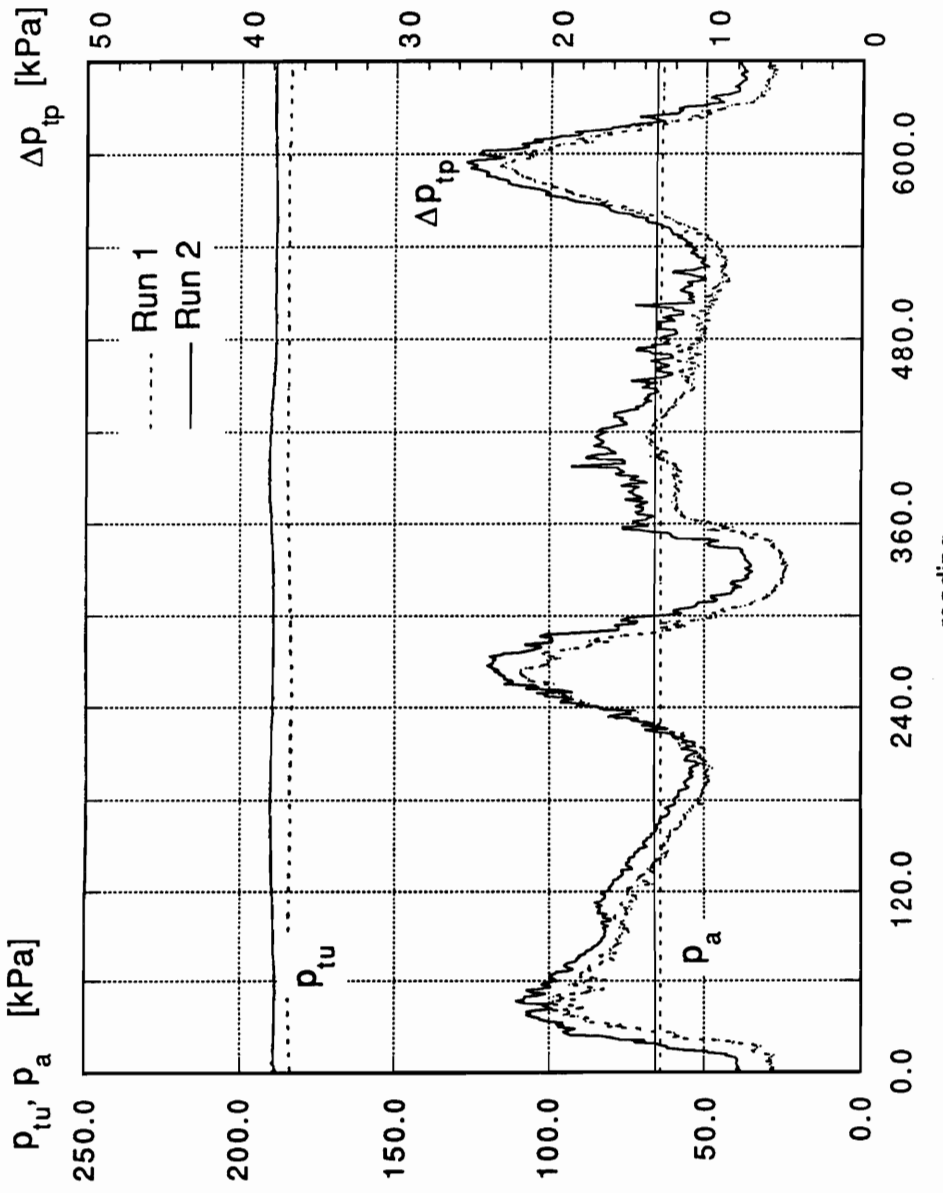


Fig.2.21 Pressure data for two runs with same M_e but different loss

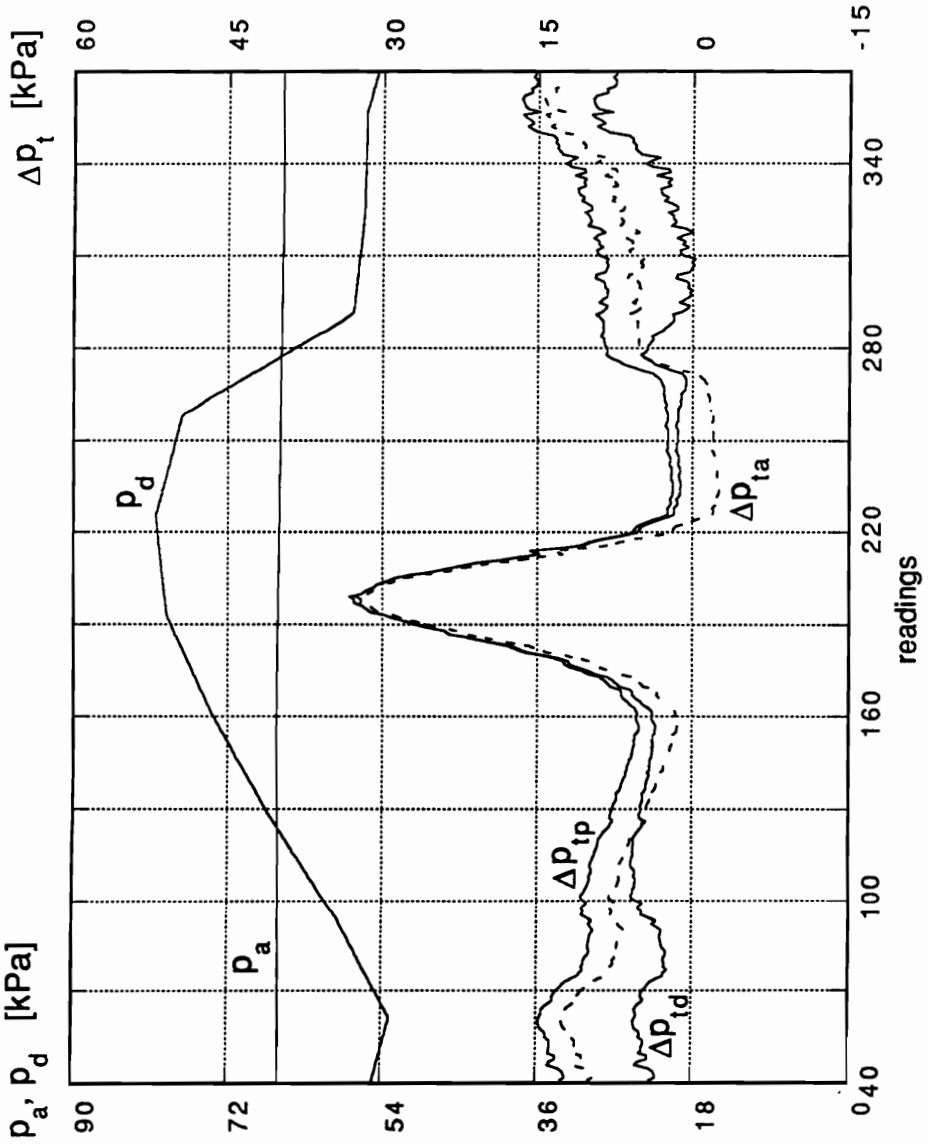


Fig.2.22 The effect of different corrections for probe bow shock

Fig.2.22 The effect of different corrections for probe bow shock

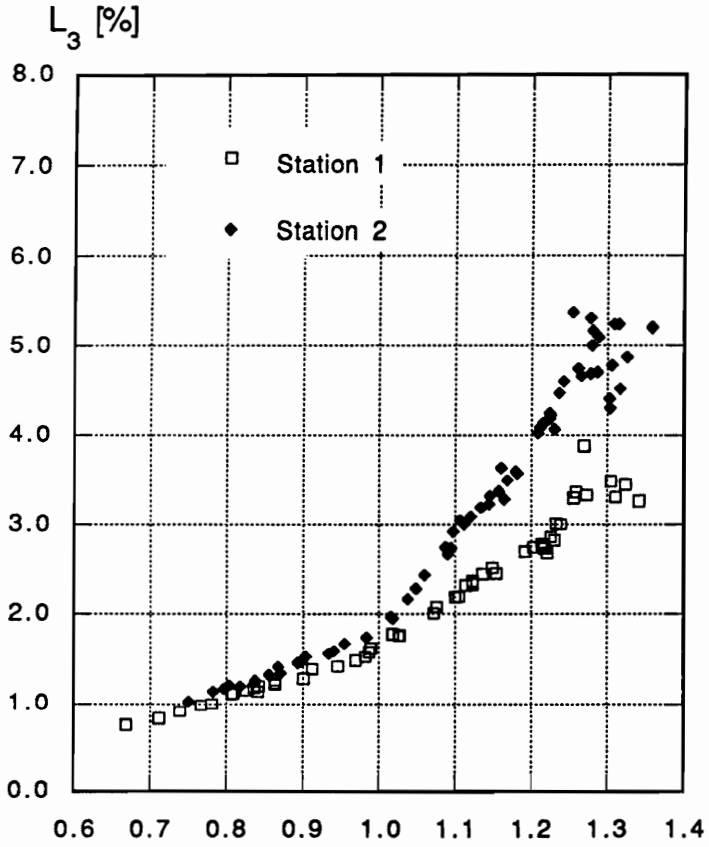


Fig.2.23 Recent data for both stations

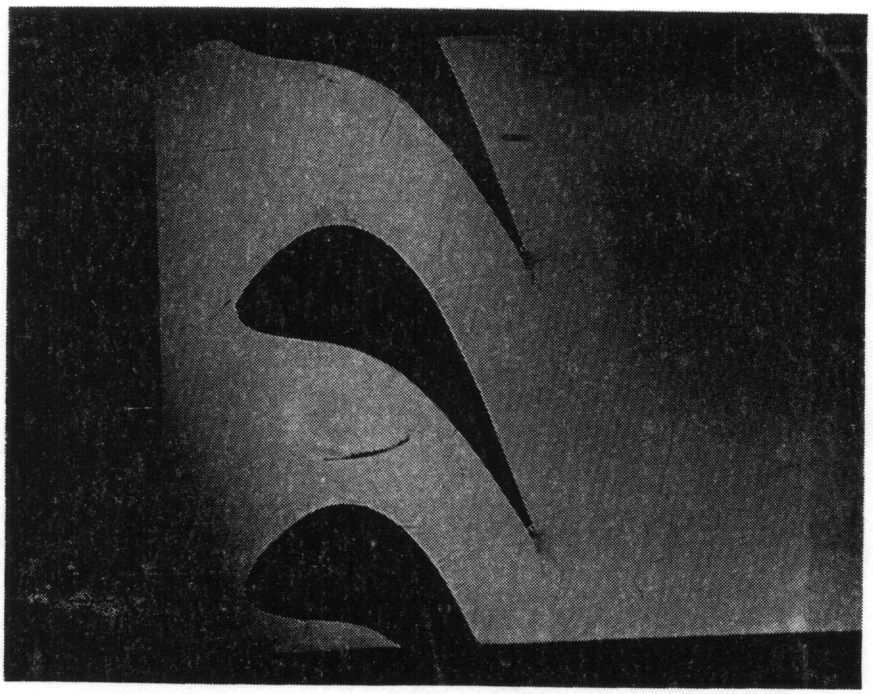


Fig.3.1 Shadowgraph, M_e=0.8

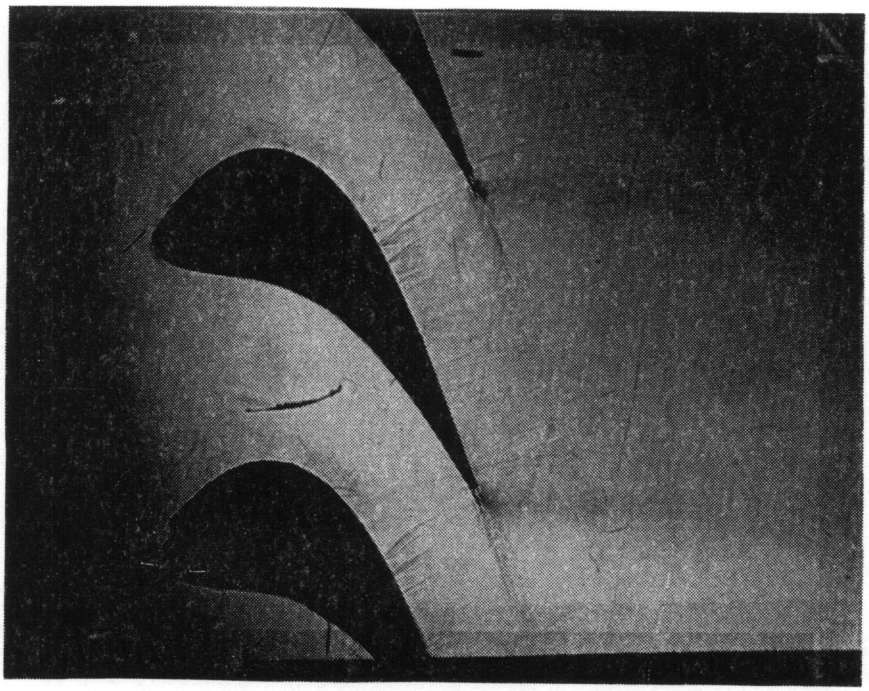


Fig.3.2 Shadowgraph, $M_e = 0.9$

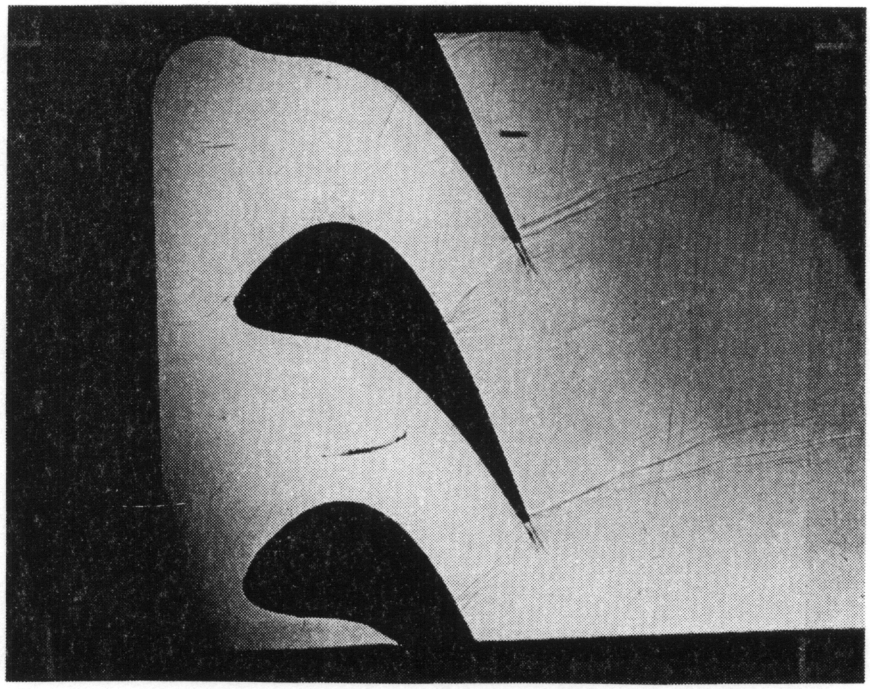


Fig.3.3 Shadowgraph, $M_e = 1.0$

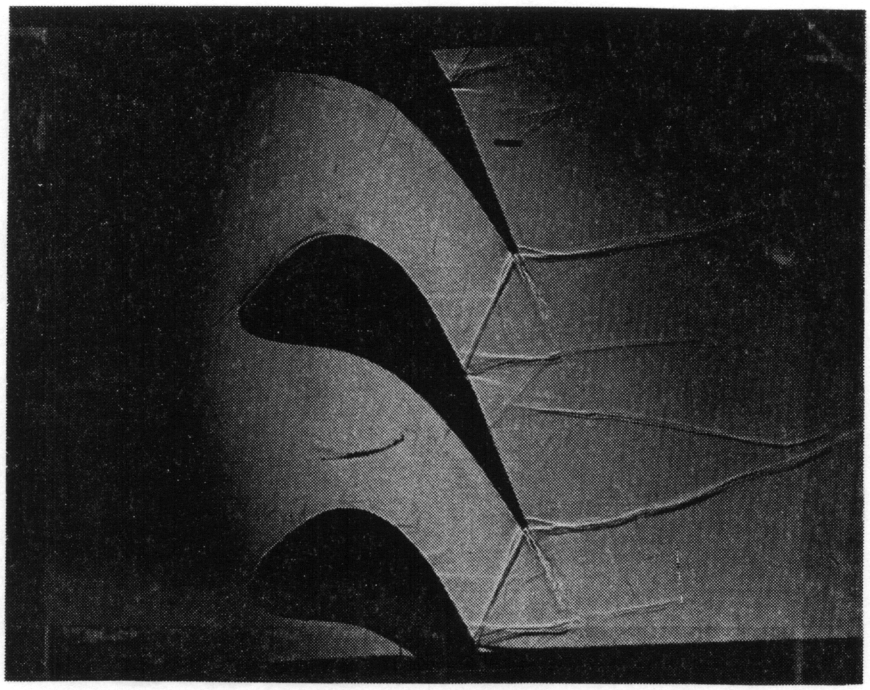


Fig.3.4 Shadowgraph, $M_e = 1.1$

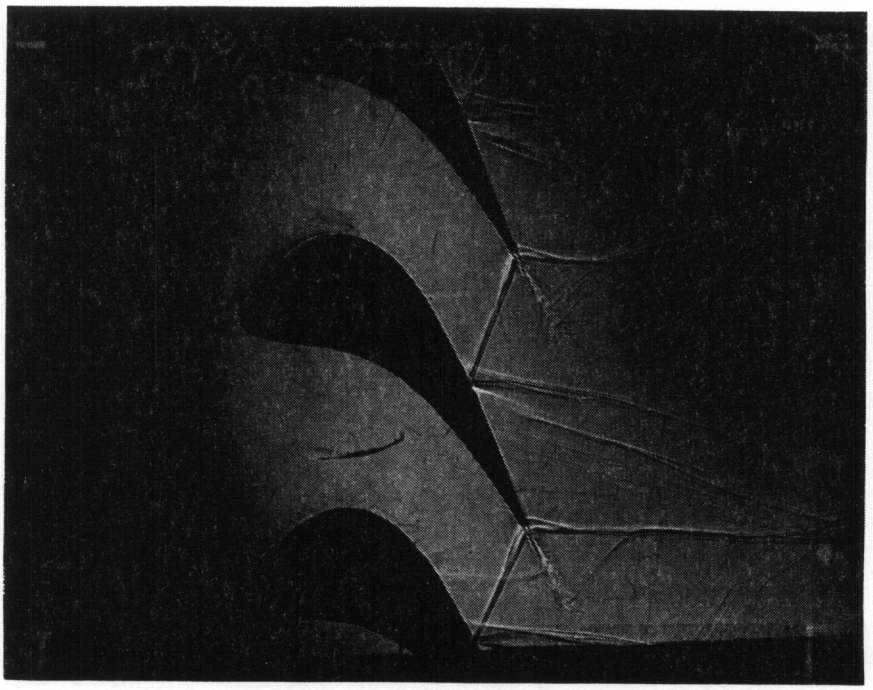


Fig.3.5 Shadowgraph, $M_e = 1.2$

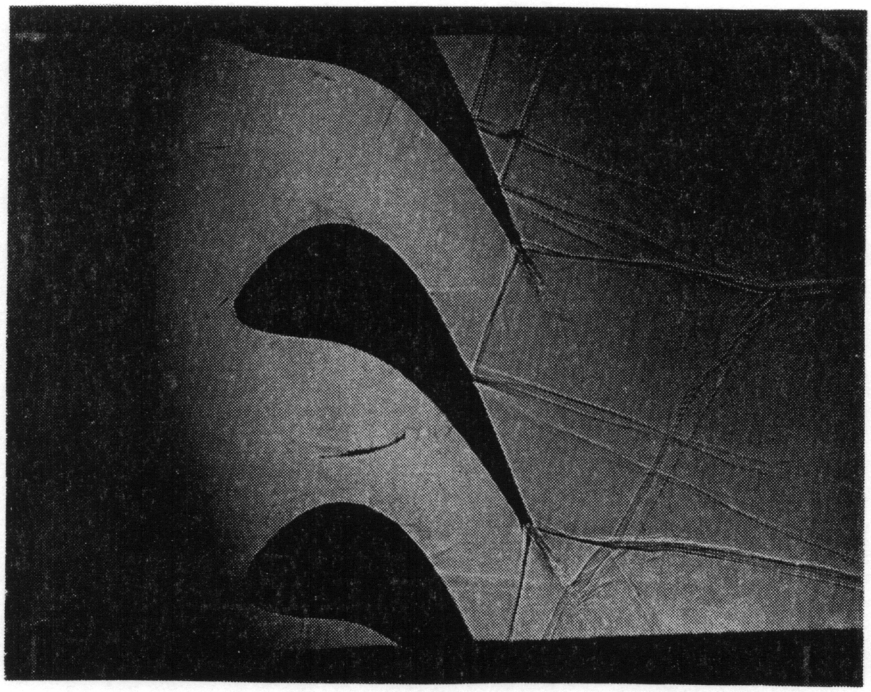


Fig.3.6 Shadowgraph, $M_e = 1.28$

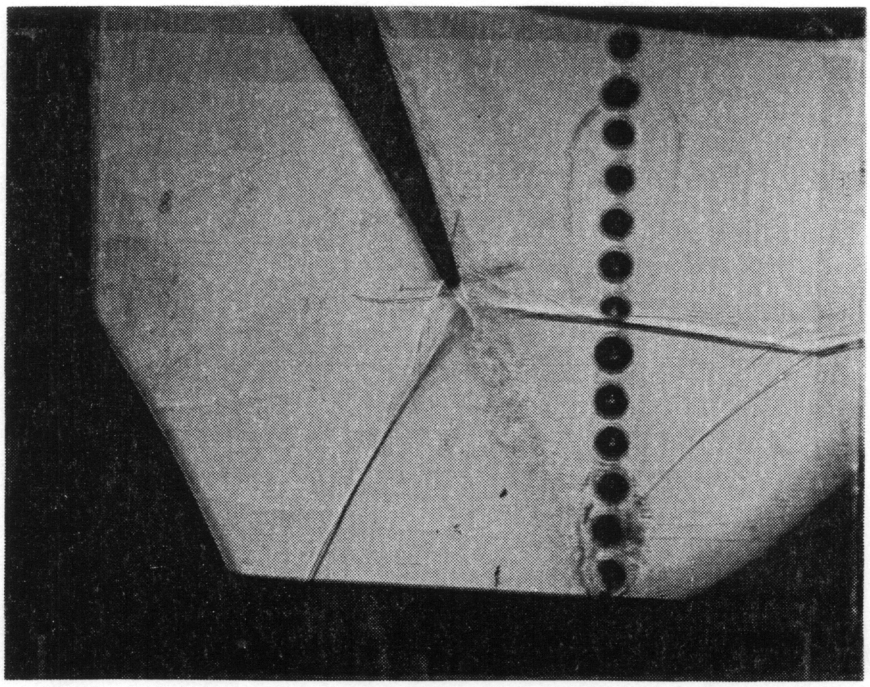


Fig.3.7 Shadowgraph, large cascade, trailing edge region, $M_e = 1.2$

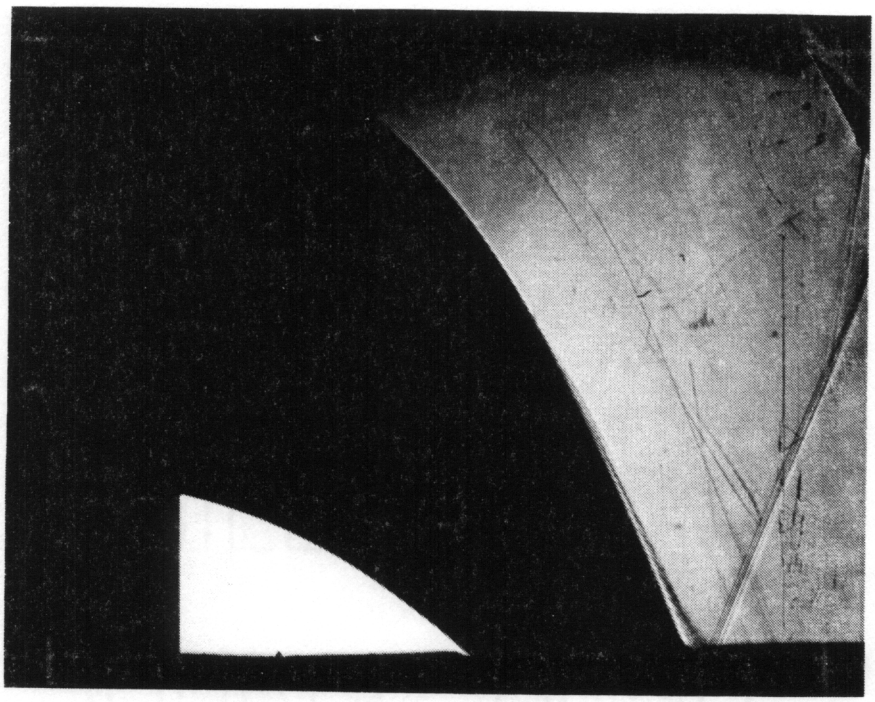


Fig.3.8 Shadowgraph, large cascade, suction side transition, $M_e = 1.2$

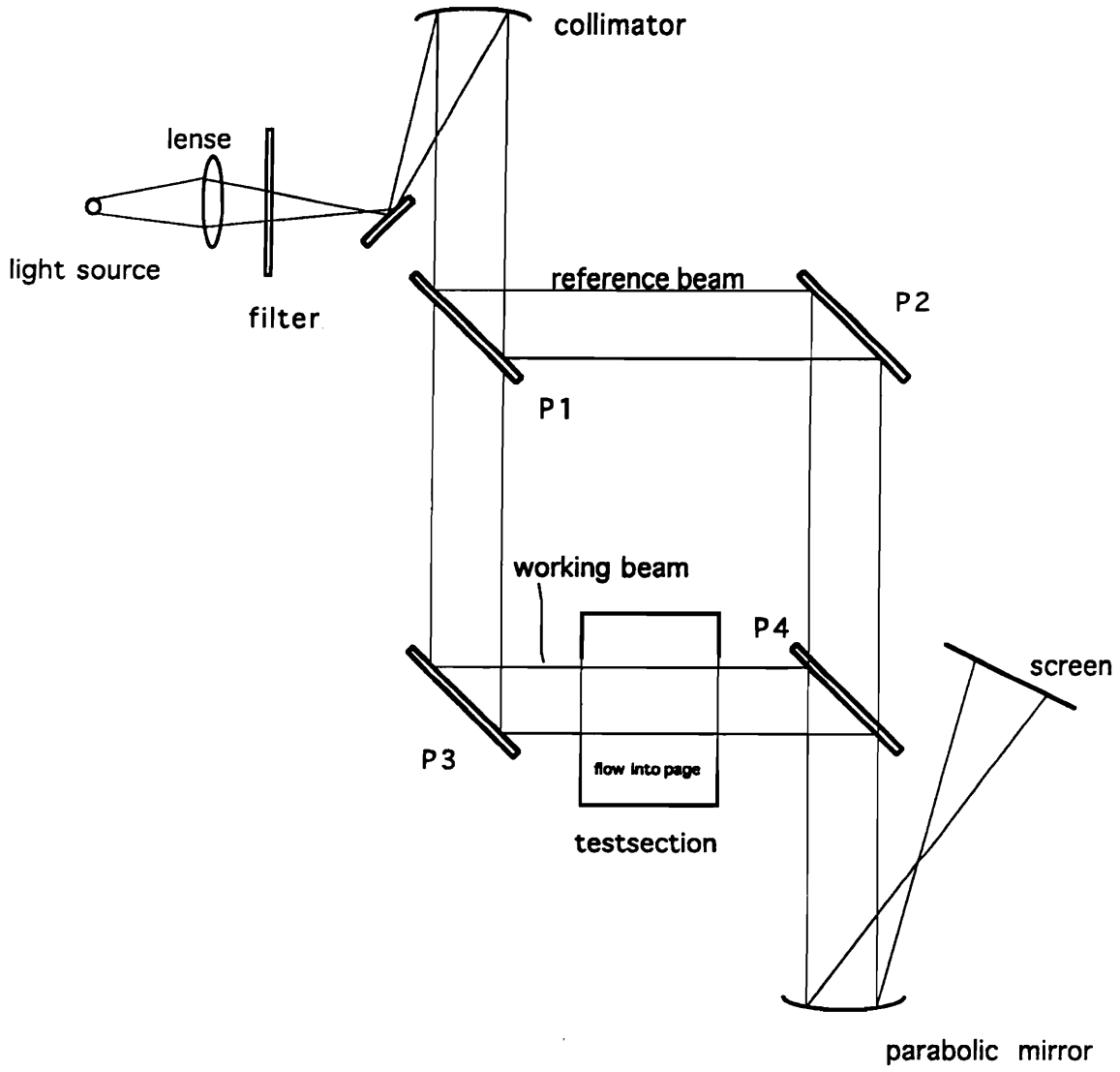


Fig.3.9 The Mach-Zehnder interferometer

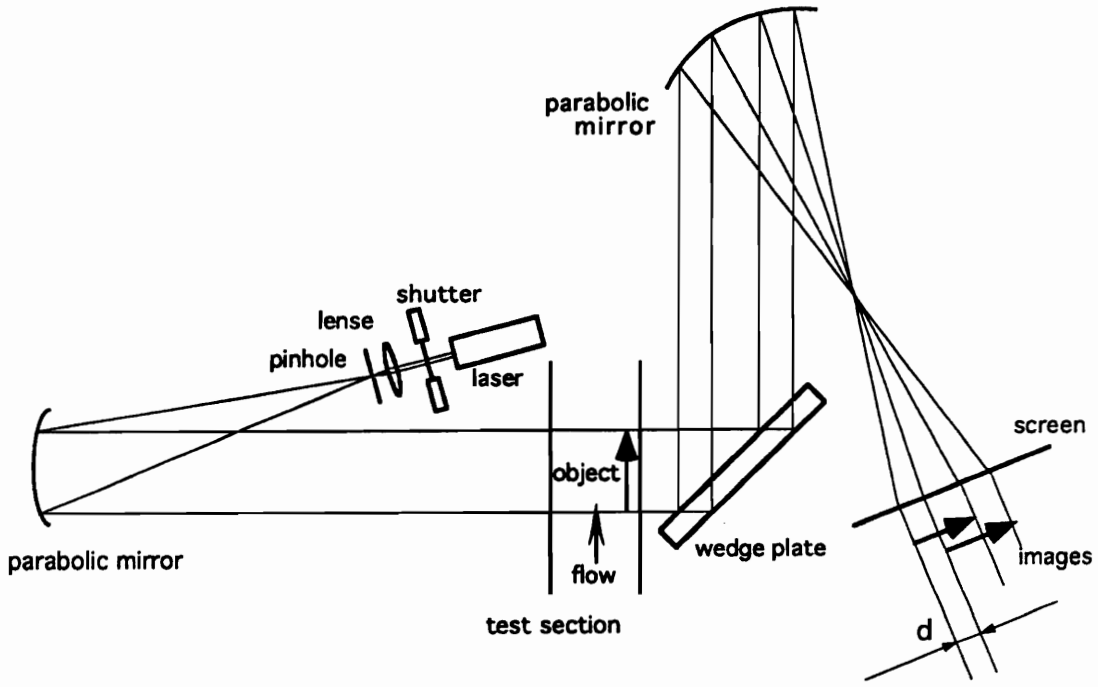


Fig.3.10 The single-plate interferometer

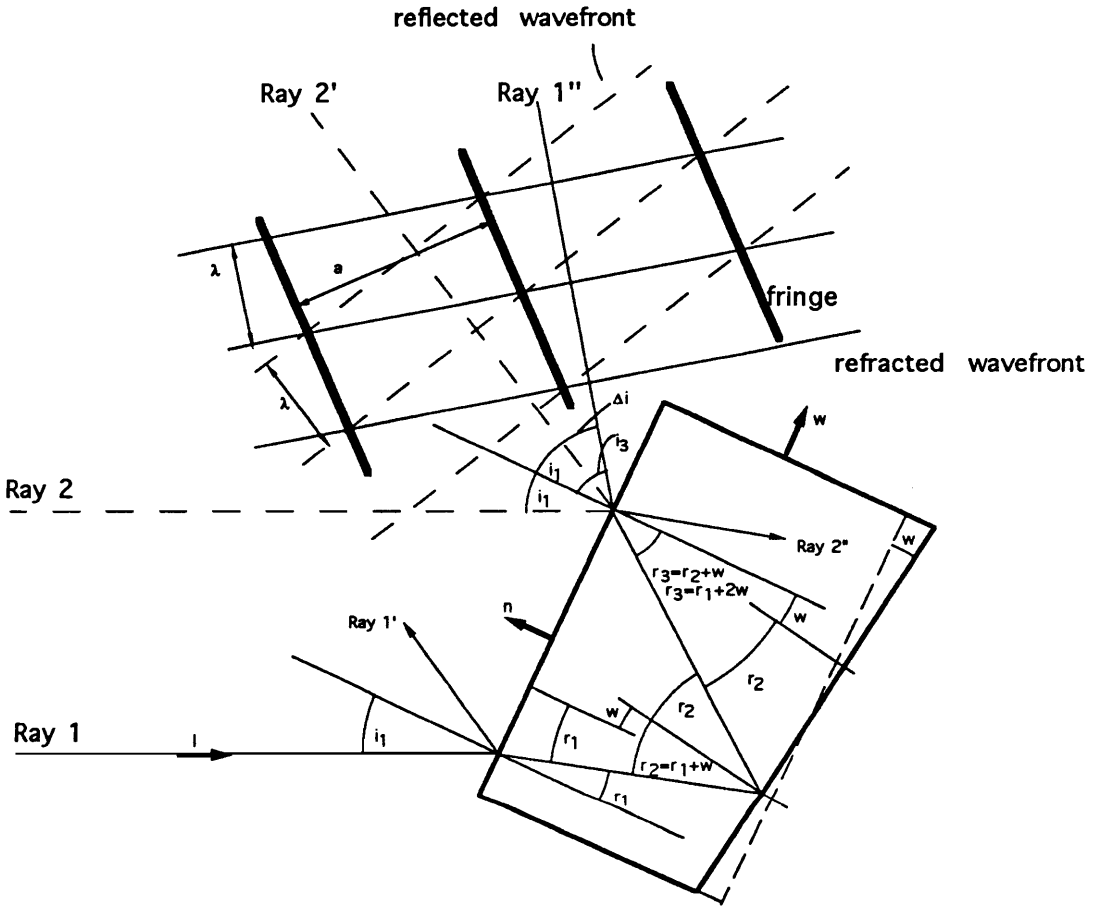


Fig.3.11 Fringe spacing vs. wedge angle

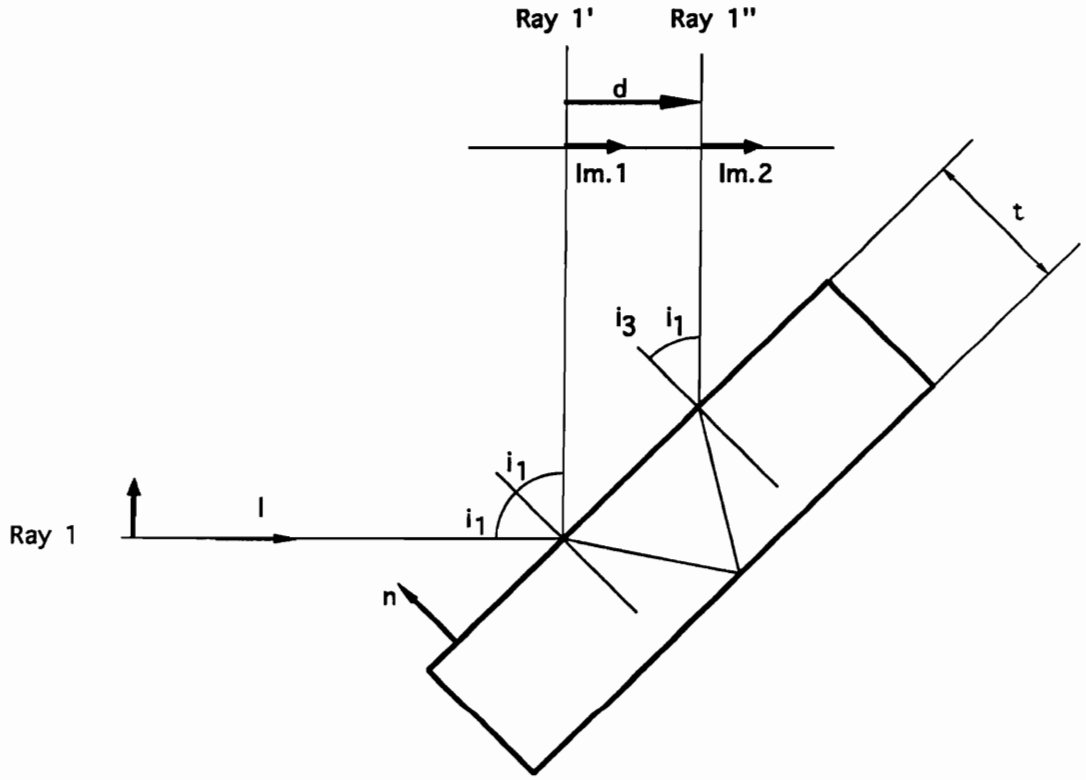


Fig.3.12 Image separation

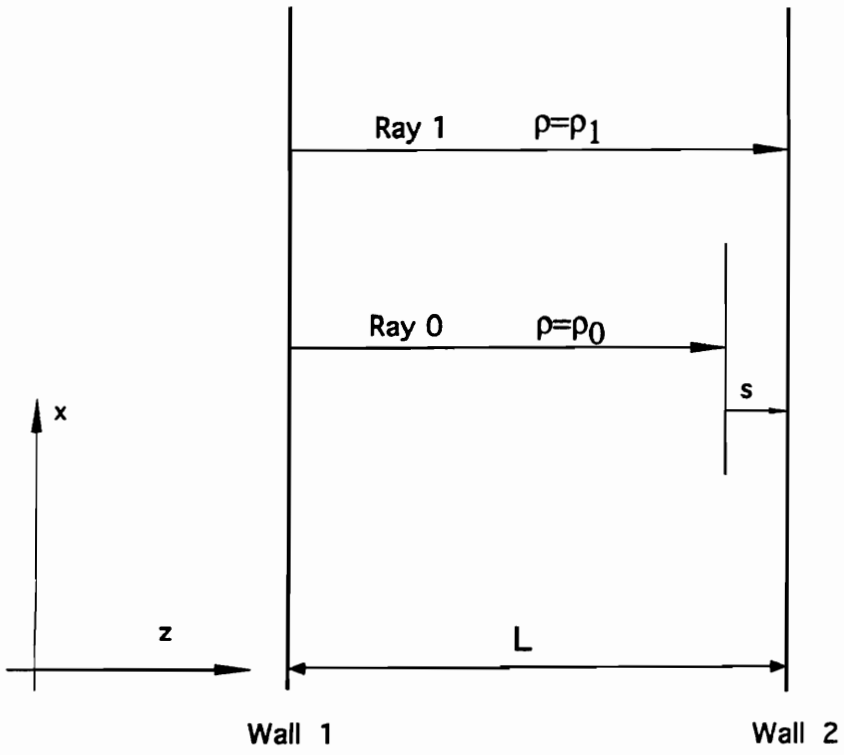


Fig.3.13 Figure for Equation (3.10)

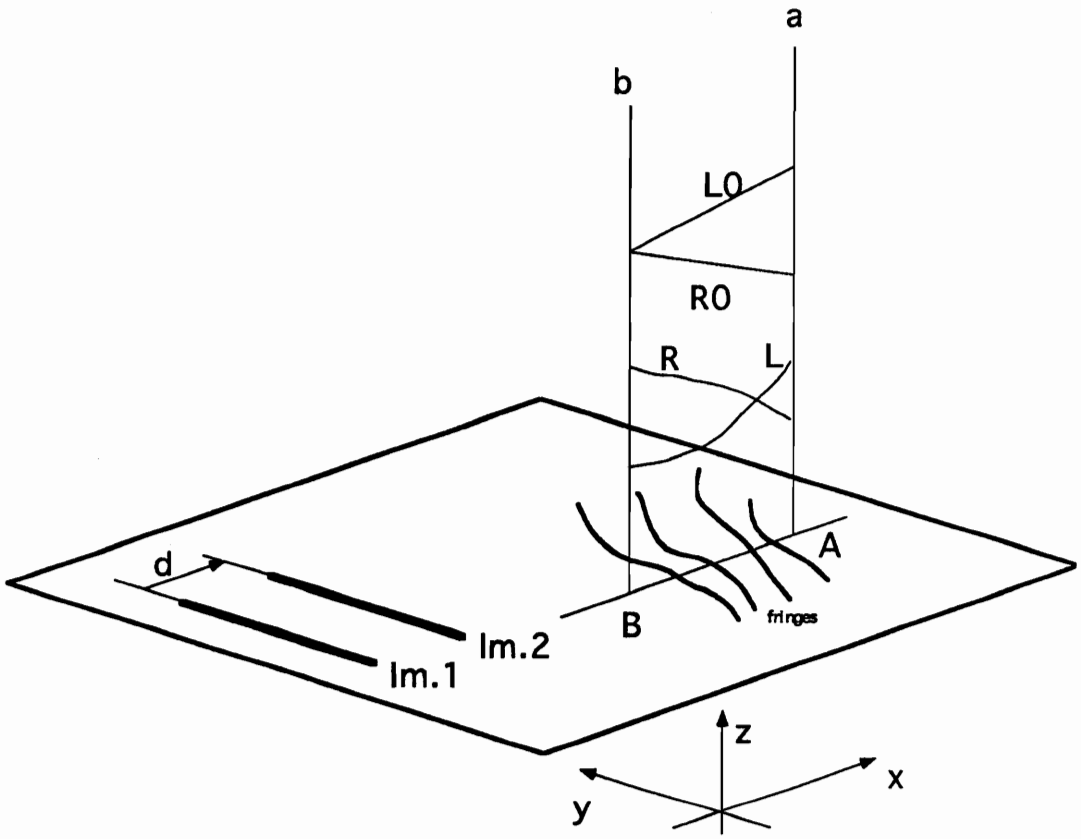


Fig.3.14 Interpretation: A and B separated in the x direction

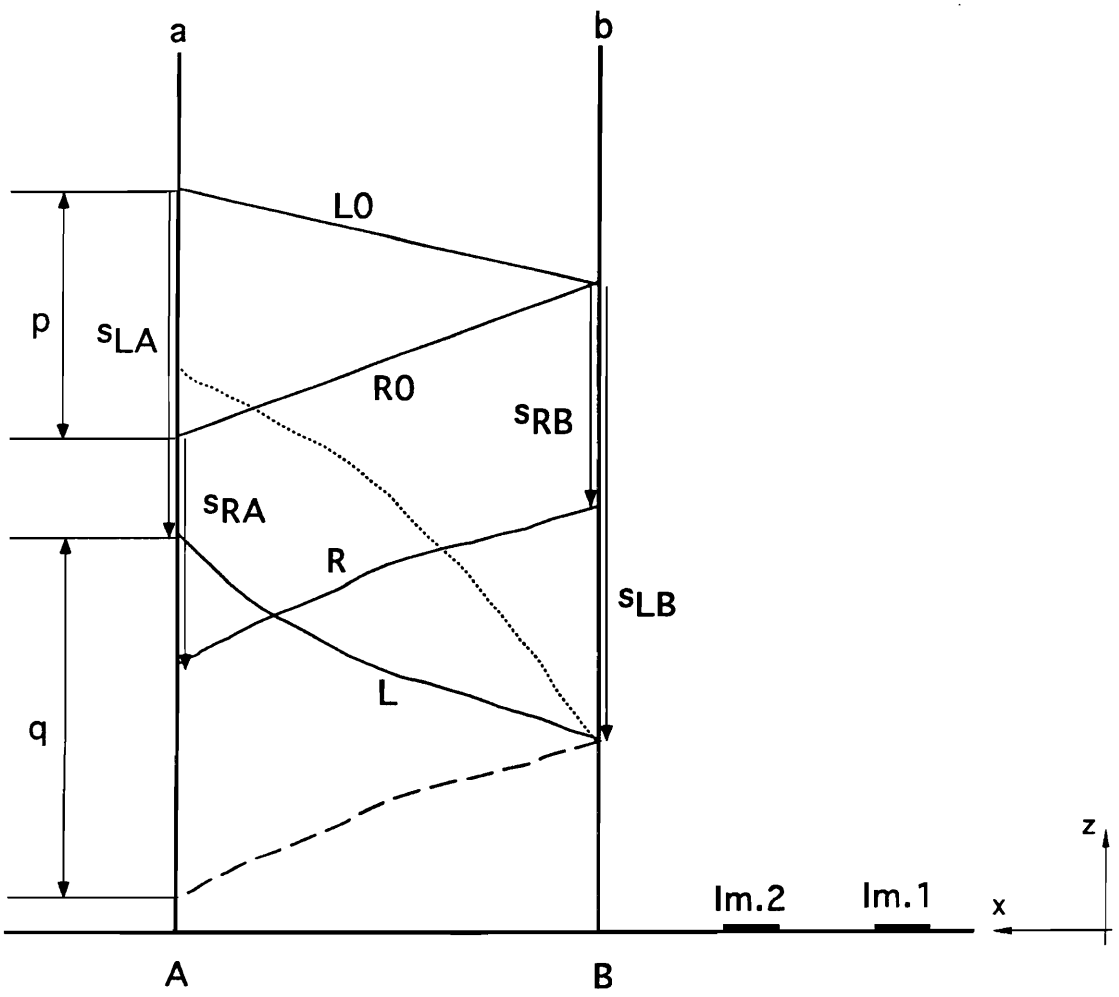


Fig.3.15 Figure 3.14 viewed from the y direction

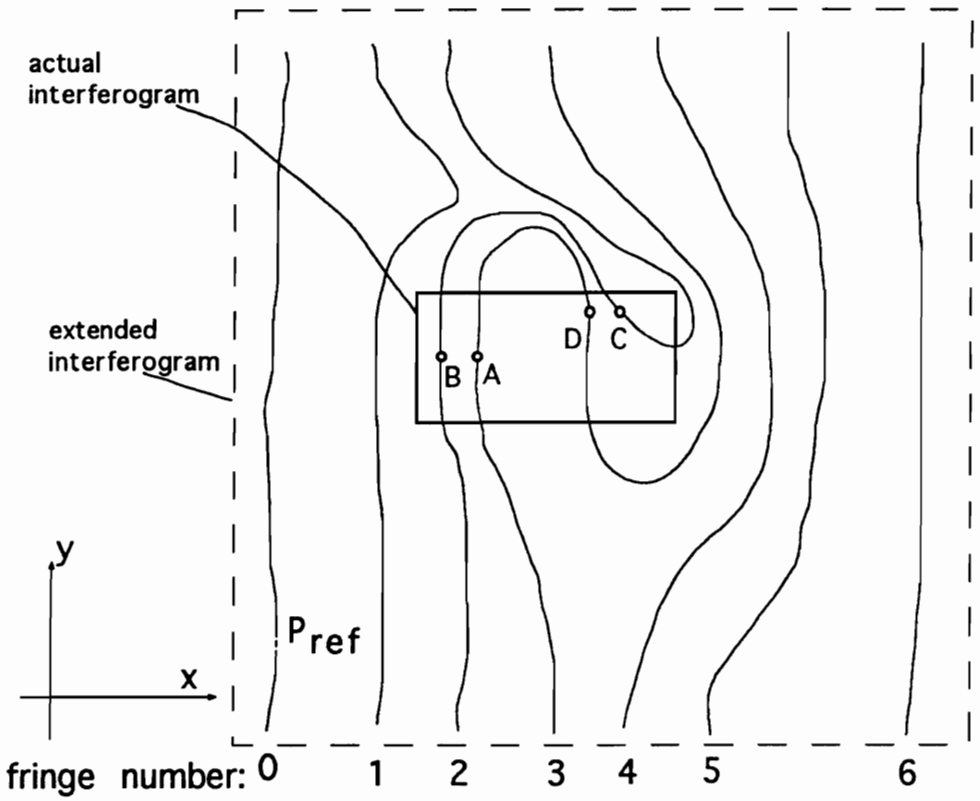


Fig.3.16 Extension of interferogram into a homogeneous density field

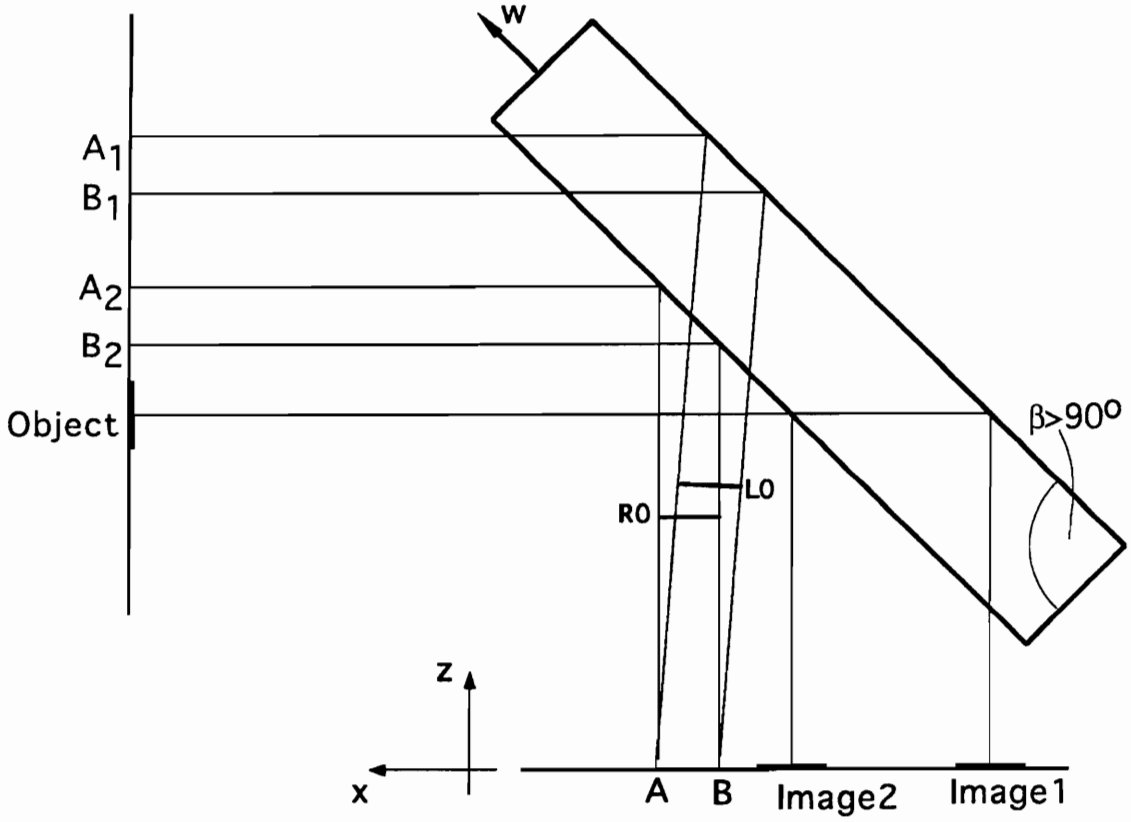


Fig.3.17a Setup when Eqs.(3.18a), (3.22a) and (3.28a) hold

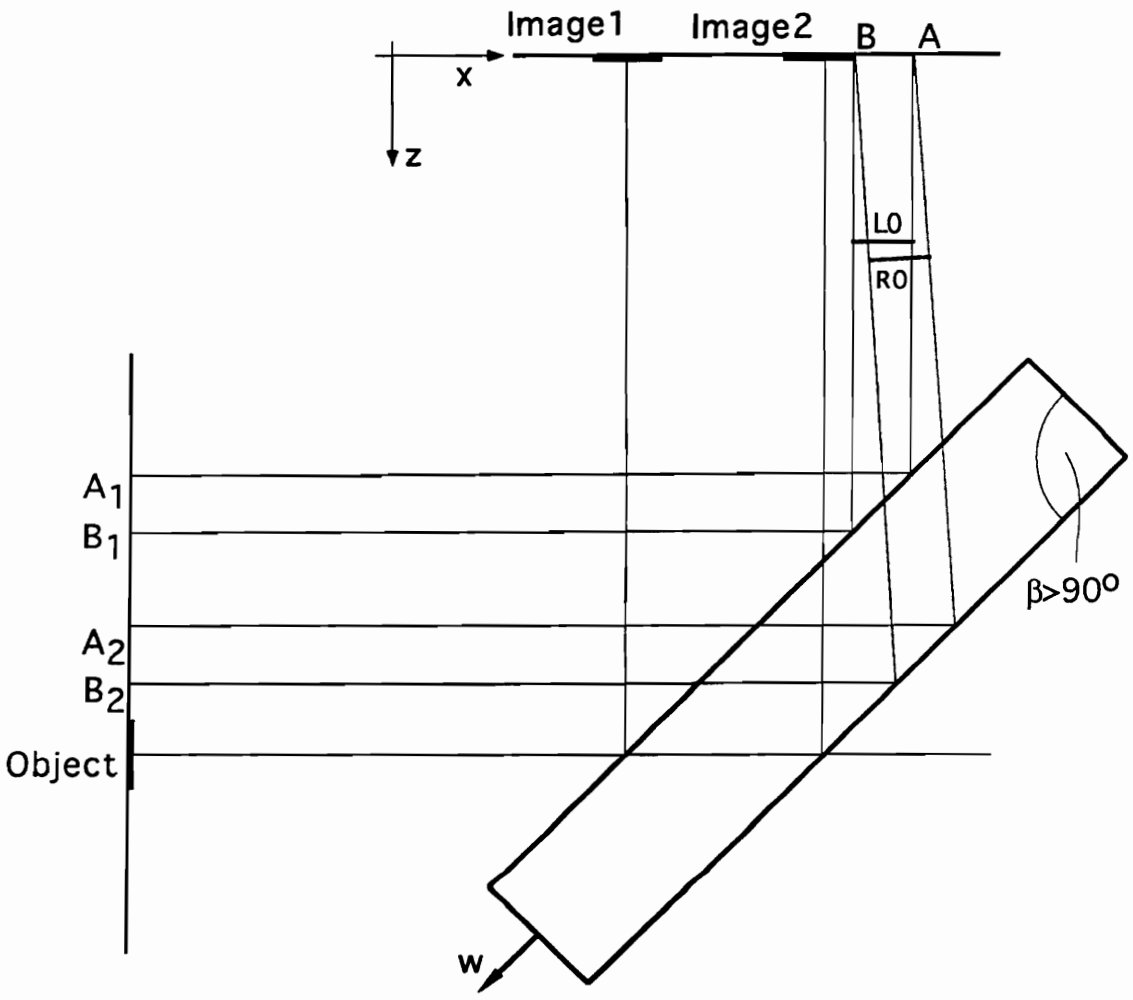


Fig.3.17b The second setup when Eqs.(3.18a), (3.22a) and (3.28a) hold

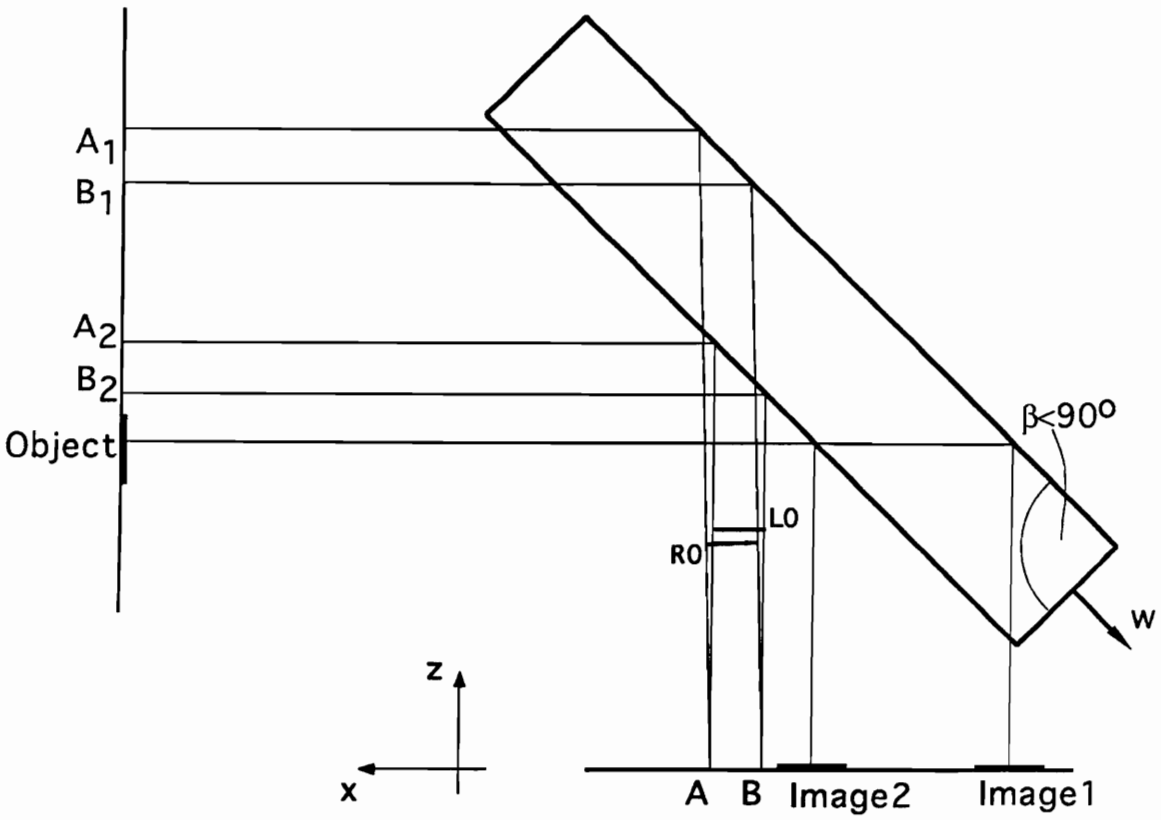


Fig.3.17c Setup when Eqs.(3.18b), (3.22b) and (3.28b) hold

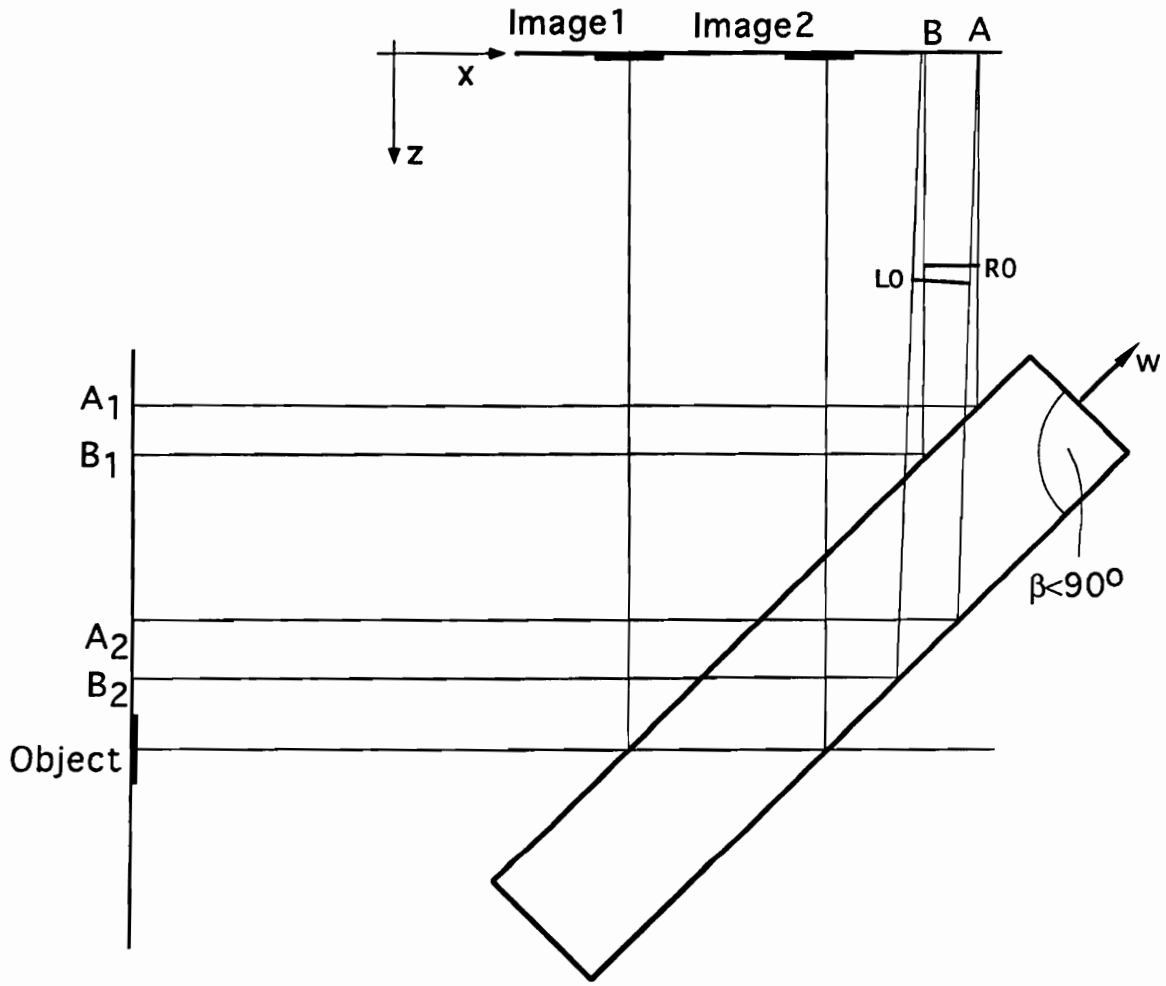


Fig.3.17d The second setup when Eqs.(3.18b), (3.22b) and (3.28b) hold

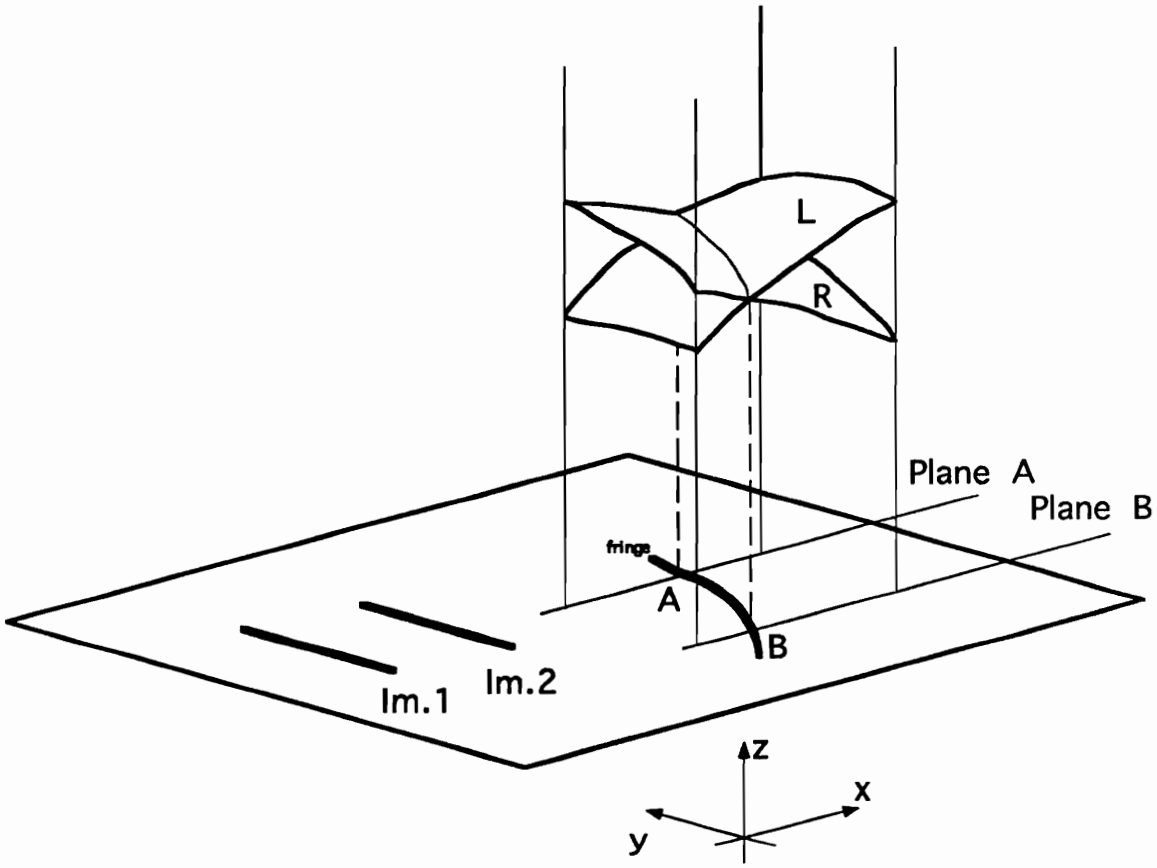


Fig.3.18 Interpretation: A and B are on the same fringe

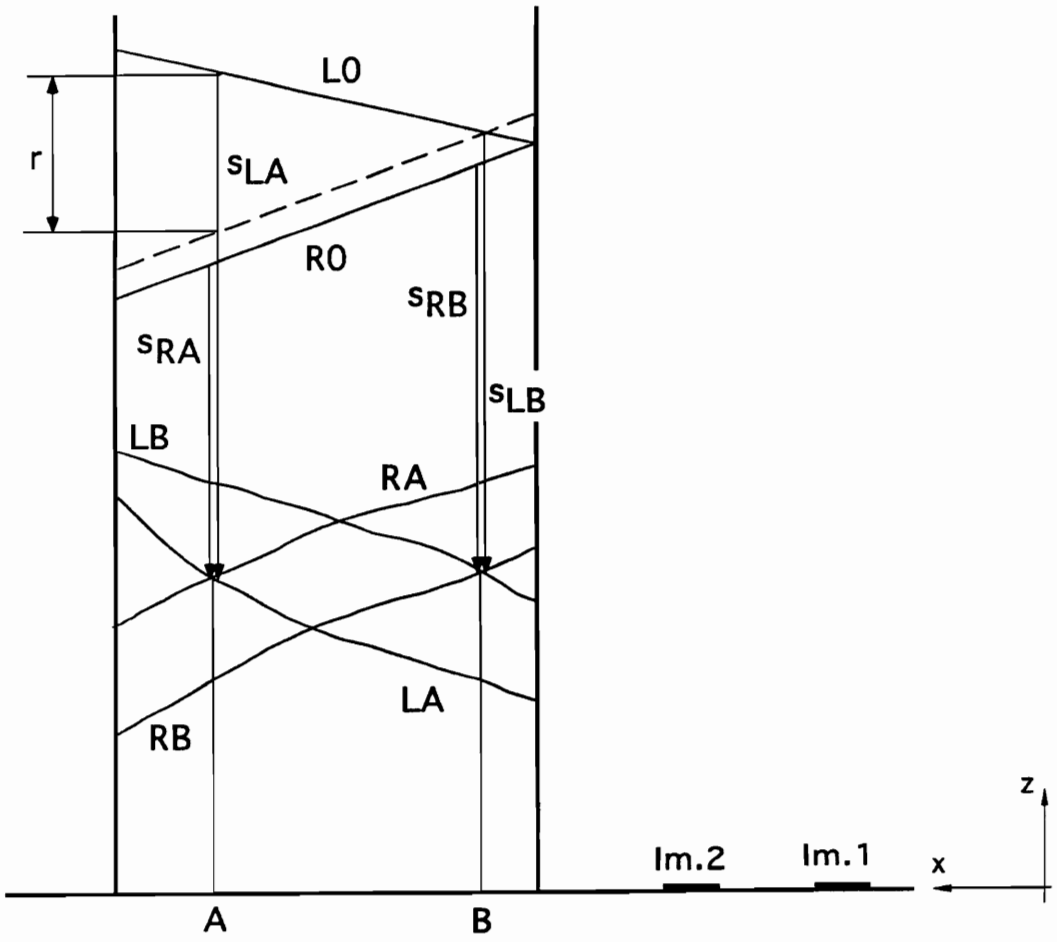


Fig.3.19 Figure 3.18 when viewed from the y direction

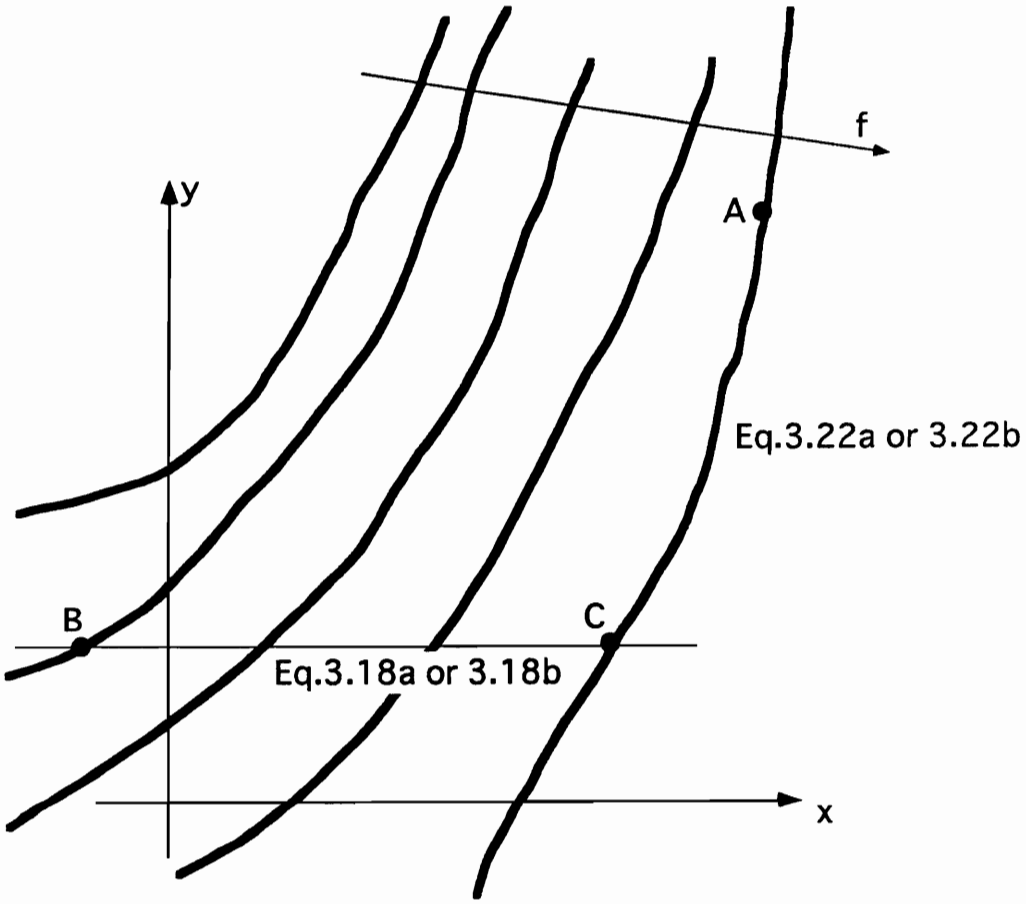


Fig.3.20 Generation of the combined rule

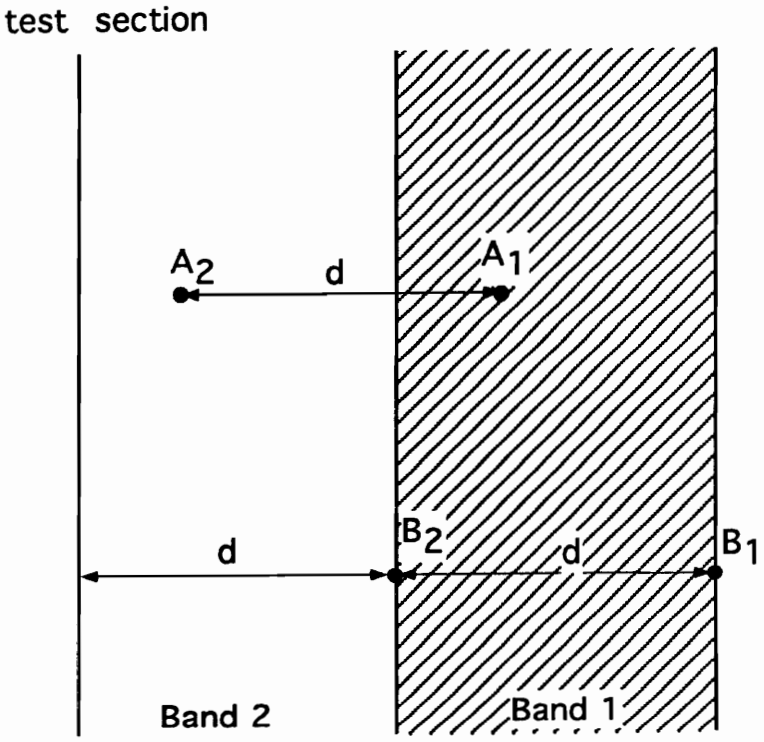


Fig.3.21 Strategy to determine the density field

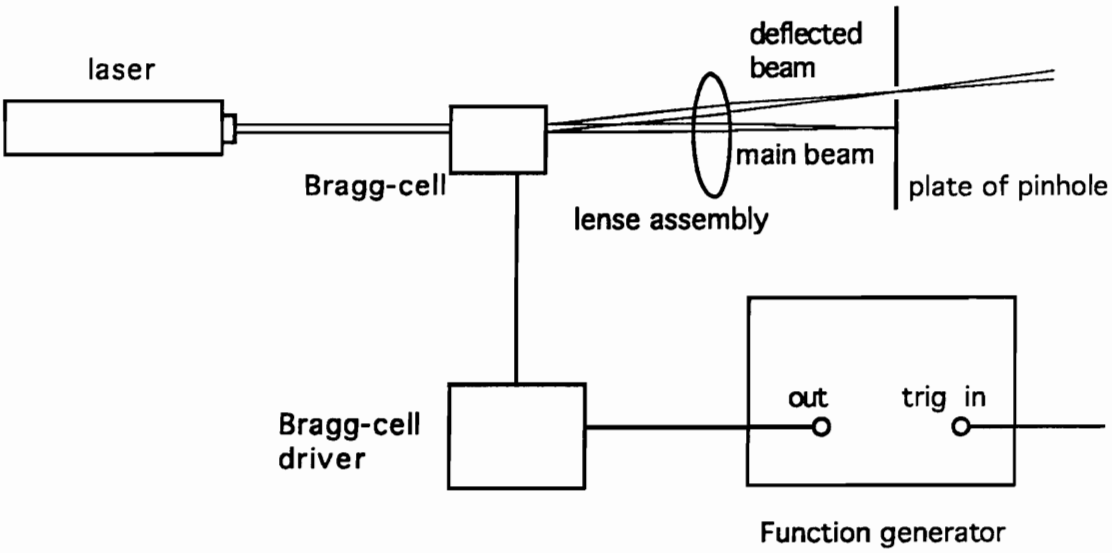


Fig.3.22 The basic idea of the Bragg-cell shutter

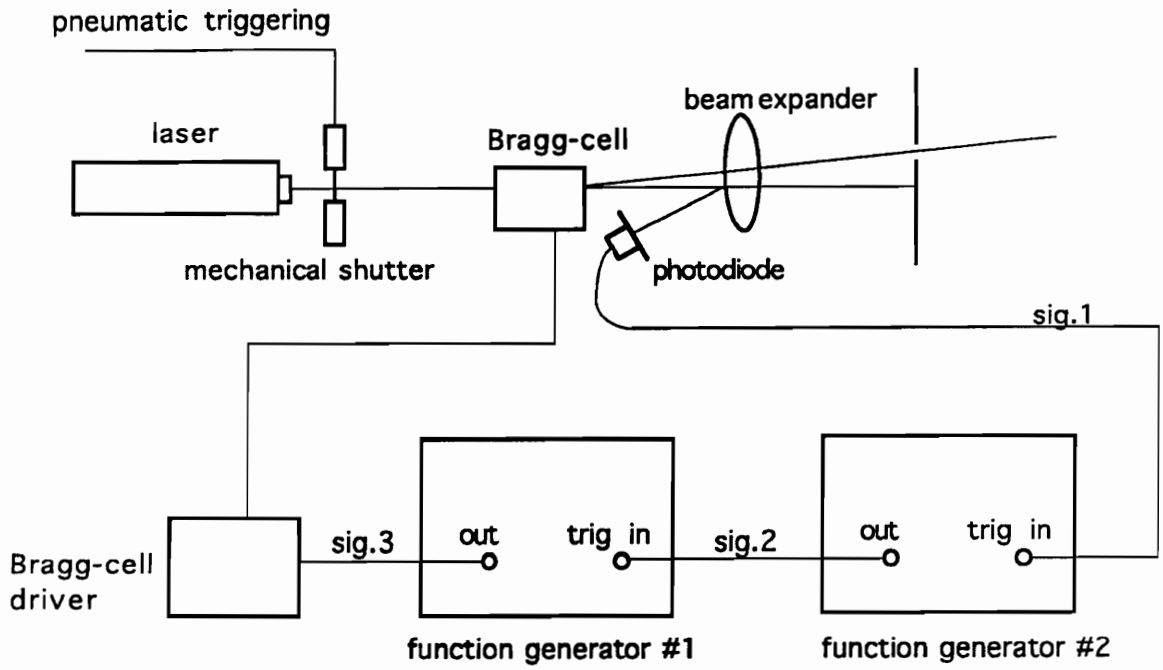


Fig.3.23 The complete Bragg-cell shutter

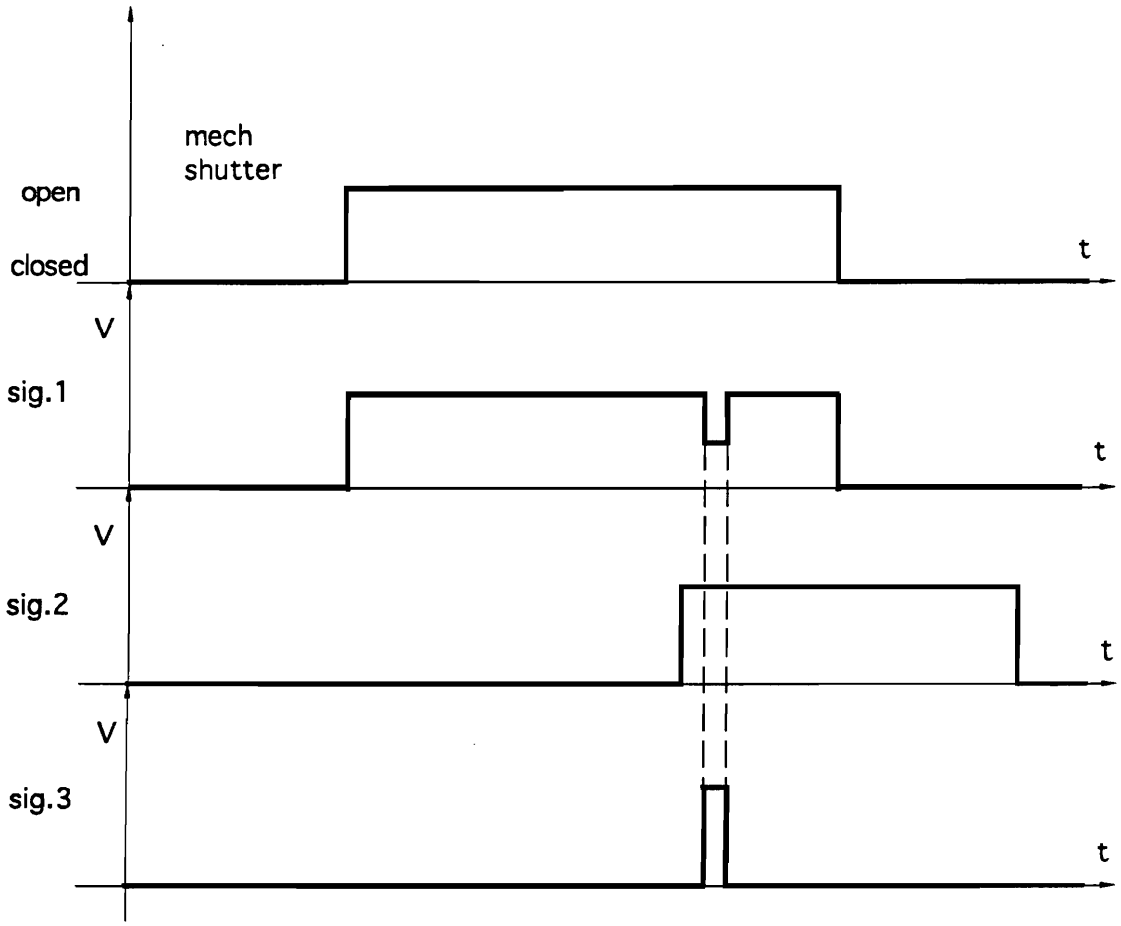


Fig.3.24 Time dependence of the signals defined in Fig.3.23

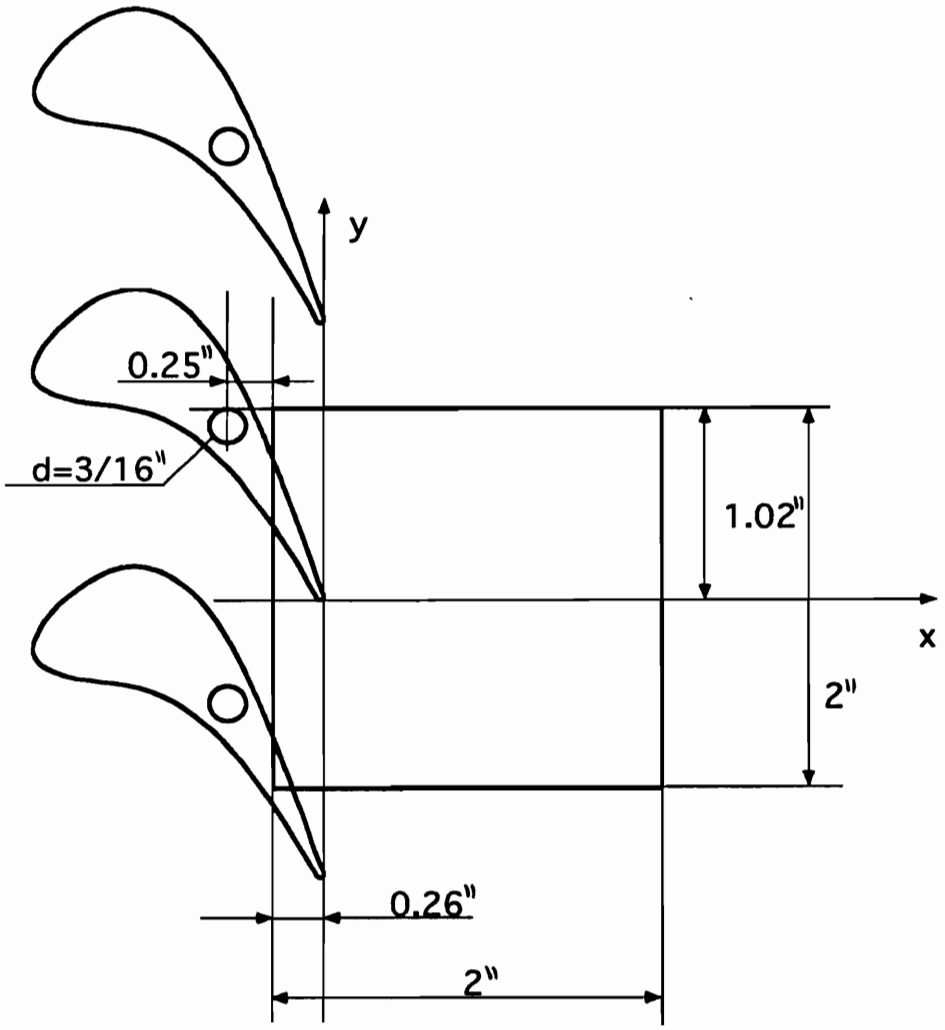


Fig.3.25 The placement of the glass windows in the original cascade

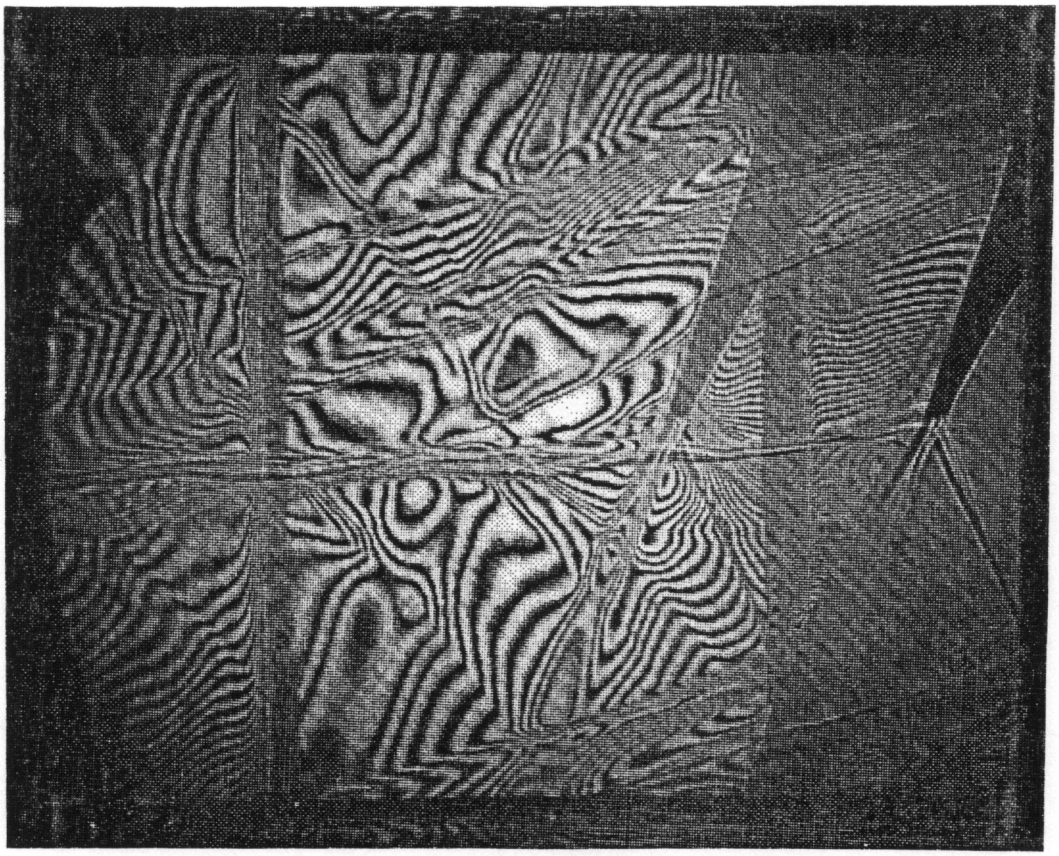


Fig.3.26 Interferogram: Original cascade with tailboard. $M_e = 1.2$

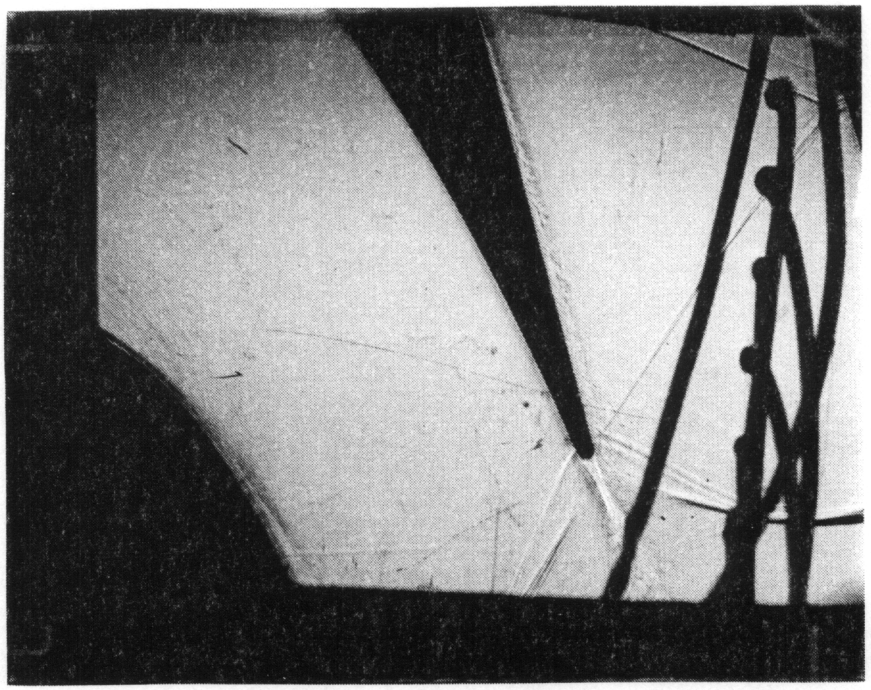


Fig.3.27 Shadowgraph: Large cascade, Blade #2

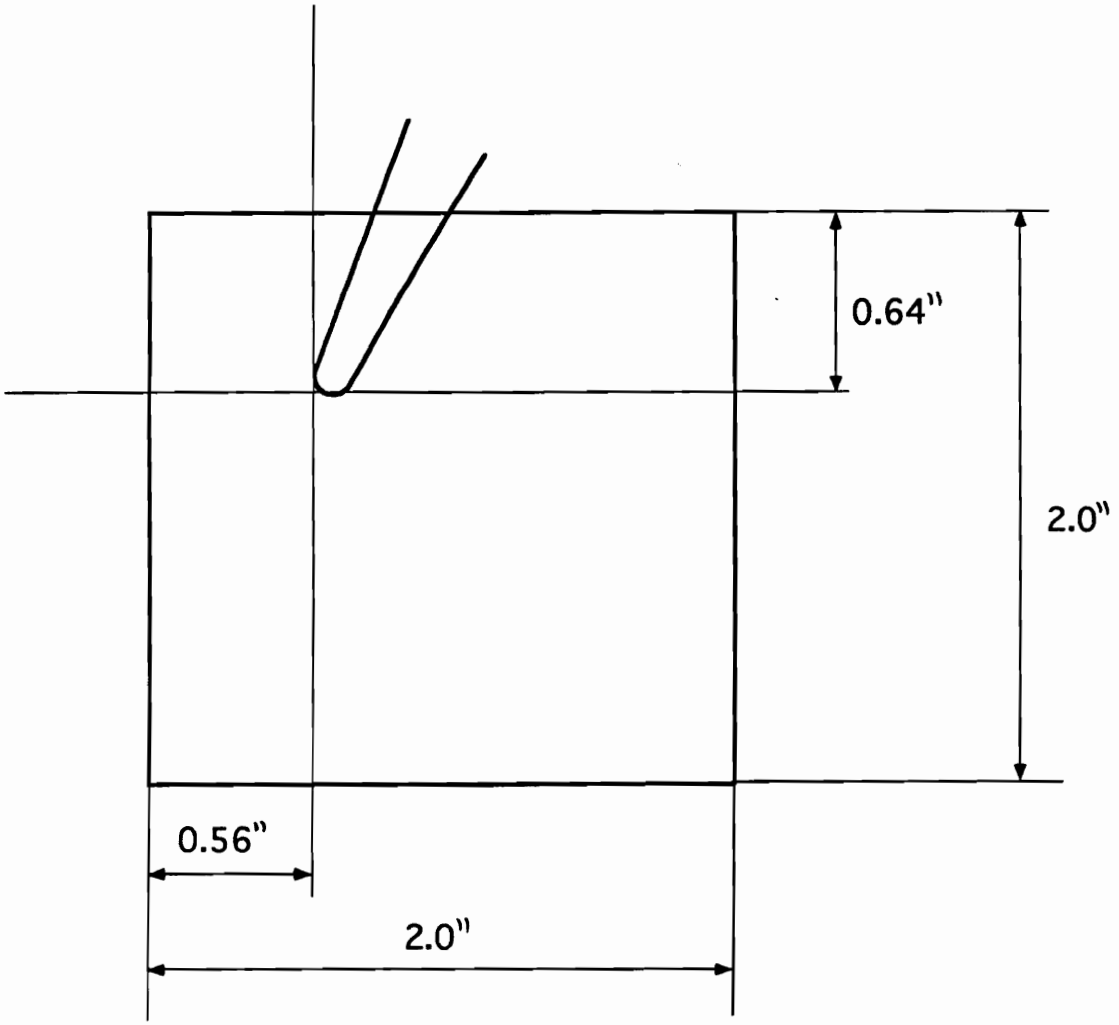


Fig.3.28 The placement of the glasswindows in the large scale cascade

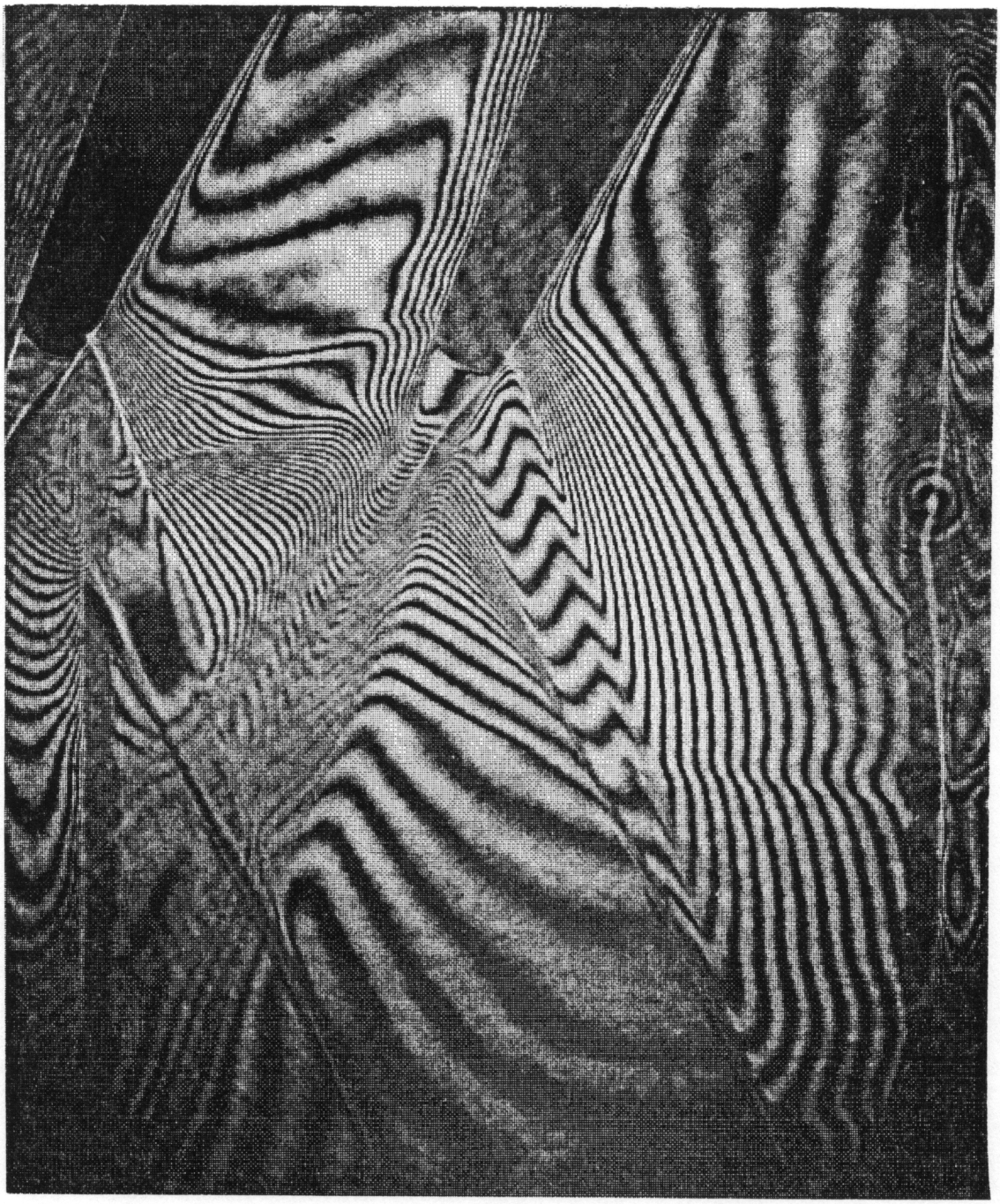


Fig.3.29 Large cascade interferogram. $M_e = 1.2$

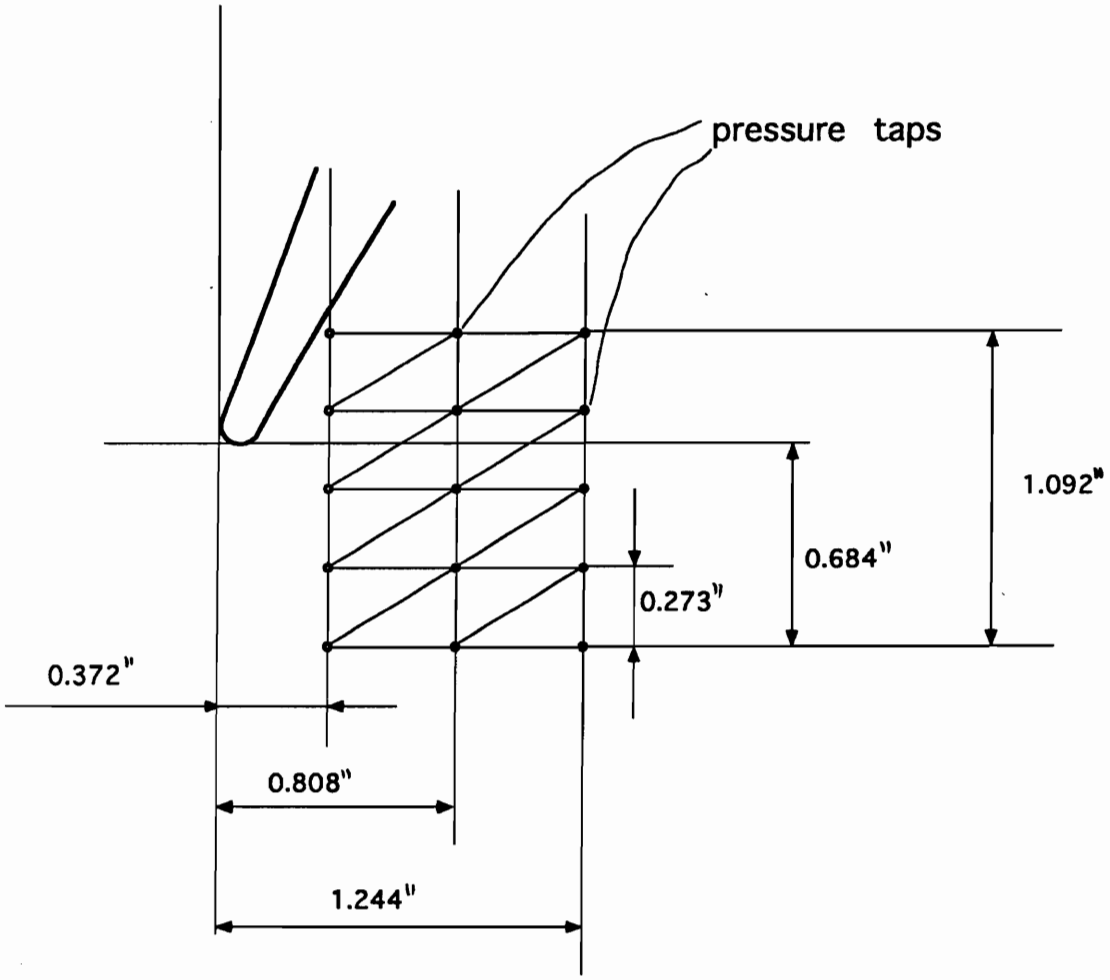


Fig.3.30 The arrangement of the pressure taps in the reference domain

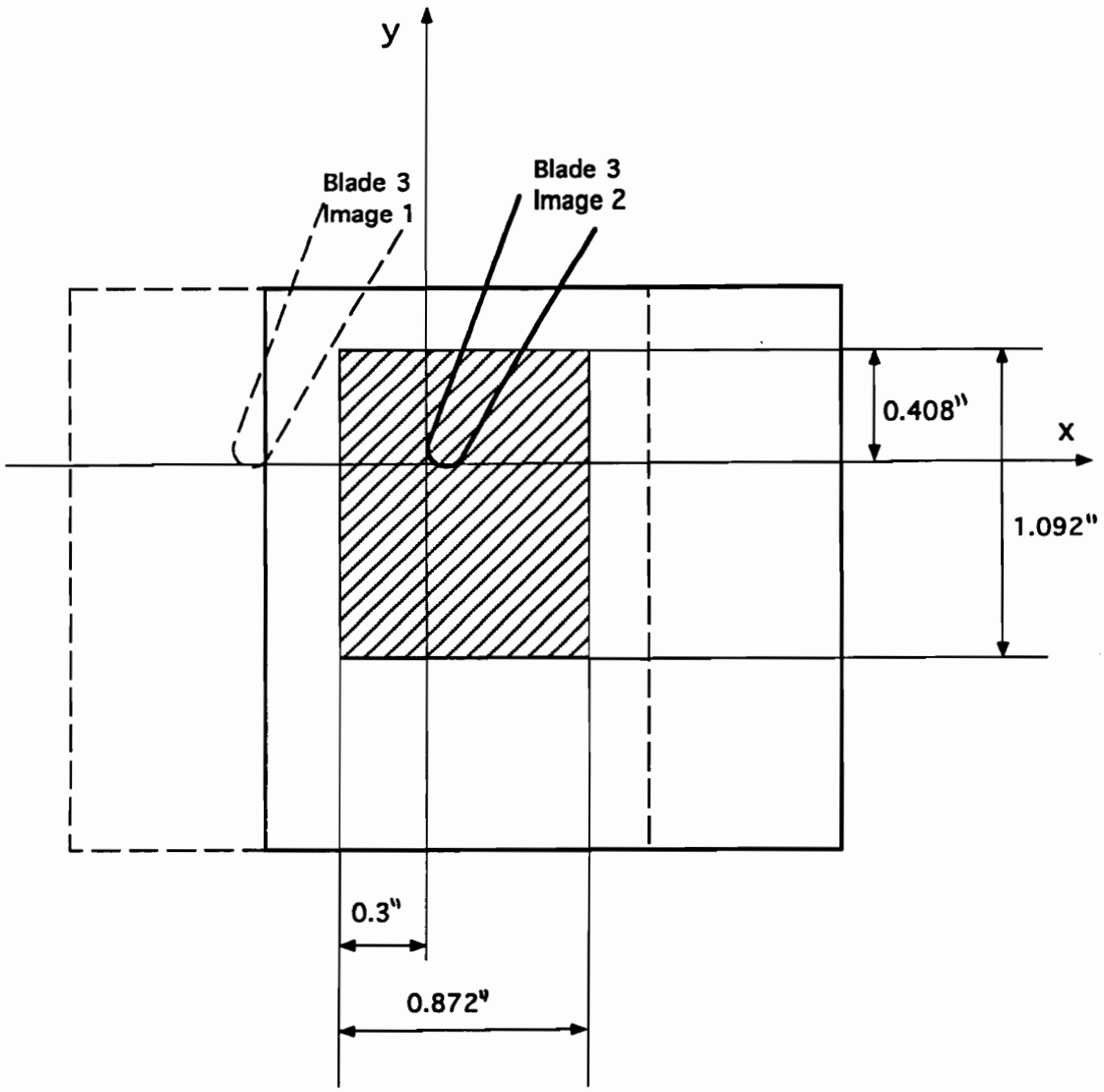


Fig.3.31 The geometry of the working domain

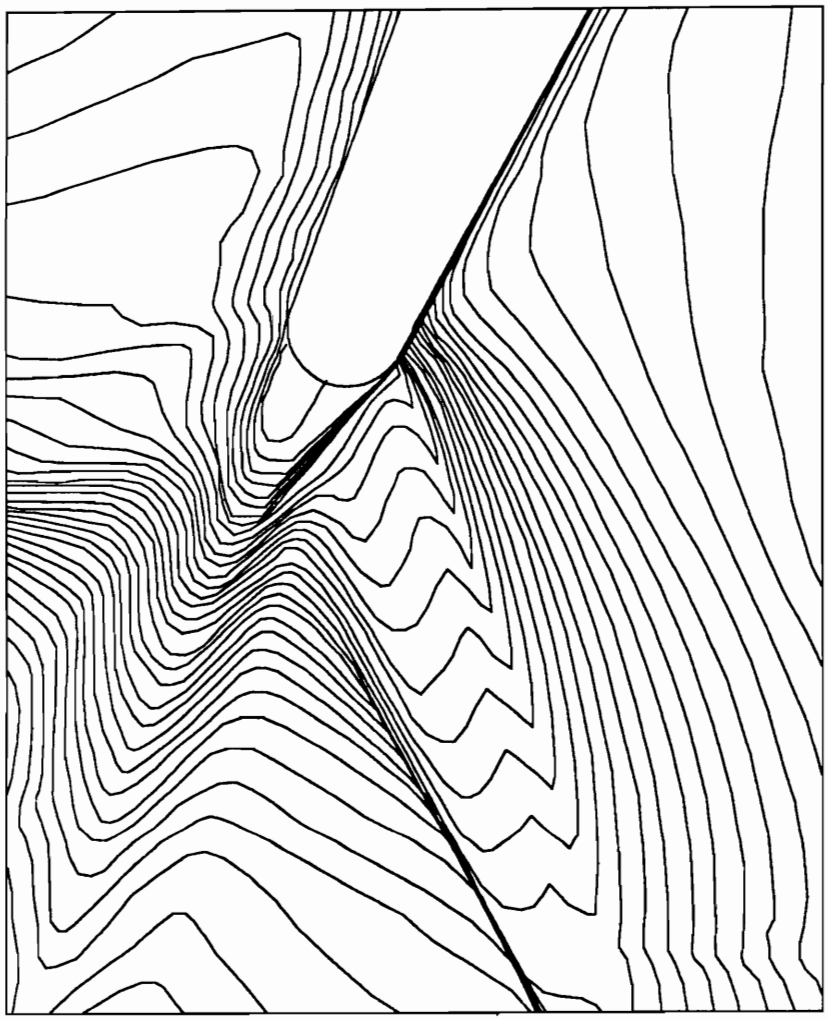


Fig.3.32 Digitized fringes of the working domain

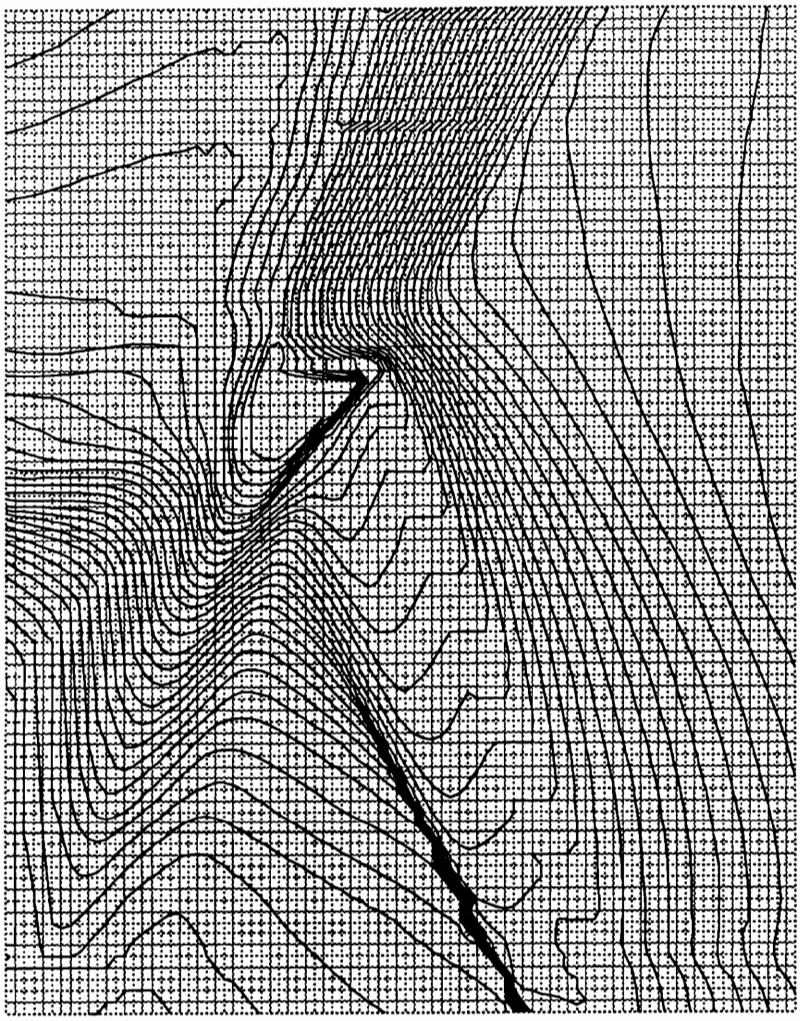


Fig.3.33 Contour lines of the fringe function interpolated on a 88 by 90 grid

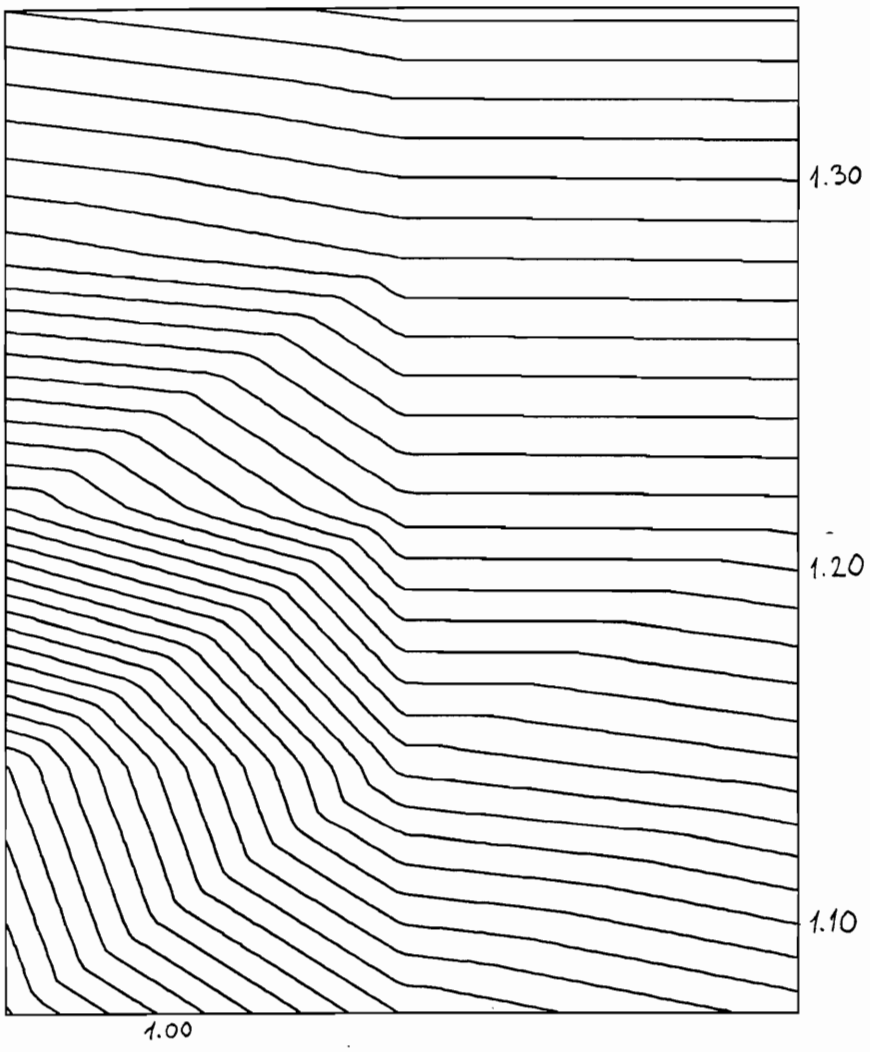


Fig.3.34 Contour lines of the ρ/ρ_{inlet} field in the reference domain

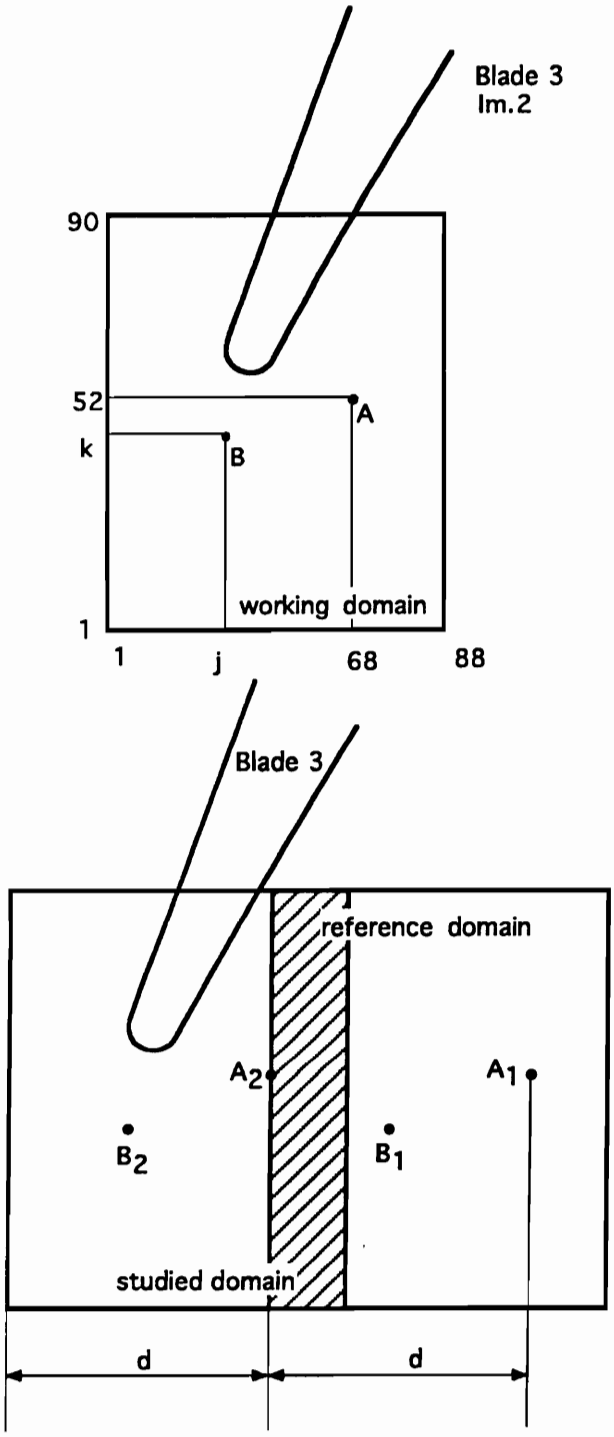


Fig.3.35 The evaluation of the trailing edge interferogram

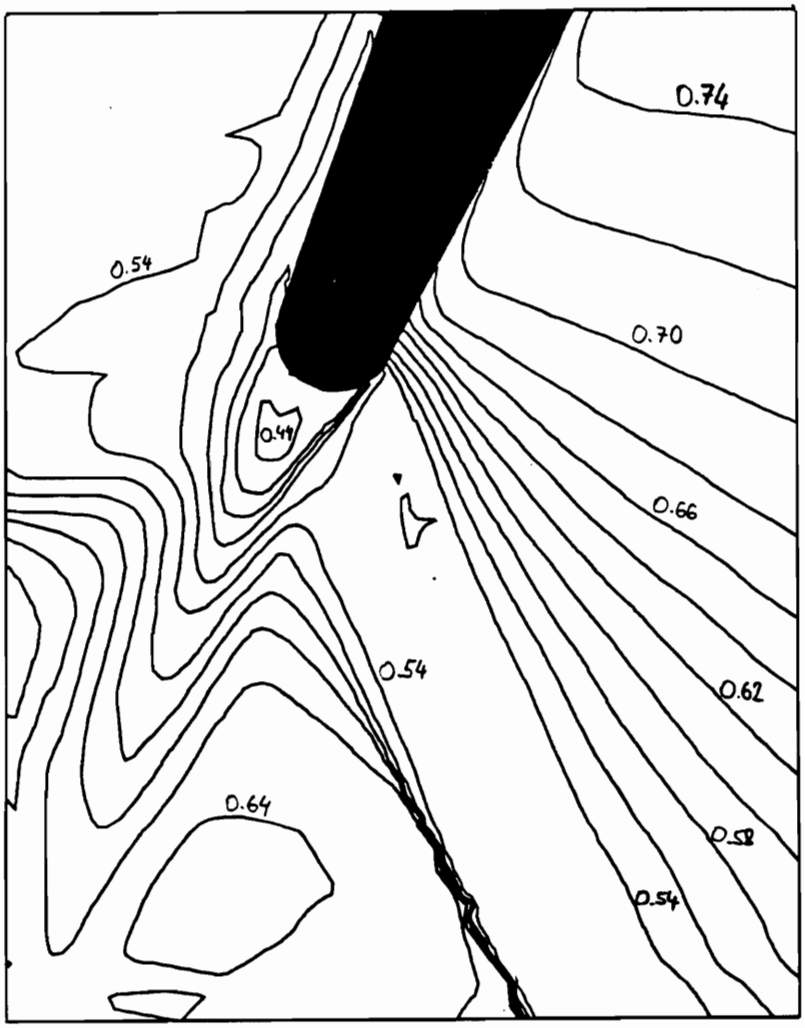


Fig.3.36 The ρ/ρ_{inlet} contour lines obtained from the interferogram

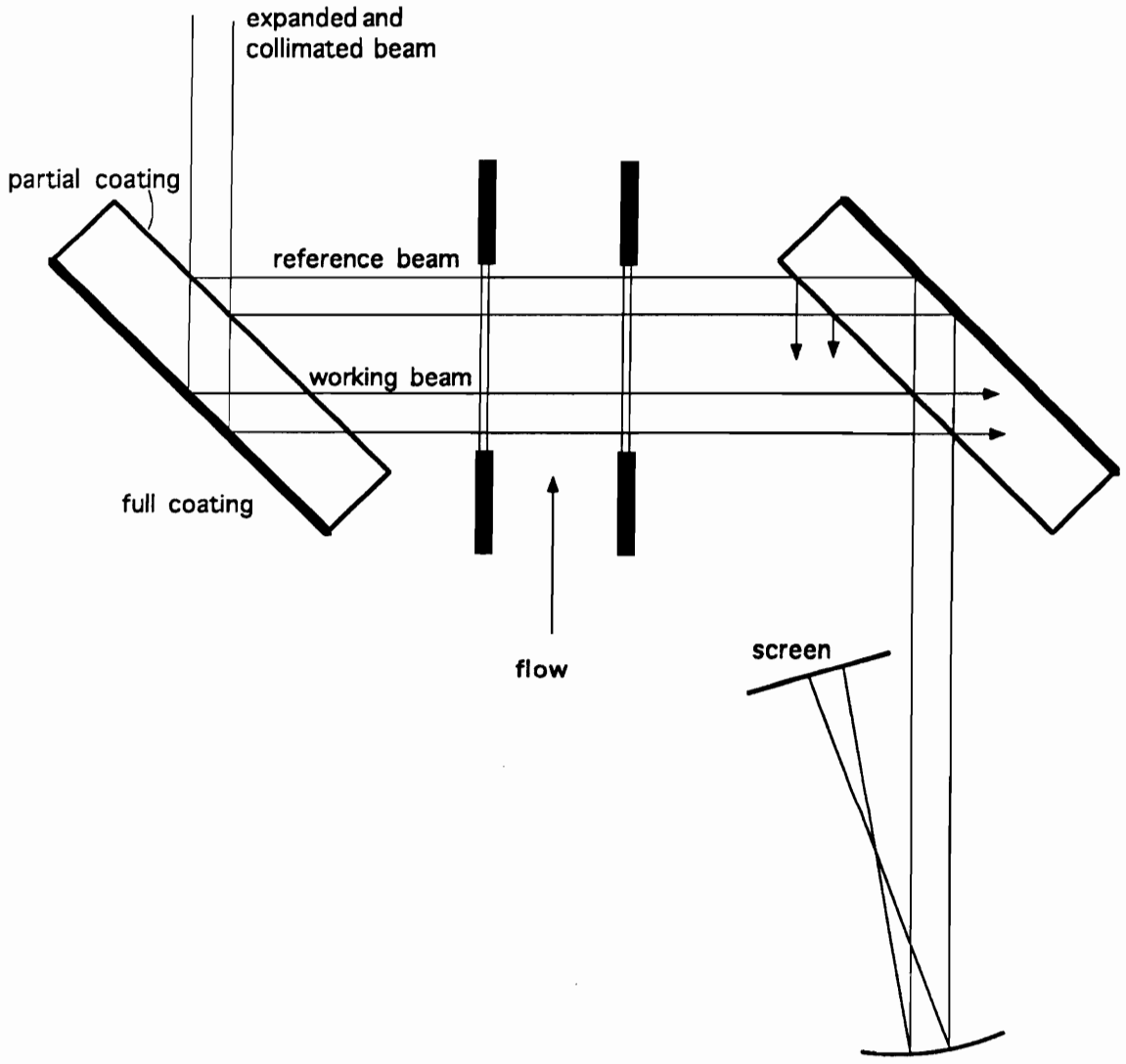


Fig.3.37 The "two-plate" interferometer

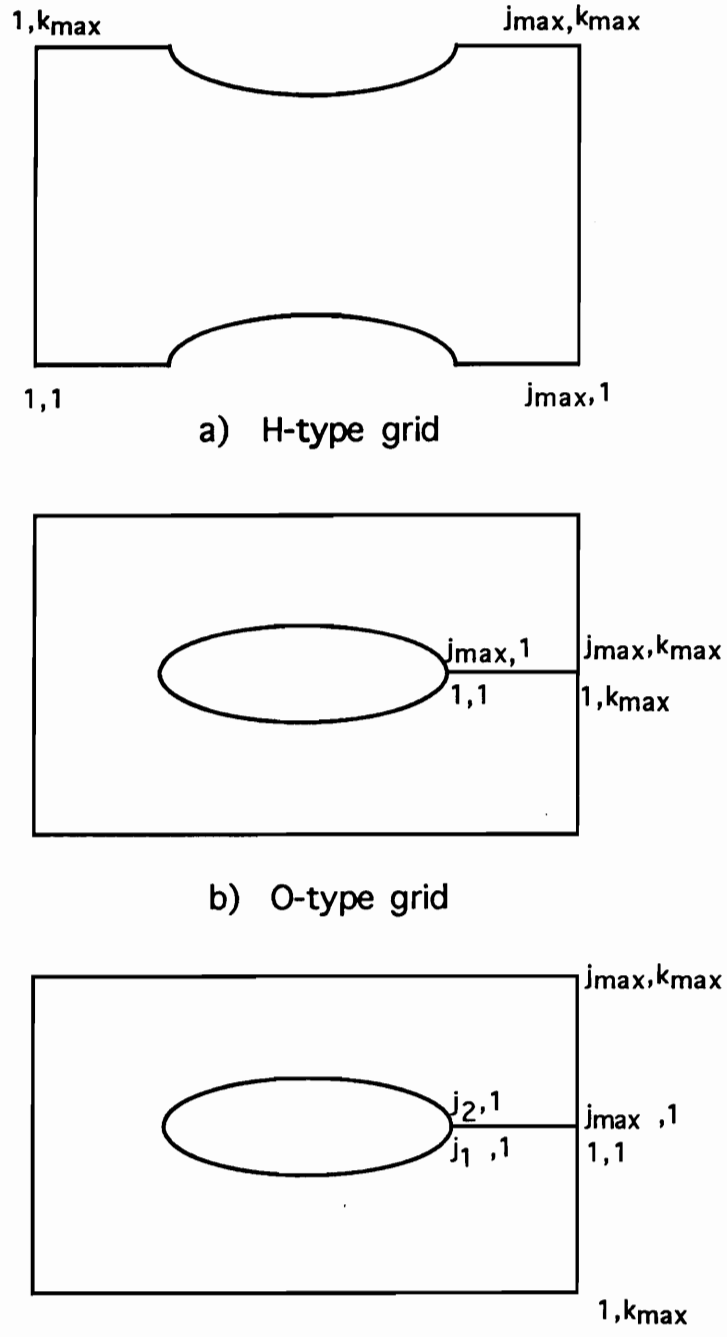


Fig.4.1 H-, O-, and C-type grids

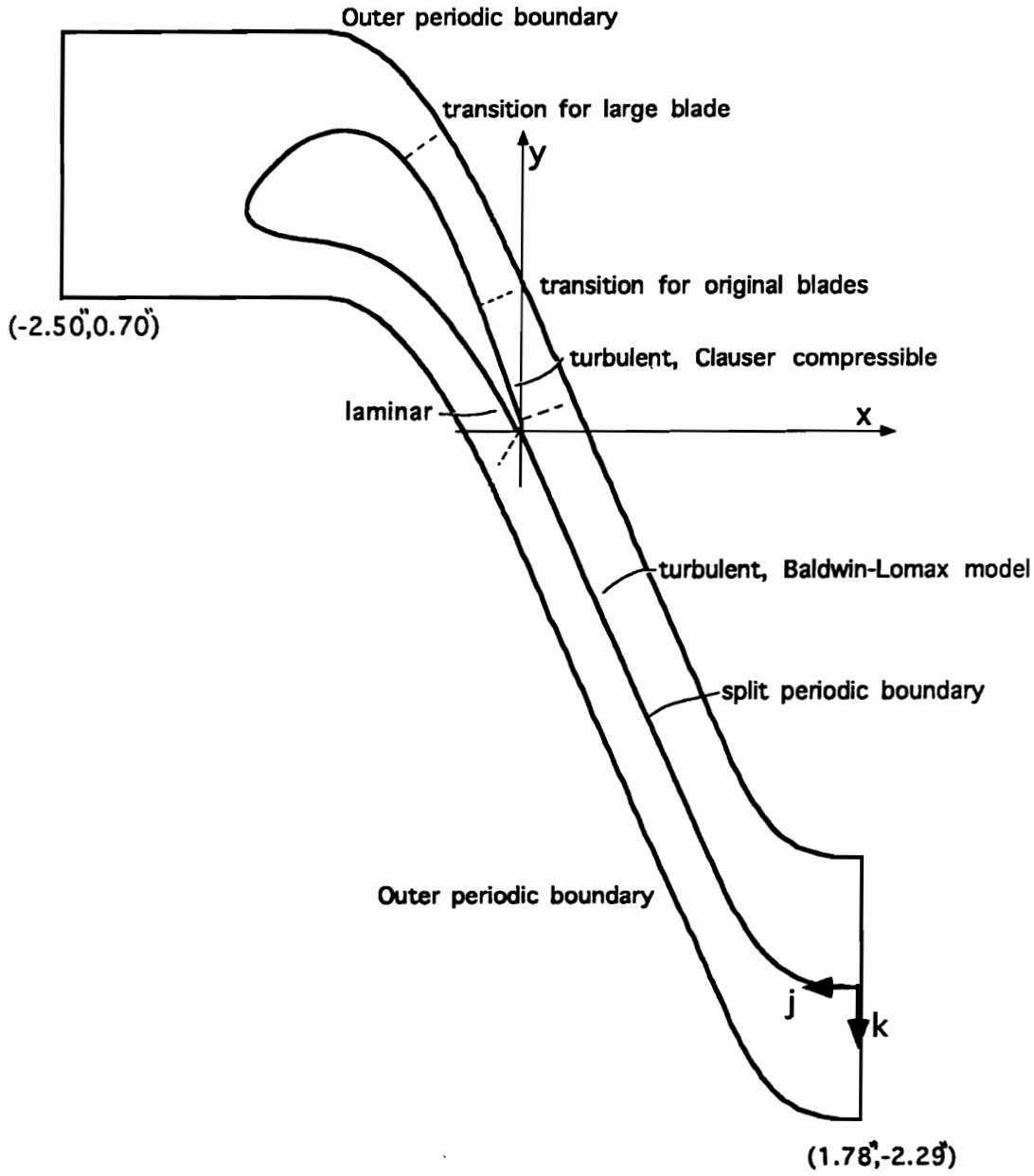


Fig.4.2 Computational domain and turbulence modeling

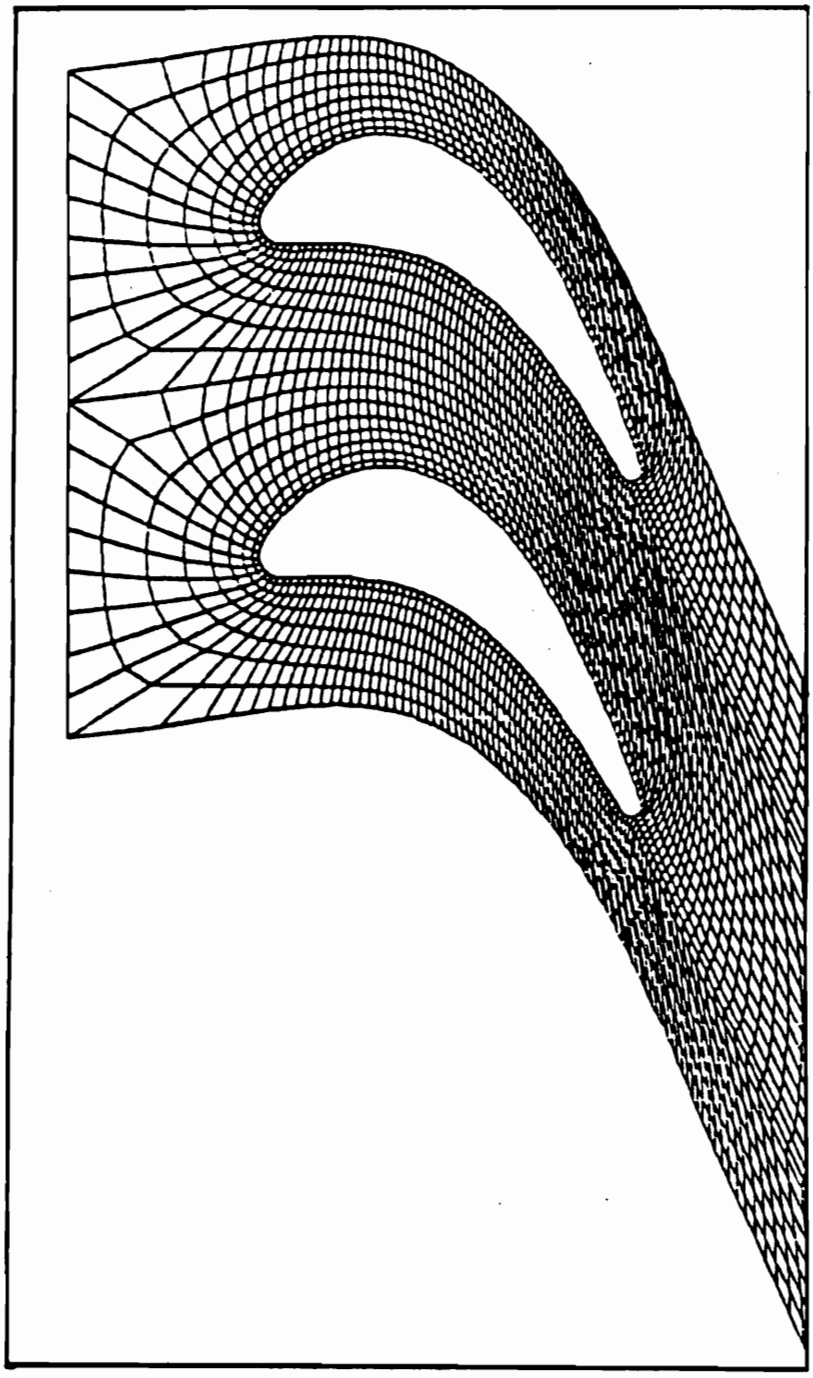


Fig.4.3 C-type grid, periodic on the periodic boundaries (from Ref.[27])

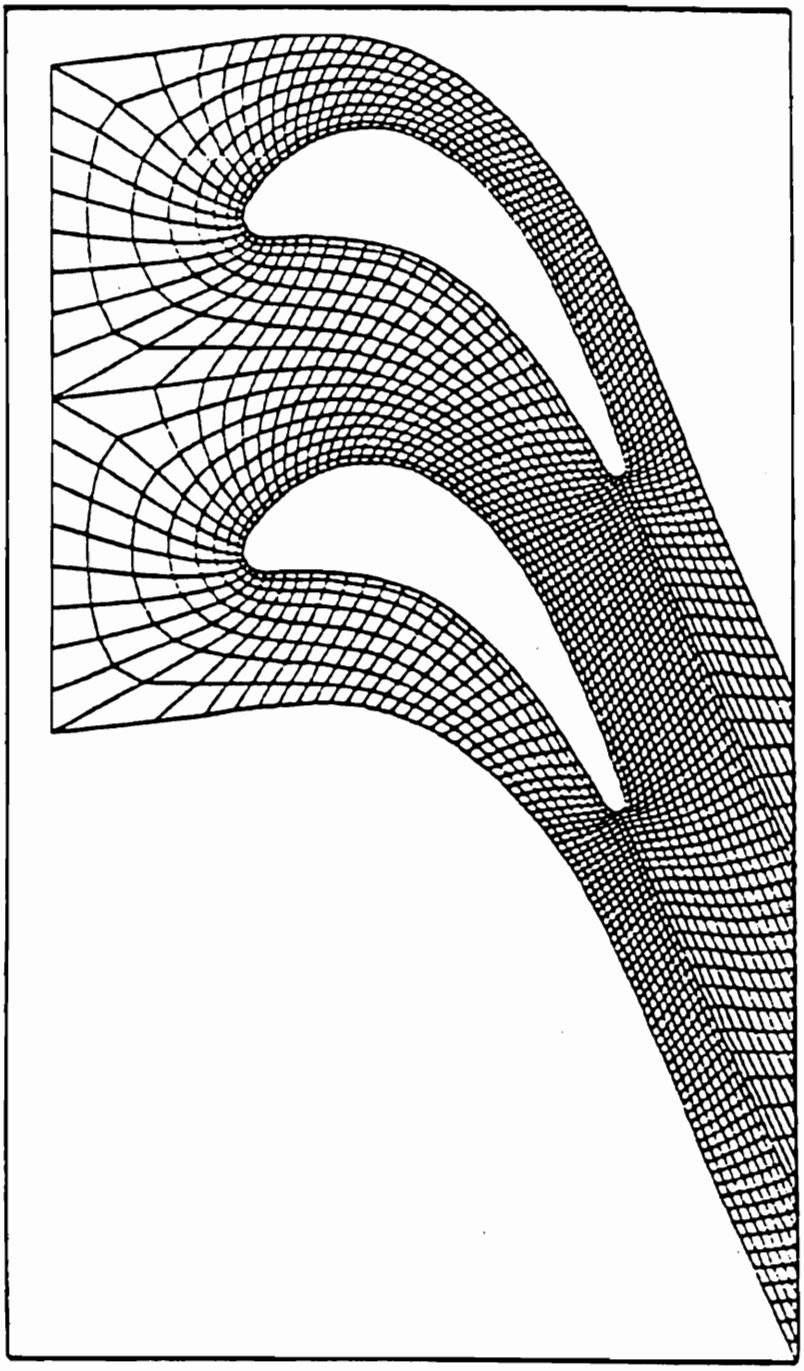


Fig.4.4 Non-periodic C-type grid from Ref.[27]

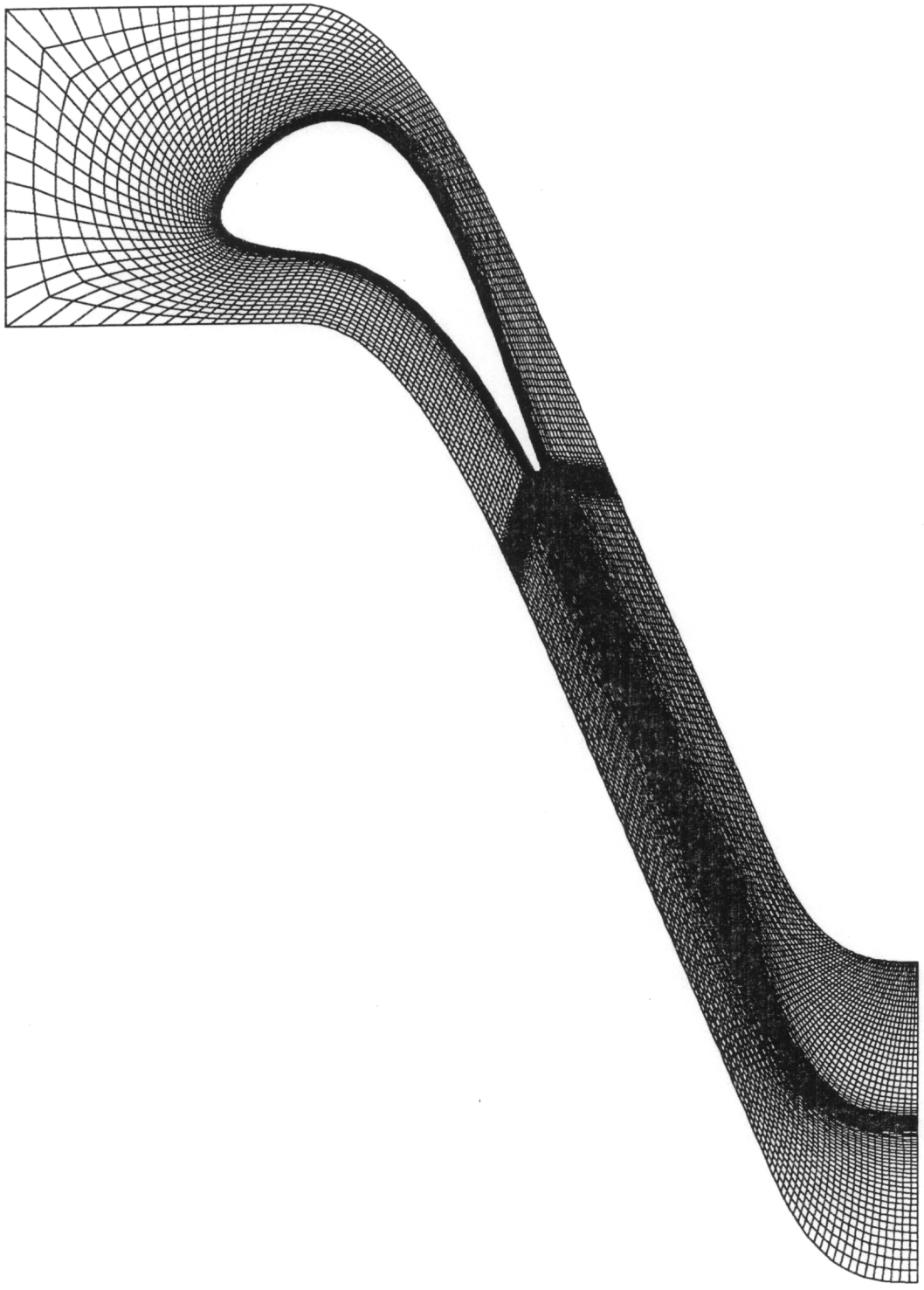


Fig.4.5 The non-periodic C-type grid used for the present studies

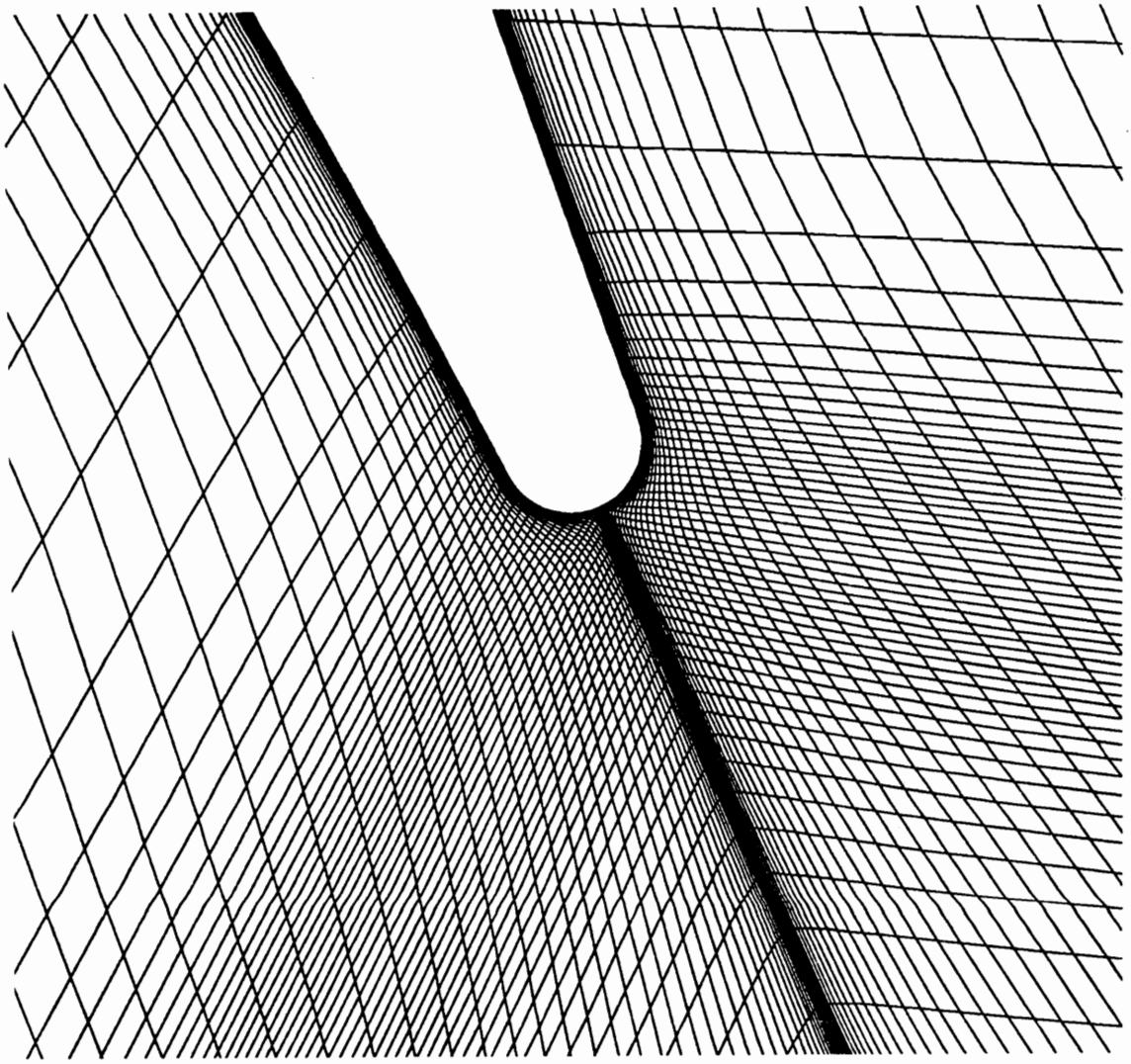


Fig.4.6 Trailing edge region of the 437×45 grid

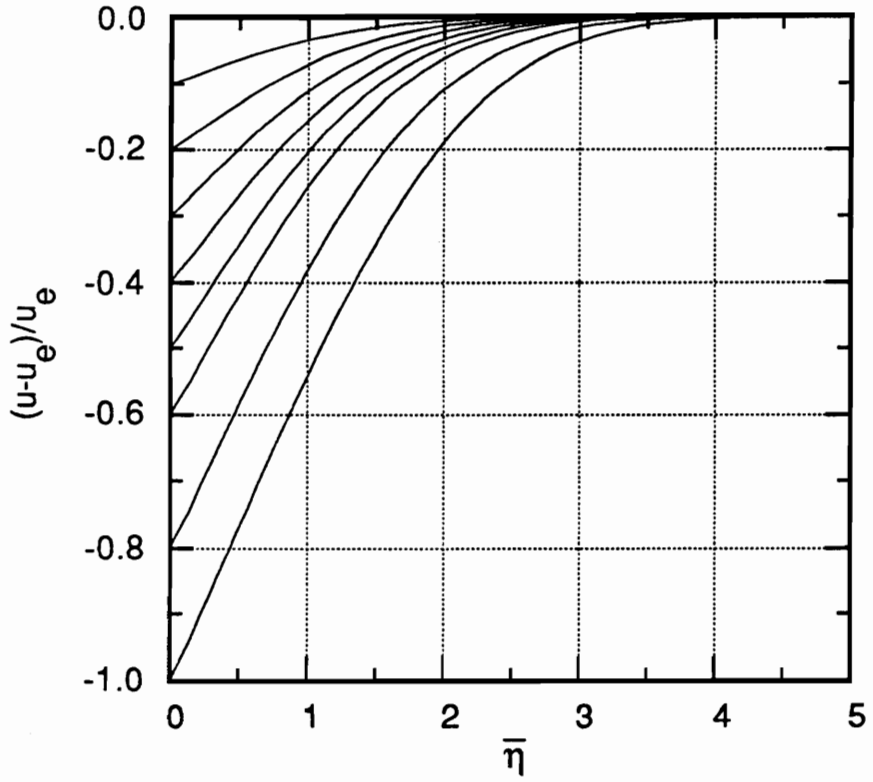


Fig.4.7 Incompressible, pseudo-laminar profiles

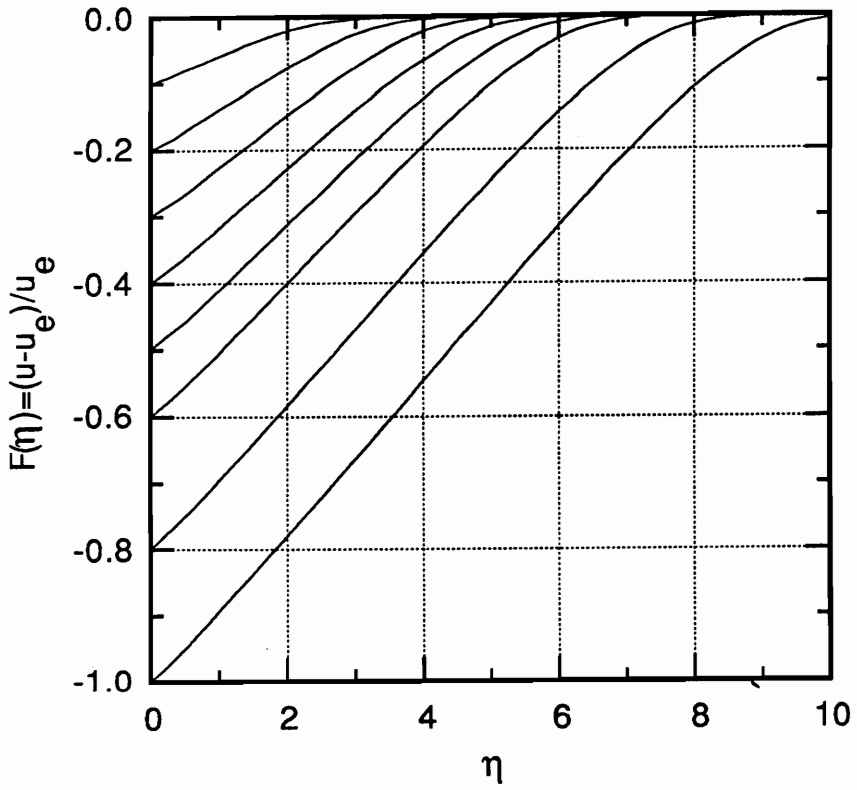


Fig.4.8 Pseudo-laminar, compressible profiles for $M_e = 4$

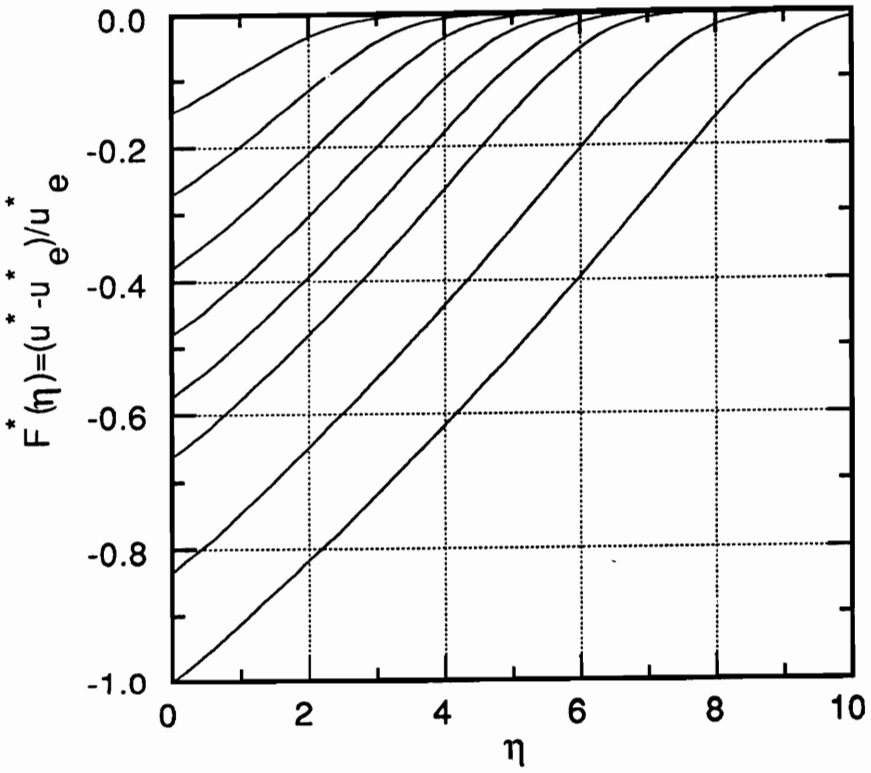


Fig.4.9 Van Driest transformed pseudo-laminar profiles for $M_e = 4$

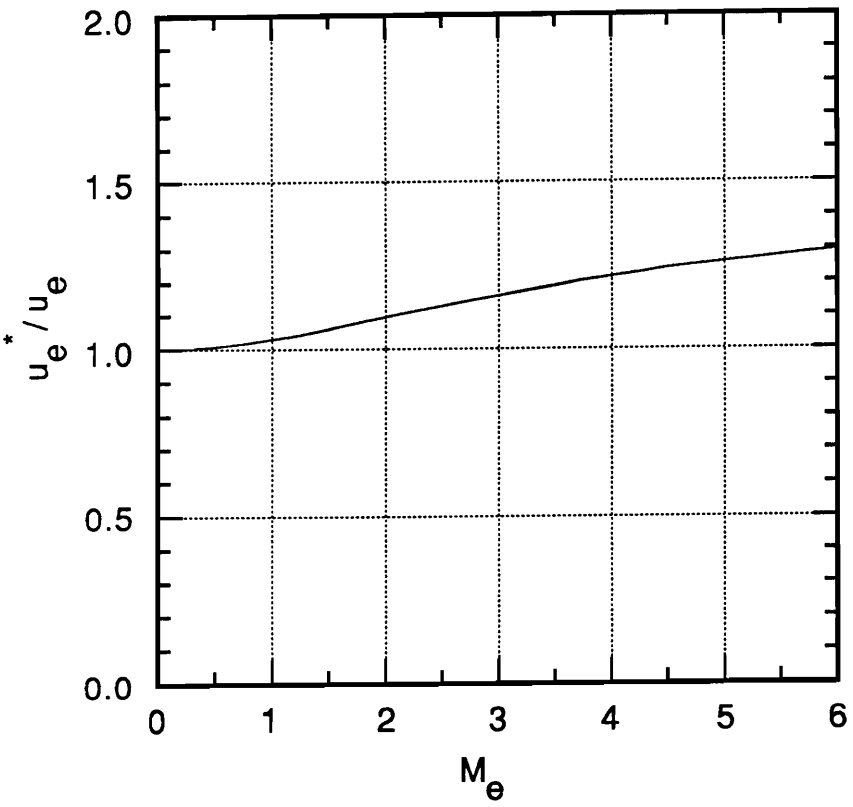


Fig.4.10 The effect of the Van Driest transformation on the edge velocity

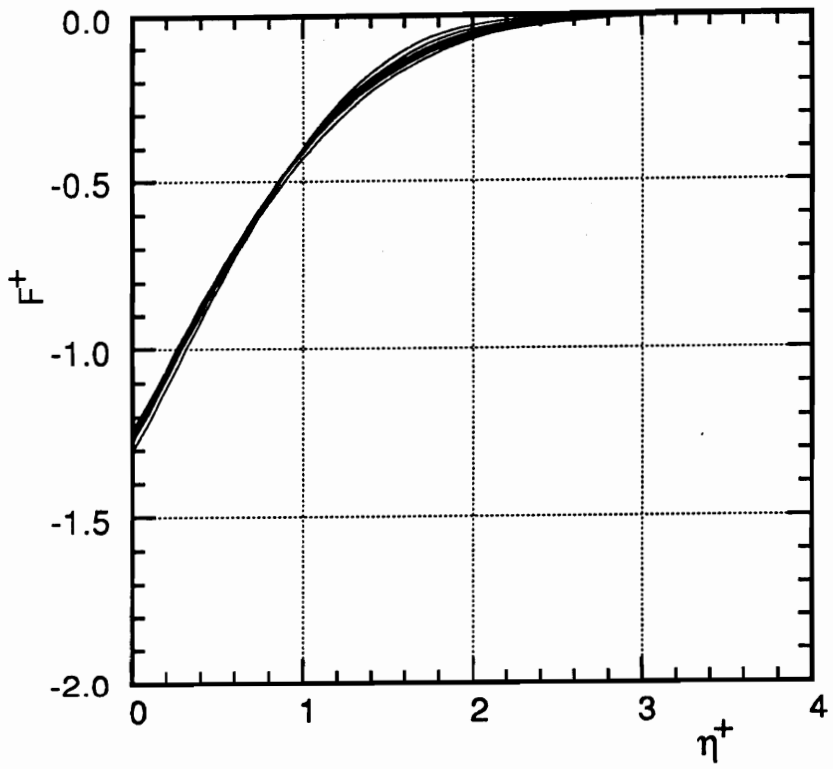


Fig.4.11a Defect law-type plot of the transformed pseudo-laminar profiles, $M_e = 0$

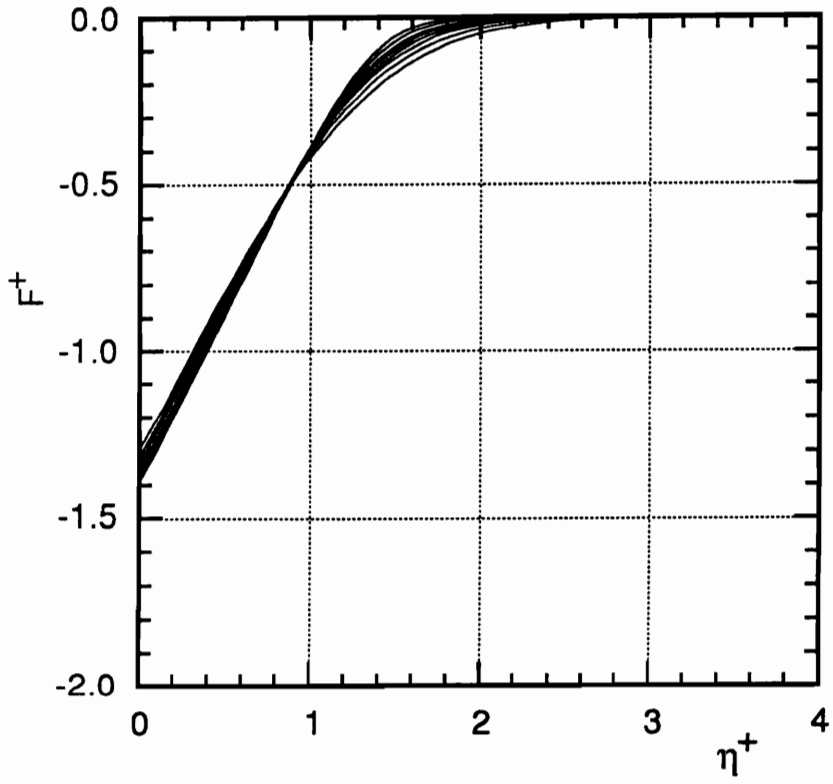


Fig.4.11b Defect law-type plot of the transformed pseudo-laminar profiles, $M_e = 2$

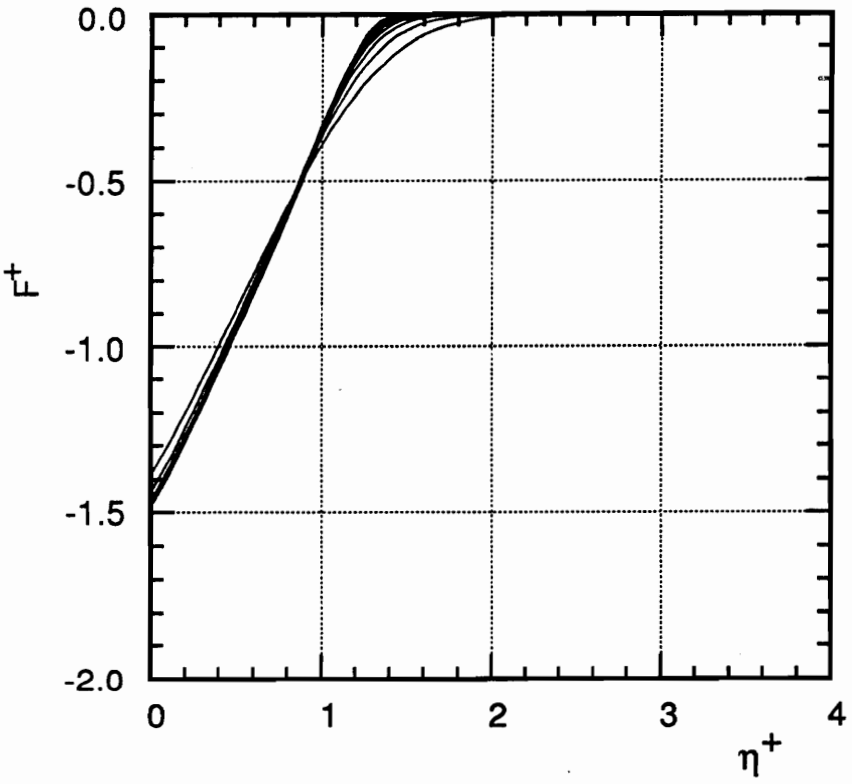


Fig.4.11c Defect law-type plot of the transformed pseudo-laminar profiles, $M_e = 4$

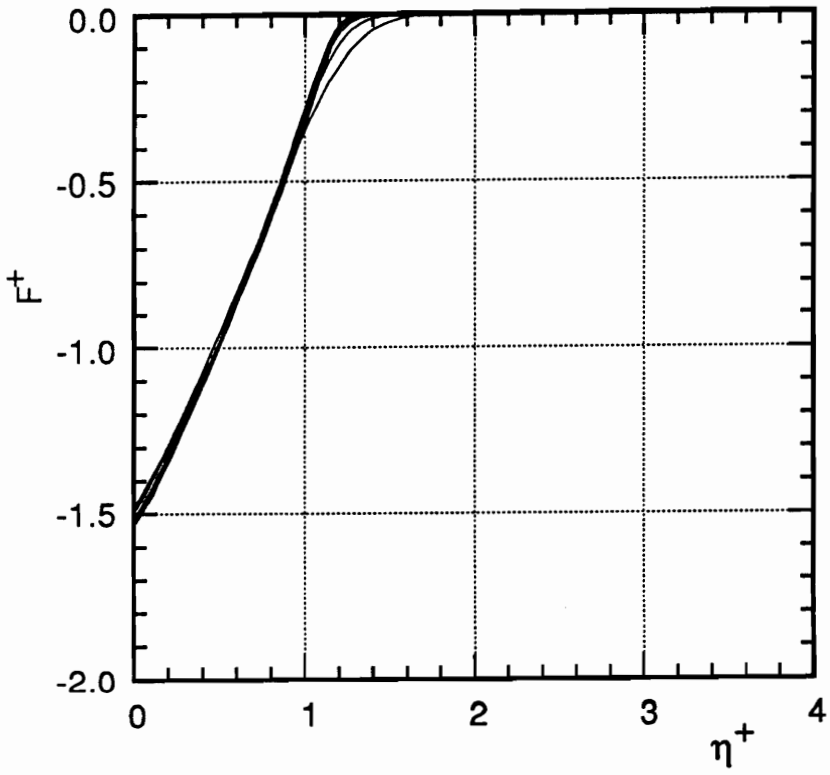


Fig.4.11d Defect law-type plot of the transformed pseudo-laminar profiles, $M_e = 6$

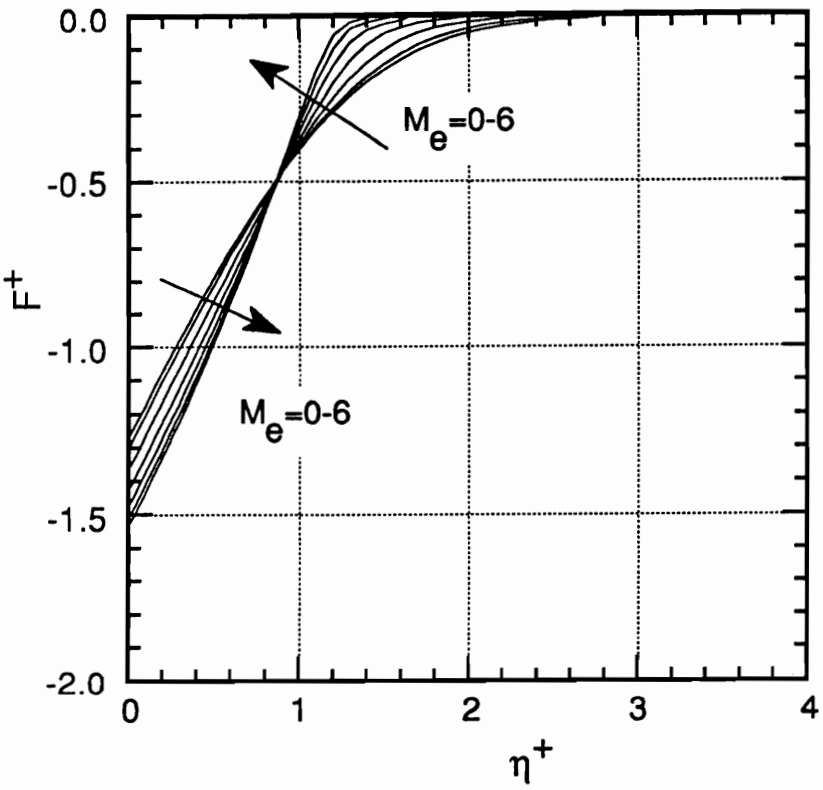


Fig.4.12 Transformed pseudo-laminar profiles for all edge Mach numbers

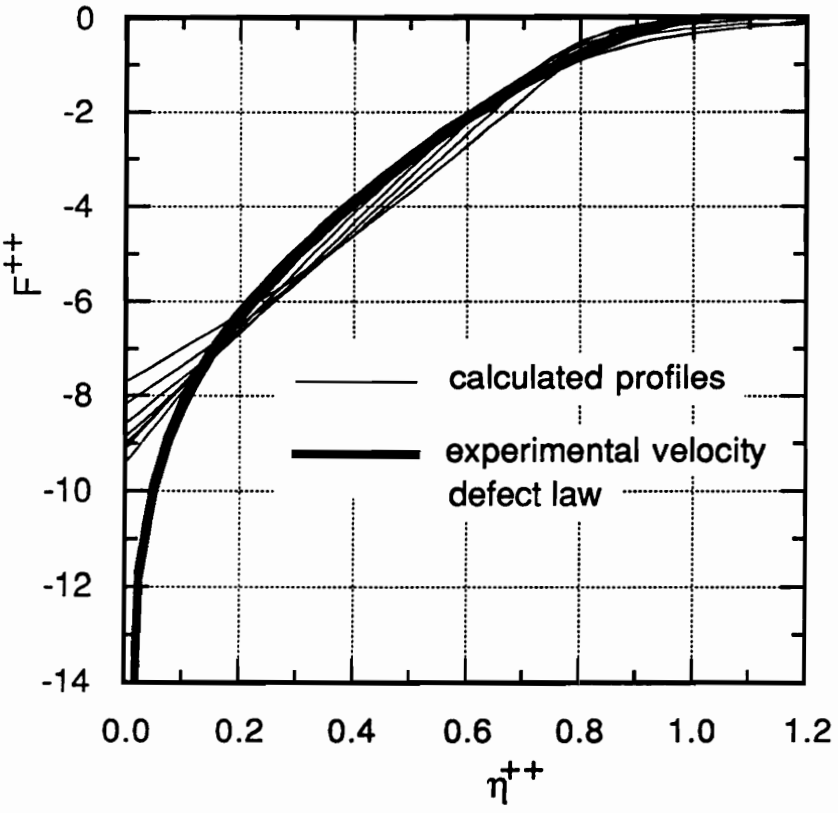


Fig.4.13 The transformed pseudo-laminar velocity profiles and velocity defect law

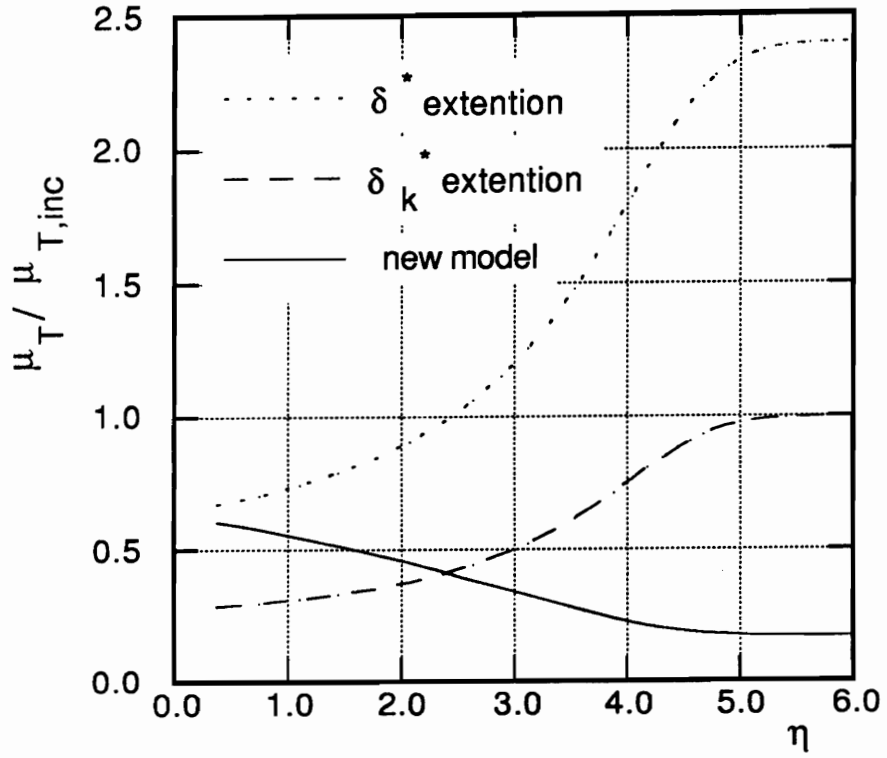


Fig.4.14a Normal variation of the predicted eddy viscosity $M_e = 4$, $u_0/u_e = 0.4$

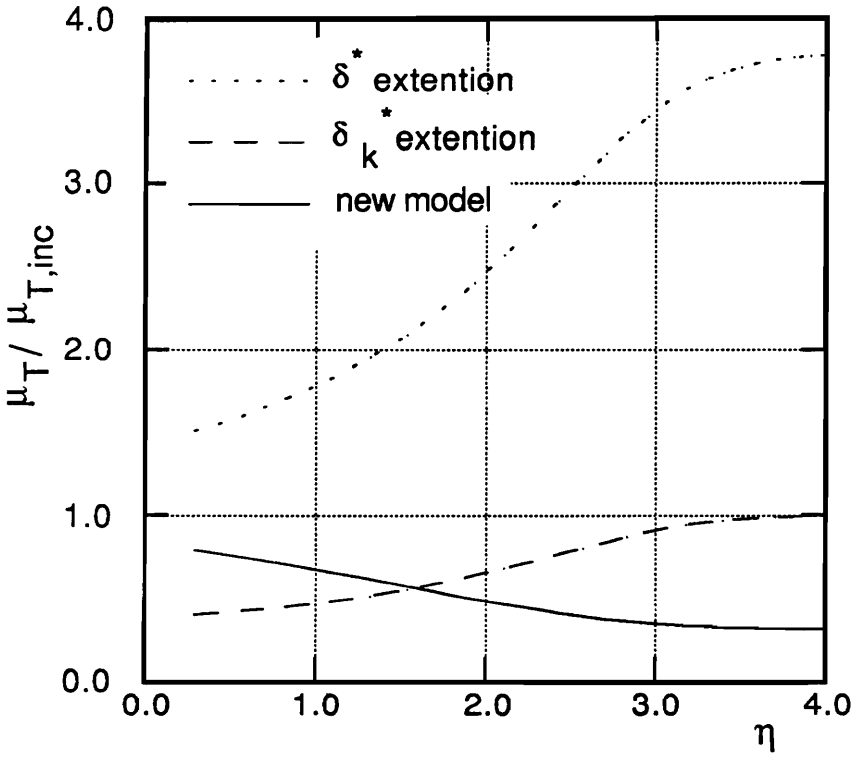


Fig.4.14b Normal variation of the predicted eddy viscosity $M_e = 4$, $u_0/u_e = 0.7$

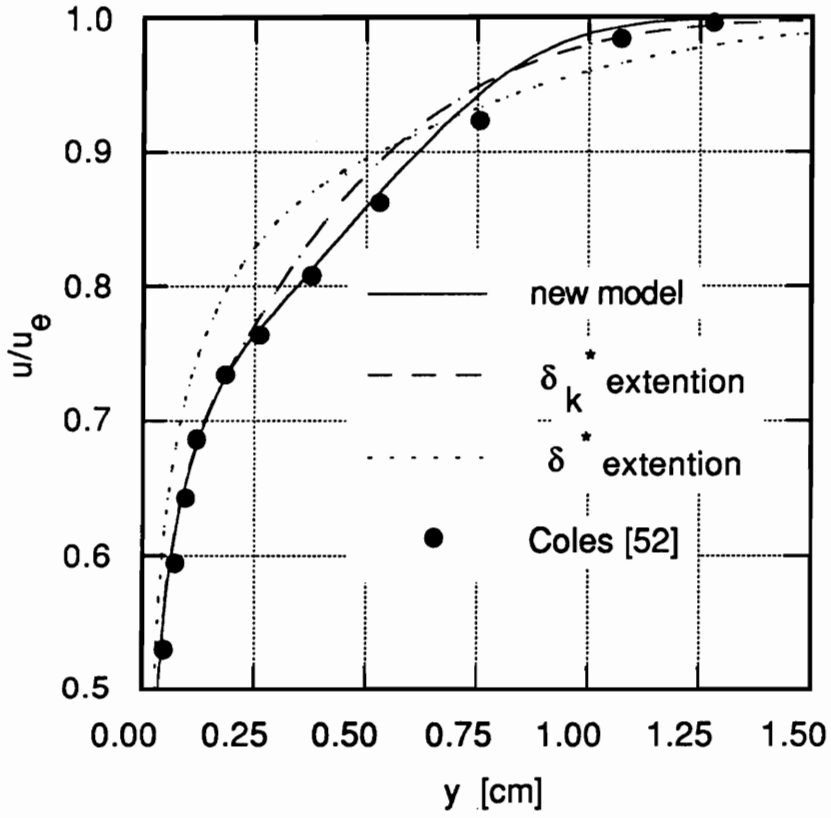


Fig.4.15 Calculated and measured velocity profiles for $M_e = 3.7$ experiment [52]

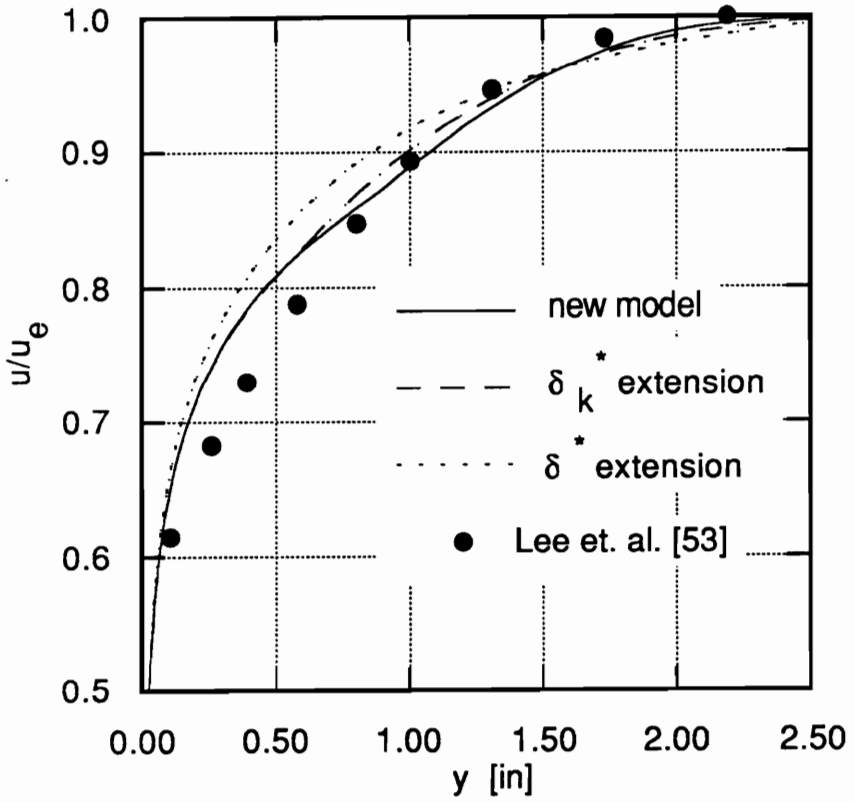


Fig.4.16 Calculated and measured velocity profiles for $M_e = 4.86$ experiments [53]

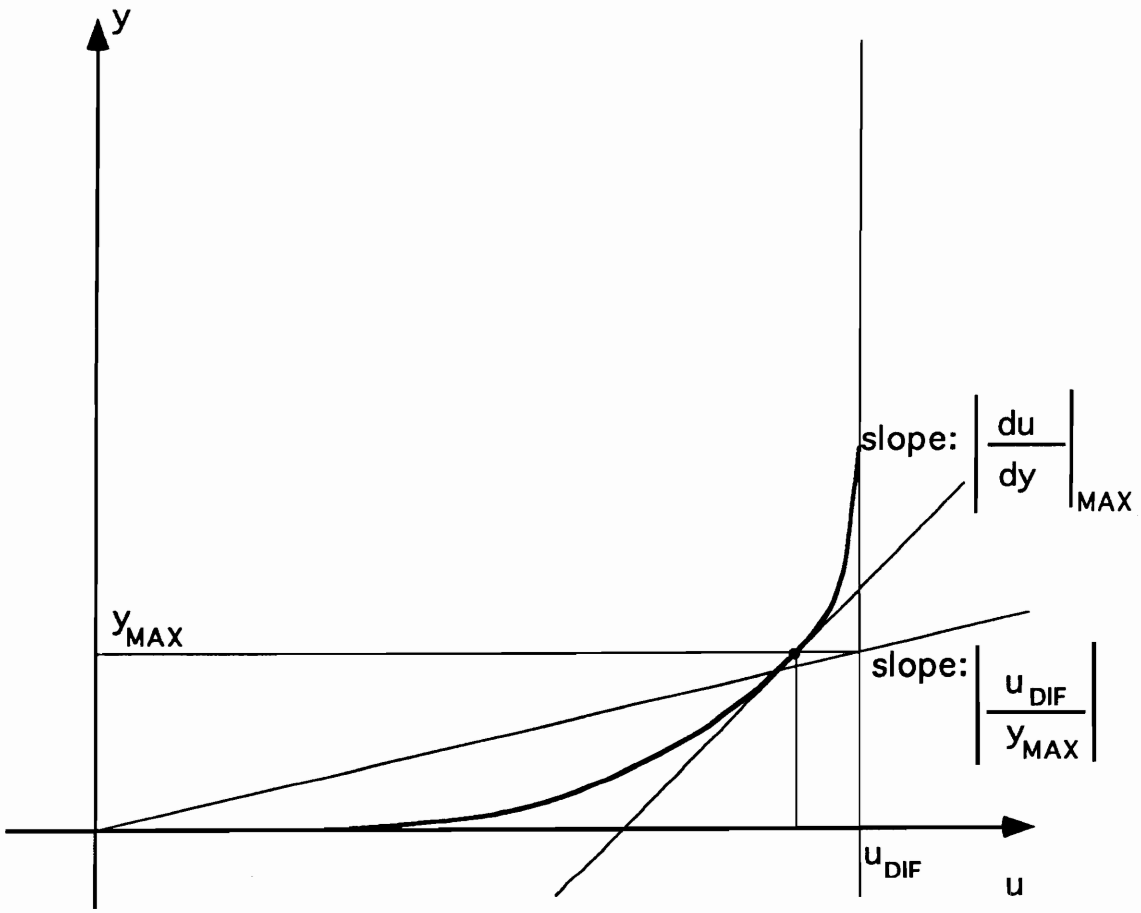


Fig.4.17 F_{WAKE} selection for attached boundary layer

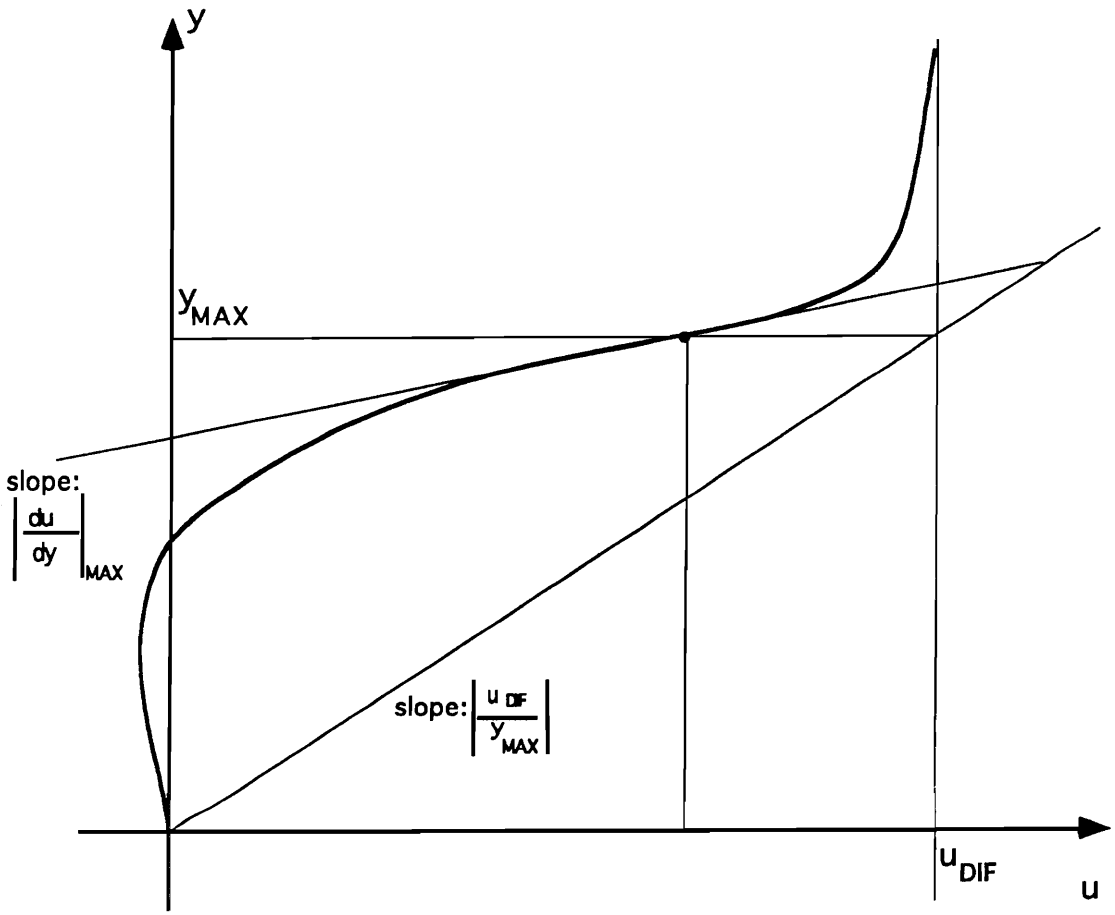


Fig.4.18 F_{WAKE} selection for separated boundary layer

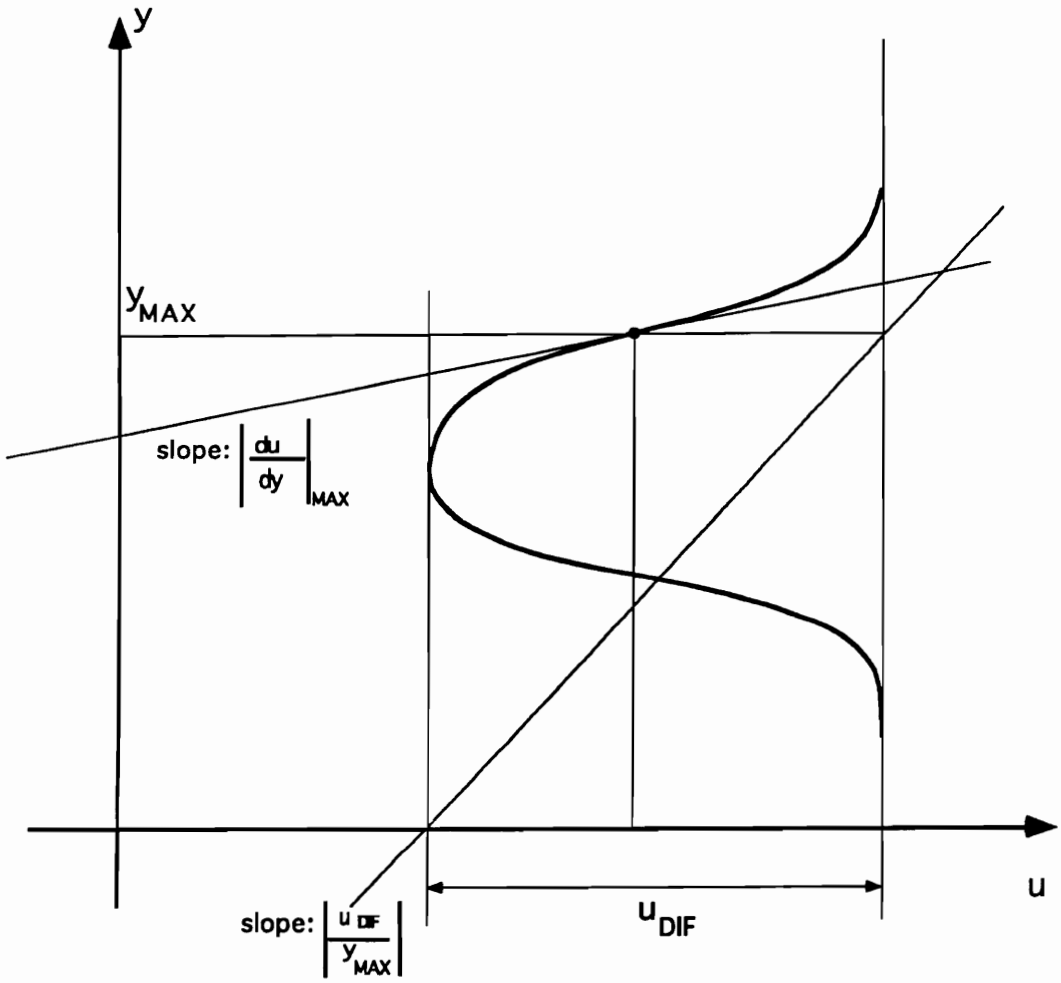


Fig.4.19 F_{WAKE} selection for wake

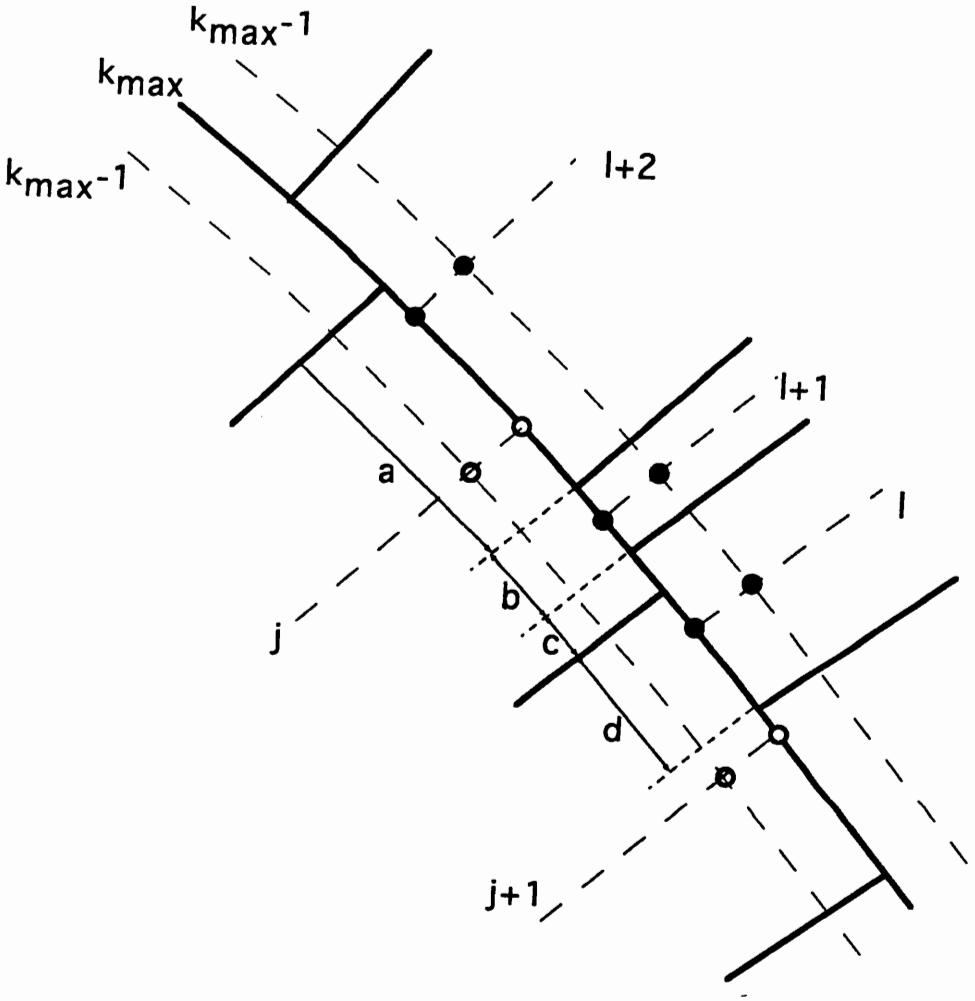


Fig.4.20 Periodic boundary condition for non-periodic grid

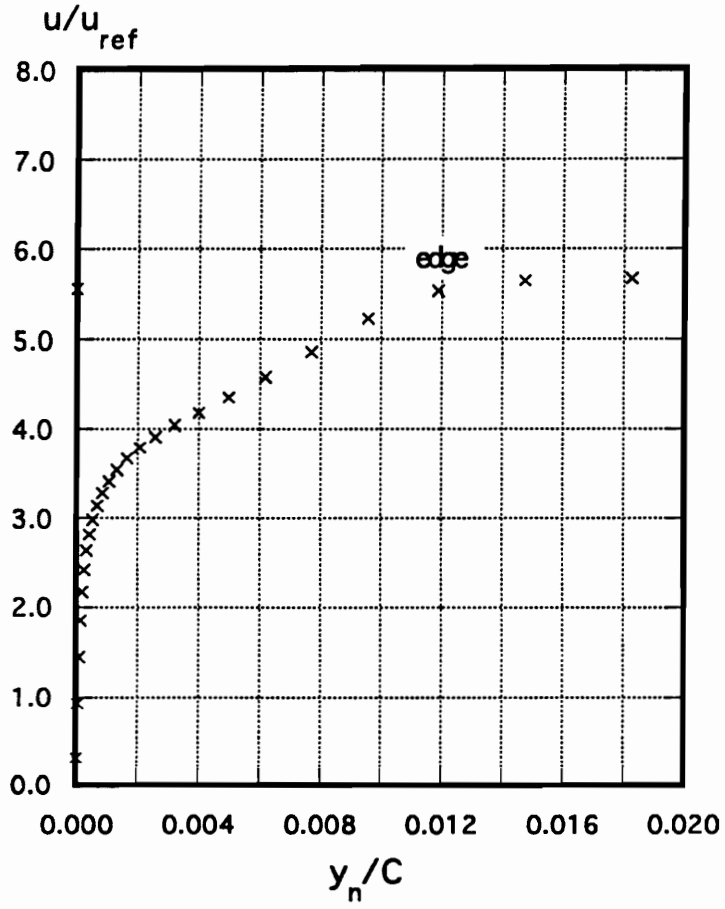


Fig.4.21 Turbulent boundary layer with edge defined by $\omega_e/\omega_{max} = 0.01$ rule

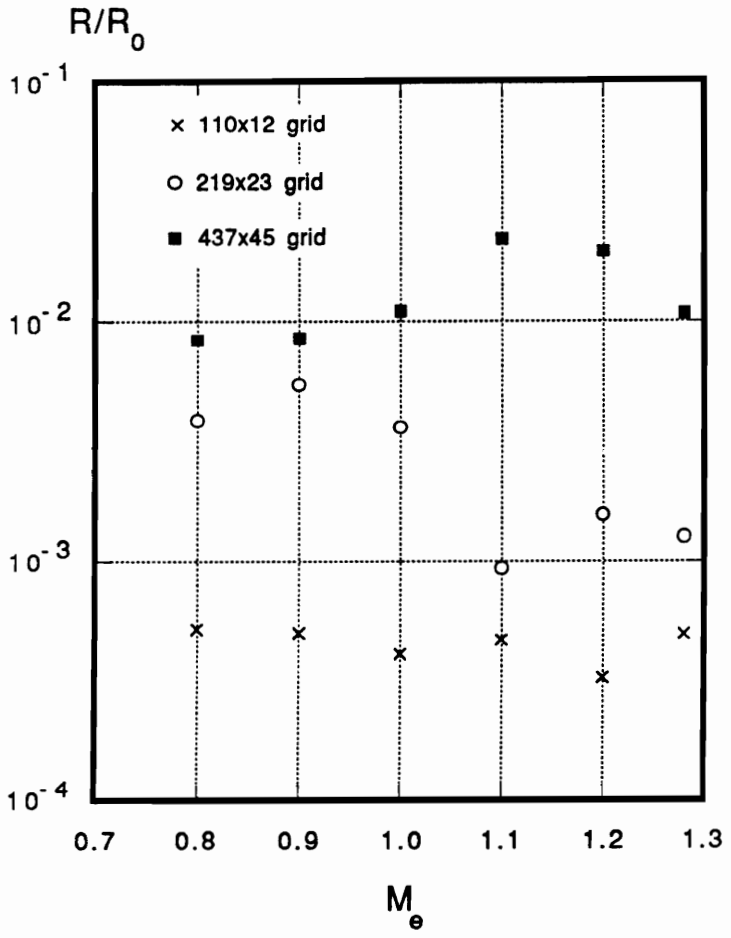


Fig.4.22 Residual drop for all Mach numbers and all grids

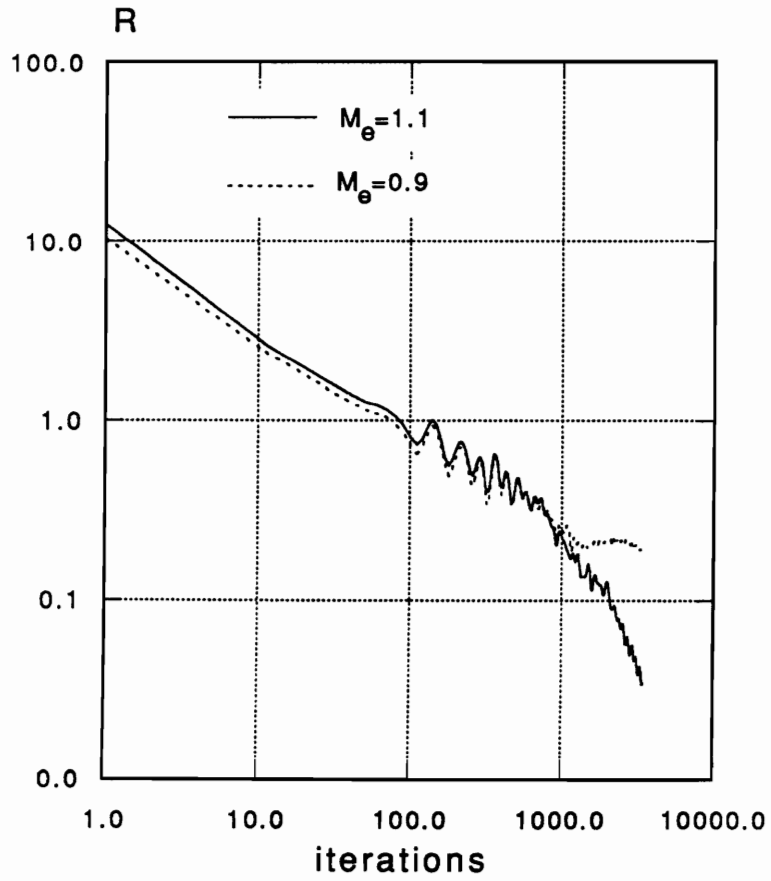


Fig.4.23 Residual history for converging and oscillating solutions (219 × 23 grid)

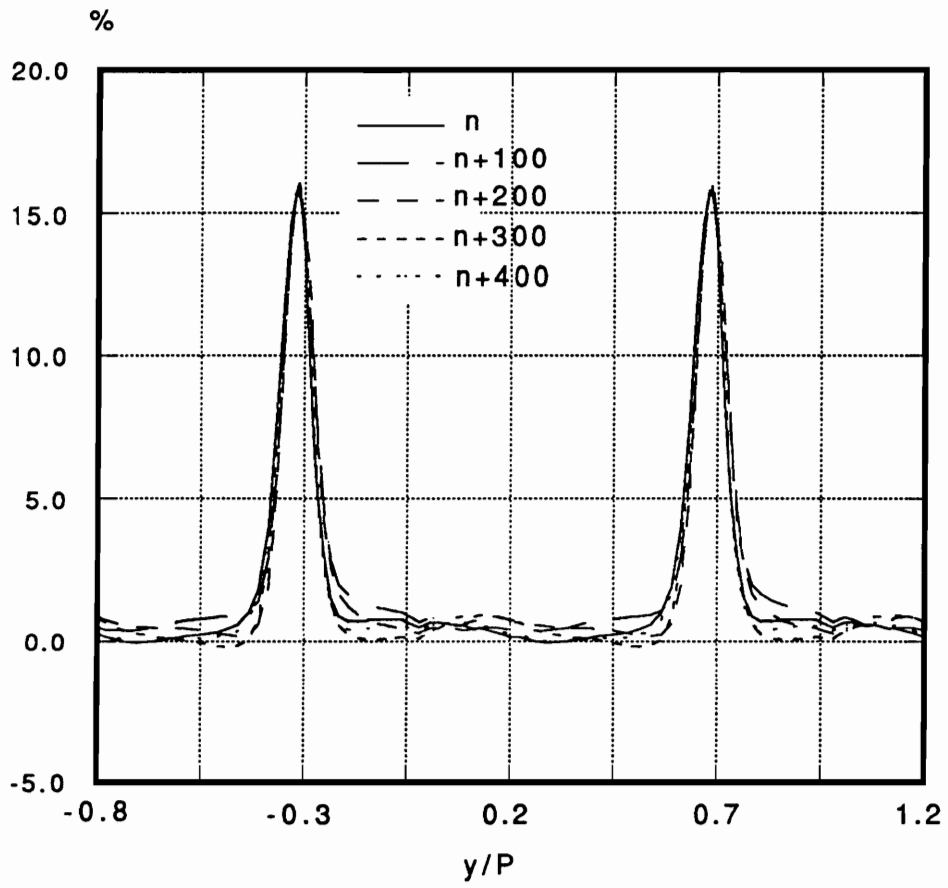


Fig.4.24 Pitot pressure drop traverses, $M_e = 0.9$, 219×23 grid

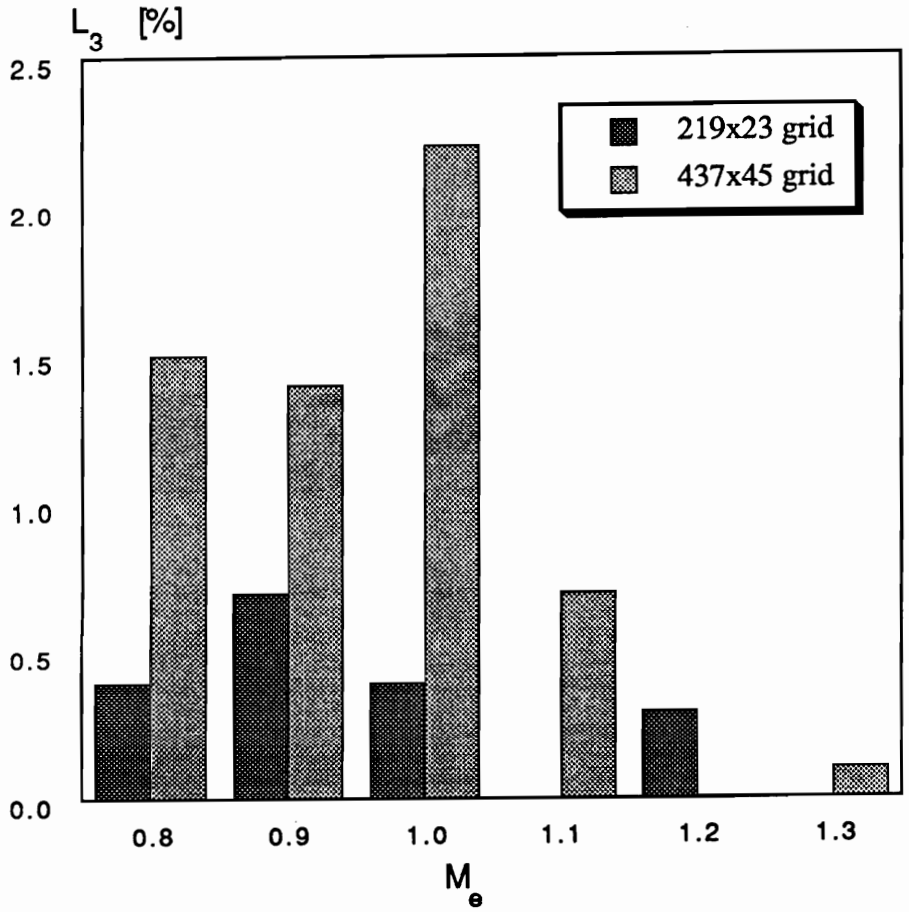


Fig.4.25 Oscillation in loss coefficient

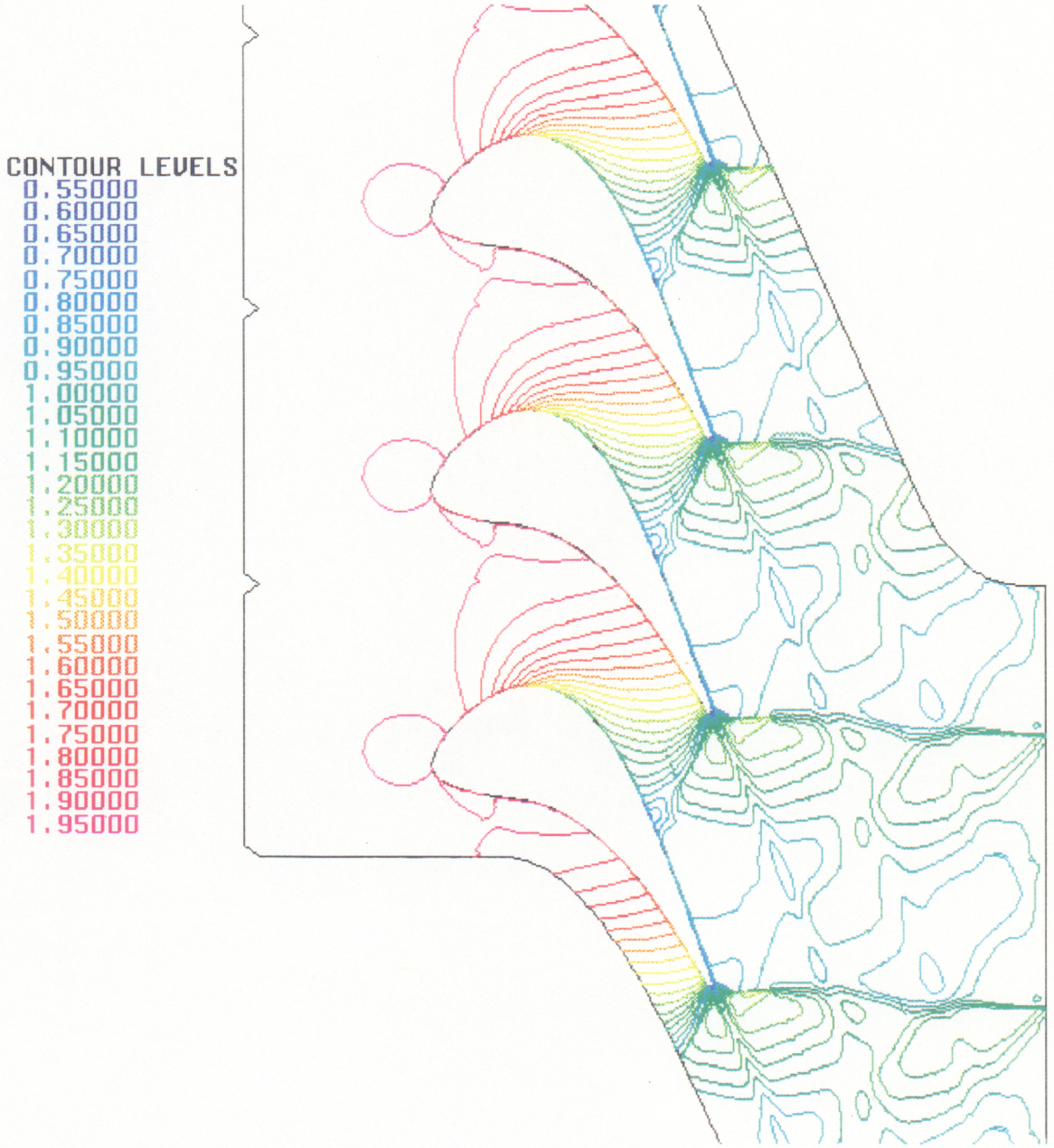


Fig.4.26 Density contours [kg/m^3] for $M_e = 1.2$

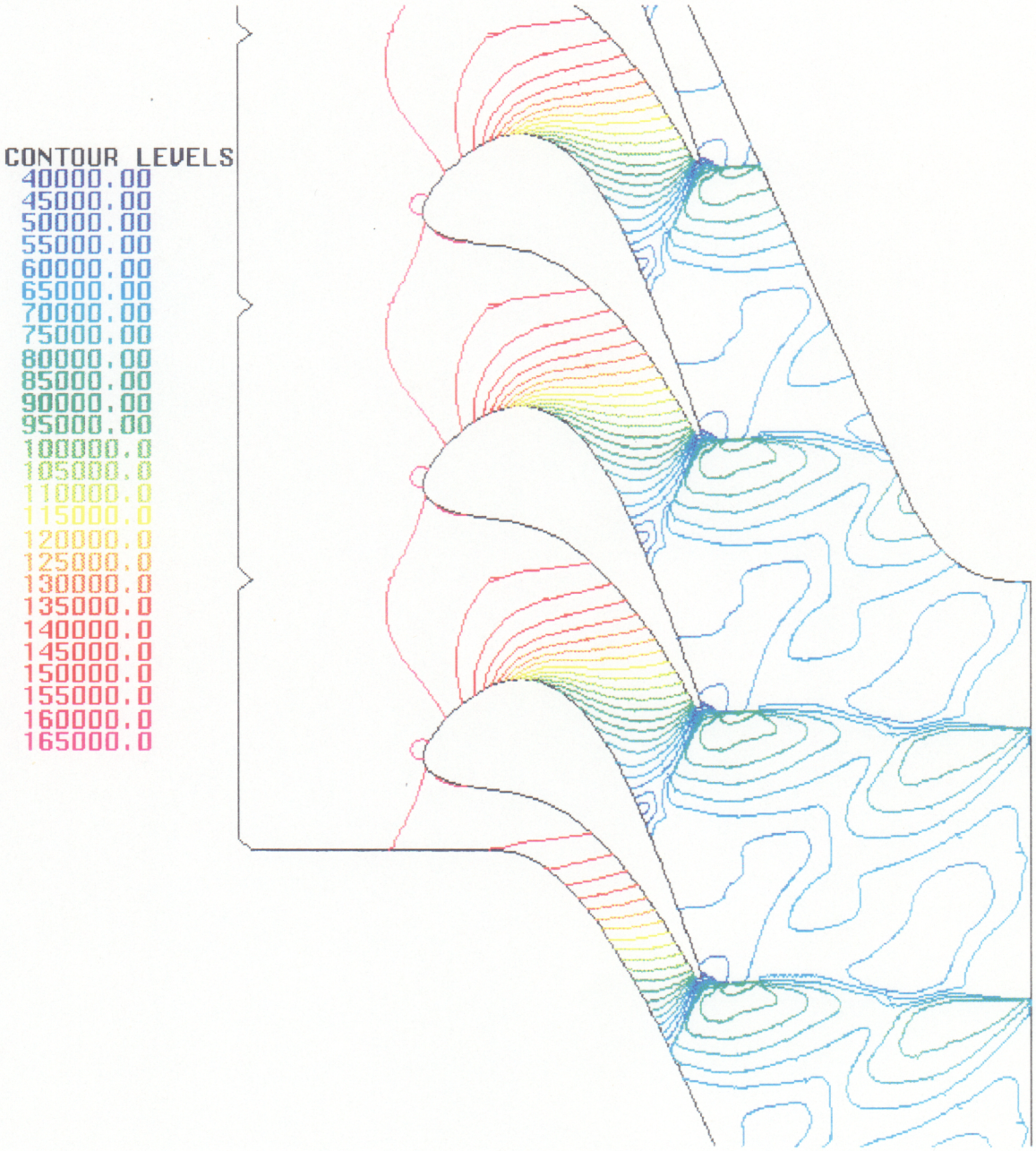


Fig.4.27 Pressure contours [Pa] for $M_e = 1.2$

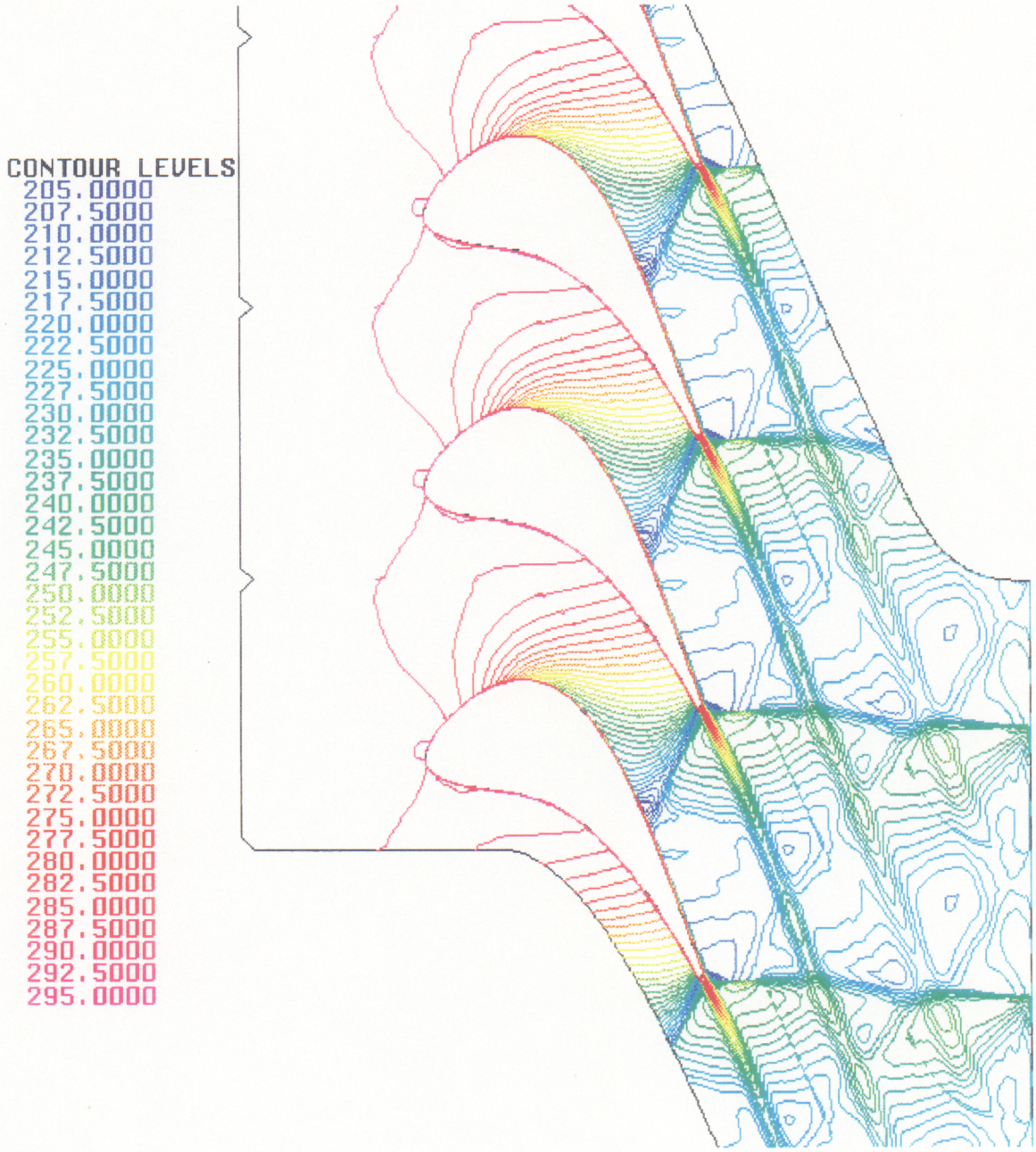


Fig.4.28 Temperature contours [°K] for $M_e = 1.2$

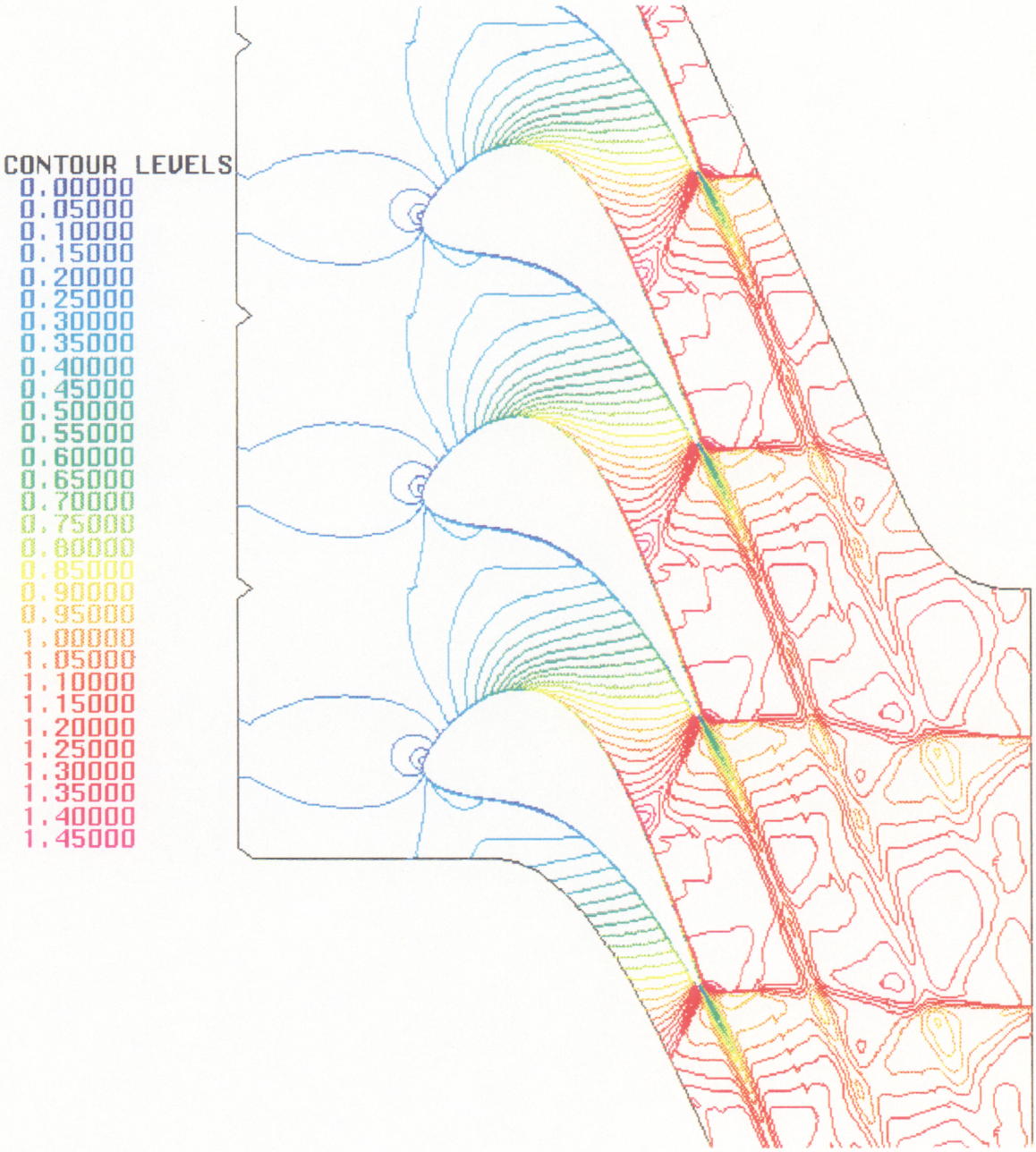


Fig.4.29 Mach number contours for $M_e = 1.2$

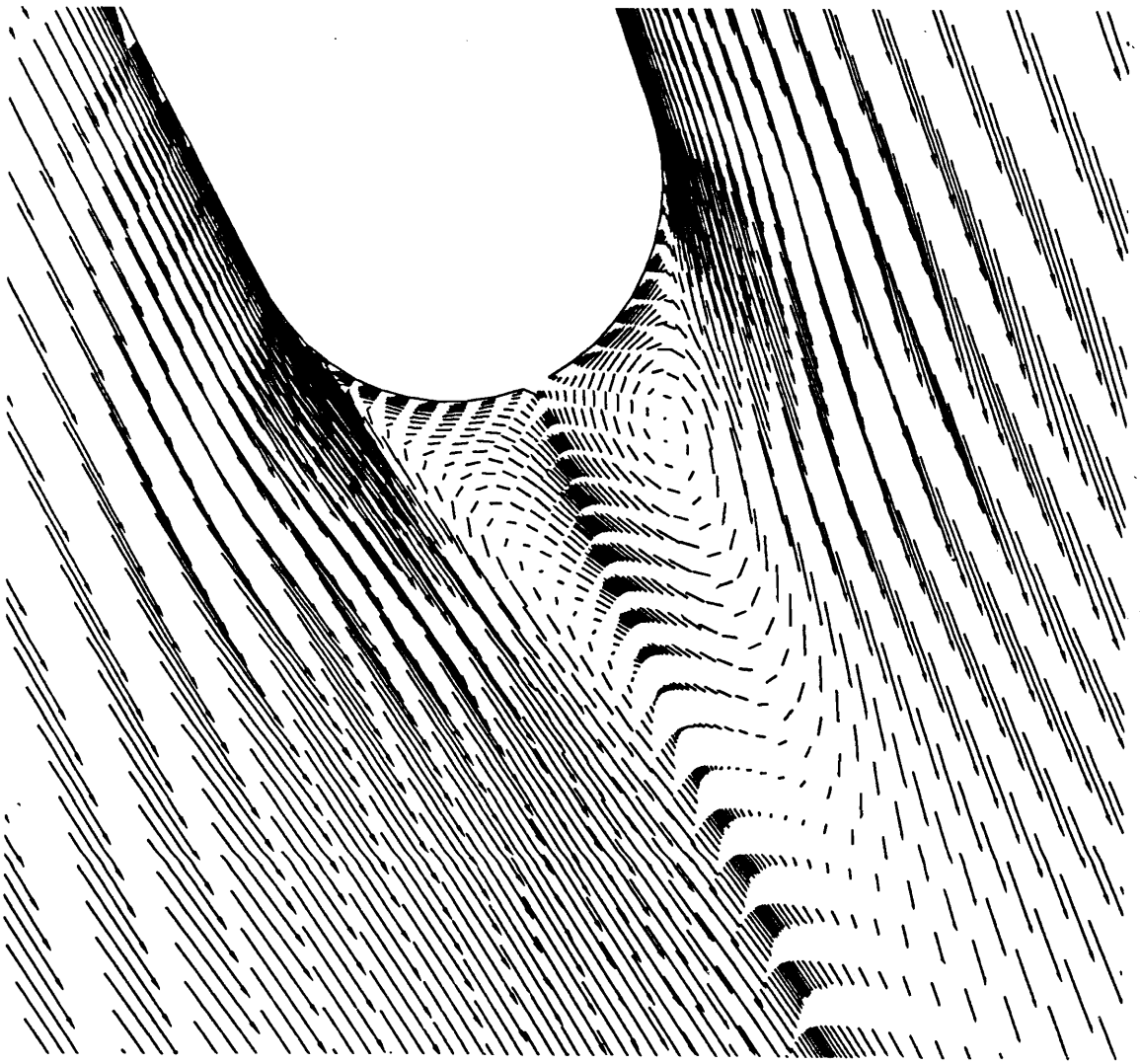


Fig.4.30 Velocity vectors around the trailing edge for $M_e = 1.2$

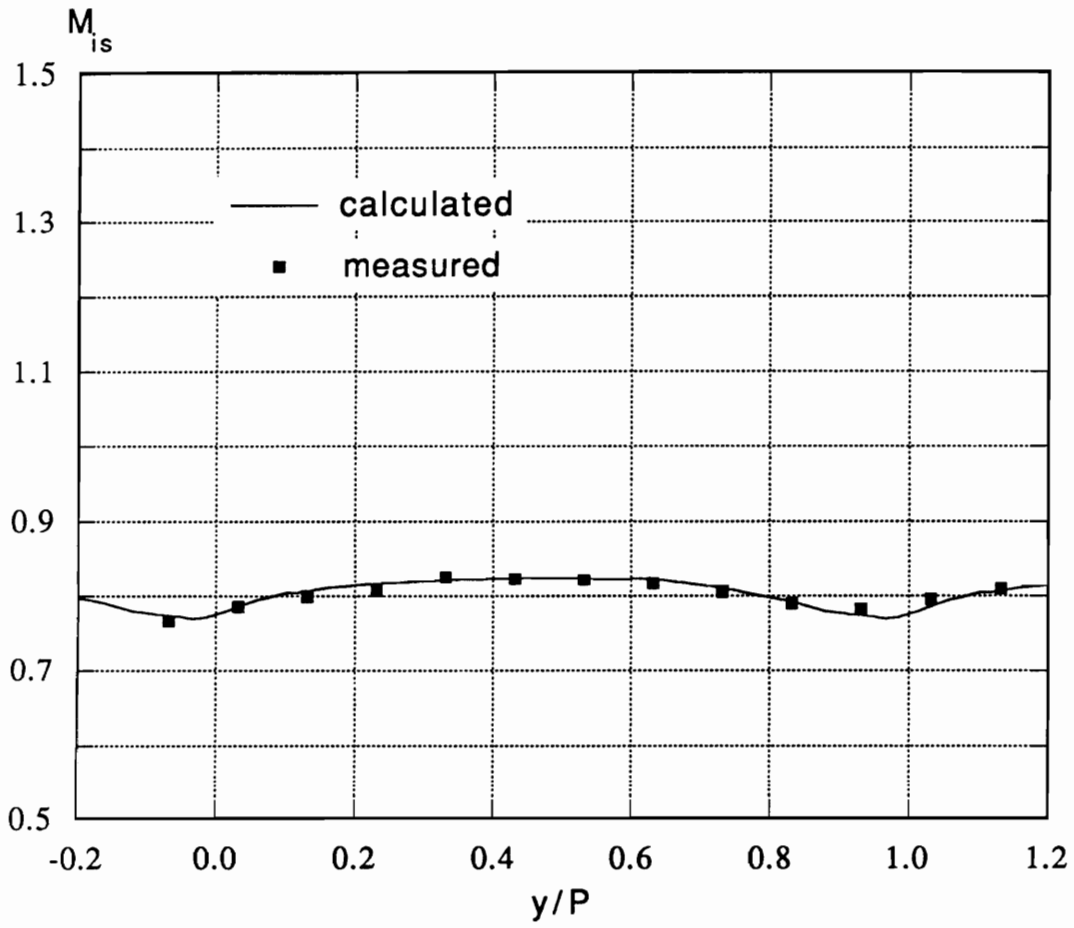


Fig.4.31 Isentropic Mach number profiles, $M_e = 0.8$, Station 1

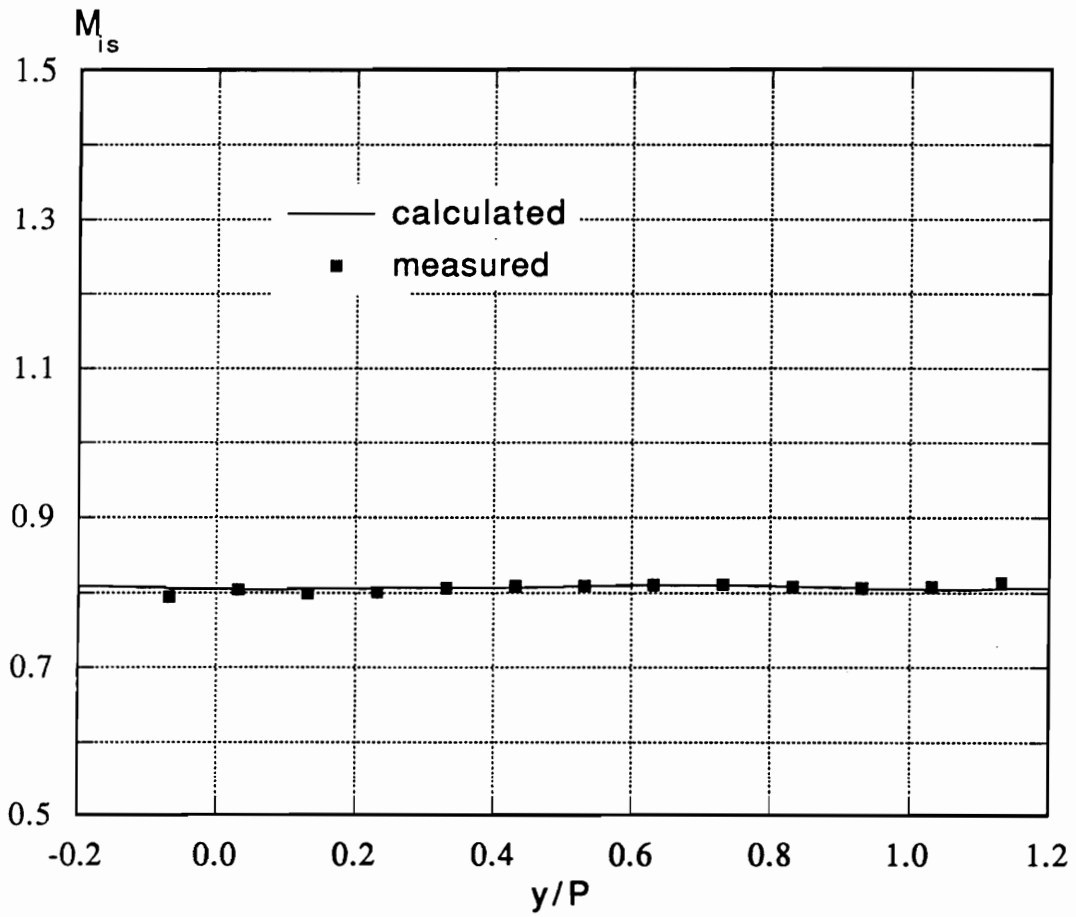


Fig.4.32 Isentropic Mach number profiles, $M_e = 0.8$, Station 2

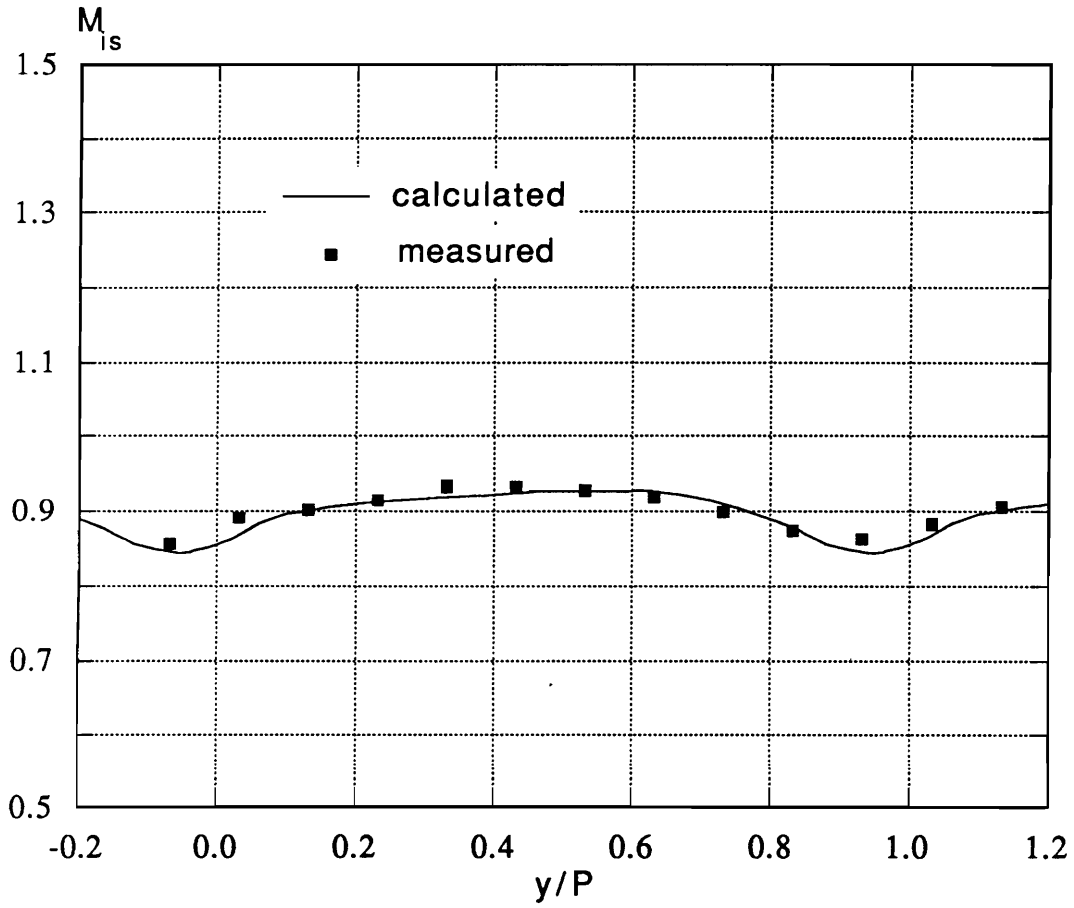


Fig.4.33 Isentropic Mach number profiles, $M_e = 0.9$, Station 1

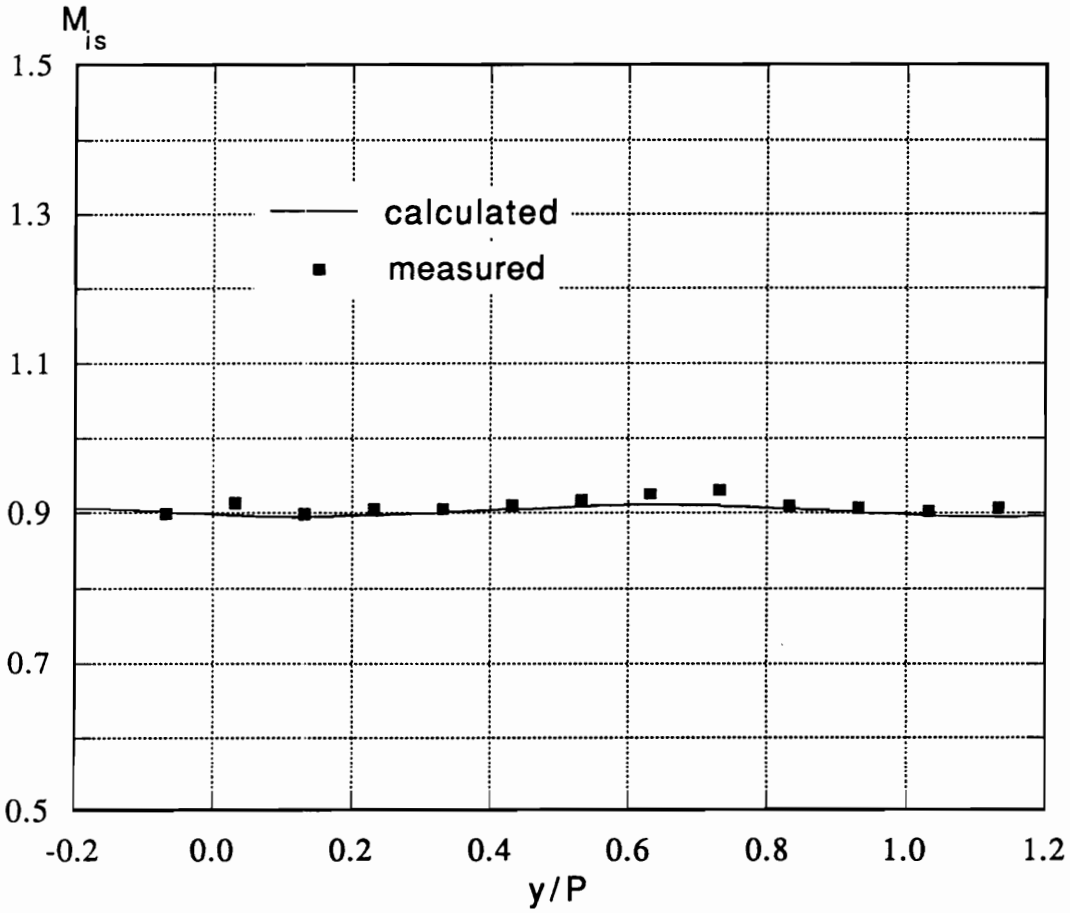


Fig.4.34 Isentropic Mach number profiles, $M_e = 0.9$, Station 2

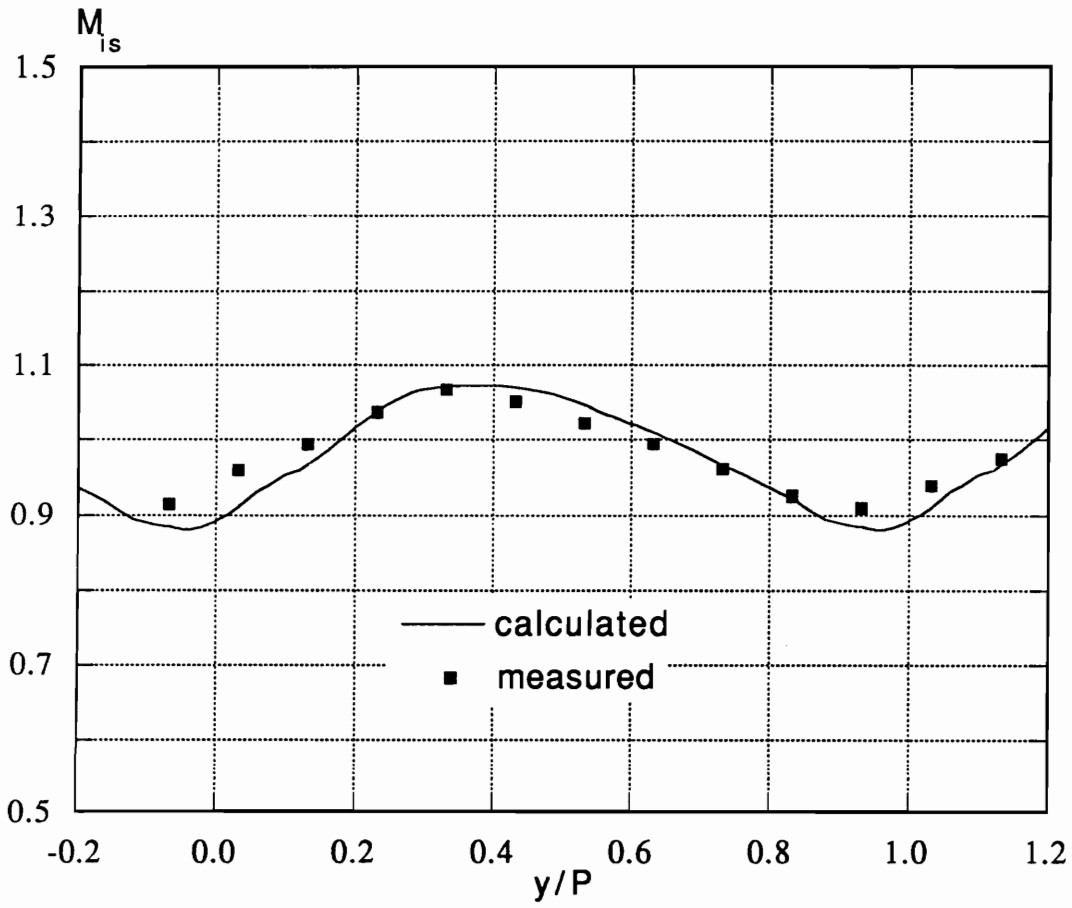


Fig.4.35 Isentropic Mach number profiles, $M_e = 1.0$, Station 1

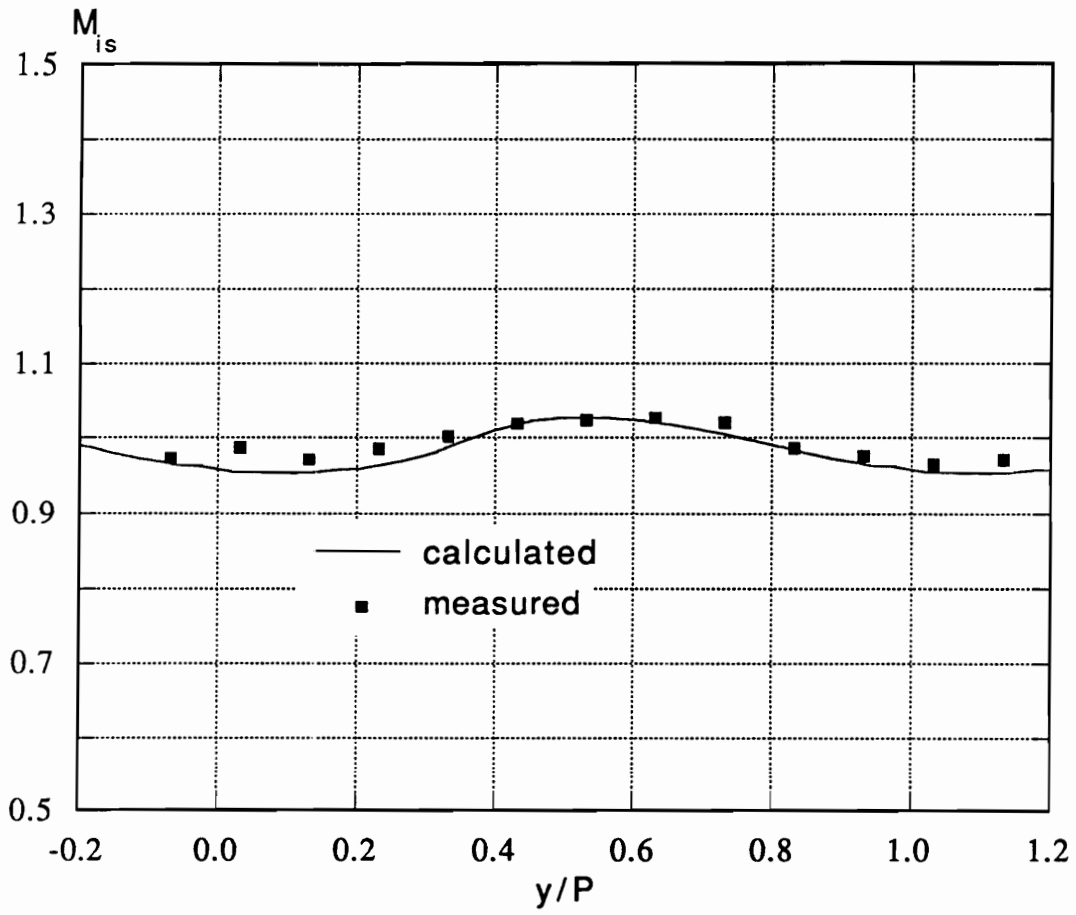


Fig.4.36 Isentropic Mach number profiles, $M_e = 1.0$, Station 2

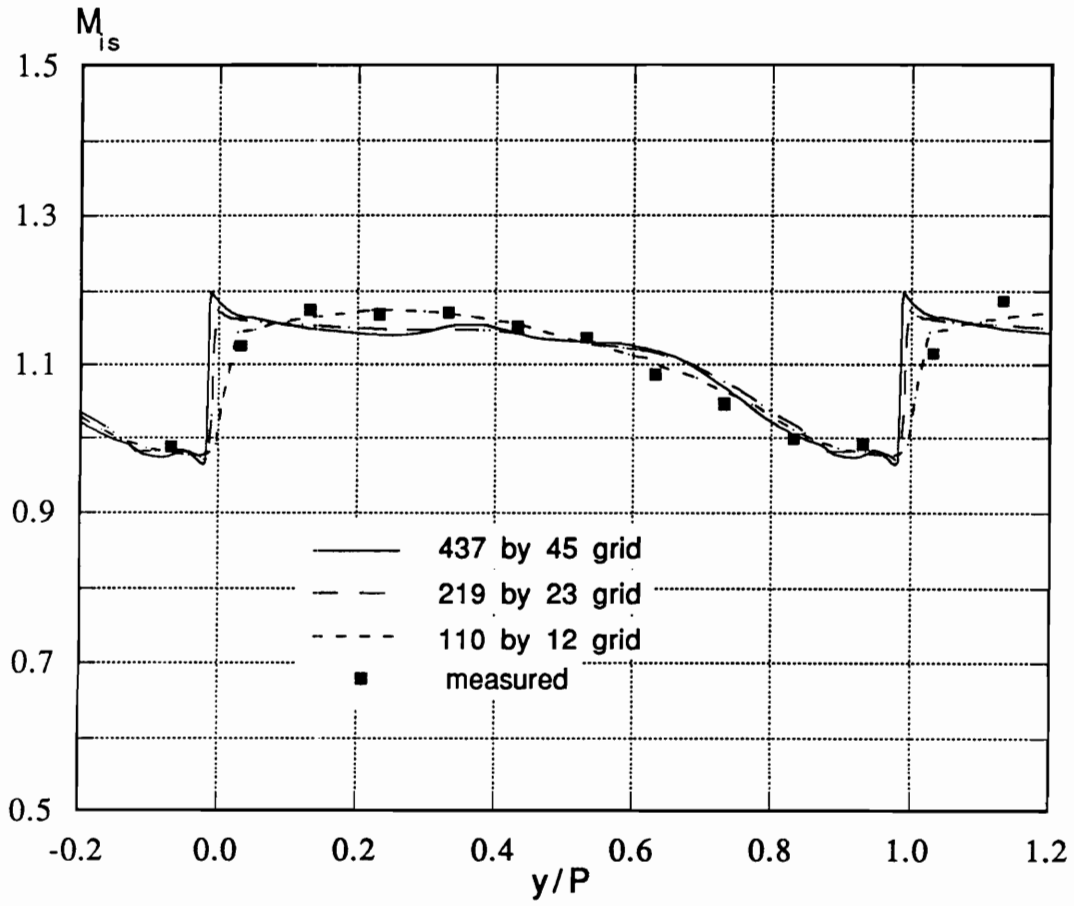


Fig.4.37 Isentropic Mach number profiles, $M_e = 1.1$, Station 1

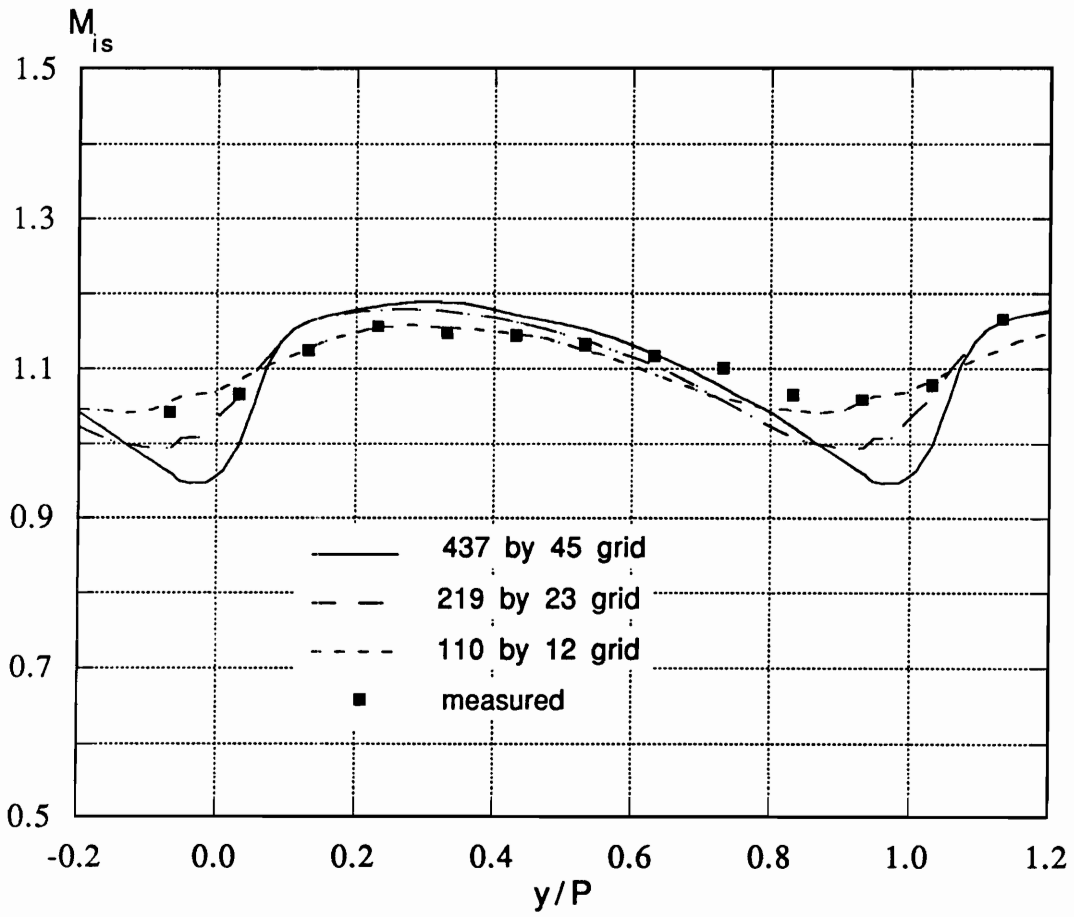


Fig.4.38 Isentropic Mach number profiles, $M_e = 1.1$, Station 2

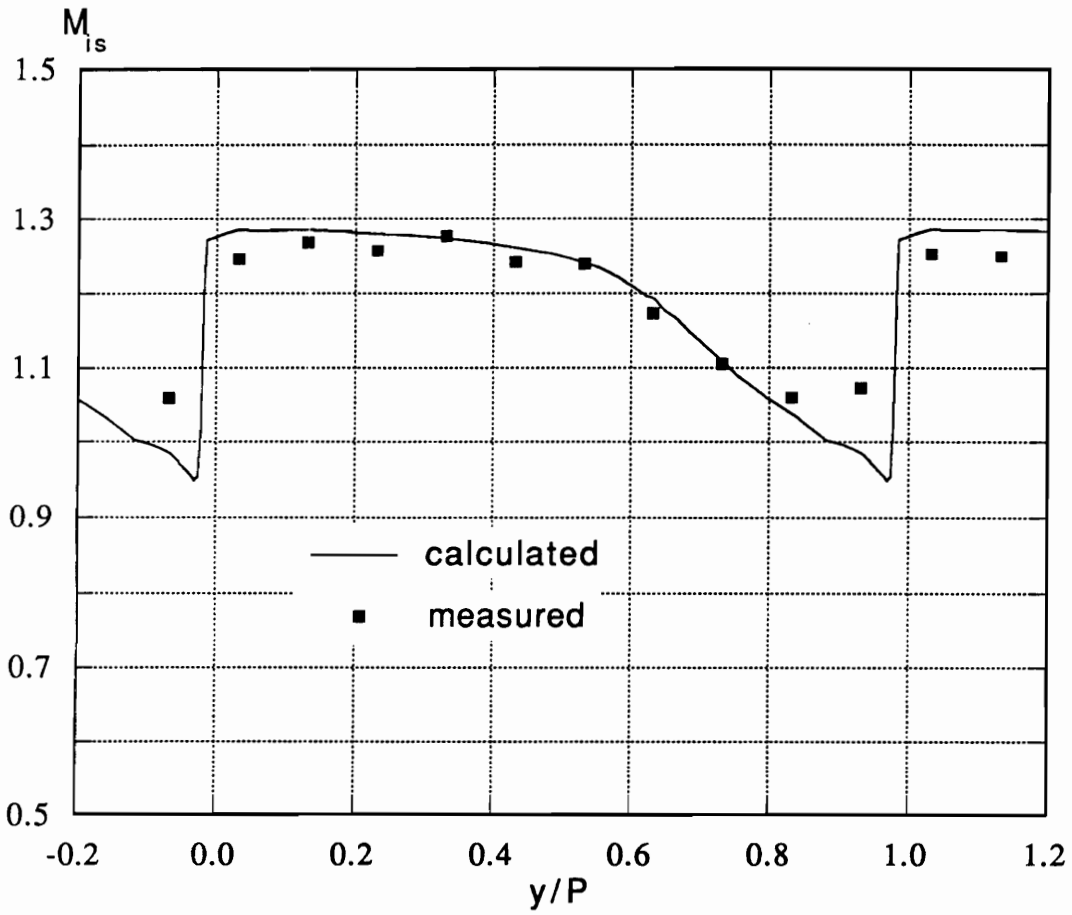


Fig.4.39 Isentropic Mach number profiles, $M_e = 1.2$, Station 1

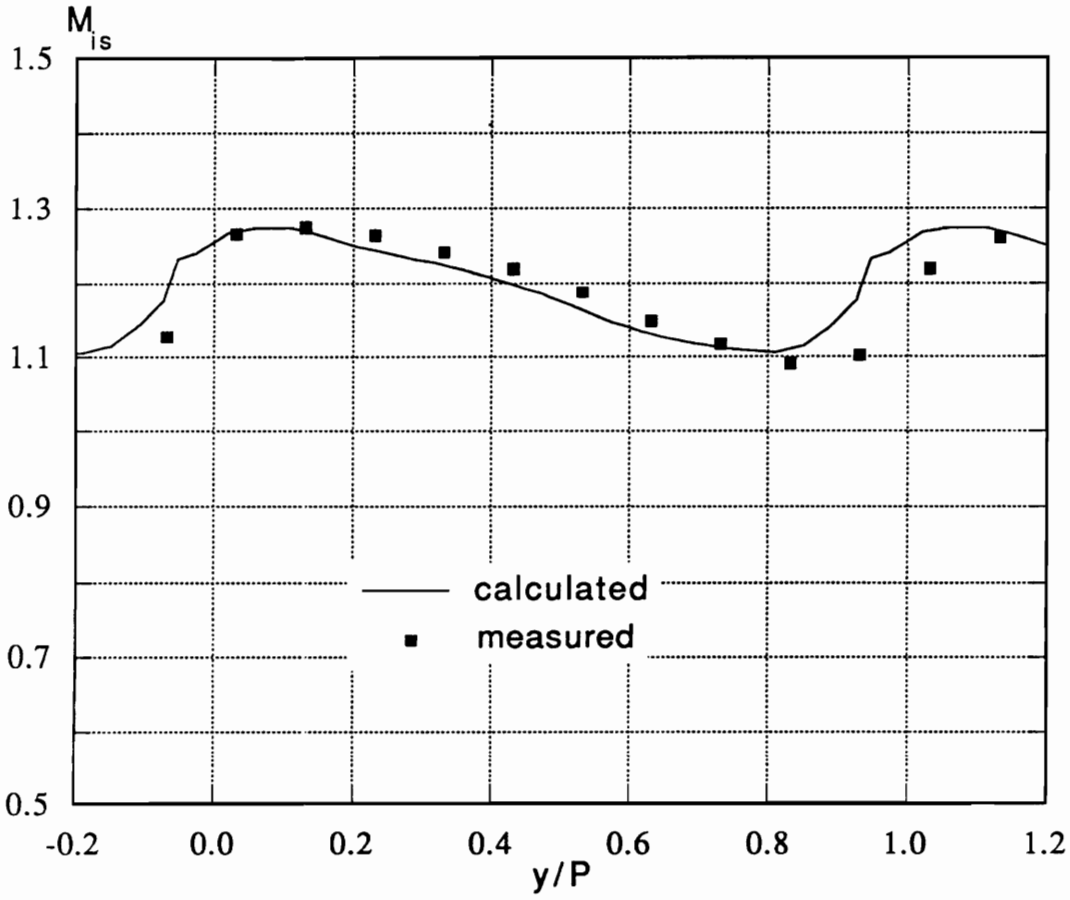


Fig.4.40 Isentropic Mach number profiles, $M_e = 1.2$, Station 2

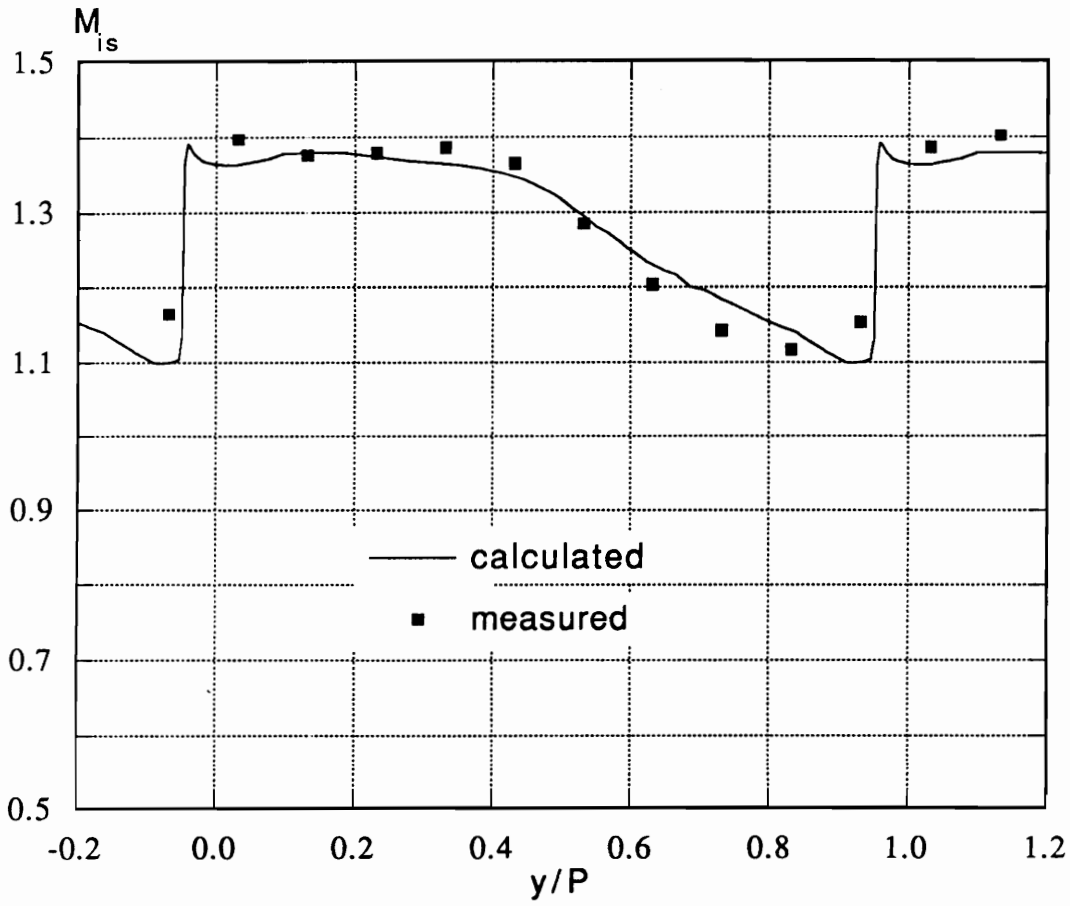


Fig.4.41 Isentropic Mach number profiles, $M_e = 1.28$, Station 1

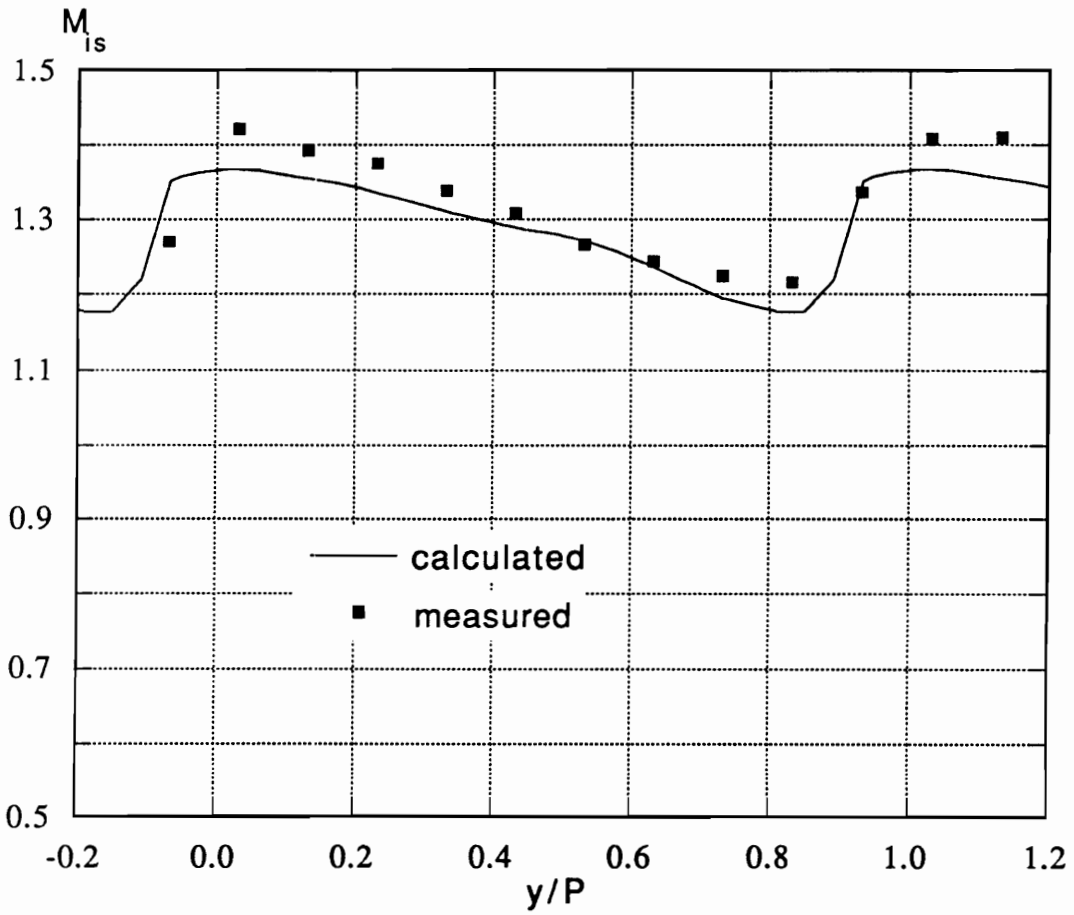


Fig.4.42 Isentropic Mach number profiles, $M_e = 1.28$, Station 2

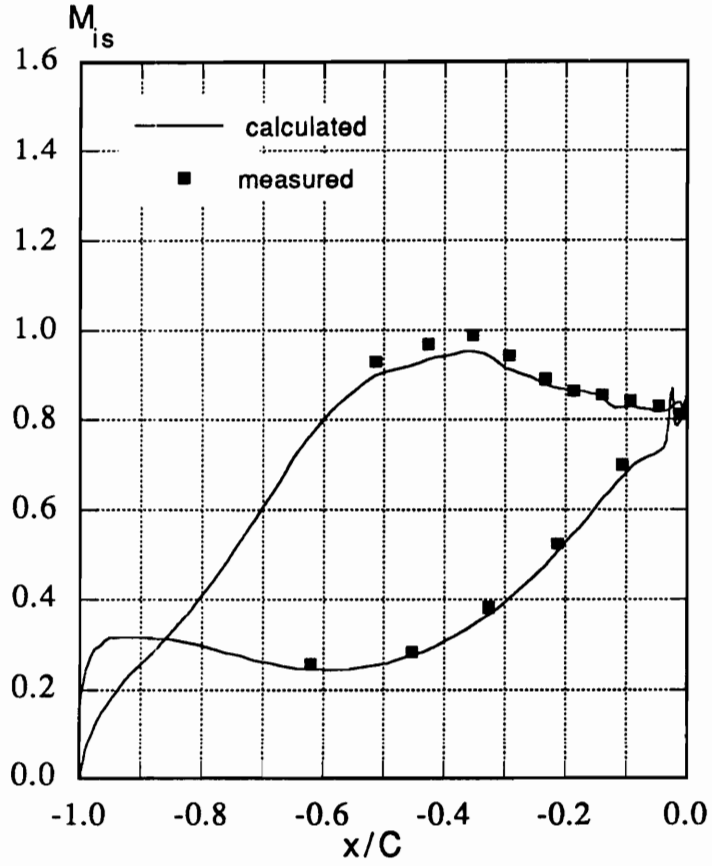


Fig.4.43 Blade surface isentropic Mach numbers, $M_e = 0.8$

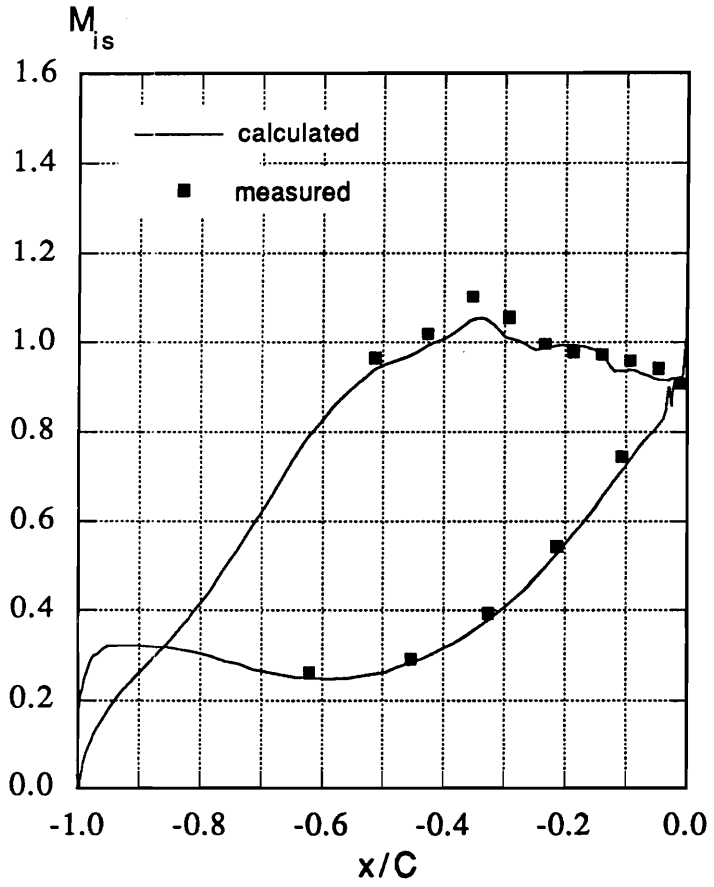


Fig.4.44 Blade surface isentropic Mach numbers, $M_e = 0.9$

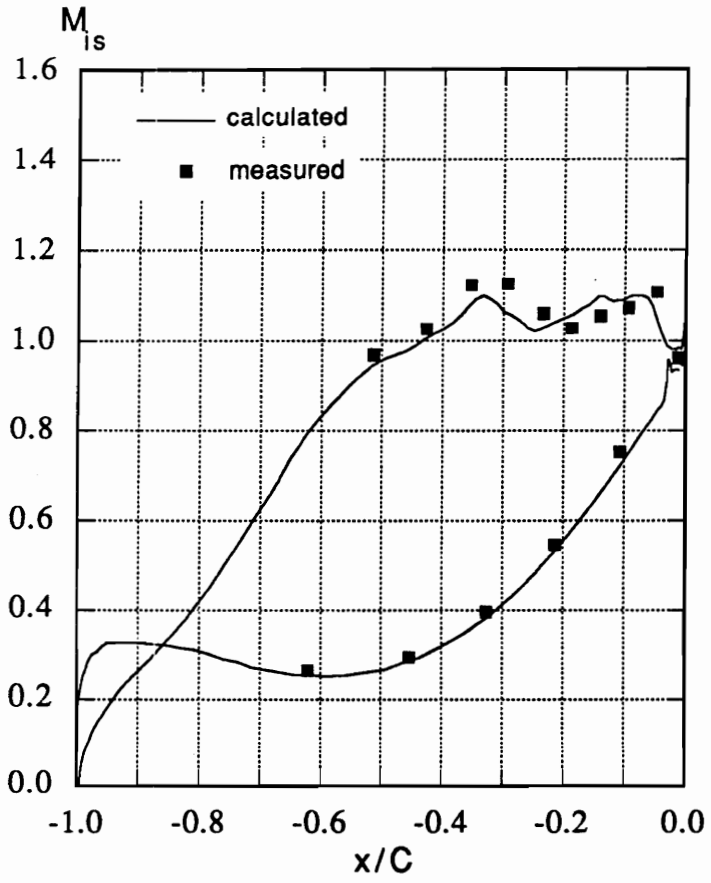


Fig.4.45 Blade surface isentropic Mach numbers, $M_e = 1.0$

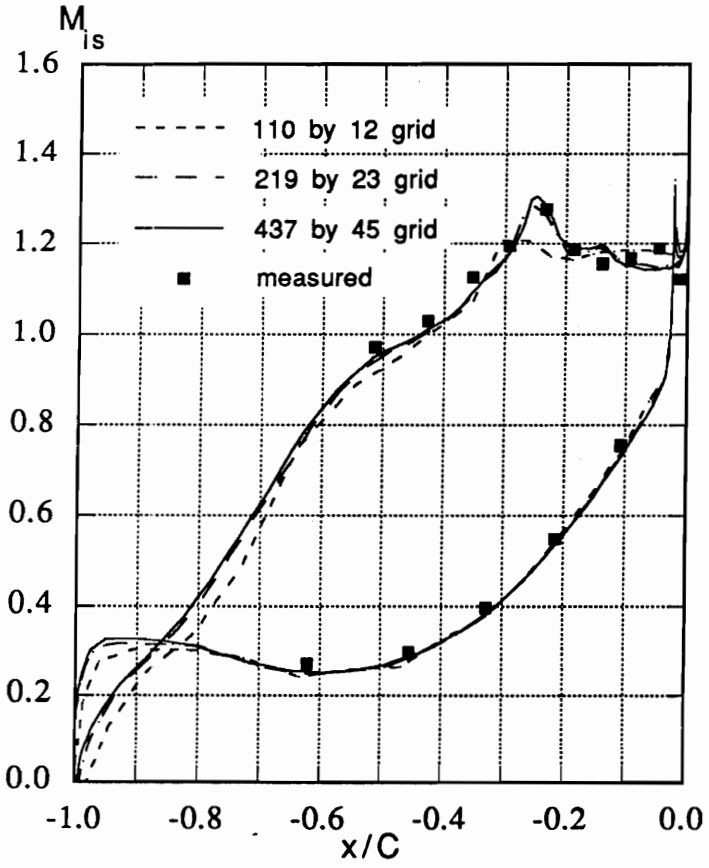


Fig.4.46 Blade surface isentropic Mach numbers, $M_e = 1.1$

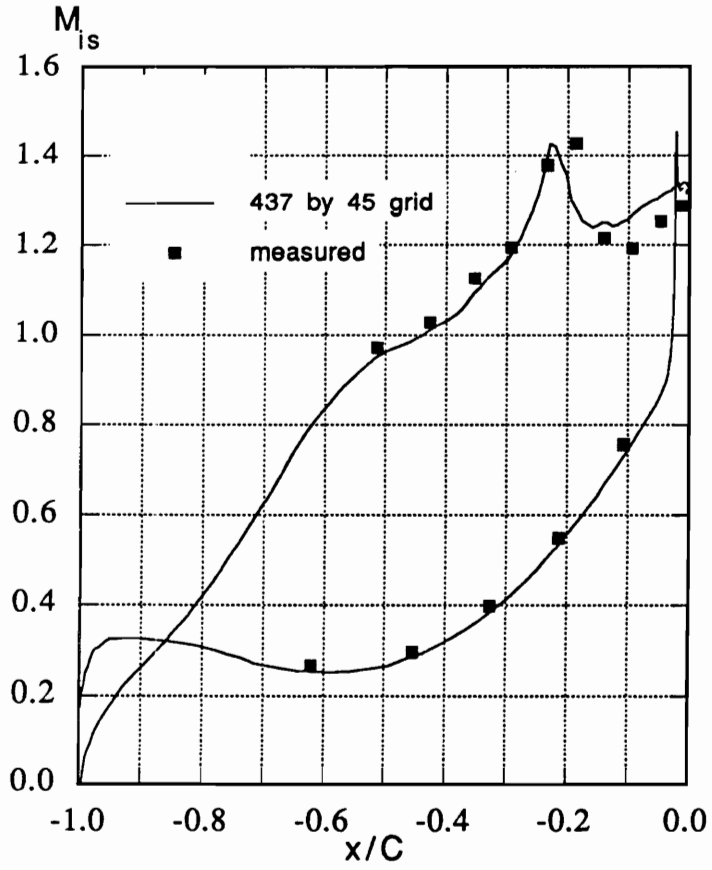


Fig.4.47 Blade surface isentropic Mach numbers, $M_e = 1.2$

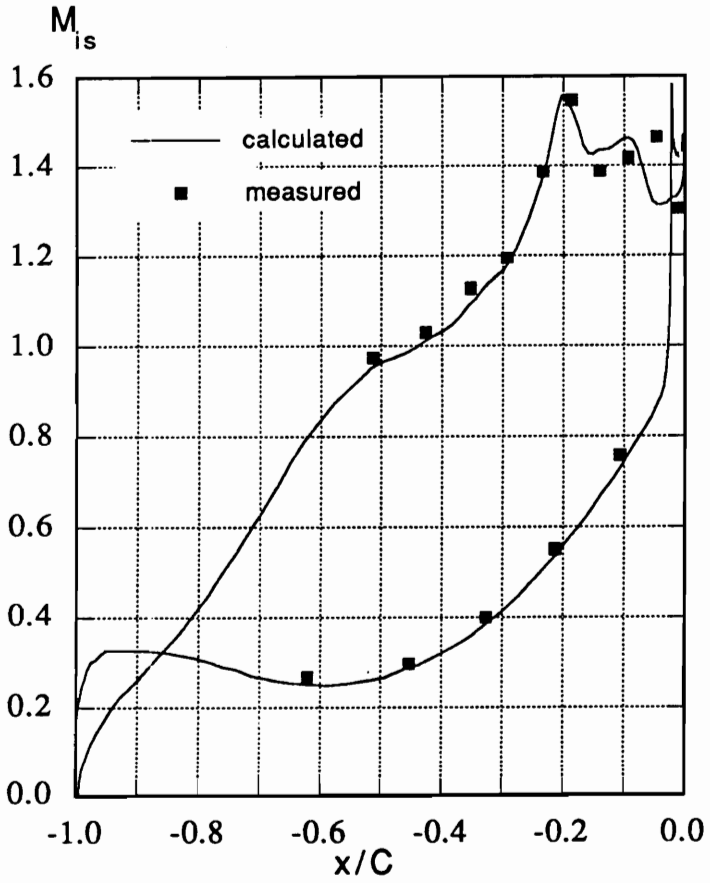


Fig.4.48 Blade surface isentropic Mach numbers, $M_e = 1.28$

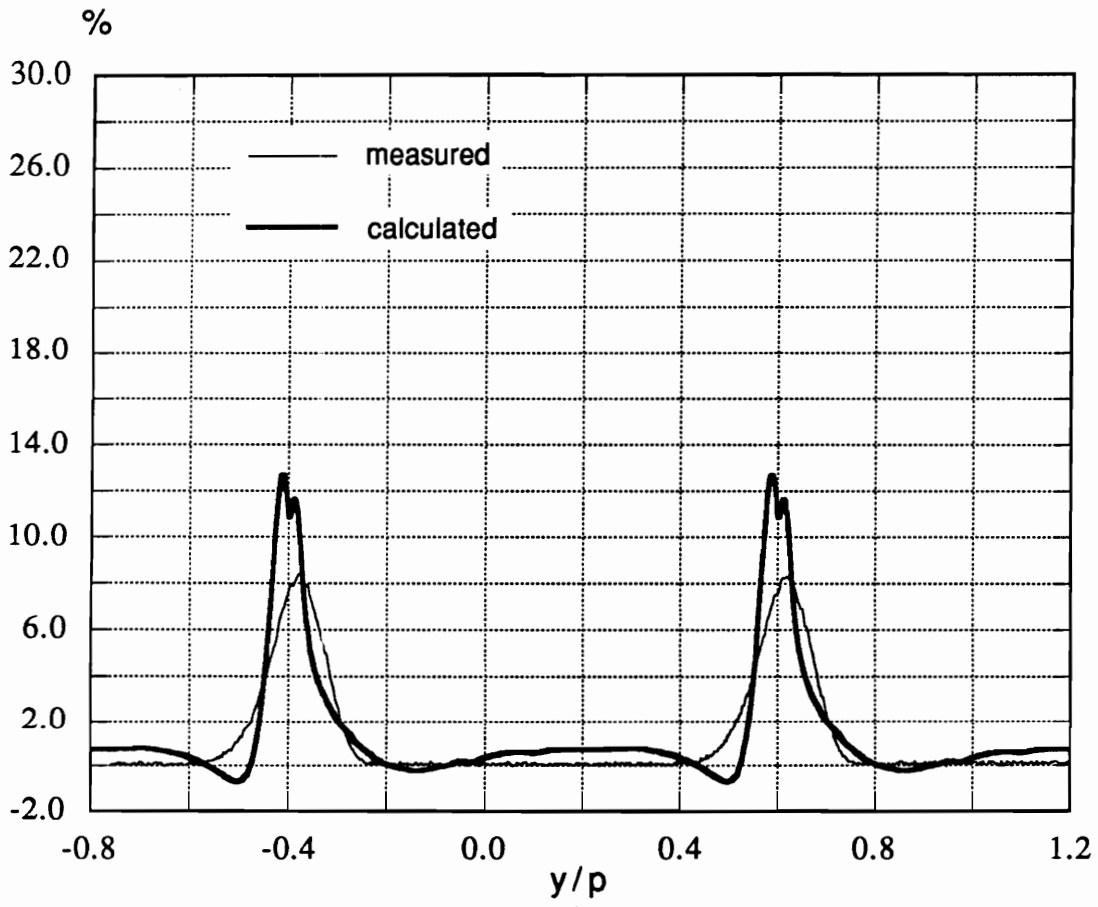


Fig.4.49 Pitot pressure drop, $M_e = 0.8$, Station 1

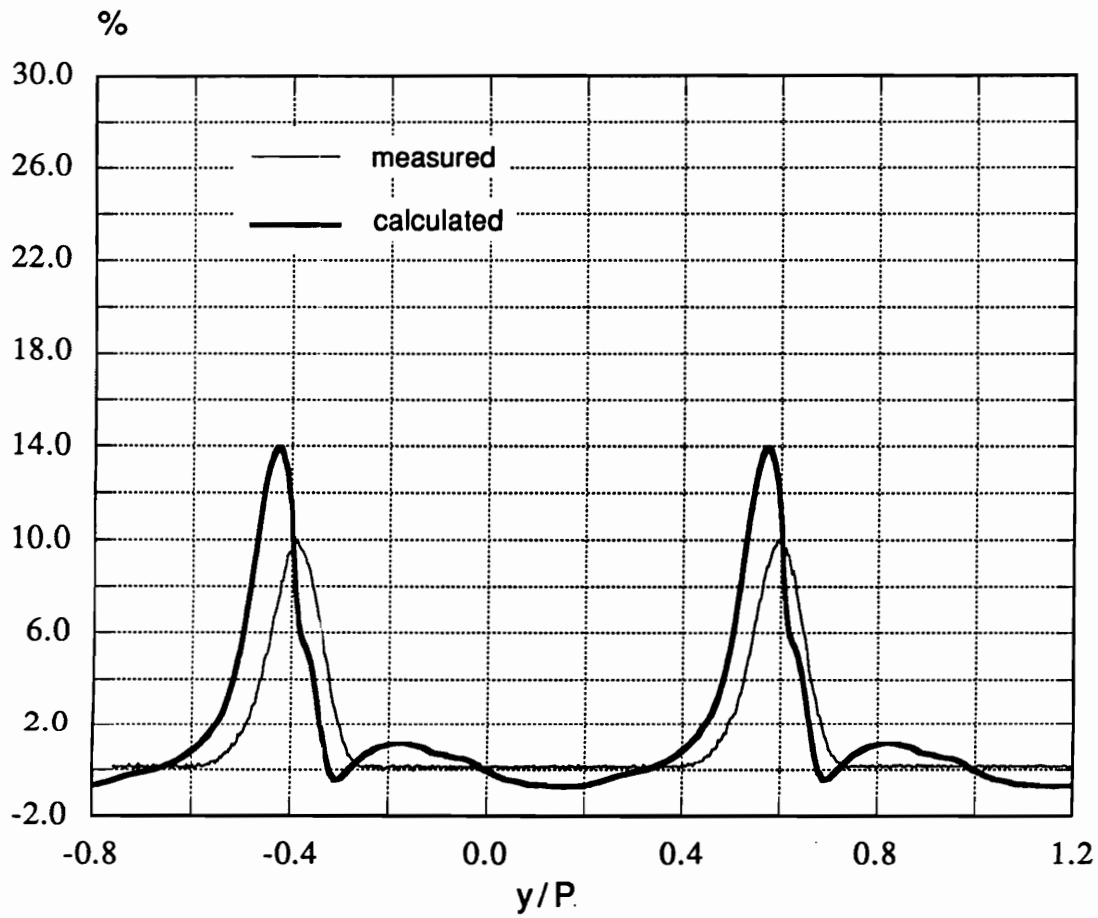


Fig.4.50 Pitot pressure drop, $M_e = 0.9$, Station 1

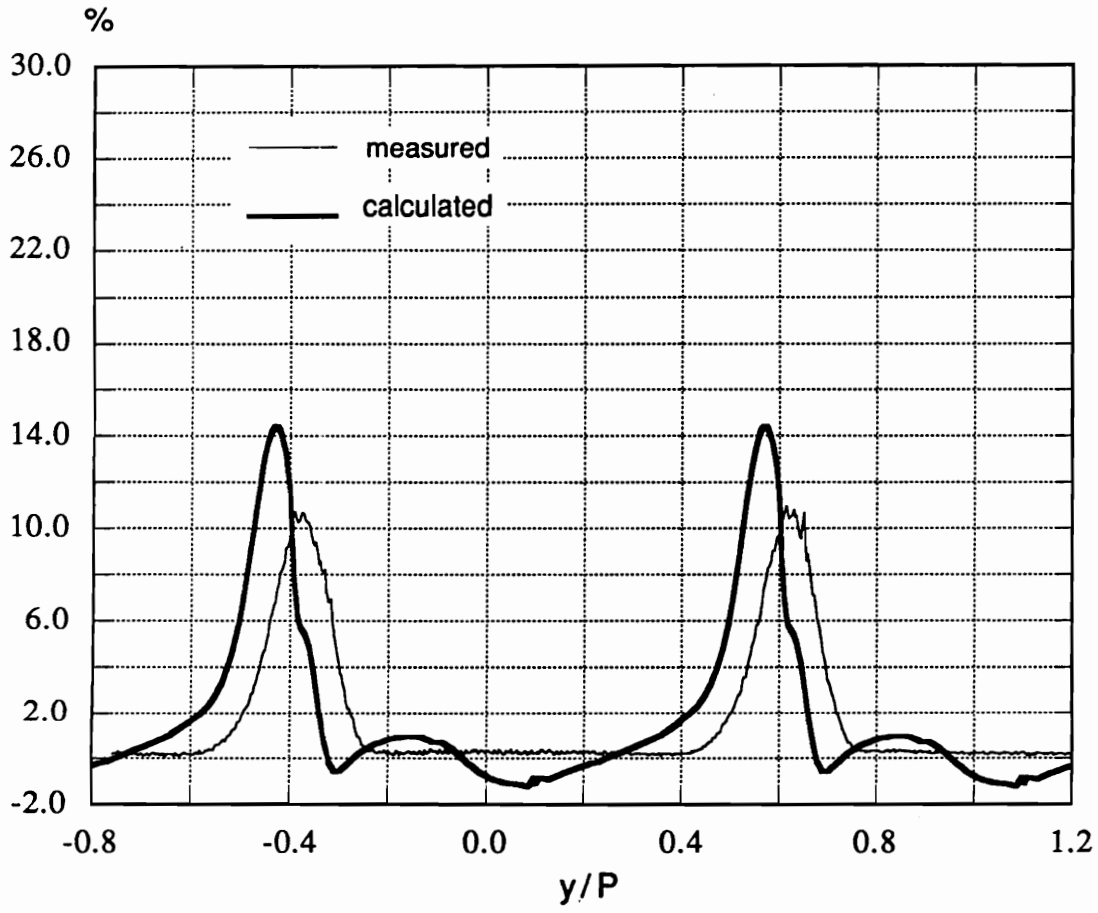


Fig.4.51 Pitot pressure drop, $M_e = 1.0$, Station 1

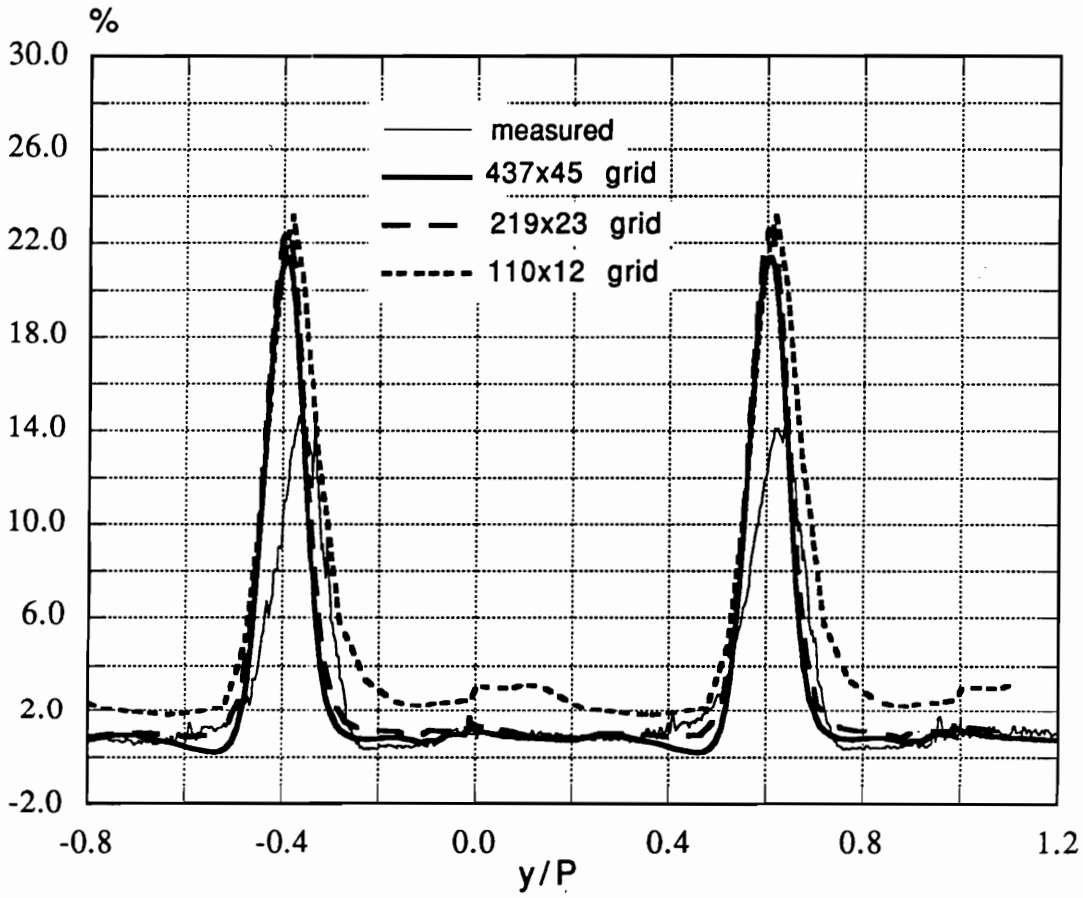


Fig.4.52 Pitot pressure drop, $M_e = 1.1$, Station 1

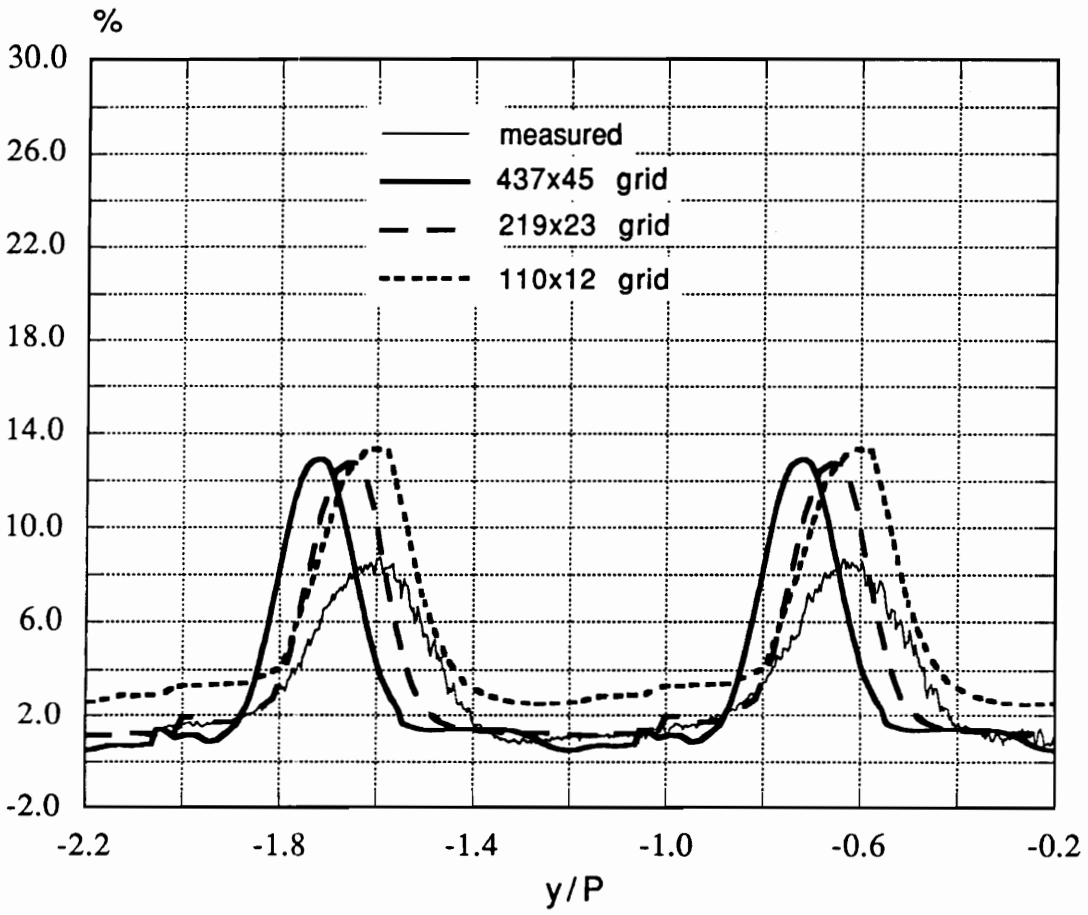


Fig.4.53 Pitot pressure drop, $M_e = 1.1$, Station 2

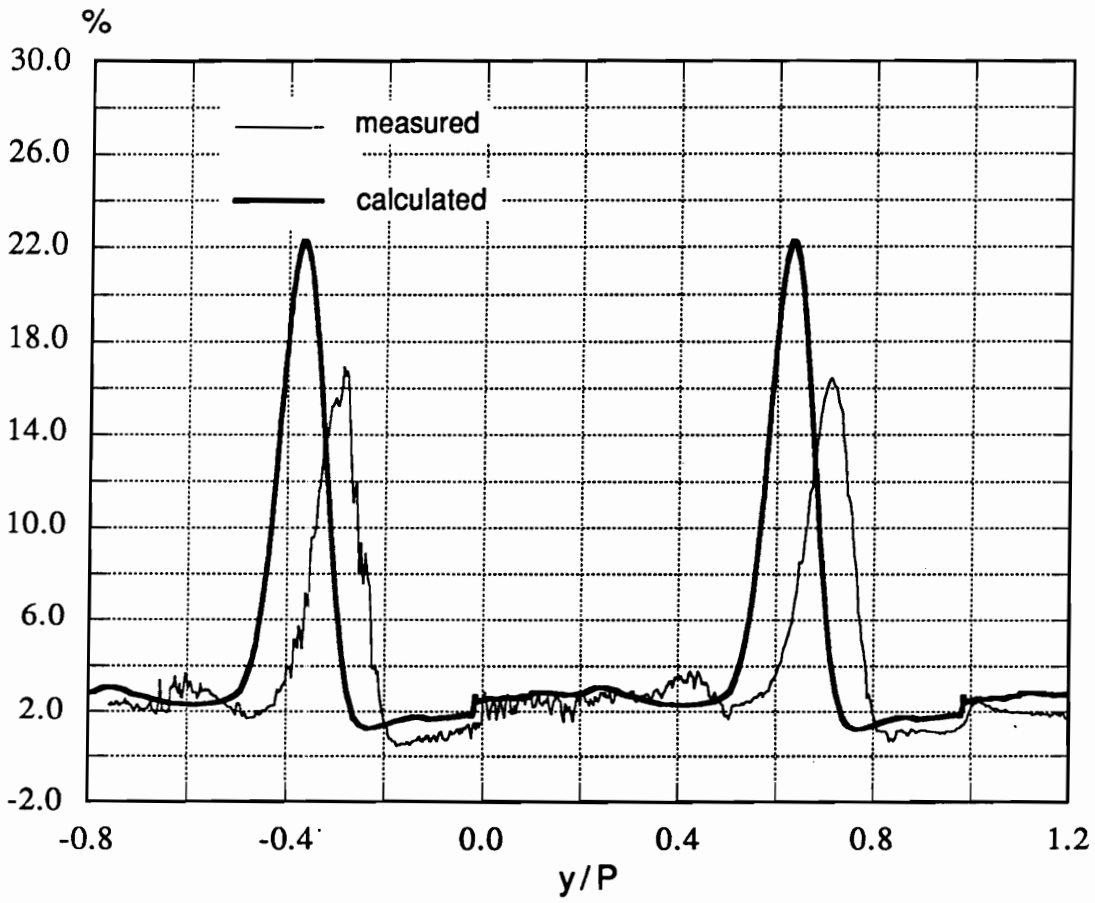


Fig.4.54 Pitot pressure drop, $M_e = 1.2$, Station 1

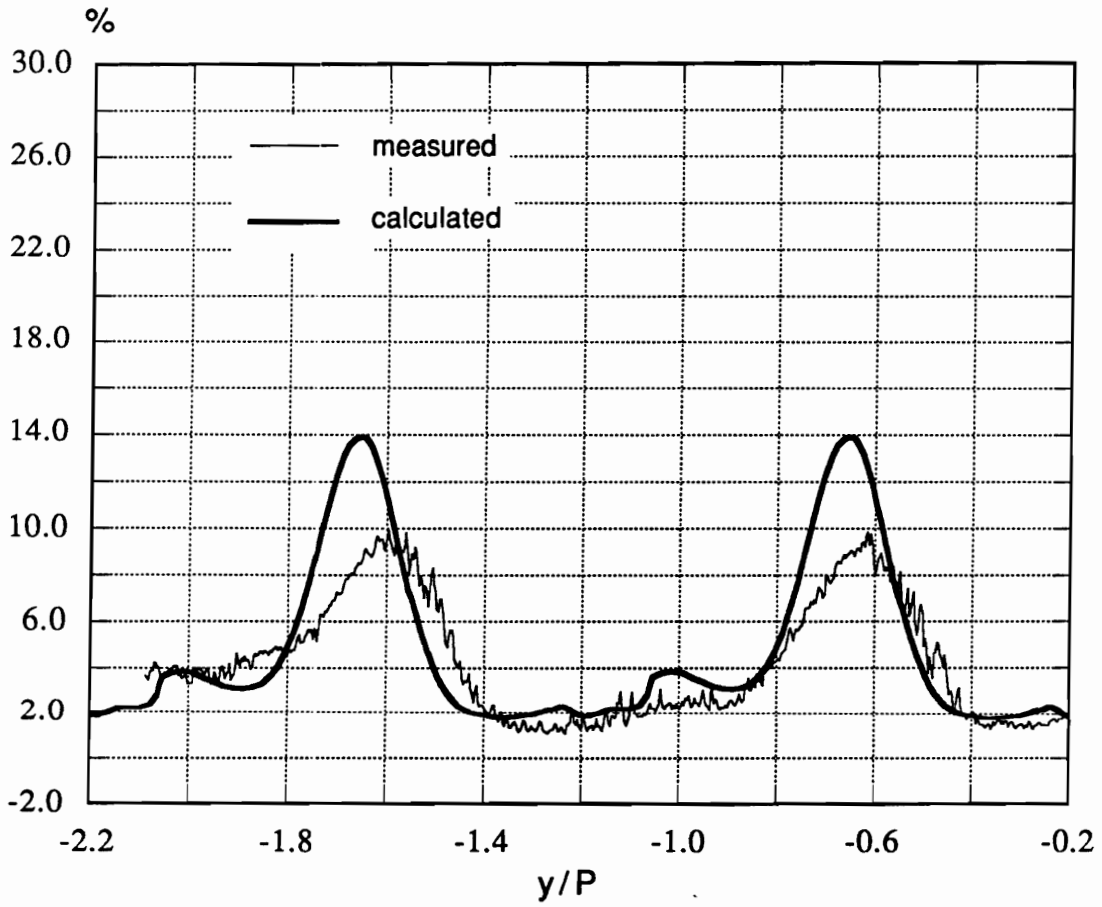


Fig.4.55 Pitot pressure drop, $M_e = 1.2$, Station 2

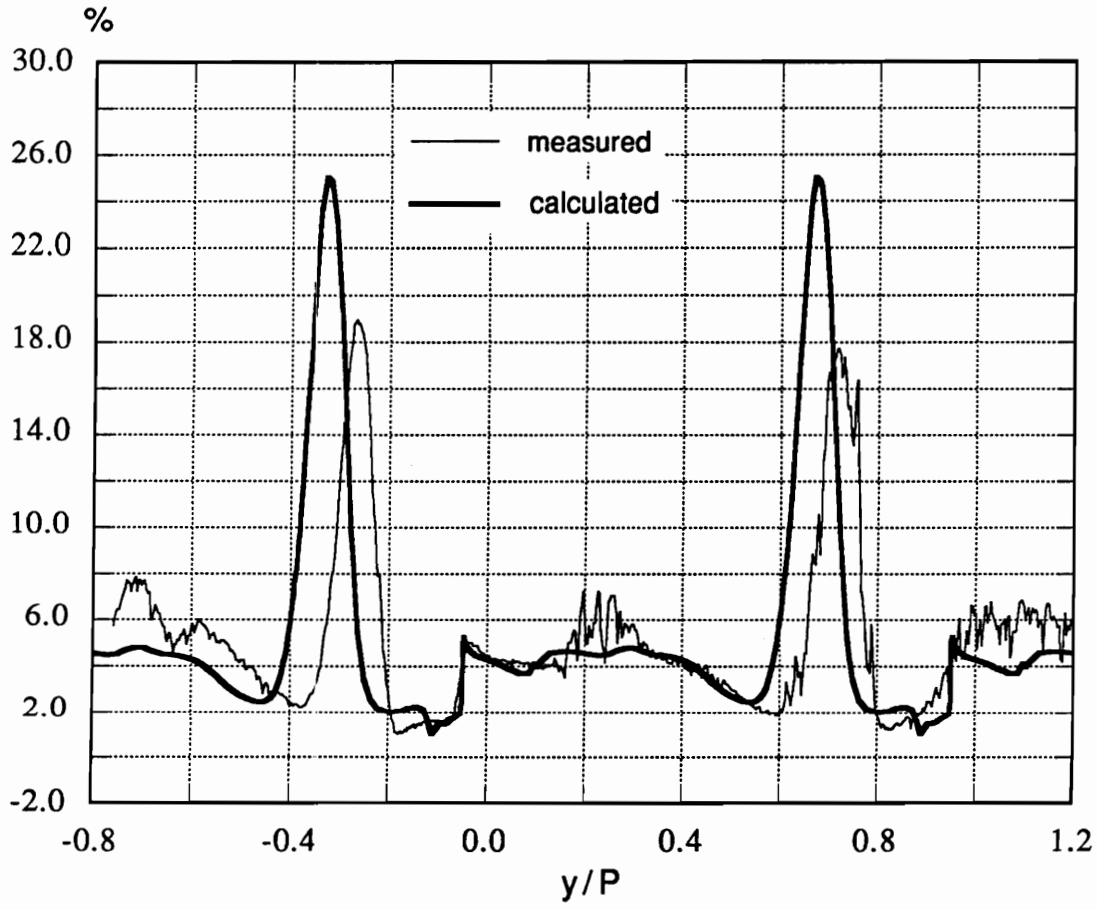


Fig.4.56 Pitot pressure drop, $M_e = 1.28$, Station 1

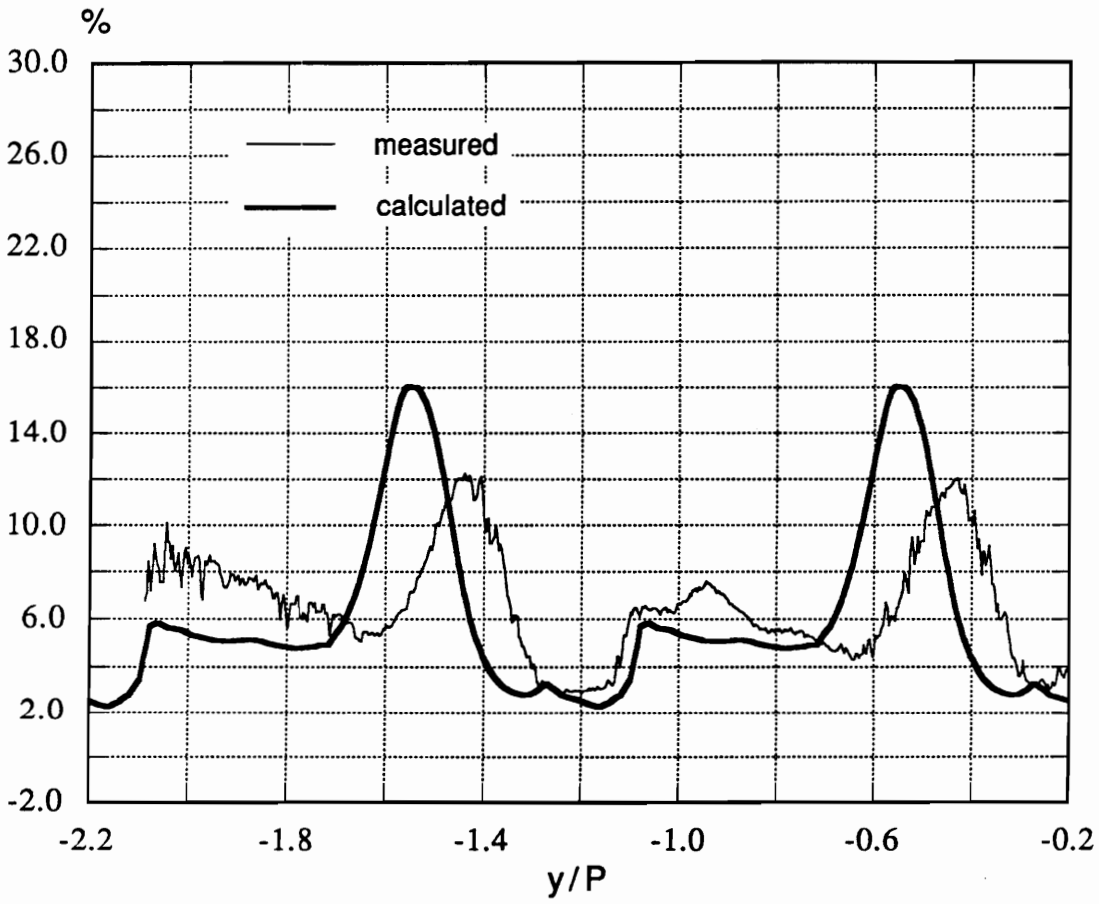


Fig.4.57 Pitot pressure drop, $M_e = 1.28$, Station 2

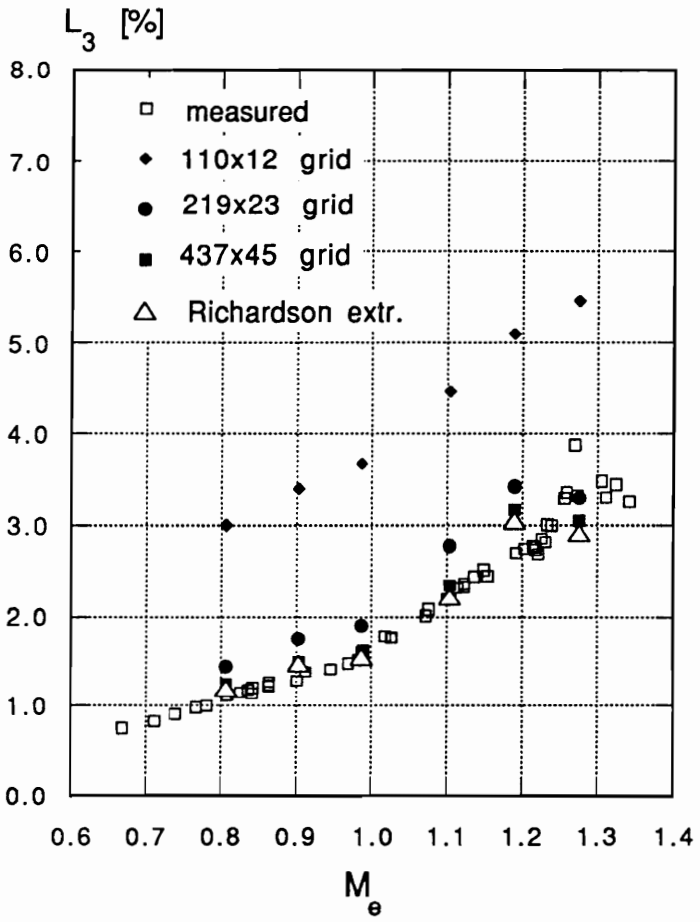


Fig.4.58 Measured and calculated loss coefficients, Station 1

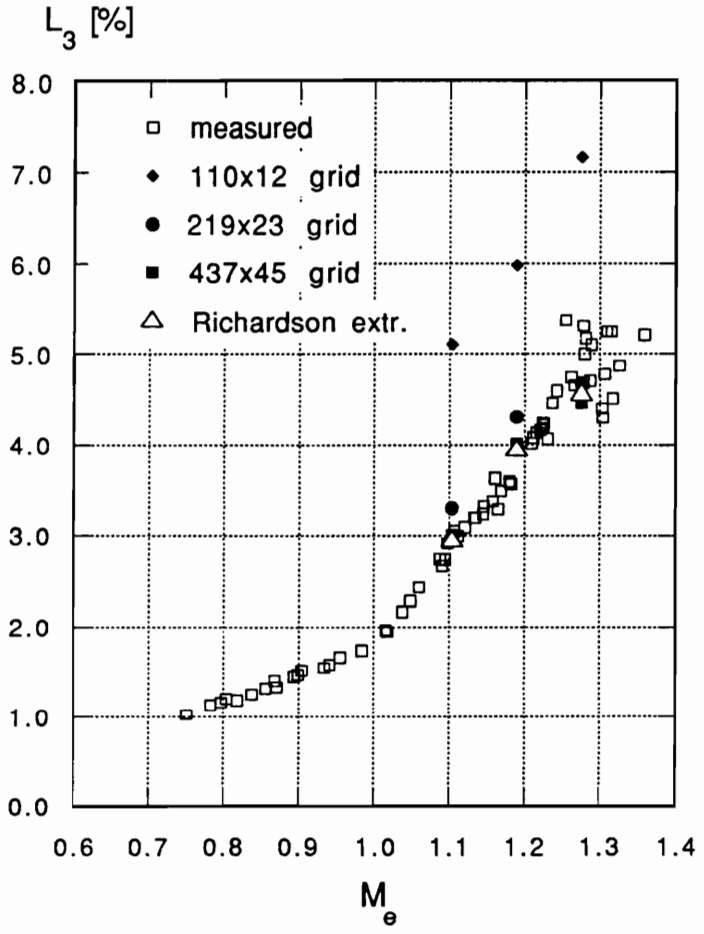


Fig.4.59 Measured and calculated loss coefficient, Station 2

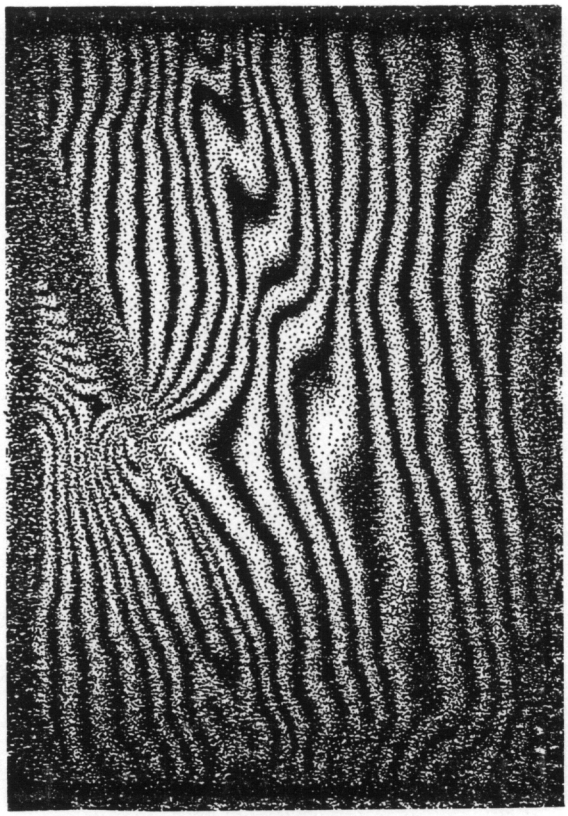


Fig.4.60 Interferogram, $M_e = 0.8$, setup of Fig.3.17b

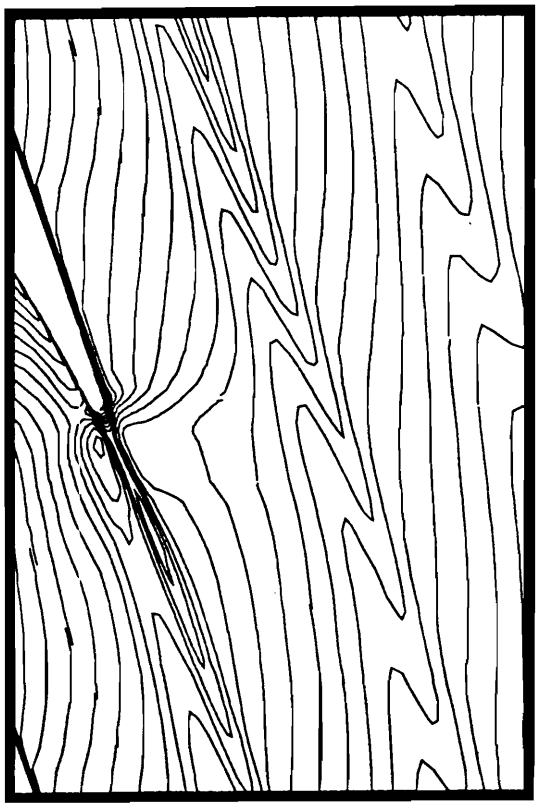


Fig.4.61 Numerical interferogram, $M_e = 0.8$, setup of Fig.3.17b



Fig.4.62 Interferogram, $M_e = 0.9$, setup of Fig.3.17b

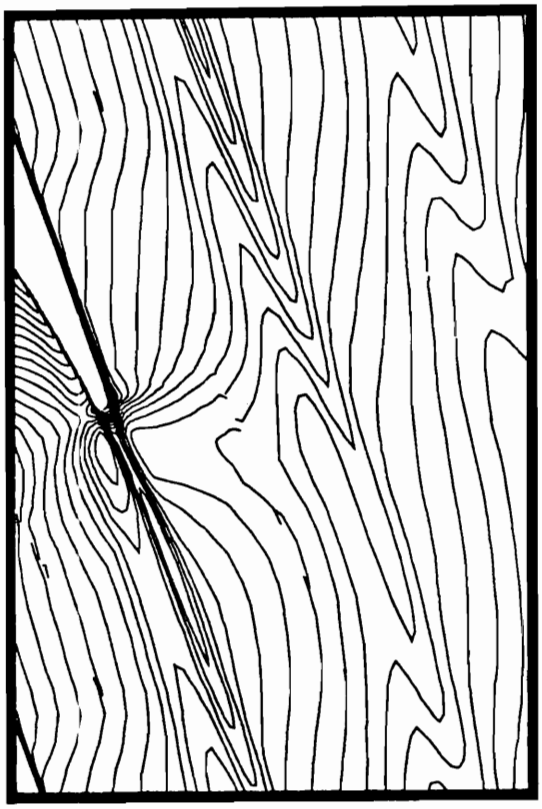


Fig.4.63 Numerical interferogram, $M_e = 0.9$, setup of Fig.3.17b



Fig.4.64 Interferogram, $M_e = 1.0$, setup of Fig.3.17b

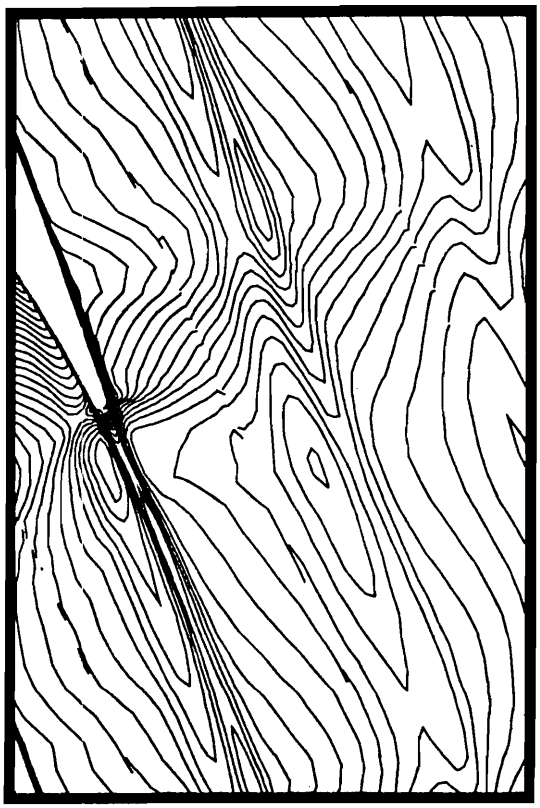


Fig.4.65 Numerical interferogram, $M_e = 1.0$, setup of Fig.3.17b

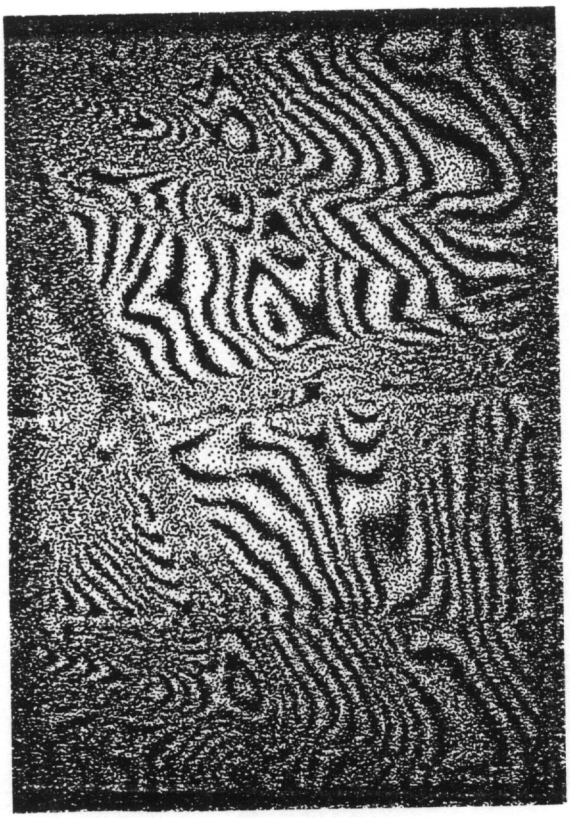


Fig.4.66 Interferogram, $M_e = 1.1$, setup of Fig.3.17b

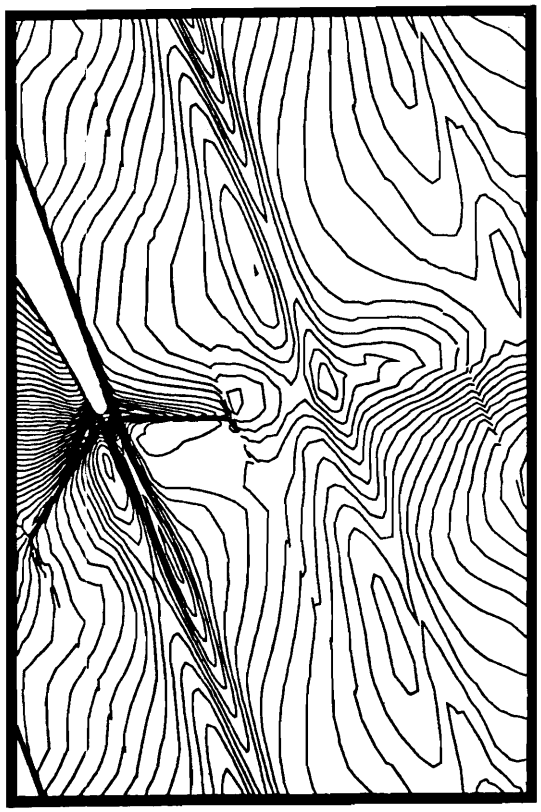


Fig.4.67 Numerical interferogram, $M_e = 1.1$, setup of Fig.3.17b



Fig.4.68 Interferogram, $M_e = 1.2$, setup of Fig.3.17b



Fig.4.69 Numerical interferogram, $M_e = 1.2$, setup of Fig.3.17b



Fig.4.70 Interferogram, $M_e = 1.28$, setup of Fig.3.17b

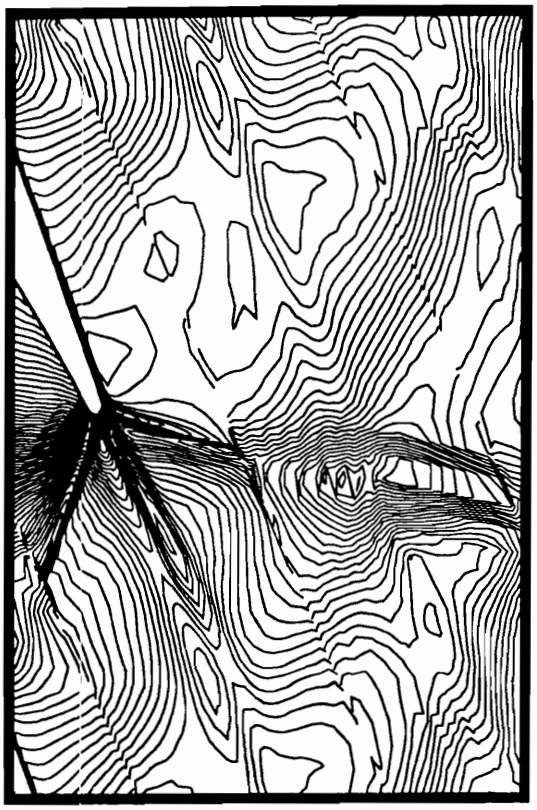


Fig.4.71 Numerical interferogram, $M_e = 1.28$, setup of Fig.3.17b



Fig.4.72 Interferogram, $M_e = 0.8$, setup of Fig.3.17d

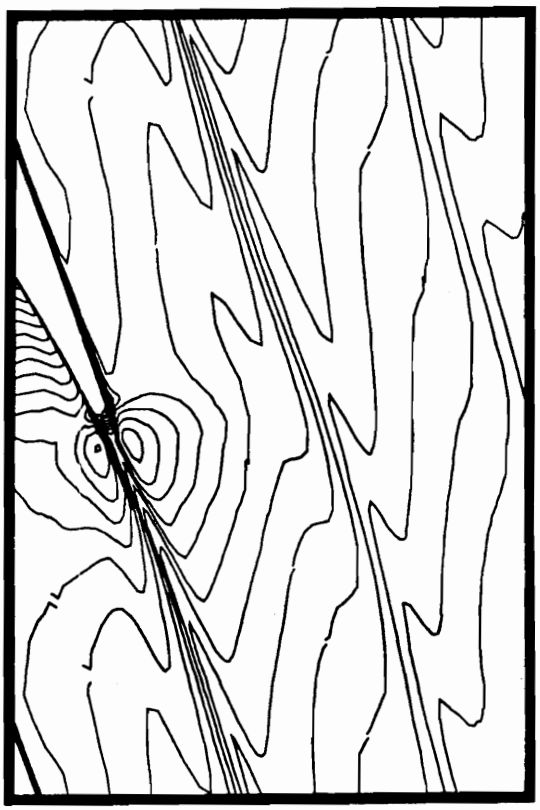


Fig.4.73 Numerical interferogram, $M_e = 0.8$, setup of Fig.3.17d



Fig.4.74 Interferogram, $M_e = 0.9$, setup of Fig.3.17d



Fig.4.75 Numerical interferogram, $M_e = 0.9$, setup of Fig.3.17d



Fig.4.76 Interferogram, $M_e = 1.0$, setup of Fig.3.17d

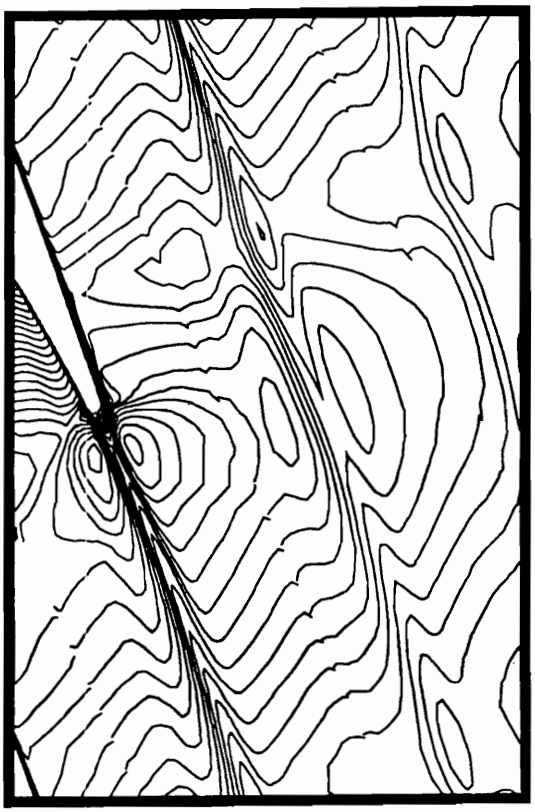


Fig.4.77 Numerical interferogram, $M_e = 1.0$, setup of Fig.3.17d



Fig.4.78 Interferogram, $M_e = 1.1$, setup of Fig.3.17d



Fig.4.79 Numerical interferogram, $M_e = 1.1$, setup of Fig.3.17d

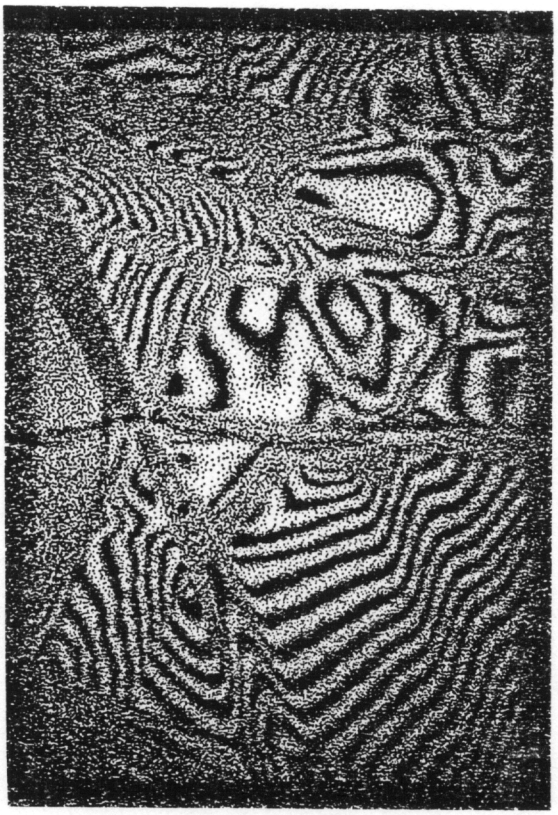


Fig.4.80 Interferogram, $M_e = 1.2$, setup of Fig.3.17d

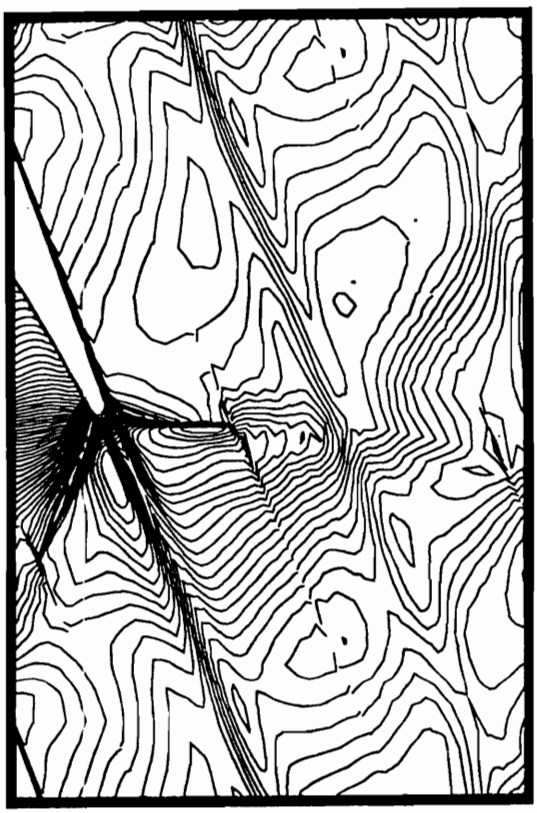


Fig.4.81 Numerical interferogram, $M_e = 1.2$, setup of Fig.3.17d



Fig.4.82 Interferogram, $M_e = 1.28$, setup of Fig.3.17d

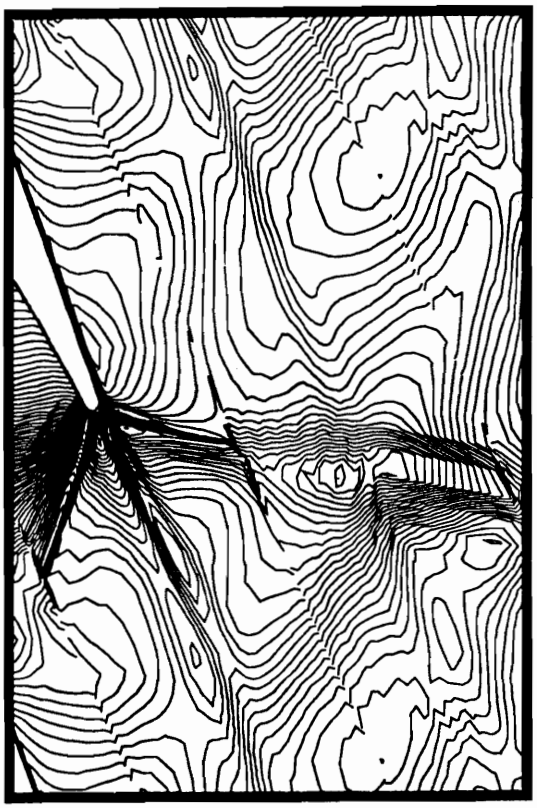


Fig.4.83 Numerical interferogram, $M_e = 1.28$, setup of Fig.3.17d

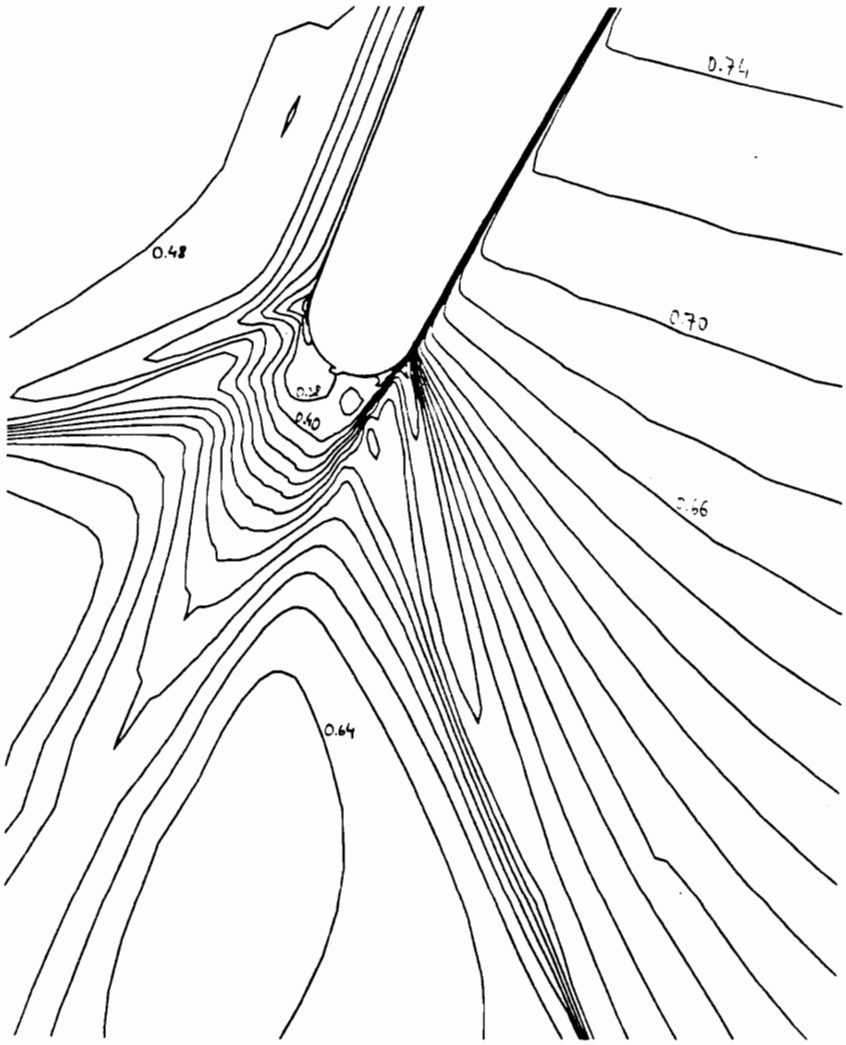


Fig.4.84 Calculated density contours, large blade, $M_e = 1.2$

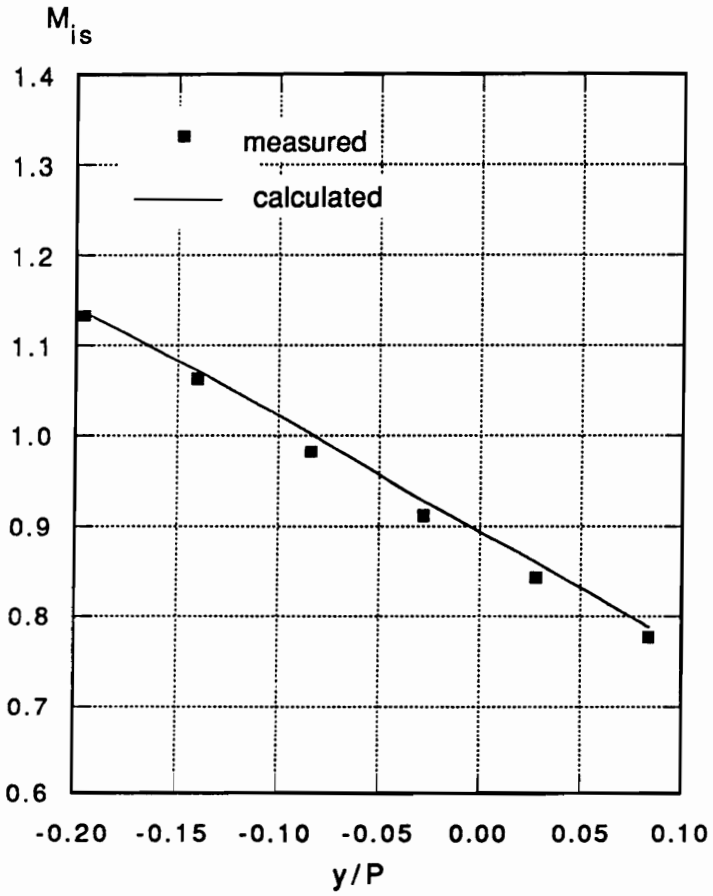


Fig.4.85 Isentropic Mach number, large cascade, $M_e = 1.2$, $x/c = -0.250$

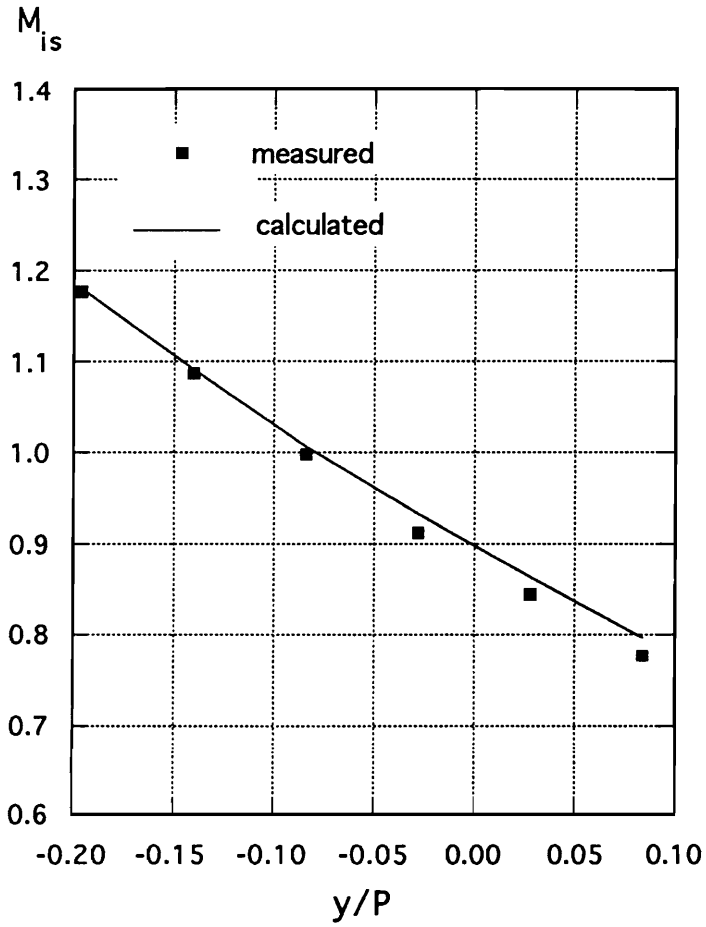


Fig.4.86 Isentropic Mach numbers, large cascade, $M_e = 1.2$, $x/c = -0.162$

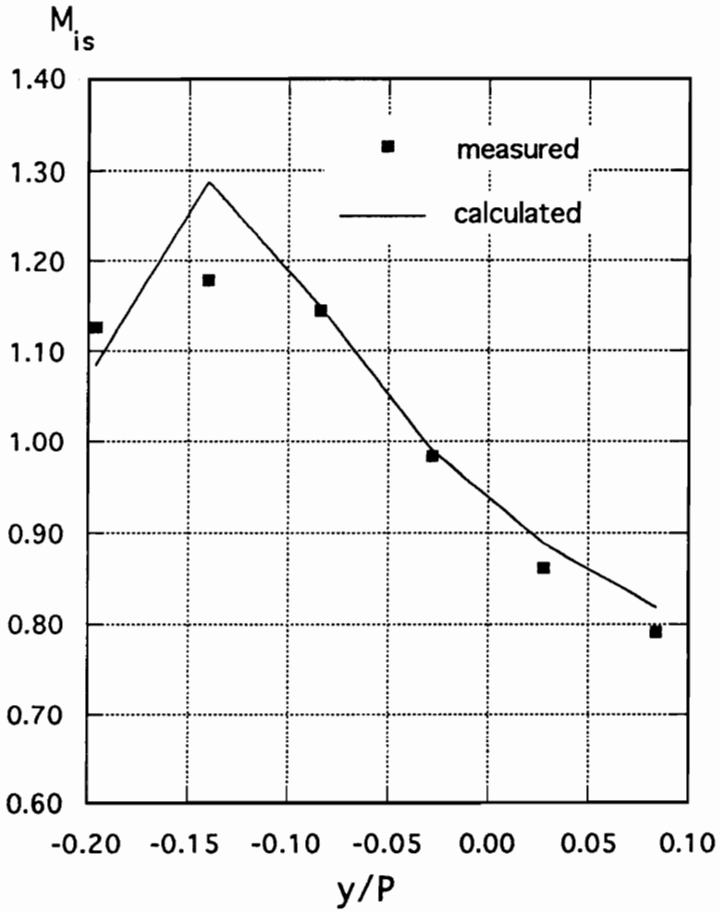


Fig.4.87 Isentropic Mach numbers, large cascade, $M_e = 1.2$, $x/c = -0.074$

VITA

The author was born on June 22, 1963 in Budapest, Hungary. He graduated from the high school "Moricz Zsigmond Gimnazium", located in Budapest, in 1981. After serving one year in the hungarian army, T. Kiss started his studies in Mechanical Engineering at the Technical University of Budapest. At the end of a five year program in 1987, he earned his Master of Science degree in the special field of "Mathematical Engineering". Then, he started working toward his Ph.D. degree in Fluid Dynamics at the same university. However, he wanted new challenges, and when the opportunity was given to him in 1989, he came to the United States to start a new Ph.D. program at VPI & SU in Aerospace Engineering.

Tibor Kiss